

UNIVERSITY OF SOUTHAMPTON
FACULTY OF ENGINEERING AND PHYSICAL SCIENCES
Optoelectronics Research Centre

**Design and simulation of integrated photonic devices based on tilted
Bragg gratings**

by

Mathias Weisen

Thesis for the degree of Doctor of Philosophy

January 2021

UNIVERSITY OF SOUTHAMPTON

ABSTRACT

FACULTY OF ENGINEERING AND PHYSICAL SCIENCES

Optoelectronics Research Centre

Doctor of Philosophy

DESIGN AND SIMULATION OF INTEGRATED PHOTONIC DEVICES BASED
ON TILTED BRAGG GRATINGS

by Mathias Weisen

Integrated photonics is a versatile technology in which optical components are integrated in a single photonic chip. This has a wide range of applications including in telecommunications, optical information processing and quantum computing. A highly flexible integrated photonics platform has previously been developed at the ORC for inscribing waveguides and tilted Bragg gratings. It has previously been used to implement devices using tilted gratings such as polarizers, spectrometers and refractometers. The potential has been identified for using this platform to implement more complex devices employing tilted Bragg gratings. For this reason, it is interesting to explore the full capabilities of this platform and see if it could be used to implement optical information processing.

In this thesis, I theoretically investigate new devices employing tilted Bragg gratings and simulate their implementations in this platform. I begin by deriving an analytical expression relating the scattering efficiency of a tilted grating to its parameters and light wavelength and I have found good agreement with numerical simulations for a moderate grating width and tilt angle.

I present a new class of devices based on two parallel single-mode waveguides in a single ridge structure. The waveguides contain tilted gratings that couple the light between them using the modes of the ridge. These devices have potential application in optical information processing and are investigated analytically and numerically using coupled mode theory.

A version of this device employing single-mode waveguides and a backward propagating cladding mode is investigated with a theoretical maximum transfer efficiency of 100%. I find that this device exhibits grating induced transparency and has high robustness to temperature and to phase-error noise. I find that, with realistic fabrication tolerances and the use of a refractive index oil, the device is theoretically fabricable. I present the results of simulations with the parameters intended for fabrication in this thesis.

In order to increase the number of inputs and outputs and thus achieve more complex information processing, I present a version of this device involving two-mode waveguides, and show that I am able to achieve a mode division multiplexer and an arbitrary power splitter. By concatenating individual transformations, I am able to achieve any 4×4 arbitrary unitary matrix.

Finally, I present a novel device exploiting both directions of propagation of two single-mode waveguides in order to unlock more degrees of freedom in a compact device. By attaching circulators to the waveguide end facets, I can achieve a device with four input and four output ports. I identify four fundamental grating-based couplers on this device that can be concatenated to achieve any 4×4 symmetric unitary transfer matrix. I present the implementation of a compact Walsh-Hadamard gate based on superimposed gratings that can be achieved on this platform and show that an entire class of transformations can be similarly implemented.

Contents

Acknowledgements	19
Declaration of Authorship	21
1 Introduction	23
2 Background	27
2.1 Fundamental Physics	27
2.1.1 Optical Waveguides	27
2.1.1.1 Mode analysis	28
2.1.2 Bragg gratings	31
2.1.2.1 As a reflector array	32
2.1.2.2 As an array of pointlike scatterers	33
2.1.3 Applications of the different models	34
2.2 Analytical and Numerical Methods	35
2.2.1 The beam tracing approach for tilted gratings	35
2.2.2 Coupled mode theory	36
2.2.2.1 Two mode coupling - Counter-propagating modes	39
2.2.3 Transfer matrix method	41
2.2.4 Finite element method	43
2.2.5 Finite difference time domain	43
2.2.6 Beam propagation method	44
2.2.7 The methods we choose	44
2.3 Integrated Photonic Devices	45
2.3.1 Waveguide-to-waveguide Couplers	45
2.3.1.1 Evanescent directional couplers	45
2.3.1.2 Grating assisted and grating frustrated couplers	46
2.3.1.3 Long period waveguide-grating couplers	47
2.3.1.4 Radiation mode-based polarisers and polarising couplers	47
2.3.1.5 Multimode interferometers	48
2.3.2 Other devices based on Bragg gratings	49
2.3.2.1 Beam focusing and spectrometry with a chirped grating	49
2.3.2.2 Phase-shifted gratings	50
2.3.3 Phase-shifters and Mach-Zehnder interferometers	50
2.3.3.1 Thermo-optic phase-shifters	50
2.3.3.2 Mach-Zehnder interferometers	51
2.3.4 Integrated optical computing	51

2.4	Fabrication methods for devices investigated in this thesis	53
2.4.1	Why silica?	53
2.4.2	Flame hydrolysis deposition	56
2.4.3	Photosensitivity and UV-writing	57
2.4.4	Micromachining	59
3	Coupling from waveguide modes to in-chip radiation modes by a tilted Bragg grating	61
3.1	Introduction	61
3.2	Analytical solution	62
3.3	Numerical Model	66
3.3.1	Finite element simulation	66
3.3.2	Postprocessing	68
3.4	Results and Analysis	70
3.4.1	Mode Analysis of Gaussian Waveguide	70
3.4.2	Single-mode - narrow grating	72
3.4.3	Parameter scans of simulations, comparison with analytical equation	76
3.5	Conclusion	77
4	Cladding mode-based waveguide coupler	79
4.1	Introduction	79
4.2	Analytical solution to the three mode problem	81
4.2.1	General analytical solution to the three mode problem	82
4.2.2	Phase-selective grating induced transparency	87
4.3	Numerical model and methods	87
4.4	Numerical simulations using a BVP solver	90
4.4.1	Mode Analysis and coupling coefficients	91
4.4.2	Coupling to cladding modes using one grating	93
4.4.2.1	Numerical simulations	94
4.4.2.2	Comparison with analytical solution to two mode coupling	95
4.4.3	Coupling of two waveguides by cladding modes	96
4.4.3.1	Numerical simulations	96
4.4.3.2	Sensitivity of the device to its length	99
4.5	Numerical simulations using an eigenvalue method	100
4.5.1	Standardised parameters used	101
4.5.2	Numerical results	101
4.5.3	Bandwidth Control	104
4.5.4	Thermal stability	107
4.5.5	Tolerance to fabrication parameters	109
4.5.6	Using apodized gratings	111
4.5.7	Using phase-shifts to simulate grating "noise"	112
4.6	Using parameters intended for device fabrication and tuning	117
4.6.1	Standardised parameters used	117
4.6.2	Effect of the external oil	119
4.6.3	Fabrication tolerances to waveguide asymmetries	121
4.6.4	Group delay	122
4.7	Conclusion	125

5	Mode division multiplexing, interferometry and power splitting	127
5.1	Introduction	127
5.2	Mode analysis with two-mode waveguides	129
5.3	Standardised parameters	131
5.4	Mode division multiplexing	132
5.5	Four-port interference device	133
5.5.1	Analytical Solution for five-mode problem	133
5.5.2	Four-way power splitting	137
5.6	Implementation of any arbitrary 4×4 unitary matrix	138
5.7	Conclusion	141
6	Four-port device based on counter-propagating waveguide modes	143
6.1	Introduction	143
6.2	Numerical device model	145
6.3	Analytical solutions to the six-mode problem and transfer matrices	148
6.3.1	General analytical solution to the six-mode problem	148
6.3.2	Analytical derivations of "fundamental" transformations with transfer matrices	152
6.3.2.1	Standard Bragg gratings in either waveguides	152
6.3.2.2	Long-period waveguide-to-waveguide couplers	153
6.3.2.3	Counter-directional coupler based on a long- and a short-period grating in different waveguides	154
6.3.2.4	Phase shifts	155
6.3.3	Transforming the matrices into unidirectional form	155
6.3.4	Construction of an arbitrary symmetric unitary matrix	158
6.3.5	Symmetric unitary matrix examples	161
6.3.6	Compact transformations using superimposed gratings	164
6.4	Long-period wide-angle tilted waveguide gratings	167
6.4.1	Coupling coefficients vs tilt angle	167
6.4.2	Coupling to cladding modes	168
6.4.3	Tilted long-period waveguide grating couplers	169
6.5	Counter-directional waveguide-to-waveguide coupling using both long- and short-period waveguide gratings	174
6.5.1	Propagation properties and bandwidth	174
6.5.1.1	Gratings of equal coupling coefficients	174
6.5.1.2	Short-period grating weaker than the long-period grating	176
6.5.2	Effect of grating phase mismatch	179
6.6	Compact Walsh-Hadamard transform	183
6.6.1	Effect of grating phase mismatch	183
6.7	Numerical method for finding compact transformations	185
7	Conclusions and Future Work	189
7.1	Conclusion	189
7.2	Future Directions for Research	191
A	Publications	195
	References	197

List of Figures

2.1	Schematic of a channel waveguide inside a raised index planar core layer. The light propagates in the z direction, is confined in the y direction by the planar layer and in both the x and y direction by the channel waveguide. The lower index regions are the underclad and overclad which we define in the later Section 2.4.2.	28
2.2	Individual Fresnel reflections from a Bragg grating. Here, we assume the simplest case when the grating consist of regions of alternating high (black) and low (white) refractive index that are equally spaced out and of equal size. Reflections occur at each change in refractive index with a π phase shift if the refractive index increases but not if it decreases. If all reflections interfere constructively, Bragg reflection will occur.	32
2.3	Individual reflections from two planes of a grating one grating period apart with tilt angle θ and period Λ_g . Light reflected from the second plane travels an extra distance of $\Lambda_g + \delta$ before travelling parallel to the first beam.	33
2.4	Coupling of modes to backwards propagating modes and cladding modes with a grating.	34
2.5	Scattering from a point-like grating. The angle between the incident and scattered radiation α is dependent on the light wavelength in the grating and the grating period. Scattering occurs in both directions defined by that angle. Λ_g is now the distance between the pointlike scatterers.	34
2.6	Evanescent directional coupler between two waveguides.	46
2.7	Grating frustrated directional coupler between two waveguides.	47
2.8	A long-period waveguide grating coupler between two waveguides.	47
2.9	A grating based polarising waveguide-to-waveguide coupler between two waveguides. Also shown is the mechanism for splitting the polarisations.	48
2.10	A selection of MMIs connected to single modes waveguides via input and output ports. With (a) connecting one input port to one output port, (b) connecting one input port to three output ports, (c) connecting two input ports to two output ports.	49
2.11	Chirped grating used for focusing a beam onto a single spot. Note that to avoid aberrations, one must used the spatial chirp given by Equation (18) of (Field 2020).	50
2.12	Optical information processing chip for implementing an $N \times N$ unitary matrix. Mach-Zehnder interferometers are depicted as crosses. The scheme presented in this picture is the one used in Carolan 2016.	52
2.13	Silica wafer produced through flame hydrolysis deposition. Shown are the substrate, core, underclad and overclad layers.	57

2.14	Image courtesy of (Sima thesis). (a) UV-writing system for simultaneous inscription of waveguides and Bragg gratings. The sample is placed on top of an air-bearing translation stage which allows the fabrication of Bragg gratings with highly precise grating periods. (b) Interference of the two beams creating an interference pattern in which the grating is fabricated.	59
3.1	In (a), addition of reflections from individual planes for a non 45° grating. Discrete planes shown in (b) are those separated by n planes from one another. The ray at $x = 0$ hits the m th plane at $z = z_p$	62
3.2	Spectral response of the grating ($\theta = 10^\circ$) for different values of $w_1 K_g$. When $w_1 K_g$ is larger, the bandwidth becomes smaller and the response more Gaussian.	66
3.3	These plots show the spectral response of the grating ($w_1 K_g = 10$) for different values of θ . When θ is larger, the bandwidth becomes greater and the response more Gaussian.	66
3.4	Refractive index along centre of simulated waveguide and grating in the z -dimension as shown in Figure 3.5. This is with top-hat (a, $L = 80\mu m$) and super-Gaussian (b, $\varsigma = 40\mu m$) apodization. Note, the modulations visible in (a) and to some extent in (b) are the result of undersampling.	68
3.5	(a) 3D schematic of the device showing the core layer containing the waveguide and grating on top of the underclad and substrate. The overclad is not shown in this picture. (b) Geometry of the simulated model inside of the core layer, showing waveguide, start and end of grating, input port and cross sections for measurement of output power flow. Blue are the perfectly matched layers (PMLs) that act as near perfect absorbers of electromagnetic waves. Note that the waveguide width shown on the graph is 4σ or double the $1/e$ waveguide diameter.	69
3.6	Effective refractive indices of fundamental (blue) and first (green) and second (red) higher order modes of a Gaussian waveguide of width $\sigma = 1.5\mu m$ against grating depth.	71
3.7	Threshold of second-order mode against waveguide width.	71
3.8	Shape of input mode with Gaussian fit and waveguide outline for various values of σ . The width of the mode w_0 and the effective width w_1 are shown on each figure. $\delta n = 0.01$	71
3.9	Beam width (a) and effective width (b) of mode of waveguide with Gaussian-index profile with $\delta = 0.01$ as the width of the waveguide is increased.	72
3.10	Electric field (z -component) inside the simulate area of the core layer, defined in Figures 3.5(a) and 3.5(b), of light scattered by a gratings with a selection of grating periods and apodization profiles. Here (a, b) show backreflection into the counter-propagating waveguide mode with $\Lambda_g = 530nm$, (c, d) show scattering out of the waveguide at resonance with $\Lambda_g = 540nm$ and (e, f) show scattering off-resonance at a higher angle and with lower scattering efficiency with $\Lambda_g = 620nm$. Results using both Top-hat (a, c, e) and super-Gaussian apodization (b, d, f) are shown for comparison with better beam collimation in the latter case. The diagonal black lines are the lines along which the Poynting vector is integrated to calculate the power flowing through them. On the right shows the colour scale for the electric field strength (normalised) that applies to all figures.	74

3.11	Graphs of reflectance (a), transmittance (b), back-reflectance (c) and secondary (downwards) reflectance (d) against grating period for both top-hat and Super-Gaussian apodization.	75
3.12	Graph of angle of scattered radiation against grating period for a top-hat (a) and super-Gaussian apodized (b) grating.	75
3.13	Graphs of reflectance (a) and back-reflectance (b) against input wavelength for different grating widths and constant tilt angle (20°). Solid are the computational results and dotted are the results from Equation (3.11).	76
3.14	Graphs of reflectance (a) and back-reflectance (b) against input wavelength for different tilt angles and constant grating width ($\sigma = 1.5\mu m$). Solid are the computational results and dotted are the results from Equation (3.11).	77
4.1	Schematics of the cladding mode-based waveguide coupler showing (a) a 3D model of the device showing the ridge structure, the photosensitive core layer and the two single-mode waveguides and gratings and (b) a cross section inside the core layer superimposed with a ray diagram of the two waveguides and gratings coupled together by a cladding mode.	80
4.2	Transverse index profile inside the photosensitive core layer with two channel waveguides (waveguide depth exaggerated to make them easier to see).	88
4.3	Mode plots of the device with symmetric (a) and antisymmetric (b) core modes as well as two cladding modes (c-d). The waveguides have a depth of $\delta n = 0.01$, a width of $\sigma = 2.0\mu m$, are at a distance of $x_0 = 10\mu m$ from the centre and the cladding has a width of $W = 34\mu m$	91
4.4	Effective refractive index against mode number with $\delta n = 0.01$, $\sigma = 2.0\mu m$, $x_0 = 10\mu m$ and $W = 34\mu m$	92
4.5	(a) Coupling coefficients of the grating in waveguide 0 between the core mode of waveguide 0 and selected cladding modes as a function of K_t . With a grating in both waveguides, overlaid coupling coefficients (b) between the two waveguides and a cladding mode (35). Curves are indistinguishable as the coupling coefficients are identical. Plots in (c) are of the coupling coefficient against mode number for different values of K_t . $\delta n = 0.01$, $\sigma = 2.0$, $x_0 = 10\mu m$, $W = 34\mu m$	93
4.6	Results of numerical simulations of the reduced ("full") system with $\Lambda_g = 587.3nm$, $\theta = 17.19^\circ$ and $\delta n_g = 0.0025$ and eleven cladding modes on top of the core mode. Overlaid where applicable, results of numerical simulations with only two core modes and the resonant cladding mode of number 35. There is a near perfect match. The system is phase matched so the exponential behaviour seen here is expected.	95
4.7	Plots of (transformed) amplitudes (left) and phases (right) of the core (top) and cladding (number 35, bottom) modes. Parameters used are $\Lambda_g = 587.0nm$, $\theta = 17.19^\circ$ and $\delta n_g = 0.005$	96
4.8	Graphs showing the amplitudes of the top and bottom waveguide modes as well as the 35th cladding mode for the "full" system with eleven cladding modes on top of the core mode as well as the system with just three modes. Parameters used are $\Lambda_g = 587.3nm$, $\theta = 17.19^\circ$ and $\delta n_g = 0.0025$. Also (bottom right) graph showing the amplitude of the top waveguide mode with $\delta n_g = 0.0001$	97

4.9	Graphs results showing the amplitudes of the top and bottom waveguide modes as well as the 35th cladding mode for the "full" system with eleven cladding modes on top of the core mode as well as the system with just three modes. Parameters used are $\Lambda_g = 587.0nm$, $\theta = 17.19^\circ$ and $\delta n_g = 0.0025$. Also (bottom right) graph showing the amplitude of the top waveguide mode with $\Lambda_g = 587.15nm$	98
4.10	Mode amplitude in waveguide 0 with $\theta = 17.19^\circ$ and $\delta n_g = 0.005$ and $\Lambda_g = 587.3nm$. This graph shows that the output power of waveguide 0 deviates slightly from the 25% that is analytically predicted. This is a result of numerical error.	98
4.11	Plots of the power in the top waveguide and in the cladding for $\Lambda_g = 586.8nm$, $\theta = 17.19^\circ$ and $\delta n_g = 0.005$. The length is changed by integer multiples of the core to cladding coupling period which keeps the behaviour the same.	99
4.12	Using $\Lambda_g = 586.8nm$, $\theta = 17.19^\circ$ and $\delta n_g = 0.005$, the filled area shows the full spectrum of possible behaviours of the top waveguide as the device length is changed. This is a key result as it shows that despite the dependence on $\sin \Omega L$ and $\cos \Omega L$ of the analytical solution it is possible to design grating based waveguide couplers whose coupling properties are very stable with the device length.	100
4.13	Graphs showing the power propagating through the top and bottom waveguide modes as well as the 35th cladding mode for (a) $\lambda_0 = 1.55\mu m$ (inside the bandgap) and (b) $\lambda_0 = 1.54975\mu m$ (outside the bandgap). We plot the numerical solution of the system with all cladding modes on top of the core modes (solid) alongside the results from the analytical solution (dashed).	102
4.14	Power output of waveguide 0 (blue) and waveguide 1 (red) as the wavelength is swept around the Bragg wavelength.	103
4.15	Wavelength dependence of the frequency terms 2Ω , $\Delta K/2 - \Omega$ and $\Delta K/2 + \Omega$ outside of the bandgap.	103
4.16	Evolution of propagating power in the two core waveguide modes and in the resonantly coupled cladding mode (35th mode) with parameters chosen such that there is as close as possible to complete transfer between the waveguides by supporting n cladding mode oscillations. Solid curves are a numerical solution including all cladding modes, dashed curves are the analytical solution including only one cladding mode. Here, the parameters are (a) $\Lambda_g = 587.409nm$, $L = 9.737mm$ (b) $\Lambda_g = 587.420nm$, $L = 12.570mm$ and (c) $\Lambda_g = 587.432nm$, $L = 14.873mm$	105
4.17	Fractional output power from waveguides 0 (blue) and 1 (red) as a function of wavelength where at the input light is launched only into waveguide 0. Parameters are $\Lambda_g = 587.409nm$, $L = 9.737mm$	106
4.18	Dependence of the bandwidth of the device (full-width half maximum) on (a) the index contrast of the gratings and its length and (b) the tilt angle of the gratings.	107

4.19	Plot of the wavevectors against temperature showing (black) the sum of the propagation constants of the core and cladding mode (blue and green, dashed) the contributions from the core and cladding mode respectively and (red), the grating wavevector. Parameters are (at $T = 300K = 26.85^\circ C$) $W = 34.0\text{ nm}$, $x_0 = 10.0\text{ nm}$, $\sigma = 2.0\text{ }\mu\text{m}$, $\Lambda_g = 585.068\text{ nm}$, $\alpha_L = 5.5 \times 10^{-7}/K$, $\lambda_B = 1.55\text{ }\mu\text{m}$ and refractive index given by Leviton 2006 (citation in text).	108
4.20	Fractional output power from waveguides 0 (blue) and 1 (red) as a function of temperature where at the input light is launched only into waveguide 0. Parameters are $\Lambda_g = 587.34\text{ nm}$, $\theta = 17.23^\circ$, $L = 20\text{ mm}$, $\delta n_g = 0.001$, $\lambda_0 = 1.55\text{ }\mu\text{m}$.	109
4.21	Power output of waveguides 0 (blue) and 1 (red) as a function of device width for $\Lambda_g = 587.409\text{ nm}$ and $L = 9.737\text{ mm}$.	110
4.22	Power propagation with apodized grating index contrast defined by Equations (4.30) and (4.31) in text with $\delta n_{g,0} = 0.001$ and $z_0 = 20\text{ mm}$. We use super-Gaussian orders $n_{SG} = 1$ (a), 2 (b), 4 (c) and 10 (d)	112
4.23	Power output of waveguide 0 (blue), waveguide 1 (red) and the backwards propagating cladding mode (black) as the wavelength is swept around the Bragg wavelength. We use the same parameters as Figure 4.22 with $n_{SG} = 2$.	113
4.24	Power output from both waveguide with "noisy" gratings composing of $N = 100$ segments with a noise amplitude of $\sigma_\phi = 0.1$ (top) and $\sigma_\phi = 1.2$ (bottom). Both sets of noise have been generated from the same seed.	114
4.25	Power output from both waveguide with "noisy" gratings composing of $N = 40000$ segments with a noise amplitude of $\sigma_\phi = 0.1$ (top) and $\sigma_\phi = 1.2$ (bottom). Both sets of noise have been generated from the same seed.	115
4.26	Power output from both waveguide with "noisy" gratings composing of $N = 4000$ segments with a noise amplitude of $\sigma_\phi = 0.1$ (top) and $\sigma_\phi = 1.2$ (bottom). Both sets of noise have been generated from the same seed.	116
4.27	Dimensions and refractive indices of the wafers available that could be used for fabricating the device. We chose the wafer NB15 on the right.	118
4.28	Waveguide outputs with external oil index varied. In (a), $\Lambda_g = 545.652\text{ nm}$, $\theta = 8.60^\circ$ and $L = 19.167\text{ mm}$ and the 33^{rd} cladding mode is used. In (b), $\Lambda_g = 548.861\text{ nm}$, $\theta = 9.65^\circ$ and $L = 19.076\text{ mm}$ and the 37^{th} cladding mode is used. Finally, in (c) $\Lambda_g = 551.518\text{ nm}$, $\theta = 10.42^\circ$ and $L = 19.058\text{ mm}$ and the 40^{th} cladding mode is used.	120
4.29	Output power of waveguide 1 as a function of external index oil and device length.	120
4.30	Maximum output power of waveguide 1 as a function of device length that can be achieved for any external oil index within the range $1.32 - 1.36$.	121
4.31	Power output of waveguide 0 (blue) and waveguide 1 (red) against the position of waveguide 1 (labelled a here) where $a_0 = 16\text{ }\mu\text{m}$ is the position of waveguide 0.	122
4.32	Power output of waveguide 0 (blue) and waveguide 1 (red) against the index contrast of waveguide 1 (labelled δn here) where $\delta n_0 = 16\text{ }\mu\text{m}$ is the index contrast of waveguide 0.	122
4.33	Group delay at outputs of waveguide 0 (left) and waveguide 1 (right).	123
4.34	GVD outputs of waveguide 0 (left) and waveguide 1 (right).	124

5.1	(top) 3D model of the device including, ridge structure, core layer and channel waveguides. Also, fundamental and high-order core modes. The superimposed gratings aren't shown here. (middle) Same as top left but showing the cladding mode instead of the core modes. (bottom) Cross section of device inside the core layer, showing waveguides and superimposed Bragg gratings with ray diagram of light in both modes, with (as an example) the fundamental mode of waveguide 0 coupled to the cladding mode and the higher-order mode of waveguide 0 transmitted.	128
5.2	Effective indices against waveguide width. Here $W = 34\mu m$, $x_0 = 10\mu m$. The different colours represent the different modes with blue and green (who are close together) representing the 0th and 1st modes, i.e. the symmetric and anti-symmetric superpositions of the fundamental waveguide modes. Red, cyan, violet, yellow, black, blue (dashed) and green (dashed) represent, in order, modes 2 to 8.	130
5.3	Effective indices against waveguide distance from center. $W = 2x_0 + 14\mu m$, $\sigma = 4\mu m$. The colours represent the same modes as Figure 5.2 with the addition of modes 9 and 10 in red (dashed) and cyan (dashed).	130
5.4	Difference between effective indices of both waveguides against waveguide distance from center for the higher order waveguide modes, 2 and 3. $W = 2x_0 + 14\mu m$, $\sigma = 4\mu m$	131
5.5	Coupling coefficient vs tilt angle between the fundamental (blue) and higher-order (red) waveguide modes and a selection of cladding modes. Here we use $W = 54\mu m$, $\sigma = 4.0\mu m$, $x_0 = 20\mu m$ and $\Lambda_g = 584.947nm$ (blue) and $\Lambda_g = 586.121nm$ (red).	131
5.6	Power output of waveguide 1 against wavelength with fundamental (blue) and higher-order (red) mode of waveguide 0 pumped with gratings in both waveguide of period $\Lambda_g = 584.947nm$ (a) and $\Lambda_g = 586.121nm$ (b).	132
5.7	Power output of mode 0 of waveguide 0 (blue) and all three other modes (red) against light wavelength with all four gratings of index contrast $\delta n_g = 0.001$ and therefore of equal coupling coefficient ($c = d = e = f$).	137
5.8	Power propagation through device in mode 0 of waveguide 0 (blue), all other waveguide modes (violet) and backward propagating cladding mode (red). Here we have superimposed gratings in each waveguide of periods $\Lambda_g = 585.014nm$ and $586.189nm$, grating index contrast of $\delta n_g = 0.001$ and device length of $L = 10.190mm$	138
5.9	Power output of mode 0 of waveguide 0 (blue) and every other core mode (red) as wavelength is swept. Here we have superimposed gratings in each waveguide of periods $\Lambda_g = 585.014nm$ and $586.189\mu m$, grating index contrast of $\delta n_g = 0.001$ and device length of $L = 10.190mm$	138
5.10	Power propagation through device in mode 0 of waveguide 0 (blue), in mode 1 of waveguide 0 (cyan), mode 0 of waveguide 1 (green), in mode 1 of waveguide 1 (magenta) and the backward propagating cladding mode (red). The device parameters for the respective plots are found in Table 5.1	139
6.1	(a) 3D Schematic of integrated four-port waveguide coupler exploiting both directions of propagation (superimposed gratings and circulators not shown). (b) Cross section and ray diagram of coupler inside the core layer including superimposed long- and short-period gratings and the circulators. We colour the tilted long- and short-period gratings in cyan and black respectively and label the inputs and outputs of the circulators.	144

6.2	Concatenated coupler used to implement any arbitrary symmetric unitary matrix. In the red boxes we show the individual couplers that make up the device including, from left to right, a standard Bragg grating in waveguide 1, a counter-directional coupler of the sort we introduced in Section 6.3.2.3 consisting of a long-period grating in waveguide 0 and a short-period grating in waveguide 1, a standard Bragg grating in waveguide 0 and a long-period waveguide-to-waveguide coupler. The phase shifts between the individual blocks are not shown. Shown also are the circulators connected to the waveguide that are used to separate the input and output light fields.	161
6.3	(top) 3D schematic of a CNOT gate implemented on this platform (external phase shift not shown). It consists of a single Bragg grating in waveguide 0. (bottom) Truth table of the quantum gate. The two left columns represents the states of the qubits at input whereas the right column represents their states at the outputs. Qubit Q_0 is implemented in at which side of the device the photon is inputted or detected, qubit Q_1 is implemented in which waveguide the photon is.	164
6.4	Refractive index distribution of a waveguide and long-period waveguide grating against propagating direction (horizontal) and transverse direction (vertical). Axes show position in μm . The colour bar shows refractive index levels.	167
6.5	Coupling coefficient of long-period waveguide grating for a selection of cladding modes as the tilt angle is varied. Grating period is different for each cladding mode that coupled to in order that the gratings are always longitudinally phase-matched and is given by $117\mu m$ for mode 5, $32.1\mu m$ for mode 15 and $12.3\mu m$, $6.20\mu m$ and $3.56\mu m$ for modes 25, 35 and 45 respectively.	168
6.6	Power propagation in core mode (blue) and forward propagating cladding mode (magenta) for a device with a single long-period waveguide grating in one of the waveguides. Here, $\lambda_0 = 1.55\mu m$ (a) and $\lambda_0 = 1.548\mu m$ (b).	169
6.7	power output of core mode and cladding mode for a device with a single long-period waveguide grating in one of the waveguides.	169
6.8	Power propagation in core modes of waveguide 0 (blue) and 1 (green) and forward propagating cladding mode (magenta) for a device with identical long-period waveguide grating in each waveguides. Here, $\lambda_0 = 1.55\mu m$ (a) and $\lambda_0 = 1.548\mu m$ (b).	170
6.9	Power output of core modes (blue and green for waveguide 0 and 1, respectively) and cladding mode (magenta) for a device with identical long-period waveguide grating in each waveguide. In the two devices the length is $L = 20mm$ (a) and $L = 5.623mm$ (b).	171
6.10	Power propagation in core mode of waveguide 0 (blue), of waveguide 1 (green), and forward propagating cladding mode (magenta) for a device with one long-period waveguide grating in each waveguides. The gratings in waveguides 0 and 1 have $\delta n_g = 0.001$ and $\delta n_g = 0.0004142$ respectively in (a) and switched round in (b). Here, $L = 40mm$	172
6.11	Power output of core mode and cladding mode for a device with a long-period waveguide grating in each waveguide. Here, we have the same parameters as in Figure 6.10 except with $L = 7.346mm$	173

6.12	Grating index contrast ratio and device length required to achieve any desired power splitting with a long-period waveguide-to-waveguide coupler. Here, $\delta n_{g,0} = 0.001$ is the grating index contrast of one of the gratings and δn_g is the grating index contrast of the other.	173
6.13	Power propagation of the forward propagating core mode of waveguide 0 (blue), the backward propagating core mode of waveguide 1 (yellow) and either the forward (magenta) or backward (red) propagating cladding mode a device with a long-period waveguide grating in one waveguide and a short-period grating in the other. With a long-period grating in waveguide 0 and a short-period grating in waveguide 1, we present the numerical results with a length of $L = 20mm$ (a) and $L = 50mm$ (b). With the gratings swapped we present the results with a length of $L = 20mm$ (c) and $L = 50mm$ (d).	175
6.14	Power propagation in forward propagating core mode of waveguide 0 (blue), the backward propagating core mode of waveguide 1 (yellow) and forward propagating cladding mode (magenta) for a device with a long-period waveguide grating in one waveguide and a short-period grating in the other. We use a light wavelength of $\lambda_0 = 1.5498\mu m$ in order to show the behaviour away from phase-matching. We pump waveguide 0 in the forward propagating direction. With a long-period grating in waveguide 0 and a short-period grating in waveguide 1, we present the numerical results with a length of $L = 50mm$	176
6.15	Power output of core mode and cladding mode for a device with a period waveguide grating in one waveguide and a short period grating in the other. Here, blue is the power output of the core mode of waveguide 0 in the forward direction, yellow is that of waveguide 1 in backwards direction, and magenta and red are that of the cladding mode in the forwards and backwards direction respectively where applicable. In both cases, we use a length is $L = 50mm$. In (a) we pump the waveguide with the long-period grating and in (b) the waveguide with the short-period grating.	177
6.16	Power propagation in forward propagating core mode of waveguide 0 (blue), the backward propagating core mode of waveguide 1 (yellow) and forward propagating cladding mode (magenta) for a device with a long-period waveguide grating in one waveguide and a short-period grating in the other. The long-period grating has a grating index contrast of 0.001, whereas the short-period grating has a grating index contrast of 0.0004142. With a long-period grating in waveguide 0 and a short-period grating in waveguide 1, we present the numerical results with a length of $L = 8.734mm$ (a), $L = 26.200mm$ (b) and $L = 43.668mm$ (c). With the gratings swapped we present the results with a length of $L = 8.7336mm$ (d).	178
6.17	Power output of core modes and cladding mode for a device with a long-period waveguide grating in one waveguide and a short period grating in the other. The device parameters are the same as in Figure 6.16. The length of the device is $L = 17.467mm$. In (a) we pump the waveguide with the long-period grating and in (b) the waveguide with the short period grating.	179

6.18	Grating index contrast ratio and device length required to achieve any desired power splitting with a waveguide-to-waveguide coupler consisting of a long-period grating in one waveguide and a short-period grating in the other. Here, we use $\delta n_{g,0} = 0.001$ as the grating index contrast of the long-period grating and define δn_g to be the index contrast of the short-period grating.	180
6.19	Power output of waveguide 0 in the co-propagating direction (a) and waveguide 1 in the counter-propagating direction (b) for a device with a long-period grating in one waveguide and a short period grating in the other. The gratings have equal index contrast.	181
6.20	Power output of waveguide 0 in the co-propagating direction (a) and waveguide 1 in the counter-propagating direction (b) for a device with a long-period grating in one waveguide and a short period grating in the other. Here, the gratings have unequal index contrast and the parameters are the same as in Figure 6.16	182
6.21	Power propagation in forward and backward propagating core mode of waveguide 0 (blue and cyan, respectively), the forward and backward propagating core mode of waveguide 1 (green and yellow, respectively) and forward and backward propagating cladding mode (magenta and red, respectively) for a device with superimposed long- and short period waveguide gratings in each waveguide. The parameters are given in text. We present the results pumping the device at inputs I_0 (a), I_1 (b), I_2 (c) and I_3 (d).	184
6.22	Power output against wavelength of core modes and cladding mode for a device with superimposed long- and short period waveguide gratings in each waveguide with the parameters are defined in text.	184
6.23	Power output against grating period at outputs O_0 (a), O_1 (b) O_2 (c) and O_3 (d) for a device with superimposed long- and short period waveguide gratings in each waveguide with parameters defined in text.	185
6.24	Device found numerically to achieve a certain power-splitting. Here, the blue and cyan are the forward and backward propagating modes of waveguide 0, green and yellow are the respective modes of waveguide 1 and magenta and red are the forwards and backwards propagating cladding modes. For (a), we target the output powers defined by $b_0 = \frac{1}{3}$ and $b_1 = \frac{1}{2}$. We achieve this with a grating index contrast of 0.001 and 0.0004126 for the long-period gratings in waveguides 0 and 1 and of 0.0001850 and 0.0003179 for the respective short-period grating. The grating phases respectively are 1.377 and 3.339 for the long-period gratings and 0.1968 and 0 for the short-period gratings. The length of the device is 7.182mm. For (b), we target the output powers defined by $b_0 = \frac{1}{2}$ and $b_1 = \frac{1}{3}$. The grating index contrasts used to achieve that are 0.0004635 and 0.001 for the long-period gratings in waveguides 0 and 1, 0.0005273 and 0.0003443 for the respective short-period gratings and the grating phases respectively are 1.8848 and 2.8275 for the long-period gratings and -0.3147 and 0 for the short-period gratings. The length of the device is 8.788mm.	187

- 7.1 Thermally reconfigurable 4×4 coupler based on bidirectional propagation implementing any arbitrary symmetric unitary matrix. Thermo-optic phase shifters (zig-zag lines) are placed in strategic locations in order to achieve thermal reconfigurability. Each box represents a part of the device that can be used to implement the most general form of the fundamental. 193

Acknowledgements

I wish foremost to thank my primary supervisor Dr. Peter Horak for his advice and support throughout my project.

I would also like to thank Prof. Peter Smith, Dr. James Gates, Prof. Corin Gawith (secondary supervisors) and Dr. Matt Posner for useful discussions on the applications of my project and its direction.

And thank you to Dr. Nina Podoliak for providing the (earliest version of the) COMSOL model for coupling to radiation modes and the derivation of the analytical solution for $ab45^\circ$ tilted grating on which part of this project builds.

And many thanks to Dr. Ioannis Begleris for technical help in setting up an Ubuntu desktop with the needed software and for general advice on coding and software practice.

I would also like to thank Mr. James Field, Dr. Rex Bannerman and Dr. James Gates for collaborating with me on finding the parameters needed for fabricating the device.

I would like to thank especially Dr. James Gates and also Dr. Christopher Holmes and Dr. Rex Bannerman for patiently answering my questions on the fabrication methods for which the devices investigated in this project are intended for fabrication.

And thank you to Mr. Sam Senior for helping me set-up my office desktop for home working during the coronavirus pandemic.

Importantly, I would like to thank Mr. Dean Clarke, Mr. Joe Campling, Mr. Stuart MacFarquhar, Mr. Jake Prentice, Mr. Alan Gray and many others for interesting discussions on life, the universe and everything.

And finally, many thanks to EPSRC for funding my PhD project, without which it wouldn't be possible.

Declaration of Authorship

I, Mathias Weisen, declare that the thesis entitled *Design and simulation of integrated photonic devices based on tilted Bragg gratings* and the work presented in the thesis are both my own, and have been generated by me as the result of my own original research. I confirm that:

- This work was done wholly or mainly while in candidature for a research degree at this University.
- Where any part of this thesis has previously been submitted for a degree or any other qualification at this University or any other institution, this has been clearly stated.
- Where I have consulted the published work of others, this is always clearly attributed.
- Where I have quoted from the work of others, the source is always given. With the exception of such quotations, this thesis is entirely my own work.
- I have acknowledged all main sources of help.
- Where the thesis is based on work done by myself jointly with others, I have made clear exactly what was done by others and what I have contributed myself.
- Parts of this work have been published as:
 - M. J. Weisen et. al. "Low-loss wavelength-selective integrated waveguide coupler based on tilted Bragg gratings", Journal of the Optical Society of America B, Vol. 36, pp. 1783-1791 (2019)
 - M. J. Weisen et. al. "Four-Port Interference Device on an Integrated Photonics Platform Based on Tilted Bragg Gratings", CLEO/Europe-EQEC 2019, Munich, Germany, (2019)
 - M. J. Weisen et. al. "24-by-4 integrated waveguide coupler based on bi-directional propagation in two single-mode waveguides", IEEE. Photon. J. (accepted 2020)

Signed:.....

Date:.....28/01/2021.....

Chapter 1

Introduction

Optics is the field of study of how light propagates and interacts with matter and how it can be manipulated to meet a desired end. At first, this was only achieved through the (in general) free space propagation of light and the use of bulk instruments (lenses, mirrors, bulk lasers etc.) to create and control the light. However, this has a disadvantage in that it requires the manual alignment of the optical elements. This can be difficult for setups involving a large number of optical components. It also leads to devices made from such components taking up an entire optical bench and thus not being portable or scalable [1]. The solution is to integrate all the components of the device into a single chip. Instead of propagating in free space, the light is routed around the chip using what are known as waveguides and manipulated by components that are directly integrated into the chip. This is known as integrated photonics [1].

Integrated photonics provides several advantages over bulk optics. The width of the waveguides only needs to be of the same order of magnitude as the wavelength of the light in order to confine it. This means that, as the wavelength of light is very short, the width of the waveguides can be made very narrow and this allows for miniaturisation by several orders of magnitude compared to conventional (non-integrated) optics. Also, the optics within the chip has a very stable alignment, which means that now a major source of difficulty is removed. Both these advantages also mean that devices made from integrated optics are easily portable and scalable [1].

Integrated photonics also offers great potential advantages to integrated electronics for information transfer and processing. This is because in electrical conductors, the attenuation of an AC electrical signal as it propagates along the transmission line results from the property of electrical impedance which is a combination of the resistance and reactance of the conductor [2]. This electrical impedance and thus attenuation increases with frequency [2] and so provides a hard limit to the transmission rate of information dependent on distance [1]. However, if electromagnetic waves are transmitted through a non-conducting material, this source of loss is eliminated and the frequency of the

electromagnetic waves, and thus of the transmitted signal, can be increased to optical frequencies.

The electrical transmission line is replaced with a waveguide (or an optical fibre for long-distance communications, the basic principles are the same). This waveguide is made out of a dielectric material to which light is transparent at the frequencies used. It is based on the principle that by having a higher refractive index within the waveguide light will be trapped due to total internal reflection. This light is contained in a finite number of modes (propagation "states" of the waveguide) [3, 4]. The waveguides can thus be used to route light between the components in the chip. So far, many devices have been developed for use in integrated photonics for a large number of applications [1, 5, 6]. An architecture based on couplers between optical waveguides has been implemented as a basis for both classical and quantum information processing [7].

By introducing a periodic pattern to the waveguide, thus creating diffraction gratings, we can couple the modes of the waveguide to each other in a controlled way. Established applications include Bragg gratings that are used as mirrors [8] (by coupling to backwards propagating modes) and grating couplers that couple light in and out of the chip [9]. If one gives the grating a tilt angle with respect to the propagation direction, it can be used to couple light efficiently in any direction out of the waveguide and more efficiently to higher order waveguide modes. So far this has had only a limited number of applications in integrated photonics including polarisers [10], spectrometers [11] and refractometers [12].

Silica is a promising platform for integrated photonics. The reason for this is due to its low absorption in the 1550nm wavelength region and efficient coupling to optical fibre, enabling good integration with telecommunication networks. Here, waveguides and Bragg gratings are fabricated by exposure to UV laser light. Bragg gratings are defined by modulating the refractive index along the propagation direction of the waveguides. The ORC has previously developed highly flexible technology for simultaneous inscription of waveguides and Bragg gratings in a silica integrated photonics platform [13] with a tilt angle [10].

The aim of this thesis is twofold: to numerically investigate the versatility of this platform in implementing complex devices based on tilted Bragg gratings and to explore its potential usefulness for optical information processing.

To this end, this project will use analytical and numerical models to simulate the behaviour of light in these devices. First, an expression for the coupling of light to radiation modes using an arbitrary tilt angle is developed and verified using COMSOL simulations. Then, a new class of devices is investigated based on tilted gratings that couple light between two different waveguides using one of the modes of a planar ridge structure in which they are both written.

The background chapter, Chapter 2, of this report will first go over the theory behind waveguides and how the waveguide modes are calculated. It will then introduce the reader to the basic physical principles behind untilted and tilted gratings. Then, it will go through a number of analytical and numerical methods for deriving and simulating the behaviour of devices based on tilted gratings. There will then be an overview of devices that already exist for coupling light between waveguides starting with the common directional coupler and then moving on specifically to waveguide couplers that are based on gratings. The background will also make a brief overview of a few other existing integrated photonics devices that are based on tilted gratings. The background will also show how integrated photonics can be used for both classical and quantum information processing. Finally, the background will go through the fabrication method used for integrated photonics in the ORC including a motivation for why we have chosen to design our devices for a silica platform.

Chapter 3 will go over work done in the beginning of this PhD which is the simulation of the scattering of light from a tilted grating into radiation modes inside the chip. This includes the derivation of an analytical expression that governs this behaviour and verification using numerical simulations.

The following chapters will go over the work done on the waveguide-to-waveguide couplers exploiting a single mode of a ridge structure. Chapter 4 will consider the version of that device using single-mode waveguides and a single direction of propagation. It will start by introducing and providing motivation for that device. Then, it will go through an analytical derivation of the device behaviour and show how 100% coupling can be achieved. The chapter will explain how it is simulated numerically and will move onto showing and discussing the results of simulations. I show that we can achieve a highly narrow-band waveguide to waveguide coupler. These include simulations showing the effect of fabrication tolerances, temperature, apodization and grating phase-error noise. It will then show the results of simulations with parameters chosen so as to be fabricated using existing technology at the ORC.

Chapter 5 will present an extension of the above device involving two waveguides with two modes each instead of single-mode waveguides. As such, this platform could be used for 4×4 linear optical processing. I will show how we are able to implement a mode division multiplexer on that platform and also how we can achieve any power splitting from one to four waveguide modes and any unitary transform by chaining such couplers together.

Chapter 6 will present a new device with two single-mode waveguides but exploiting both directions of propagation to double the number of modes and so achieve 4×4 optical processing. It includes circulators on the outside of the chip connected to the end facets of the waveguides to turn it into a device consisting of four input and four output ports. I will show how, by using four fundamental couplers and concatenating them in our

device, I can achieve any arbitrary symmetric unitary matrix. I will also how we can achieve certain transformations more compactly compared to existing implementations by superposing gratings and will give the example of a highly compact Walsh-Hadamard transform.

The report will then conclude with Chapter 7 summarising the work and explaining possible directions in which I see future research building on the research presented in this thesis.

Chapter 2

Background

2.1 Fundamental Physics

2.1.1 Optical Waveguides

A waveguide is a structure that is able to confine electromagnetic waves within it and guide them along its length. For optical frequencies, this is most commonly achieved through the use of a higher refractive index material in the region defined by the waveguide (known as the core) than in the surrounding region (known as the cladding). Light is prevented from escaping the waveguide by total internal reflection at the interface with the surrounding region. Waveguides can guide light in a finite number of modes each with their own effective refractive index governing the velocity at which the light travels along the waveguide [3, 4, 14].

Waveguides come in two types: planar waveguides and channel waveguides. These confine light in only one transverse dimension (i.e. in a plane) or in both transverse dimensions, respectively. In the platform available for fabrication at the ORC (see Section 2.4), channel waveguides are buried in a two-dimensional raised index layer (i.e. a planar waveguide) that confines the light in the third dimension as shown in Figure 2.1. As explained in Section 2.1.1.1, this allows us to ignore the third dimension and so greatly reduce the size of the problem; making numerical simulations possible with the available computational resources.

Throughout this thesis, we will label the direction of propagation z , the transverse directions within and out of the planar layer x and y respectively (see Figure 2.1).

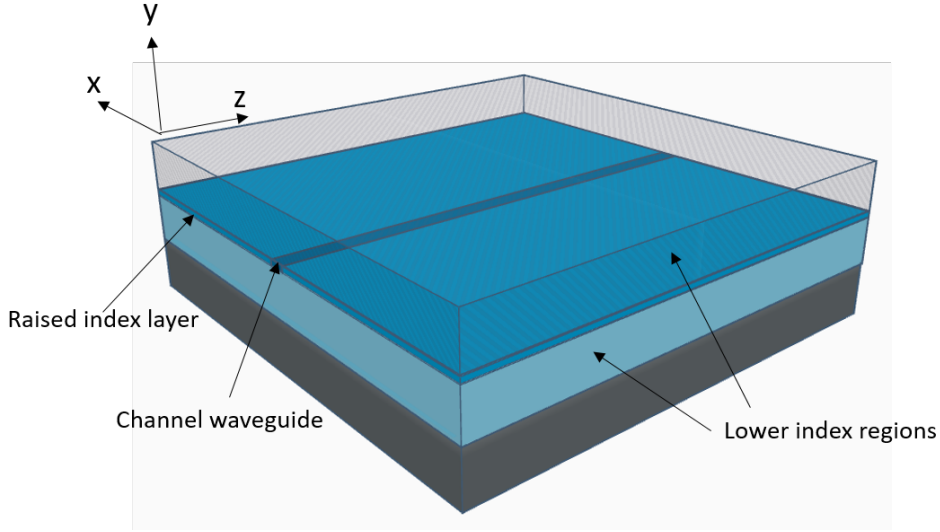


Figure 2.1: Schematic of a channel waveguide inside a raised index planar core layer. The light propagates in the z direction, is confined in the y direction by the planar layer and in both the x and y direction by the channel waveguide. The lower index regions are the underclad and overclad which we define in the later Section 2.4.2.

2.1.1.1 Mode analysis

To analyse light propagating through waveguides we must start with Maxwell's equations. In the absence of charges and currents they are given by:

$$\begin{aligned}\nabla \cdot \vec{D} &= 0 & \nabla \times \vec{E} &= -\frac{\partial \vec{B}}{\partial t} \\ \nabla \cdot \vec{B} &= 0 & \nabla \times \vec{H} &= \frac{\partial \vec{D}}{\partial t}\end{aligned}\tag{2.1}$$

where \vec{E} , \vec{D} , \vec{H} and \vec{B} are the electric field, the electric displacement field, the magnetic field and the magnetic induction respectively. In a linear, dielectric, isotropic and non magnetic medium $\vec{D} = n^2 \epsilon_0 \vec{E}$ and $\vec{B} = \mu_0 \vec{H}$ where n is the refractive index of the medium and ϵ_0 and μ_0 are the permittivity and permeability of free space. This allows us to simplify Maxwell's equations and derive the well known Maxwell wave equation:

$$\nabla(\nabla \cdot \vec{E}) - \nabla^2 \vec{E} = -\epsilon_0 \mu_0 n^2 \frac{\partial^2 \vec{E}}{\partial t^2}\tag{2.2}$$

which can be re-written as [3, 14]:

$$\nabla^2 \vec{E} + \nabla \left[\frac{1}{n^2} \nabla n^2 \cdot \vec{E} \right] - \epsilon_0 \mu_0 n^2 \frac{\partial^2 \vec{E}}{\partial t^2} = 0\tag{2.3}$$

For the magnetic field, using similar steps to the above, we can also find a wave equation:

$$\nabla^2 \vec{H} + \frac{1}{n^2} \nabla n^2 \times \nabla \times \vec{H} - \epsilon_0 \mu_0 n^2 \frac{\partial^2 \vec{H}}{\partial t^2} = 0 \quad (2.4)$$

In a planar waveguide, the refractive index varies only in one transverse dimension. In the case of the confinement by the planar core layer, this is the y direction. However, we model the channel waveguides as being infinitely extended along y as explained later in this section and thus varying only with x . In this case, the Maxwell wave equation has solutions in the following form:

$$\begin{aligned} E_j &= E_{j,0}(x) e^{i(\omega t - \beta z)} \\ H_j &= H_{j,0}(x) e^{i(\omega t - \beta z)} \end{aligned} \quad (2.5)$$

where E_j and H_j are the components of the electric and magnetic field in an arbitrary direction we define as j , $E_{j,0}(x)$ and $H_{j,0}(x)$ are the transverse profile of the fields, ω is the angular frequency of the electromagnetic waves and β is the propagation constant. Substituting Equations (2.5) back into Equations (2.1) yields the following [3, 4]:

$$\left\{ \begin{array}{ll} i\beta E_y &= -i\omega \mu_0 H_x \\ \frac{\partial E_y}{\partial x} &= -i\omega \mu_0 H_z \\ -i\beta H_x - \frac{\partial H_z}{\partial x} &= i\omega \epsilon_0 n^2(x) E_y \end{array} \right. \quad (2.6)$$

$$\left\{ \begin{array}{ll} i\beta H_y &= i\omega \epsilon_0 n^2(x) E_x \\ \frac{\partial H_y}{\partial x} &= i\omega \epsilon_0 n^2(x) E_z \\ -i\beta E_x - \frac{\partial E_z}{\partial x} &= -i\omega \mu_0 H_y \end{array} \right. \quad (2.7)$$

The equations above can be reduced to two independent sets of three equations each. The equations in (2.6) involve only E_y , H_x and H_z whereas the equations in (2.7) involve E_x , E_z and H_y . Their solutions correspond to transverse electric (TE) and transverse magnetic (TM) modes respectively. These sets of modes are so-called because in TE (TM) modes the electric (magnetic) field is purely transverse.

The two sets of modes correspond to two axes of polarisation, with polarisation in the y and x directions corresponding to the TE and TM modes respectively. This means that for TE modes we can re-write the electric field as $\vec{E} = E_y \hat{y}$. As $n = n(x)$, we can deduce that $\nabla n^2(x)$ is a vector with only a component in the x direction and thus $\nabla n^2 \cdot \vec{E} = 0$. Equation (2.3) reduces to the following [3, 4, 14]:

$$\nabla^2 \vec{E} - \epsilon_0 \mu_0 n^2(x) \frac{\partial^2 \vec{E}}{\partial t^2} = 0 \quad (2.8)$$

Substituting Equation (2.5) into (2.8) yields:

$$\frac{d^2 E_y}{dx^2} + k_0^2 [n^2(x) - n_{eff}^2] E_y = 0 \quad (2.9)$$

where $n_{eff} = \frac{\beta}{k_0}$ is the effective refractive index of the mode. The above is an eigenvalue/eigenvector equation that can be used to find the TE modes of any graded slab waveguide. It is possible to find analytically the solutions of a waveguide with a step index and parabolic index profile [4].

There is a scaling law by which a waveguide with one set of parameters will behave similarly to a waveguide with a different set. This law is described by the normalised frequency parameter, also known as the V-number, which is given by [3]:

$$V = k_0 a \sqrt{n_{core}^2 - n_{clad}^2} \quad (2.10)$$

where k_0 is the wavenumber of the light in free space and a is the dimension of the waveguide in the x direction. For the same V-number, light travelling through it will show the same propagation behaviour. Here, n_{core} and n_{clad} are the refractive indices of the waveguide core (maximum index for graded index waveguides) and of the surrounding cladding.

As explained in Section 2.4, the planar core layer has an asymmetric step-index index profile. We include here the solutions for the effective refractive indices for such a planar waveguide. There are three parameters that are important and determine the effective refractive index. These are the V-number V which is defined similarly to Equation (2.10), the waveguide parameter b and the asymmetry parameter a^{TE} . For TE modes, they are given by the following equations [4]:

$$V = k_0 a (n_2^2 - n_3^2)^{\frac{1}{2}} \quad (2.11)$$

$$b = \frac{n_{eff}^2 - n_3^2}{n_2^2 - n_3^2} \quad (2.12)$$

$$a^{TE} = \frac{n_3^2 - n_1^2}{n_2^2 - n_3^2} \quad (2.13)$$

where n_2 is the refractive index of the waveguide core, n_1 and n_3 are the refractive indices of the cladding on either side of the core (also known as the overclad and underclad). The parameters are related by the following equation:

$$V \sqrt{1 - b} = p\pi + \tan^{-1} \left(\sqrt{\frac{b}{1 - b}} \right) + \tan^{-1} \left(\sqrt{\frac{b + a^{TE}}{1 - b}} \right) \quad (2.14)$$

where p is the mode number, starting from 0.

To calculate the effective index of an asymmetric slab waveguide we therefore need to first use Equations (2.11) and (2.13) to calculate V and a^{TE} from the values of n_1 , n_2 , n_3 and a . Then we need to find the value of b required to solve Equation (2.14) numerically for the desired mode number(s) using a numerical method such as Brent's method [15]. Then we calculate the effective index of the mode using Equation (2.12).

The devices investigated in this thesis consist of an asymmetric step-index planar layer (that acts as a planar waveguide) extended in the x , z plane that confines light in a single mode in the y direction. Single-mode channel waveguides are written into it that confine light in the x direction as well and guide it along the z direction. Details of how the devices would be fabricated are in Section 2.4. The problem can thus be simplified approximately using a method very similar to the effective index method [4]. Here, we begin by calculating the effective index of the mode of the planar layer as described above and then by considering the system as consisting of waveguides infinitely extended along the y direction with a surrounding index equal to the effective index of the mode of the planar layer. As the index distribution in this problem is identical along each plane defined by a value of y , the electric fields are also identical which allows us to simulate the system as a two-dimensional problem in x and z . This greatly reduces the complexity of the problem by allowing us to run finite element simulations in two dimensions (see Section 2.2.4) rather than three and, in the case of coupled mode theory (see Section 2.2.2), to make mode calculations in one dimension (x) and calculate light propagation in these modes in the other dimension (z).

2.1.2 Bragg gratings

In photonics, a Bragg grating is a periodic pattern along the core of a waveguide or optical fibre. It can be fabricated in one of two ways, either through a periodic perturbation of the refractive index along the waveguide core [16] or by physically etching the grating structure onto the waveguide or fibre [17, 18]. This allows for the controlled coupling of modes of the waveguide with other modes, including core modes, cladding modes and radiation modes that escape the cladding.

In this thesis we consider Bragg gratings created through a process called UV-writing in which the silica core is doped with germanium and exposed to UV light [16] causing an increase in the refractive index. By focusing two laser beams onto the same spot, a grating will thus be formed by the interference pattern [19] as a periodic modulation of the refractive index. Previously, researchers at the Optoelectronics Research Centre (ORC) have developed a highly flexible method of simultaneous channel waveguide and grating writing [13] with any apodization function and tilt angle [10]. As the gratings are created by an interference pattern, they will have a sinusoidal index distribution. The Bragg grating based devices investigated in this thesis are designed with this fabrication

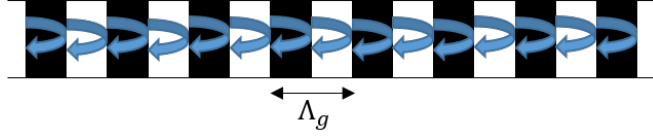


Figure 2.2: Individual Fresnel reflections from a Bragg grating. Here, we assume the simplest case when the grating consist of regions of alternating high (black) and low (white) refractive index that are equally spaced out and of equal size. Reflections occur at each change in refractive index with a π phase shift if the refractive index increases but not if it decreases. If all reflections interfere constructively, Bragg reflection will occur.

method in mind. More details exist on the fabrication method and on the motivation for choosing it in Section 2.4.

The most common use of Bragg gratings is as a reflector. These use a non-tilted grating of the correct modulation period to couple light into the backward propagating version of the original waveguide mode [8]. Gratings can also be used to couple light from the waveguide core to radiation modes and higher order guided modes, including cladding modes [8]. They come in two types, short-period gratings that couple between modes propagating in opposite directions and long-period gratings that coupled between modes propagating in the same direction. However, by introducing a tilt angle, it is possible to greatly increase the efficiency for both coupling to radiation modes at a given angle and to high-order guided modes as shown in [20] and [21] respectively. My own research, in Chapters 3 and 4 respectively, confirms this finding.

2.1.2.1 As a reflector array

The simplest type of grating to analyse are untilted Bragg gratings. Here, as a light beam passes through the grating, at each change in refractive index it suffers a small Fresnel reflection (see Figure 2.2). If all reflections are in phase, a condition known as phase-matching, they interfere constructively and the beam is backreflected. If the beam interferes destructively, however, no backreflection occurs and the beam is transmitted. This means that for there to be maximum reflection it is required that the separation between the grating fringes in the z direction, known as the grating period Λ_g , is an integer number of times one half of the effective light wavelength in the core so that the reflection from two adjacent fringes interfere constructively. This means that there is a resonance wavelength, known as the Bragg wavelength λ_B , for back-reflection which is given by:

$$m\lambda_B = 2n_{eff}\Lambda_g \quad (2.15)$$

For tilted gratings, the same principle of phase matching can be applied. Assuming that the grating is infinitely wide and is pumped by a plane wave and referring to Figure 2.3,

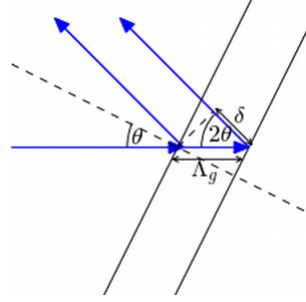


Figure 2.3: Individual reflections from two planes of a grating one grating period apart with tilt angle θ and period Λ_g . Light reflected from the second plane travels an extra distance of $\Lambda_g + \delta$ before travelling parallel to the first beam.

where the variables are defined, we find the following expression for the phase matching condition:

$$\Lambda_g + \delta = mn_{eff}\lambda_0 \quad (2.16)$$

where λ_0 is the light wavelength in free space. We make the simplifying assumption that the effective refractive indices are the same for the incident and reflected fields. The distance δ is given by the following expression:

$$\delta = \Lambda_g \cos(2\theta) \quad (2.17)$$

where θ is the tilt angle. We use the following trigonometric identity:

$$1 + \cos(2\theta) = 2 \cos^2(\theta) \quad (2.18)$$

From Equations (2.16), (2.17) and (2.18), we find that the resonance condition is at which reflection happens is (for $m = 1$):

$$\lambda_0 = 2\Lambda_g n_{eff} \cos^2 \theta \quad (2.19)$$

Away from resonance, the amount of reflection is negligible and the light does not see the grating.

2.1.2.2 As an array of pointlike scatterers

Gratings can also be analysed as consisting of a sequence of point-like scatterers that each scatter light in all directions. In this scenario, as the scatterers are equally spaced, there is only a finite number of directions in which the scattered light interferes constructively such as with a diffraction grating. By using simple geometric optics [3, 8] and Figure 2.4 we can derive the phase matching condition which governs the coupling of any two guided modes:

$$\beta_2 = \beta_1 + mK_g \quad (2.20)$$

where β_1 and β_2 are the propagation constants of bound modes (either core or cladding modes) and $K_g = \frac{2\pi}{\Lambda_g}$ is the grating wavevector. In terms of wavelengths and effective

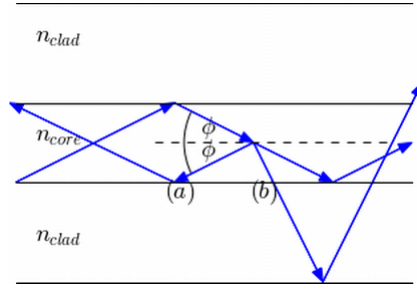


Figure 2.4: Coupling of modes to backwards propagating modes and cladding modes with a grating.

refractive indices this is given by ($m = 1$):

$$\lambda_0 = (n_{eff,1} \pm n_{eff,2})\Lambda_g \quad (2.21)$$

with a $-$ or $+$ depending on whether the coupled modes travel in the same or opposite direction. For $n_{eff,1} = n_{eff,2}$ and with $+$ this returns Equation (2.15).

For the coupling of light out of a waveguide by a grating, we begin by making the substitution $\beta_2 = k_{out,z}$ in Equation (2.20) where $k_{out,z}$ is the z component of the output wavevector. With this as a starting point, the use of simple geometry and the diagram in Figure 2.5 predicts the angle of the scattered light [22]:

$$\alpha = \cos^{-1}\left(\frac{\lambda_0}{\Lambda_g n_{clad}} - \frac{n_{eff}}{n_{clad}}\right) \quad (2.22)$$

Note that, as the grating treated as an array of pointlike scatterers, i.e. infinitely thin, there is no tilt angle and the grating does not scatter light preferentially in a single direction but in a cone of light of angle α to the waveguide.

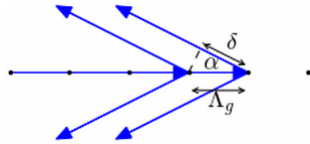


Figure 2.5: Scattering from a point-like grating. The angle between the incident and scattered radiation α is dependent on the light wavelength in the grating and the grating period. Scattering occurs in both directions defined by that angle. Λ_g is now the distance between the pointlike scatterers.

2.1.3 Applications of the different models

The different models described above apply best to different scenarios. The model of Bragg gratings as a reflector array works best if the width of the grating planes is

considerably larger than the wavelength of light. The model of a grating as pointlike scatterers applies in the limit that the width of the grating is smaller than the light wavelength. These models are good for understanding intuitively the coupling of light to radiation modes as well as Bragg reflection (coupling to the same backward propagating mode). In intermediate cases in which the light wavelength is of similar scale to the grating width there is a combination of the two processes. The direction of the radiated wave is given by Equation (2.22) for the scattering angle but the scattering is most efficient at the resonance condition given by Equation (2.19) given by the law of reflection [22]. This is confirmed by our own work in Chapter 3. In order to make quantitative predictions, and for intermediate cases, however, it is best to use one or several of the methods outlined in Section 2.2.

For example, to model analytically the coupling to radiation modes, the method developed originally in [23] and outlined in Section 2.2.1 is known to be suitable to use for gratings of a 45° tilt angle [23]. In Chapter 3 of this thesis, I investigate its generalisation to gratings of shallower tilt angle. In order to understand the coupling of light between different modes of a waveguide or between modes of the waveguide and modes of the surrounding cladding, the resonances can be found by treating the grating as pointlike scatterers and therefore using Equation (2.21). However, to make quantitative predictions, it is best to use coupled mode theory, which we outline in Section 2.2.2.

2.2 Analytical and Numerical Methods

2.2.1 The beam tracing approach for tilted gratings

Previously, an analytical method for studying reflection out of a waveguide by a tilted grating has been developed [23]. It is based on dividing the grating into a large number of thin films of equal refractive index, calculating the Fresnel reflection from each interface and summing over all the reflected fields. Turning the sum into an integral allows for the derivation of a precise result for the reflection per unit length. The work in [23] assumes that the grating is wide enough for diffraction effects to be neglected and in the limit of a low amplitude grating. The grating is assumed to be pumped by a mode of Gaussian index profile. It is also assumed to be defined by a sinusoidal index perturbation with a constant amplitude along the entire width of the mode. The original research [23] assumes that the grating has a 45° tilt angle. As we mention in Section 2.3.1.4, in the limit of low index contrast such a grating acts as a polariser and only reflects light of one polarisation. Assuming that the reflected and incident beams have the same propagation constant given by β , the device has a reflection per unit length given by [23]:

$$R = \kappa^2 \pi^2 \sqrt{2\pi} \frac{w_0}{\Lambda_g} \exp \left[-\frac{w_0^2}{2} \left(\beta - \frac{2\pi}{\Lambda_g} \right)^2 \right] \quad (2.23)$$

where $\kappa = \frac{\delta n_g}{n_{core}}$ is the fractional refractive index amplitude of a grating with an index contrast of δn_g and w_0 is the 1/e half-width (amplitude) of the mode.

More recently [24] has shown that using a grating with a Gaussian index profile (which is assumed to be similar to that of a UV written waveguide) yields the following modified version of Equation (2.23):

$$R(z_p) = \kappa^2 \pi^2 \sqrt{2\pi} \frac{w_1^2}{w_0 \Lambda_g} \exp \left[-\frac{w_1^2}{2} \left(\beta - \frac{2\pi}{\Lambda_g} \right)^2 \right] \quad (2.24)$$

where $w_1 = \frac{\sigma w_0}{\sqrt{\sigma^2 + w_0^2}}$ is the effective width of the grating perceived by the input mode. This equation has good agreement with simulations of the electromagnetics computed by the finite element method in COMSOL in 45° [24].

2.2.2 Coupled mode theory

To analyse the coupling of waveguide modes to one another by a grating, the traditional option is to use coupled mode theory. This theory is derived directly from Maxwell's equations. Here, we use a simplification in which the electric and magnetic fields are assumed to have no longitudinal components. This means they have components in only one direction which allows them to be treated as scalars. This is known as the weak guiding regime. This derivation is lifted almost entirely from [25] with the only adjustment being that it is generalised to a number of modes greater than two. Another version of the derivation can be found in [3]. The electric field is expressed as a superposition of the modes of the waveguide:

$$E(x, y, z, t) = \Psi(x, y, z) e^{i\omega t} = e^{i\omega t} \sum_n A_n(z) \psi_n(x, y) e^{-\beta_n z} \quad (2.25)$$

where $\Psi(x, y, z)$ is the electric field at time $t = 0$, ω is the frequency, $\psi_n(x, y)$, $A_n(z)$ and β_n are the mode profiles, amplitudes and propagation constants with $\psi_n(x, y)$ chosen such that there is one unit of power in each mode:

$$\frac{|\beta_m|}{2\omega\mu_0} \iint \bar{\psi}_m \psi_n dx dy = \delta_{nm} \quad (2.26)$$

where $\delta_{nm} = 1$ if $n = m$ and $\delta_{nm} = 0$ if $n \neq m$. Defining $n(x, y)$ as the refractive index profile of the waveguide and $\delta n(x, y, z)$ as an index perturbation caused for example by a grating, the total refractive index of the waveguide and the grating is given by:

$$n_{tot}(x, y, z) = n(x, y) + \delta n(x, y, z) \quad (2.27)$$

Substituting Equations (2.27) and (2.25) into (2.8) yields the following:

$$\sum_n e^{-i\beta_n z} \psi_n(x, y) \left[2k_0^2 n(x, y) \delta n(x, y, z) A_n(x, y) - 2i\beta_n \frac{dA_n(z)}{dz} \right] = 0 \quad (2.28)$$

Here we make the slowly varying amplitude approximation and so assume $\frac{d^2 A(z)}{dz^2} = 0$. We then apply the following operation to the above equation:

$$\iint (\text{2.28}) \cdot \bar{\psi}_m dx dy \quad (2.29)$$

This leads to:

$$\frac{dA_m(z)}{dz} = -i \sum_n e^{i(\beta_m - \beta_n)z} A_n(z) c_{mn}(z) \quad (2.30)$$

which governs the evolution of the light in the modes. Here, $c_{mn}(z)$ is the coupling coefficient and is defined as:

$$c_{mn}(z) = \frac{k_0}{2c\mu_0} \iint n(x, y) \delta n(x, y, z) \bar{\psi}_m(x, y) \psi_n(x, y) dx dy \cdot \begin{cases} +1 & \text{for } m \geq 0 \\ -1 & \text{for } m \leq 0 \end{cases} \quad (2.31)$$

where $m \geq 0$ and $m \leq 0$ correspond to forward and backward propagating modes, bear in mind that the sign is only a matter of notation and so the mode with $m = -0$ is the backward propagating version of $m = +0$, i.e. the fundamental mode.

If the perturbation is caused by a tilted grating it is defined by:

$$\delta n(x, y, z) = \delta n_g \sin \left(2\pi \frac{(z - x \tan \theta)}{\Lambda_g} \right) \rho(x, y) \quad (2.32)$$

where δn_g is the grating depth. Λ_g and θ are the period and tilt angle of the grating respectively. The perturbation term can be re-written in terms of wavevectors and separated into two terms as follows:

$$\begin{aligned} \sin \left(2\pi \frac{(z - x \tan \theta)}{\Lambda_g} \right) &= \sin(K_g z - K_t x) \\ &= \sin(K_g z) \cos(K_t x) - \cos(K_g z) \sin(K_t x) \end{aligned} \quad (2.33)$$

where $K_g = \frac{2\pi}{\Lambda_g}$ and $K_t = K_g \tan \theta$. This means that the coupling coefficient can be restated in terms that separate the dependence on z from the dependence on x and y .

$$c_{mn}(z) = d_{mn+} \sin(K_g z) + d_{mn-} \cos(K_g z) \quad (2.34)$$

where $d_{mn\pm}$ are given by

$$d_{mn+} = \frac{k_0}{2c\mu_0} \iint n(x, y) \delta n_g \cos(K_t x) \rho(x, y) \bar{\psi}_m(x, y) \psi_n(x, y) dx dy \cdot \begin{cases} +1 & \text{for } m \geq 0 \\ -1 & \text{for } m \leq 0 \end{cases} \quad (2.35)$$

and

$$d_{mn-} = -\frac{k_0}{2c\mu_0} \iint n(x, y) \delta n_g \sin(K_t x) \rho(x, y) \bar{\psi}_m(x, y) \psi_n(x, y) dx dy \cdot \begin{cases} +1 & \text{for } m \geq 0 \\ -1 & \text{for } m \leq 0 \end{cases} \quad (2.36)$$

Now, we define $\psi_{-m}(x, y) = -\psi_m(x, y)$. This means that, for $m \geq 0$ and $n \geq 0$, the following relations apply: $d_{m-n\pm} = -d_{mn\pm}$ whereas $d_{-mn\pm} = d_{mn\pm}$. By defining the coupling constant as:

$$c_{mn,0} = \sqrt{d_{mn+}^2 + d_{mn-}^2} \quad (2.37)$$

and the phase as:

$$\phi_{mn} = \tan^{-1} \left(\frac{d_{mn-}}{d_{mn+}} \right) \quad (2.38)$$

we can rewrite the Equation (2.34) as:

$$c_{mn}(z) = c_{mn,0} \sin(K_g z + \phi) \quad (2.39)$$

It is worth mentioning here that whether a grating is phase-matched for coupling from one mode to either the co-propagating or counter-propagating version of a different mode, the coupling coefficient is the same for equal δn_g , even though the grating period and tilt angle would be different in both cases. This is because the coupling coefficient depends directly on K_t which is the transverse component of the grating wavevector which is the same in both cases.

This allows us to derive two different but equivalent forms of the mode coupling equation by a titled grating:

$$\frac{dA_m(z)}{dz} = -\frac{1}{2} \sum_n \left(e^{i[(\beta_m - \beta_n + K_g)z + \phi_{mn}]} - e^{i[(\beta_m - \beta_n - K_g)z - \phi_{mn}]} \right) A_n(z) c_{mn,0} \quad (2.40)$$

which is useful for deriving analytical results, and:

$$\frac{dA_m(z)}{dz} = -i \sum_n e^{i(\beta_m - \beta_n)z} A_n(z) (d_{mn,+} \sin(K_g z) + d_{mn,-} \cos(K_g z)) \quad (2.41)$$

which is more computationally efficient as it allows us to then split the equation into equations relating the real and imaginary parts of A_m to the real and imaginary parts of A_n and thus calculate the numerical solution entirely with real variables.

In the case of short-period gratings, we can assume that only modes travelling in the opposite direction are coupled together. This allows us to greatly simplify the problem by manipulating Equation (2.40) in order to yield the following equation:

$$\frac{d\mathcal{R}_m(z)}{dz} = i\left[\frac{K_g}{2} - \beta_m\right]\mathcal{R}_m(z) + \frac{1}{2}\sum \mathcal{R}_{-n}(z)c_{mn}e^{-i\phi_{mn}} \quad (2.42)$$

where $\mathcal{R}_m(z) = A_m e^{i\frac{K_g}{2}z}$ whereas $\mathcal{R}_{-n}(z) = A_m e^{-i\frac{K_g}{2}z}$ are the transformed amplitudes of the device. This allows us to solve systems consisting entirely of short-period gratings by solving Equation (2.42) as an eigenvalue/eigenvector problem.

For certain analytical problems, it is useful to combine the coupling coefficient amplitude and phase into a single complex coupling coefficient given by:

$$c = c_0 e^{-i\phi} \quad (2.43)$$

where c_0 and ϕ are given by the Equations (2.37) and (2.38).

2.2.2.1 Two mode coupling - Counter-propagating modes

This section briefly looks at how coupled mode theory is applied to derive the behaviour of two counter-propagating modes. This is to derive an equation reproducing known grating physics first so that we can then find generalised solutions for a larger number of modes in Chapters 4, 5 and 6. The equations derived here are also used in Section 4.4.2.2 of Chapter 4 to verify the numerical method we use in these chapters before moving on to more complex grating-based structures. Very similar methods have been used in [8, 25]. We choose the modes denoted by the subscripts 0 and 1 respectively to correspond to the forward and backward propagating modes so $\beta_0 > 0$ and $\beta_1 < 0$. In a system with only two modes and choosing $K_g \simeq \beta_0 - \beta_1$ we use the rotating wave approximation to dismiss terms containing $\beta_1 - \beta_0 - K_g$. Defining the phase mismatch as $\Delta K = \beta_0 - \beta_1 - K_g$, Equation (2.40) can be re-written as:

$$\begin{aligned} \frac{dA_0(z)}{dz} &= -\frac{1}{2}cA_1(z)e^{+i\Delta Kz} \\ \frac{dA_1(z)}{dz} &= -\frac{1}{2}\bar{c}A_0(z)e^{-i\Delta Kz} \end{aligned} \quad (2.44)$$

Here c is as defined in Equation (2.43). We make the substitutions [25]:

$$\begin{aligned} R_0(z) &= A_0(z)e^{-\frac{i}{2}\Delta Kz} \\ R_1(z) &= A_1(z)e^{+\frac{i}{2}\Delta Kz} \end{aligned} \quad (2.45)$$

and obtain the following equation in matrix form:

$$\frac{d}{dz} \begin{bmatrix} R_0(z) \\ R_1(z) \end{bmatrix} = \frac{1}{2} \begin{bmatrix} -i\Delta K & -c \\ -\bar{c} & i\Delta K \end{bmatrix} \begin{bmatrix} R_0(z) \\ R_1(z) \end{bmatrix} \quad (2.46)$$

This has the general solution of:

$$\begin{bmatrix} R_0(z) \\ R_1(z) \end{bmatrix} = q_- e^{-\gamma z} \begin{bmatrix} i\Delta K + 2\gamma \\ \bar{c} \end{bmatrix} + q_+ e^{\gamma z} \begin{bmatrix} i\Delta K - 2\gamma \\ \bar{c} \end{bmatrix} \quad (2.47)$$

where $\gamma = \frac{1}{2}\sqrt{|c|^2 - \Delta K^2}$ is the positive eigenvalue, q_- and q_+ are both constants.

We reproduce the well known result that a Bragg grating has what is known as a photonic bandgap [8]. That means there are two regimes of behaviour. Inside the photonic bandgap, that is so long as the phase mismatch is smaller than the coupling coefficient ($|\Delta K| < |c|$) then the amplitudes of both modes decrease exponentially with z (the backward propagating mode growing exponentially in its direction of propagation). However, if $|\Delta K| > |c|$ then we are outside of the photonic bandgap and have an oscillatory solution with period $\Omega = \frac{1}{2}\sqrt{\Delta K^2 - |c|^2}$. We can see, therefore, that the photonic bandgap has a half-width given by $|c|$, which is the absolute value of the coupling coefficient [8].

Launching light only in the forward direction means that the boundary conditions are given by $R_0(z=0) = 1$ and $R_1(z=L) = 0$. Going through some analytical derivation yields us the following values for the transmitted and reflected mode amplitudes for $\Delta K = 0$:

$$\begin{aligned} R_1(0) &= \frac{\kappa^2 - 1}{1 + \kappa^2} e^{i\phi} \\ R_0(L) &= \frac{2\kappa}{1 + \kappa^2} \end{aligned} \quad (2.48)$$

where $\kappa = e^{\frac{|c|L}{2}}$ and L is the length of the grating.

Outside the bandgap, where the system is oscillatory, we find by setting the boundary conditions that q_+ is given by the following:

$$q_+ = \frac{[U + iV]e^{\frac{i\phi}{2}}}{\bar{c}D} \quad (2.49)$$

and $q_- = \frac{1}{\bar{c}}e^{\frac{i\phi}{2}} - q_+$ with:

$$\begin{aligned} U &= \frac{\sin(\Omega L)^2 \Delta K^2 + 2\Delta K \Omega + 4 \cos(\Omega L)^2 \Omega^2}{D} \\ V &= \frac{\cos(\Omega L) \sin(\Omega L) [\Delta K^2 - 4\Omega^2]}{D} \\ D &= 2(\sin(\Omega L)^2 \Delta K^2 + 4 \cos(\Omega L)^2 \Omega^2) \end{aligned} \quad (2.50)$$

where U and D are decompositions of the constant q_+ . By taking the modulus square, we are able to derive the power in the forward and backward propagating modes:

$$\begin{aligned} |R_n(z)|^2 &= 1 - 2V \sin(2\Omega z) + (2V^2 - 2U + 2U^2)(1 - \cos(2\Omega z)) \\ |R_m(z)|^2 &= S - 2V \sin(2\Omega z) + (2V^2 - 2U + 2U^2)(1 - \cos(2\Omega z)) \end{aligned} \quad (2.51)$$

with $S = \frac{1}{|c|^2} [(\Delta K + 2\Omega)^2 - 8\Omega U(\Delta K + 2\Omega) + 16\Omega^2(U^2 + V^2)]$. This provides us an analytical result for coupling counter-propagating modes by a grating that we can then use to verify numerical models in which counter-propagating modes are coupled.

In a real experiment, the phase mismatch is dependent upon the light wavelength which is observable and directly controllable. Changing the light wavelength has the effect of changing the propagation constants of the modes and thus the phase mismatch. At phase matching, we have the strongest reflection into the backwards propagating mode. Provided that the grating is much longer than $1/|c|$ then we have an easily identifiable bandgap of width proportional to $|c|$ in which all of the light is backreflected. The reflected light drops to zero abruptly outside of the bandgap and we see a number of sidelobes on either side. The amplitude of these sidelobes decreases as the wavelength moves away from the edge of the bandgap and their frequency increases. And far away from the bandgap the reflected light approaches zero. This section replicates the findings in [8].

A similar analytical solution can be found for the behaviour of long-period waveguide gratings coupling together co-propagating waveguides modes. One of the main differences is the lack of a photonic bandgap. This means that we have oscillatory behaviour even for phase matching.

2.2.3 Transfer matrix method

In a linear system with N inputs and N outputs, it is possible to express the entire behaviour of that system as an N by N matrix \mathbf{S} [26]. Here, we express the sets of values at the inputs and outputs as vectors each with N entries that we note as \vec{I} and \vec{O} respectively. The outputs are thus simply related to the inputs as [26]:

$$\vec{O} = \mathbf{S}\vec{I} \quad (2.52)$$

In the case of linear optics, the values we place at the inputs and outputs are simply the mode amplitudes at the inputs and outputs [27]. If we have a passive optical device, that is one which is not acted upon by any outside source of energy, then we have conservation of energy in our system. This is represented in our system by the requirement that the

matrix \mathbf{S} is unitary. That means it must satisfy the condition [8, 28, 29, 30]:

$$\mathbf{S}^\dagger \mathbf{S} = \mathbf{S} \mathbf{S}^\dagger = I \quad (2.53)$$

where \dagger is the conjugate transpose of a matrix and I is the N by N identity matrix.

This method is useful for expressing complex systems of optical elements such as those used in optical information processing. As we explain in Sections 2.3.3.2 and 2.3.4, a 2×2 unitary matrix may be implemented by a Mach-Zehnder interferometer and these may be brought together in a network to achieve an $N \times N$ unitary matrix. This makes the transfer matrix method crucial in order to mathematically express these networks and thus implement any desired unitary transformation in them. In Chapters 5 and 6, we use the transfer matrix method ourselves to express our own grating-based waveguide-to-waveguide couplers as transfer matrices in order to find the full range of transformations we can build up to in our devices.

The transfer matrix representation of a system involving multiple modes is easy to derive from coupled mode theory. It is simply a matter of finding the outputs of the system for each input, with the inputs each represented by a set of boundary conditions that is equal to 1 for that input and 0 for all the other inputs. All of the outputs are then placed as the entries $s_{n,m}$ of the matrix \mathbf{S} , where n and m are the values of the n th output for the input m .

For example, to find the transfer matrix for a Bragg grating coupling counter-propagating modes with $\Delta K = 0$, as we have previously analysed in Section 2.2.2.1, we already have the outcome for one input in Equation (2.54), so we just need the outcome for the input with boundary conditions $R_n(z = 0) = 0$ and $R_m(z = L) = 1$. Using the same method we find that:

$$\begin{aligned} R_m(0) &= \frac{2\kappa}{1 + \kappa^2} \\ R_n(L) &= \frac{1 - \kappa^2}{1 + \kappa^2} e^{-i\phi} \end{aligned} \quad (2.54)$$

So that the relation between the inputs and outputs in matrix form is given by:

$$\begin{bmatrix} R_n(L) \\ R_m(0) \end{bmatrix} = \frac{1}{1 + \kappa^2} \begin{bmatrix} 2\kappa & (1 - \kappa^2)e^{-i\phi} \\ (\kappa^2 - 1)e^{i\phi} & 2\kappa \end{bmatrix} \begin{bmatrix} R_n(0) \\ R_m(L) \end{bmatrix} \quad (2.55)$$

which is in the same form as Equation (2.52) and can also express in terms of hyperbolics [8]:

$$\mathbf{S} = \begin{bmatrix} \text{sech}(\phi_\kappa) & -\tanh(\phi_\kappa)e^{-i\phi} \\ \tanh(\phi_\kappa)e^{i\phi} & \text{sech}(\phi_\kappa) \end{bmatrix} \quad (2.56)$$

2.2.4 Finite element method

In this and the following subsections I outline a number of other methods that are often used for simulating waveguides and gratings. I do this in order to give an overview of some of the other methods that are available. I give an explanation of their strengths and weaknesses and why, with the exception of the finite element method in Chapter 3, I don't use them in this thesis.

A brute force method for solving Maxwell's equations in a one, two or three dimensional system is the finite element method. This method discretizes the space in a large number of arbitrarily defined small areas or volumes that form part of what is known as a mesh. An approximate version of Maxwell's equations is defined for that discretized space and solved to achieve an approximate solution [4, 31]. This method is highly flexible and can simulate complex photonic devices with a wide variety of index distributions [4]. Due to the variability of the size of the mesh areas, it can be used to simulate detailed optical elements alongside large ones, such as waveguide gratings surrounded by a smooth cladding region [4]. I use this method in Chapter 3 in order to simulate coupling from waveguide to radiation modes. However, it is highly computationally and memory intensive [32] and thus not suitable for simulating our devices using realistic parameters. This is because our devices are far longer compared to the size of our grating structures and therefore would require a huge number of mesh points to compute, even if this were to be mitigated by aggressively varying the mesh size throughout the simulated region.

2.2.5 Finite difference time domain

This method is among the simplest to understand. The components of the electric and magnetic fields are defined in two or three dimensional grids (depending on the dimensionality of the problem) that are staggered with half a grid point of separation between them. The electric and magnetic fields are also defined half a time step apart. At each step in the simulation, the magnetic field is calculated from the electric field at the previous half-time step and then the electric field at the following half-time step is calculated from that magnetic field. The calculations are made using the finite differences equations which are derived from Maxwell's equations [33]. Much like the finite element method, it can simulate a large range of dielectric structures. What distinguishes this method from others is that it operates in the time domain. This means that it can be used to compute the entire spectral bandwidth of a system in a single computational step by simulating the propagation of a pulse through it [33].

However, in this thesis I look for stationary solutions of the device models. If I were to use the FDTD method, I would have to simulate the launching of light in the system and propagate the simulation in time until it reaches a stationary state. However, this

would take up an unnecessarily large number of computational steps. For this reason, it is better to use a frequency domain method or coupled mode theory in this case.

2.2.6 Beam propagation method

This method simulates the propagation of light in one direction in a medium with slowly varying index structure. As a result, it is not suitable for studying the devices in which light propagates in opposite directions. In this method, the electric field is propagated, then a phase delay is applied at every spatial step, then the field is propagated again [4]. In Chapters 4, 5, and 6, I simulate devices that exploit counter-propagating guided modes. I also seek to numerically verify an analytically derived equation for the coupling of light to radiation modes from Bragg gratings of arbitrary tilt angles. In particular, I consider Bragg gratings of small tilt angle that couple to counter-propagating waveguide modes. As a result, I do not use the beam propagation method.

2.2.7 The methods we choose

Coupled mode theory, which we outlined in Section 2.2.2, has a clear advantage over the finite element method (Section 2.2.4) and the finite difference time domain method (Section 2.2.5) for simulating the devices investigated in Chapters 4, 5 and 6 of this thesis. As well as the reasons given in Sections 2.2.4 and Section 2.2.5, this is because light in these devices is entirely confined by a wave-guiding ridge structure narrow enough to contain a small (< 100) number of modes. This means that it is not necessary to store and calculate the electric fields at every point along both the transverse and propagation directions at each simulation step as it is only necessary to calculate the electric fields in each mode along the propagation direction. This reduces the computational resources necessary to simulate light propagation in the device. By carefully choosing the grating parameters, it is possible to couple only between certain modes and so reduce the computational complexity even further by ignoring the remaining modes. This simplifies the problem enough to allow us to calculate analytical solutions.

The aim of Chapter 3 of this thesis is to derive an analytical solution for the coupling to radiation modes by a tilted Bragg gratings of tilt angle other than 45° . The beam tracing method developed in [23] and outlined in Section 2.2.1 was generalised to arbitrary tilt angles for this purpose. However, its suitability for arbitrary tilt angles can not simply be assumed. For this reason, a different numerical method is needed to verify it. I choose the finite element method due to its known versatility and due to the shortcomings of the finite difference time domain method for scattering at arbitrary angles (see Section 2.2.5).

2.3 Integrated Photonic Devices

In this section, we will go through some integrated photonic devices that already exist in the literature. In Section 2.3.1, we will discuss a number of types of waveguide-to-waveguide coupler that exist in the literature, including some based on Bragg gratings. In Section 2.3.2, we will discuss other integrated photonics devices based on Bragg gratings. In Section 2.3.3, we will discuss phase-shifters and Mach-Zehnder interferometers. Finally, in 2.3.4, we will discuss how integrated optics can be used as a basis for classical and quantum information processing.

2.3.1 Waveguide-to-waveguide Couplers

One of the aims of this project is the application of gratings for the design of new types of waveguide couplers, that is devices that couple light between two different channel waveguides. These have applications as beam splitters and wavelength division multiplexers. There are multiple devices already in existence that couple light between different waveguides. This section will discuss some of these devices, in particular those that use gratings, and explore their applications and also their limitations.

2.3.1.1 Evanescent directional couplers

The most traditional, and simplest, type of waveguide coupler is the evanescent directional coupler [4]. Here, two identical parallel single mode channel waveguides are brought close together as shown in Figure 2.6. This leads to an overlap of the wavefunctions of their fundamental modes. The device can thus be expressed as a complete system with two cores. The system has two modes, one symmetric mode that is expressed as the sum of the core modes of both waveguides and one anti-symmetric mode that is expressed as the difference. The modes are of slightly different effective refractive indices with the antisymmetric mode being the high-order mode and thus of slightly lower n_{eff} than the symmetric (fundamental) mode. Inputting light in one of the waveguides means exciting an equal superposition of the two modes. Their difference in n_{eff} means that the phases of the modes will evolve at different rates, accruing a phase difference as the light propagates. This manifests as a beating of the modes and thus an oscillatory transfer of energy between the two waveguides. This is known as evanescent coupling. After a certain propagation distance a phase difference of π is accrued between the modes and all the light from one waveguide has been transferred to the other. This is known as the coupling length and is given by the following equation [34]:

$$L_C = \frac{\lambda_0}{2(n_{eff,0} - n_{eff,1})} \quad (2.57)$$

where λ_0 is the free space light wavelength whereas $n_{eff,0}$ and $n_{eff,1}$ are the effective refractive indices of the symmetric and anti-symmetric modes.

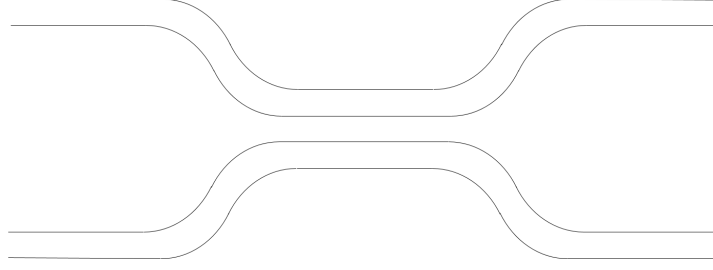


Figure 2.6: Evanescent directional coupler between two waveguides.

Complete transfer of energy is only possible in this scheme if the waveguides are identical. If the waveguides have modes with different effective refractive indices, the transfer of power is incomplete. The greater the difference, the less the possible power transfer [3].

With the addition of a phase-shift, a directional coupler can implement any 2×2 unitary transfer matrix. However, it is not as easily dynamically reconfigurable as a Mach-Zehnder interferometer with thermo-optic phase shifters (see future Section 2.3.3.2) [7].

2.3.1.2 Grating assisted and grating frustrated couplers

However, it is possible to couple between waveguides that are not identical, with complete power transfer, by corrugating the surface of one of the waveguides [35] to form a grating. This requires that the grating is phase matched, with the grating wavevector equal to the difference between the waveguide propagation constants with the equation in the form given by Equation (2.20). Such a coupler is known as a grating assisted coupler.

For directional couplers with identical waveguides, gratings can be used with the opposite intention. They can be used to introduce a phase mismatch in the coupler in order to prevent the transfer of energy between the waveguides [36]. If the grating is strong enough, light of wavelength around the Bragg wavelength inputted in one of the waveguides sees the grating and thus is forced to remain in the waveguide, however, light far from the Bragg wavelength does not see the grating and is thus transferred. This is known as a grating frustrated coupler and we show a picture of such a coupler in Figure 2.7.

A big limitation of evanescent couplers, including grating assisted/frustrated couplers, is that the two waveguides need to be brought close together in order for there to be coupling.

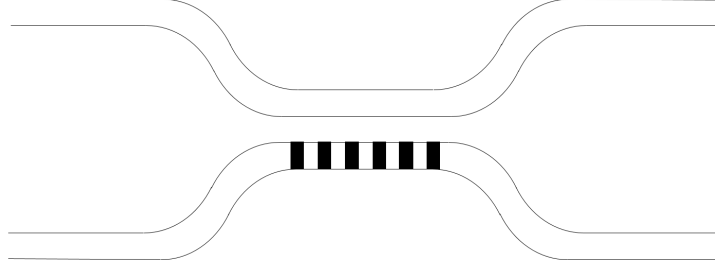


Figure 2.7: Grating frustrated directional coupler between two waveguides.

2.3.1.3 Long period waveguide-grating couplers

One alternative to evanescent couplers is to couple light between the two cores using a forward propagating cladding mode as an intermediary [37]. As shown in Figure 2.8, long-period waveguide gratings are inscribed onto both cores. They are used to couple light between the core modes and the cladding mode. This system has the advantage over evanescent coupling that there is a lower sensitivity on the waveguide separation. This scheme has been realized experimentally with rectangular waveguides in a polymer platform. It has been realized experimentally for the first time using corrugated gratings [38] with a peak coupling efficiency of around 30%. Later, using direct UV exposure to create physical gratings [39], it has been realized with a maximum coupling efficiency of around 80%. (Note that this is not the same as the UV-writing used in our platform.) By using four waveguides each with long-period waveguide gratings in parallel and phase-shifting one of the grating, this platform has been proposed as a way to implement a Walsh-Hadamard transform [40].

2.3.1.4 Radiation mode-based polarisers and polarising couplers

It has been theoretically predicted [23] and experimentally demonstrated [41, 10] that Bragg gratings with a 45° tilt angle, which is Brewster's angle in the limit of low index contrast, will radiate light of one polarization at an angle of 90° (with phase-matching) and light of the other polarisation. This leads to 45° Bragg gratings being useful as polarisers.

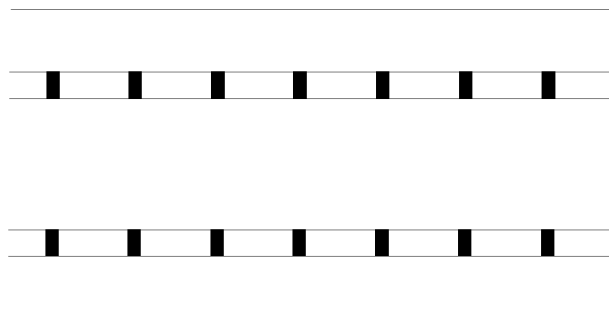


Figure 2.8: A long-period waveguide grating coupler between two waveguides.

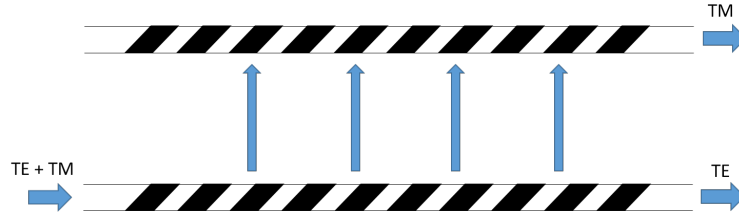


Figure 2.9: A grating based polarising waveguide-to-waveguide coupler between two waveguides. Also shown is the mechanism for splitting the polarisations.

A possible alternative to the waveguide-to-waveguide couplers described in previously in this section which is to couple between waveguides by using radiation modes. These are the continuum of modes that are not confined in the device. In this method, light from one waveguide is radiated from the waveguide using a tilted grating only to be captured by another waveguide using an identical grating [42]. M. Posner, a former researcher at the ORC, has built [41, 24] such a coupler that uses parallel 45° tilted gratings in order to transfer TM polarised light from one waveguide to another while leaving TE polarised light untouched (see Figure 2.9). Unfortunately, N. Podoliak has found that this device has a very low coupling efficiency that is limited as a result of leakage from the waveguide receiving the light [24, 43]. The remaining light may be captured by remaining waveguides containing tilted gratings [43] but this is not ideal. Experimentally, this device has been built with an extinction ratio of over $17dB$ between the two waveguides which means that a very small fraction of the light is actually captured by the second waveguide[24].

2.3.1.5 Multimode interferometers

Another way to couple between waveguides is by using a multimode interferometer (MMI). This type of device consists of multimode waveguide with a large number of modes [4, 44, 45]. A finite number of input and output ports are placed at both ends of the multimode waveguide to connect it to single-mode waveguides (see Figure 2.10). Light launched into the MMI at an input port from a single-mode waveguide will be coupled into the modes of the multimode waveguide. As each mode has a different propagation constant, there will be a distance along the propagation direction at which the light in each of the MMI modes interferes constructively and recombines into an image of the inputted light [4, 44, 45]. Cutting off the multimode waveguide at this point would allow us to couple the light into a single-mode waveguide identical to the original (see Figure 2.10(a)). With different MMI lengths, it is also possible to generalise this principle with multiple input and output ports and use it as an $N \times M$ beam splitter [44, 45]. Such a beam splitter can also be used to couple between waveguides. For example, a 2×2 beam splitter, which we show on Figure 2.10(c), can be used to couple between two waveguides [44, 46, 47, 48].

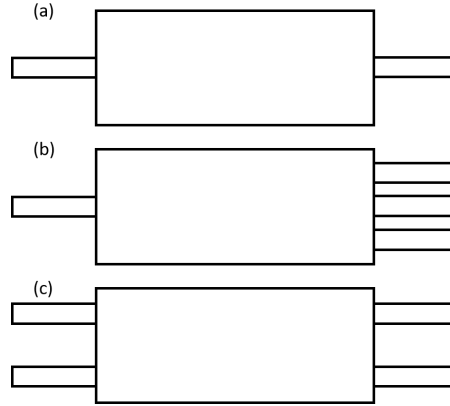


Figure 2.10: A selection of MMIs connected to single modes waveguides via input and output ports. With (a) connecting one input port to one output port, (b) connecting one input port to three output ports, (c) connecting two input ports to two output ports.

Apart from being able to couple between a moderate number of input and output ports with a single device, MMIs have certain other advantages compared to directional couplers in that they have good fabrication tolerances and are more broadband [46, 47]. However, they tend to suffer from imbalances in the power outputs and excess loss [49]. This makes them unsuitable for use in optical information processing, which typically employs directional couplers (see Section 2.3.4) and requires low losses and precise power outputs. This also disadvantages them compared to the devices we study in Chapters 4, 5, 6 as they employ gratings that can be precisely engineered (leading to precise power outputs) and can be made with low losses.

2.3.2 Other devices based on Bragg gratings

2.3.2.1 Beam focusing and spectrometry with a chirped grating

Something interesting happens when the period of a grating is varied along the propagation direction in what is known as a chirp. The direction of scattering changes along the waveguide but so does the resonant wavelength. This leads to two different effects. One is that light containing multiple frequencies will have its frequencies separated. The other is that each frequency will be focused onto a single spot. The position of that spot changes with the light frequency. This is the basis of one particular implementation of a spectrometer first introduced in [50].

More recently, a grating spectrometer has been fabricated at the ORC [11] with very high chirp using the fabrication method we outline in Section 2.4 and thus a far smaller focal length compared to [50] making it much more compact. With this spectrometer, it has also been demonstrated the prediction made in [50] that, using a specific nonlinear chirp, it is possible to correct for aberrations [11]. In the ray-picture, this is the chirp

which forces all light rays emitted from the grating to cross at a certain point and is given by Equation (18) of [11]. We show beam focusing for one frequency with that spectrometer on Figure 2.11.

Using gratings for beam focusing has also been used in set-ups in which the width of the waveguide is expanded using a taper. A grating coupler is defined in the expanded region in order to couple light out of the chip. As the light inside and after the taper has a curved phase front, the chirp is used together a curved phase front to focus the light. Beam focusing using this method has been achieved in [51] and used to couple light in to a trapped ion qubit in [52].

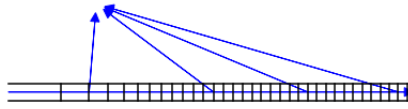


Figure 2.11: Chirped grating used for focusing a beam onto a single spot. Note that to avoid aberrations, one must use the spatial chirp given by Equation (18) of [11].

2.3.2.2 Phase-shifted gratings

Introducing a π phase-shift in a standard backreflecting Bragg grating leads to a very narrow transmission window around the Bragg wavelength. This has been widely implemented with examples in both planar photonics [53] and optical fibre [54] and have a wide variety of applications such as for single-frequency lasers [54].

2.3.3 Phase-shifters and Mach-Zehnder interferometers

In this subsection, we introduce tunable phase-shifters and Mach-Zehnder interferometers. The reason for this is that, as we will see in Section 2.3.4, they form the building blocks of integrated optical computing.

2.3.3.1 Thermo-optic phase-shifters

Phase-shifters are very commonly used in integrated optics. Their role is to provide a phase-shift in the electric field of light passing through a waveguide. This is achieved with a modulation of the effective index of the mode of the waveguide in the region affected by the phase-shifter and is typically achieved by heating the waveguide, typically

electrically, at that location to change the refractive index [55, 56]. Such a phase shifter is therefore dynamically reconfigurable.

2.3.3.2 Mach-Zehnder interferometers

A Mach-Zehnder interferometer (MZI) consists of two 50 : 50 beam splitters with the outputs of the first beam splitter connecting to the inputs of the second. While propagating between the two beam splitters, the two halves of the beam in general accrue a relative phase difference. This phase difference is the result of a difference in the optical length, which is the product of the physical length and the (effective, in the case of waveguide transmission) refractive index, between the two paths. This may result from a difference between the physical length between the two paths or due to the presence of an object causing a phase-shift in one of the two paths. The second beam splitter interferes the light from both parts and reflects/transmits the light into a superposition of the two outputs with the relative amplitudes governed by the phase shifts [57]. Any variation in the optical lengths makes it hard to control the phase-shift. As long-term stability in path length is very difficult to achieve in bulk optics, they are typically unsuitable as a platform for implementing more complex devices involving MZIs [58], such as any scheme involving multiple MZIs such as optical computing as in Section 2.3.4. This necessitates their implementation in integrated optics.

In integrated optics, a Mach-Zehnder interferometer is typically implemented as follows: the two 50 : 50 beam splitters are implemented using directional couplers between channel waveguides (see Section 2.3.1.1) and the relative phase difference is the result of a thermo-optic phase-shifter in one of the waveguides (see Section 2.3.3.1) [59, 7]. Using an additional thermo-optic phase-shifter in one of the waveguides either before the first directional coupler or after the second allows us to have a dynamically reconfigurable system that can implement any 2×2 unitary transfer matrix (see Section 2.2.3) [58, 7] with the two degrees of freedom provided by the two phase shifters.

2.3.4 Integrated optical computing

Integrated photonics provides a versatile platform for both classical and quantum information processing. Classically, it can be used to implement universal linear optics [7]. This means that it can be used to implement any linear, classical transformation of light modes. These are represented by an $N \times N$ unitary transfer matrix as defined in Section 2.2.3. It has been proven mathematically that any $N \times N$ unitary matrix can be decomposed into a product of $\frac{N(N-1)}{2}$ 2×2 unitary transformations [29, 60]. These transformations can be physically implemented in different ways.

In integrated optics, each of these 2×2 transformations can be implemented and made reconfigurable by a Mach-Zehnder interferometer consisting of two directional couplers

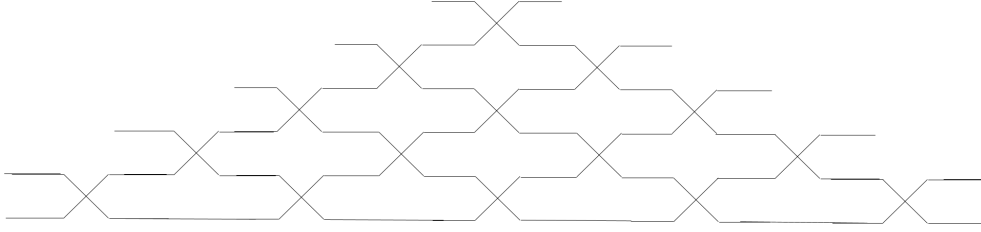


Figure 2.12: Optical information processing chip for implementing an $N \times N$ unitary matrix. Mach-Zehnder interferometers are depicted as crosses. The scheme presented in this picture is the one used in [7].

and two phase-shifters (see Section 2.3.3.2) [7]. In order to implement an $N \times N$ unitary transfer matrix, the device consists of N parallel waveguides and thus N input and N output ports at the end facets of each waveguide on either side of the device. The MZIs couple light between parallel waveguides. Multiple schemes have been proposed for decomposing unitary matrices [29, 60, 61] with [61] providing a more compact design with lower losses compared to [29] on this platform. Neural networks have been demonstrated in this platform for implementing machine learning algorithms [62]. We show the scheme used in [7] in Figure 2.12.

The use of integrated photonic in quantum information processing has been the topic of extensive research [63]. This is because photons are ideal for transmitting quantum information. This is the result of their high speed, the ease with which they can be manipulated and over long lengths through free space or optical fibre while retaining their quantum coherence due to lack of interaction with the environment [64, 63]. Of particular interest, is the use of integrated photonic platforms in the manipulation of quantum states. This uses the same architecture as above based on directional couplers and phase shifters [64, 65, 7].

Each quantum bit, also known as a qubit, is encoded in a single photon that can be detected in either one or two waveguides [64]. The photon is in the superposition state of being in either waveguide and this superposition state represents a qubit. Quantum gates are represented by unitary matrices with an n qubit quantum gate represented by a $2^n \times 2^n$ unitary matrix. The most obvious implementation of a universal qubit gate would therefore be the same way as an $N \times N$ unitary matrix as described above and to encode n qubits as a single photon in a superposition of 2^n waveguides. However, this is not scalable as the number of waveguides needed quickly becomes massive. As a result, it is better to implement each qubit on individual photons in a superposition state of a pair of waveguides [7].

Nonetheless, any single qubit transformation can be implemented the same way as a 2×2 unitary transformation, by a Mach-Zehnder interferometer as in Section 2.3.3.2 [58]. The other most important type of quantum gate for use in quantum computing is the C-NOT

gate. This is because any universal quantum gate can be built by a combination of C-NOT gates and unitary single qubit gates [66]. A C-NOT gate acts on two qubits. One that is called the control qubit and the other the target qubit. Depending on which state the control qubit is in, the target qubit is either flipped or not flipped between its two basis states. The basis states in this case are the non-superimposed waveguide states.

In order to implement a C-NOT gate in quantum photonics, a Mach-Zehnder interferometer is used on the target qubit that provides a π -phase shift inside one of the arms provided that the control qubit is in the correct state [58]. The target qubit then outputs the MZI in the opposite state compared to if there wasn't a π -phase shift. This is the result of interference in the second directional coupler in the MZI. Simple C-NOT gates of this form have been implemented using 6 waveguides [58], or using 4 waveguides and taking advantage of the polarisation [67]. However, these implementations only have a $\frac{1}{9}$ probability of working. An implementation employing many more waveguides has been able to implement any arbitrary 2-qubit gate, including a C-NOT gate with a success probability of $\frac{1}{4}$ as well as quantum gates with more qubits [68].

Architectures involving directional couplers and phase-shifters have also been used to implement quantum fast Fourier transforms [69] and quantum transport simulations [70].

2.4 Fabrication methods for devices investigated in this thesis

In this section, we will go through how the devices that we investigate in this thesis would be fabricated. In Section 2.4.1, we explain why we choose a silica integrated photonics platform in which to implement our devices. In Section 2.4.2, we go through the flame hydrolysis deposition (FHD) technique that would be used to fabricate our silica substrate. In Section 2.4.3, we will go on to explain the phenomenon of photosensitivity in germanium doped or germanium and boron co-doped silica and how that can be used to fabricate waveguides and Bragg gratings with UV-writing. Finally, in Section 2.4.4, we will explain how trenches can be created in the wafer by micromachining to create a large guiding ridge structure which is crucial to the fabrication of some of the devices that are investigated in this project.

2.4.1 Why silica?

Silica is a useful platform for integrated photonics, including quantum photonics [58] as it can be used to easily fabricate waveguides with low propagation losses [71, 72] and with negligible losses coupling to a fibre [73, 74]. At the ORC, a platform has recently

been developed by the OEQP group for UV-writing waveguides in silica simultaneously with high quality Bragg gratings of arbitrary tilt angle [13, 10].

The main reason for using a silica platform in this research is the ease of fabricating high quality tilted Bragg gratings with high fabrication tolerances. As we outline in Section 2.4.3, it is very easy to write Bragg gratings with any tilt angle simultaneously with a waveguide in a silica platform using UV light. These gratings are of high quality due to the waveguides and gratings being highly uniform along the propagation direction [25]. In contrast, other material platforms do not have these advantages. In silicon photonics, for example, because the core has a high index contrast with the cladding, the waveguides must be fabricated to very small size in order to be single mode and therefore require a high degree of precision during fabrication. This can lead to a relatively high amount of variation in the effective index along the waveguide, which leads to lower quality gratings. Not only that, but UV-writing is simply not available in silicon photonics. Instead, gratings must be physically etched onto the waveguide. This challenging fabrication method often leads to minute defects in the etched period as well as variation in modal propagation. Such gratings are rectangular in shape and are therefore more likely to lead to unwanted coupling between modes as a result of additional Fourier components. Bragg gratings in silicon photonics typically have one of the following purposes: standard back-reflecting Bragg grating-based devices for filtering [75, 76], grating couplers to couple from a waveguide to a fibre [9] and subwavelength gratings [77, 78] that reduce the refractive index of the material as seen by the light. Fabricating tilted gratings is far more difficult in silicon photonics and, as far as we are aware, has only been achieved by one team [79] for subwavelength gratings. The same team have then gone on to fabricate a polarizing waveguide-to-waveguide coupler based on subwavelength gratings, with one of them tilted [80].

Another advantage of the silica platform is that it can be used to easily couple to optical fibres with negligible loss [73, 74]. This is because the fibre and the optical chip are both made out of the same material and both are made out of a raised index core that guides the light surrounded by a cladding with a typically similar index contrast between them. This means that, if they are both single-mode, the waveguide and the core of the fibre will also be of similar size and so they will each support a fundamental mode of similar profile. The fraction of the electric field amplitude that is transferred from the waveguide to fibre or vice versa is given by the spacial overlap between the two modes [74]. In fact, the mode profile can be made identical in which case the coupling loss between the waveguide and fibre is negligible [73].

In practice, however, the index contrast and core width of the waveguide and fibre are typically not the same. The typical single-mode fibre has an index contrast of 0.005 between the core and the cladding and a diameter of $8\mu m$. Silica waveguides in a planar platform, however, typically have a higher index profile and consequently smaller size of the core in order to increase the density of integrated components that is possible on this

platform. This leads to modes that are of smaller radius compared to those of the fibre. The solution in this case is to slowly increase the waveguide size at the end that connects to the fibre in what is known as a taper. This brings the mode profiles to the same size and thus brings down the coupling loss [74]. Nonetheless, this is far easier than in other material platforms (such as silicon) that have a higher index contrast between the core and cladding than optical fibres as they have waveguides with a smaller guiding core for single-mode operation. This means that the size of the modes guided by the waveguides in these platforms are much smaller than the modes carried by optical fibres. This is particularly the case in silicon photonics where single-mode waveguides have a mode profile that is tiny in comparison with optical fibres. This makes coupling to an optical fibre very difficult and requiring more complex structures such as grating couplers and aggressive tapers to couple with insertion losses of $0.25dB$ - $5dB$ [9, 81, 82] that are still much higher than for a silica platform. Also, these structures are difficult to fabricate. A plug-and-play fibre to silicon waveguide interconnect has been developed that employs a silicon grating coupler and an intermediary polymer waveguide [82]. However, this has an insertion loss of $4.7dB$ [82]. It is also likely to be much more expensive compared to the very cheap and simple interconnects between optical fibre and silica waveguides.

Another competitor optical platform is polymer. Polymer integrated waveguides can be fabricated with sufficient control over the spatial distribution of the refractive index to create step index waveguides [83]. Also, waveguide structures can be physically fabricated by direct UV exposure [83, 84]. (Note: not to be confused with UV-written silica waveguides (see Section 2.4.3).) Etching can be used to fabricate both short-period [85] and long-period [86] gratings. Long-period grating structures can also be fabricated with direct UV exposure [87] and has been used to fabricate long-period waveguide gratings couplers [39]. However, polymers have a higher variability in local effective index than silica. This leads to a higher variability in effective index along the waveguide and thus to worse grating performance. Also, precise engineering is more challenging, particularly for the small features required for short-period gratings.

Also, polymer waveguides typically have high propagation losses at $1550nm$ due to material absorption with $0.79dB/cm$ [88] reported for single-modes waveguides. A non-negligible fibre-to-waveguide coupling loss of $0.78dB$ was also reported for the same waveguides [88]. This is despite the fact that these waveguides are made with a small index contrast between the core and the cladding, similar to that in silica, which should in theory allow good modal matching to fibre. This makes polymer waveguides unsuitable for the devices investigated in this thesis as they rely on efficient coupling to fibre, particularly for the device in Chapter 6. The index contrast of polymer waveguides can also be made reasonably high [89] but not high enough to compete with silicon photonics in terms of integration density.

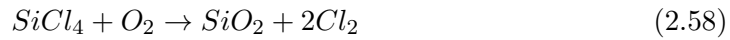
To conclude, silica is the best material platform for fabricating the devices investigated in this thesis as it can be used to fabricate waveguides with low propagation loss and

low insertion loss from a fibre at $1550nm$ for more cheaply and easily than with other platforms such as silicon and polymer photonics. Most importantly, the UV-writing process can also be used to fabricate tilted Bragg gratings far more easily, and with grater precision, than other platforms.

2.4.2 Flame hydrolysis deposition

The silica material platform is fabricated through a process known as flame hydrolysis deposition (FHD). This process was first used to fabricate silica/titanium oxide waveguides in the early 1980's and was at the same time proposed for silica/germanium oxide waveguides [90]. The process used at the ORC is explained concisely in [41] and in more detail in [91]. A silica glass soot is deposited onto a planar wafer via a flame after which the soot is fused in a furnace. By doping the soot with impurities, such as germanium, phosphorus and boron, it is possible to control the optical properties of the layer such as, most importantly, its refractive index and photosensitivity (see Section 2.4.3).

The silica soot is created by burning silicon tetrachloride ($SiCl_4$) together with oxygen and hydrogen in what is known as an oxyhydrogen burner. It undergoes the following chemical reactions [41, 91]:



Germanium, phosphorous and boron dopants are inserted by adding $GeCl_4$, PCl_3 and BCl_3 to the burner and reacting them through the same process. Both germanium and phosphorus cause an increase in the refractive index whereas boron causes a decrease. Germanium causes an increase in the photosensitivity which is greatly enhanced by co-doping with boron [92]

The wafers for our devices are fabricated layer by layer. First, a silicon wafer is used as a substrate. A silica underclad layer is grown on top of it by reacting the silicon in an oxygen-rich high-temperature environment what is known as thermal oxidization [41]. Then, a raised-index core layer is deposited onto the underclad layer through the FHD process with germanium and boron dopants added in order to increase the layer's photosensitivity. The amount of each dopant is chosen so as to control the refractive index with more germanium leading to an increase and more boron leading to a decrease. The overclad layer is deposited on top of the core layer using boron and phosphorous dopants with the levels controlled in order to have a similar refractive index in the overclad and underclad and thus have a symmetrical fundamental mode in the y (up/down) direction and thus have good modal matching to optical fibre [41].

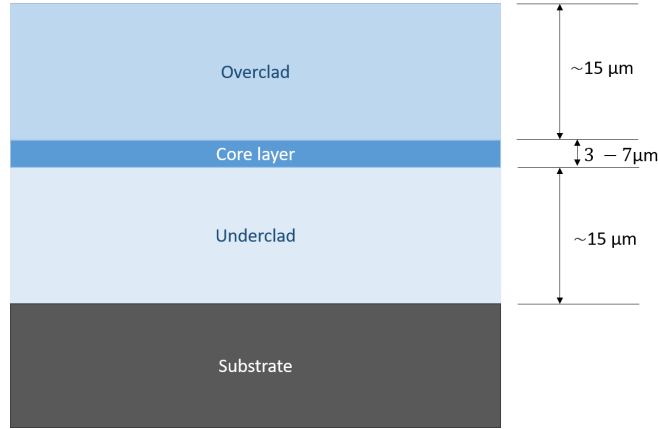


Figure 2.13: Silica wafer produced through flame hydrolysis deposition. Shown are the substrate, core, underclad and overclad layers.

The outcome is the fabrication of a silica wafer with a photosensitive raised-index layer in which structures, such as waveguides and Bragg gratings, can be fabricated using UV-writing. The core layer can be made narrow enough to confine light in a single mode in the y direction. We show a schematic of the produced wafer on Figure 2.13. Note that there are stresses induced as a result of the difference in thermal expansion coefficient between the silica and silicon layers [93]. These are mitigated in the fabrication process by having a thick underclad layer [41] but can lead to curvature in the layer surfaces of the chip that needs to be adjusted for during the UV-writing process for device lengths of longer than $20mm$ [41].

2.4.3 Photosensitivity and UV-writing

Photosensitivity is the phenomenon by which shining light on certain materials causes a change in their material properties. In the context of photonics in silica, it is typically used to refer to the increase in the refractive index of a material as a result of radiation by light. It was first discovered accidentally when researchers [94] launched $488nm$ light through a germanium doped silica fibre and found that it produced a grating inside the fibre. They found that it resulted in light reflected from the opposite end of the fibre causing an interference pattern with the incident light. It was found that it was caused by a two photon process; later work showed that UV light could be used directly through the side of the fibre to generate Bragg gratings [95].

The mechanism for photosensitivity in germanosilicate is not fully understood and multiple possible explanations have been suggested. Once again, we refer to [41] for a brief introduction to this topic. Doping with germanium and/or boron results in defects in the molecular structure of the glass resulting from oxygen deficiency [16]. One example of such a deficiency causes silicon and germanium to be directly bonded to one another.

The role of these colour centres here is simply to provide an absorption window to couple light energy into the material [96]. Radiation by UV light at these wavelengths (e.g. 240nm) results in changes in the bond structure which leads to a change in the refractive index. However, this does not provide the full picture and it is likely that other mechanisms also contribute to photosensitivity. In addition, results suggest that refractive index change is not only caused by colour centres directly but also by compaction of the molecular structure of the glass leading to an increase in its density, and stress, and thus refractive index [97, 96].

Prior work has shown that the change in refractive index is roughly linearly proportional to the fluence (irradiated energy per unit area) incident upon the photosensitive material but levels off as it approaches a maximum [25]. Loading hydrogen into the material using high pressures greatly increases the photosensitivity and the maximum index contrast that can be achieved between the waveguide core and the surrounding material up to $\delta n = 0.01$ [98]. The use of hydrogen causes a problem, however, as a result of outgassing which leads to more variability in the devices fabricated [99].

UV-writing has become a common technique for creating gratings by focusing two laser beams onto the same spot to create an interference pattern [19]. At the interference maxima, the material has greater exposure to UV light and so sees a greater increase in the refractive index. This forms a grating whose refractive index changes periodically along the z axis. This method has been used to fabricate gratings in optical fibres [100], as well as waveguides [101] and gratings [102, 13] in a silica integrated photonics platform. Whereas fibre gratings are developed on pre-existing optical fibres, which leads to an increase in the average refractive index of the waveguide in the location of the grating, this is not the case for waveguide gratings. This is because they are produced simultaneously with the waveguide and lead to no change in the average refractive index [102]. By modulating the intensity of the beam as the spot is moved along the waveguide, a sinusoidal index grating can be produced. The period of the grating is defined not only by the wavelength of the UV light but also by the modulation period of the beam [102], allowing greater control and flexibility in the creation of gratings with arbitrary periods.

The UV-writing method currently used at the ORC works by modulating the phase of one of the interfering beams [13] using an electro-optic modulator (see Figure 2.14). This produces a rolling interference pattern as the spot travels along the waveguide allowing for the fabrication of gratings with a very different grating period to the wavelength of the UV light and with any arbitrary apodization profile. The sample is placed on an air-bearing translation stage in order to move it relative to the interfering beams with a high degree of precision. The fabrication process is controlled entirely by a computer. A tilt angle can be created simply by rotating the sample [41]. This method can produce a refractive index change of up to $\delta n_g = 0.001$ for standard backreflecting gratings [25]. A current minor flaw in this system is the introduction of phase-shifts along the grating as

the electro-optic modulator resets [25]. More recently, a grating refractive index contrast as high as 0.0032 has been achieved at the ORC with this method [10] for 45° degree tilted gratings of a longer grating period for 90° radiation. This large refractive index change is due to a large tilt angle and larger grating period compared to standard Bragg gratings. Standard Bragg gratings have been fabricated in this platform without the use of hydrogen [99] by using 213 nm light which eliminates the problems caused by outgassing. Recently, superimposed Bragg gratings have been fabricated in an optical fibre at the ORC [103].

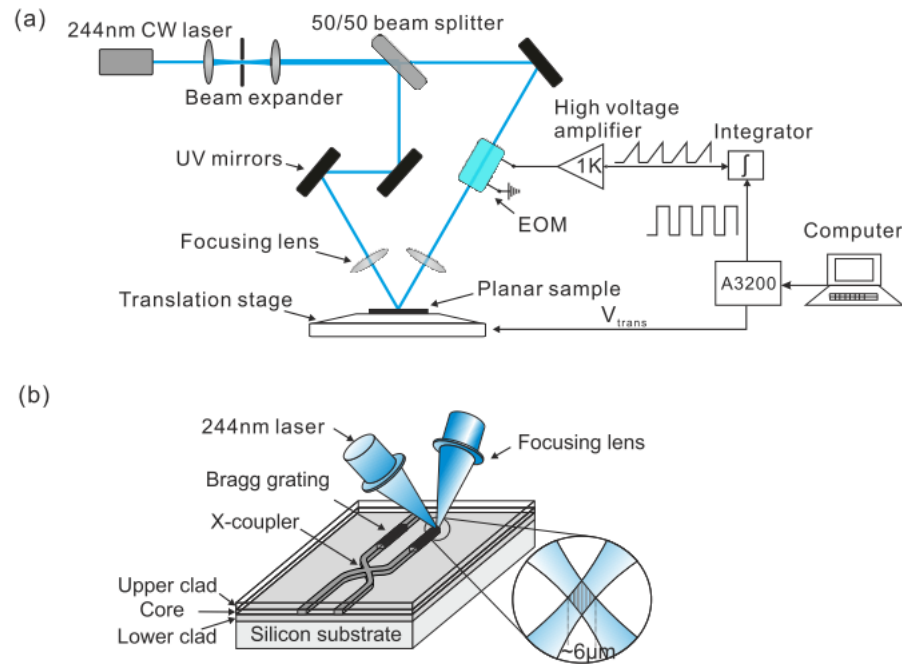


Figure 2.14: Image courtesy of [25]. (a) UV-writing system for simultaneous inscription of waveguides and Bragg gratings. The sample is placed on top of an air-bearing translation stage which allows the fabrication of Bragg gratings with highly precise grating periods. (b) Interference of the two beams creating an interference pattern in which the grating is fabricated.

2.4.4 Micromachining

A part of the fabrication process that is important for the fabrication of the majority of the devices investigated in this thesis (Chapters 4, 5, 6) is micromachining. It involves the use of a dicing saw with a diamond impregnated blade to cut trenches in the wafer [12]. Cutting two parallel trenches in the chip leads to large "waveguide" that confines light in the transverse x -direction. The index contrasts between the core and cladding layers confines light in the y -direction; and leads to a discrete number of modes confined in the core layer. These modes are often referred as "cladding" modes throughout this thesis, as opposed to the "core" modes of the UV-written waveguides, in analogy with

the core and cladding modes of optical fibres. Micromachining has previously been employed at the ORC to fabricate refractometers, [12] including one taking advantage of surface plasmons [104], for integrated optics as well as a multimode interferometer in a flat-fibre platform [105]. Micromachining has also been used at the ORC to fabricate PPLN waveguides [106, 107].

Chapter 3

Coupling from waveguide modes to in-chip radiation modes by a tilted Bragg grating

3.1 Introduction

The overall aim of my PhD was to design and simulate devices based on tilted Bragg gratings for use in integrated photonics. As such it was crucial to understand the physics of tilted Bragg gratings and how they operate. In order to achieve this, I spent the first part of my PhD studying the coupling of light from waveguide to in chip radiation modes via a Bragg grating. These are modes confined in the planar layer of the chip but not by the chip's external boundary with the air. They can also be used to describe the modes of the chip if it is so wide compared to the light wavelength that it can be assumed to be infinite and so the modes of the chip can be assumed to exist in a continuum.

To achieve this, the aim of the first part of the PhD was to find an analytical expression for the scattering of light from a tilted Bragg grating inscribed in a single mode waveguide. This was achieved by extending the analysis in Section 2.2.1 and [23] to smaller angles by finding a generalised version of Equation (2.24) and to compare the predictions with finite element simulations of the electromagnetics in COMSOL. The reason for this is that for smaller angles the grating was expected to have both a narrower bandwidth and a higher scattering efficiency [20]. This would allow for the separation of light of a desired wavelength for capture by a second waveguide similarly to [24]. Finding a generalised analytical solution applicable to a wide range of tilted gratings could unlock the study of more sophisticated types of grating such as chirped gratings in which the direction of scattering varies along its length.

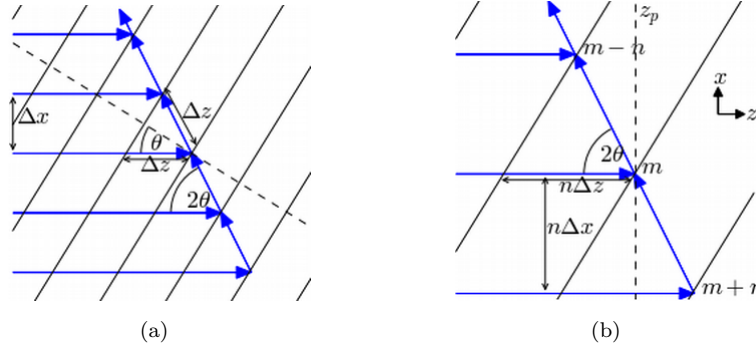


Figure 3.1: In (a), addition of reflections from individual planes for a non 45° grating. Discrete planes shown in (b) are those separated by n planes from one another. The ray at $x = 0$ hits the m th plane at $z = z_p$

This would allow researchers to study analytically the separation of frequencies to build a spectrometer as in [50, 11] or the focusing of light onto a single spot as in [52] (see Section 2.3.2.1 for more detail on both technologies).

We derive the analytical solution for coupling to radiation modes in Section 3.2. We present the numerical method for computing light scattering in this system in Section 3.3. Finally, we present the results of the numerical method and compare to the analytical solution in Section 3.4.

3.2 Analytical solution

The analytical solution for coupling to radiation modes is derived very similarly to [23]. However, due to the generalisation to arbitrary tilt angles, there are some modifications that need to be taken into account. This method of derivation consists of an analytical beam tracing method similar to that outlined in Section 2.2.1. As explained in that section, this method consists of dividing the grating into a large number of parallel thin films with little reflections at the interfaces between them that are added up as shown in Figure 3.1(a).

First we take Equation (11) from [23] for the reflectivities of each individual plane and generalise it for gratings of an arbitrary profile and tilt angle:

$$r_m(x) = -\frac{1}{2 \cos^2 \theta} \kappa(x) \cos \left[2\pi \frac{m \Delta z}{\Lambda_g} \right] \left(2\pi \frac{\Delta z}{\Lambda_g} \right) \quad (3.1)$$

Here, θ and Λ_g are the grating tilt angle and period, Δz is the plane separation and m is the index of the plane and $\kappa(x)$ is the envelope of the transverse profile of the grating.

As explained in Section 2.4.3, the waveguides and gratings are written using UV laser light. Since the index change is approximately linear with the fluence of the UV light

[25] and the laser emits a Gaussian beam, we assume the the waveguide and grating both have a transverse profile with a Gaussian envelope. This envelope is given by:

$$g(x) = \exp\left(-\frac{x^2}{\sigma^2}\right) \quad (3.2)$$

where σ is the $1/e$ half-width of the transverse profile of the waveguide and grating. As such, $\kappa(x)$ is given by the following:

$$\kappa(x) = \kappa_0 g(x) \quad (3.3)$$

where $\kappa_0 = \frac{\delta n_g}{n_{core}}$ is the fractional index contrast of the grating with δn_g the absolute index contrast and n_{core} the refractive index in the center of the waveguide.

Unfortunately, no exact analytical solution exists for the modes of a waveguide with a Gaussian index profile [108]. We will show in the future Section 3.4.1 that the fundamental mode of a Gaussian waveguide can be approximated by a Gaussian for the parameters considered in this Chapter. In this derivation, we assume that the pump mode has a Gaussian profile:

$$f(x) = \exp\left(-\frac{x^2}{w_0^2}\right) \quad (3.4)$$

At integration point z_p along the z axis we can find the following equation for an individual reflection similar to Equation (13) of [23]:

$$\begin{aligned} E_{r,m}(z_p) &= -E_1(z_p) r_m(x) f(x) \exp(-i\beta\mathcal{D}) \\ &= -E_1(z_p) \frac{1}{2 \cos^2 \theta} \kappa_0 \exp\left(-\frac{x^2}{w_1^2}\right) \cos\left[2\pi \frac{m\Delta z}{\Lambda_g}\right] (2\pi \frac{\Delta z}{\Lambda_g}) \exp(-i\beta\mathcal{D}) \end{aligned} \quad (3.5)$$

where $w_1 = \frac{w_0\sigma}{\sqrt{w_0^2 + \sigma^2}}$ is a quantity we henceforth call the effective width and \mathcal{D} is the path length of the ray. Here, we assume, as in [23], that the propagation constant is the same for the incident and reflected beams.

We define the integration point such that the ray at $x = 0$ reflects off the m th plane at $z = z_p$, i.e. $z_p = m\Delta z$. We can then re-label the remaining planes as $m + n$. We can then use the identities $(z - z_p) = n\Delta z$ and $x = n\Delta x$ where Δx is defined in Figure 3.1(a). Referring to Figure 3.1(b) we find that $\Delta x = \Delta z \sin(2\theta)$ thus we can make the substitution $x \rightarrow (z - z_p) \sin(2\theta)$ in Equation (3.5).

On Figure 3.1(b) we can also find that the path length is equal to $\mathcal{D} = m\Delta z + n\Delta z \cos(2\theta) + n\Delta z = z_p + (z - z_p)(1 + \cos(2\theta))$. Bringing all of this together we find

that the sum over all individual reflections is given by:

$$\begin{aligned}
 E_r(z_p) = -E_1(z_p) \frac{1}{2 \cos^2 \theta} \kappa_0 \frac{\pi}{\Lambda_g} \sum_n \exp \left[-\frac{(z - z_p)^2 \sin^2(2\theta)}{w_1^2} \right] \\
 \cdot \left(\exp \left[2\pi i \frac{(m+n)\Delta z}{\Lambda_g} \right] + \exp \left[-2\pi i \frac{(m+n)\Delta z}{\Lambda_g} \right] \right) \\
 \cdot \exp [-i\beta(z_p + (z - z_p)(1 + \cos(2\theta)))] \Delta z
 \end{aligned} \tag{3.6}$$

As Δz becomes infinitesimally small, the sum becomes an integral:

$$\begin{aligned}
 E_r(z_p) = -E_1(z_p) \frac{1}{2 \cos^2 \theta} \kappa_0 \frac{\pi}{\Lambda_g} \int_{-\infty}^{\infty} \exp \left[-\frac{(z - z_p)^2 \sin^2(2\theta)}{w_1^2} \right] \\
 \cdot \left(\exp \left[i \frac{2\pi}{\Lambda_g} z \right] + \exp \left[-i \frac{2\pi}{\Lambda_g} z \right] \right) \\
 \cdot \exp [-i\beta(z_p + (z - z_p)[1 + \cos(2\theta)])] dz
 \end{aligned} \tag{3.7}$$

Using Mathematica we find the result of the integral:

$$\begin{aligned}
 E_r(z_p) = -E_1(z_p) \frac{\sqrt{\pi}}{2 \cos^2 \theta} \frac{\pi}{\Lambda_g} \frac{\kappa_0 w_1}{\sin(2\theta)} \exp \left[i \left(\frac{2\pi}{\Lambda_g} - \beta \right) z_p \right] \\
 \cdot \exp \left[-\frac{1}{4} \frac{w_1^2}{\sin^2(2\theta)} \left(\frac{2\pi}{\Lambda_g} - (1 + \cos(2\theta))\beta \right)^2 \right]
 \end{aligned} \tag{3.8}$$

From which we can tell that the total reflected field has a transverse wavevector of $\frac{2\pi}{\Lambda_g} - \beta$ and using the value of the amplitude of the reflected wavevector in the core ($|k_{out}| = k_0 n_{core}$) we reproduce Equation (2.22) for the output angle. This is striking because, although this derivation is based on the limit of a wide grating represented as an array of reflectors, it reproduces a result from the opposite limit, that of pointlike scatterers. We also reproduce Equation (2.19) for the resonance condition. The radiation per unit length can be found using the following equation:

$$R = \frac{|E_r|^2 \sin \alpha}{\int_{-\infty}^{\infty} |E_1(x)|^2 dx} = \frac{r^2}{w_0 \sqrt{\frac{\pi}{2}}} \sin \alpha \tag{3.9}$$

where $r = |E_r|/|E_1|$ and the $\sin \alpha$ term is due to the power flowing at an angle α other than 90° which we assume to be given by Equation (2.22) in Section 2.1.2.2 in the background, which we restate here:

$$\alpha = \cos^{-1} \left(\frac{\lambda_0}{\Lambda_g n_{clad}} - \frac{n_{eff}}{n_{clad}} \right) \tag{3.10}$$

This yields the following equation:

$$R = \frac{1}{\cos^4 \theta} \frac{\pi^2 \sqrt{2\pi}}{16} \frac{\kappa_0^2 w_1^2}{\Lambda_g^2 w_0} \frac{\sin \alpha}{\sin^2 \theta \cos^2 \theta} \exp \left(-\frac{\pi^2}{2} w_1^2 \frac{1}{\sin^2 \theta \cos^2 \theta} \left[2 \cos^2 \theta \frac{n_{eff}}{\lambda_0} - \frac{1}{\Lambda_g} \right]^2 \right) \quad (3.11)$$

For $\theta = 45^\circ$ and $\alpha = 90^\circ$ this result is the same as that found by N. Podoliak which is given by Equation (2.24) in Section 2.2.1 of the background [24].

In terms of wavevectors, Equation (3.11) can be restated as:

$$R = R_0 \frac{\sin \alpha}{64 \sin^2 \theta \cos^6 \theta} \exp \left[-\frac{1}{2} \frac{w_1^2}{\sin^2(2\theta)} (K_g - (1 + \cos(2\theta))\beta)^2 \right] \quad (3.12)$$

with:

$$R_0 = \sqrt{2\pi} K_g^2 \kappa_0^2 w_1^2 \quad (3.13)$$

The Gaussian shape of the bandwidth in β space is a result of the assumption of a Gaussian input beam and waveguide index profile. However, this spectrum is modulated by a $\sin \alpha$ term and so has the effect of distorting the shape of the response, making it asymmetrical as a function of β . R drops to zero where $\alpha = 0$ as that corresponds to backreflection. When α is undefined (i.e. when $\beta < \frac{1}{2}K_g$), the grating is of a too short period compared to the light wavelength and so the grating is no longer able to longitudinally phase-match the waveguide mode to any of the radiation modes or even the backward propagating mode. The light only sees the average index of the grating which is the waveguide with no modulation. In such cases, we declare that $R = 0$. This shows that the distortion of the line-width is greatest when the angle of the diffracted beam, and therefore θ , is closest to zero. Ignoring the $\sin \alpha$ term and setting $R = R_0 e^{-1}$ shows that the $1/e$ bandwidth of the grating is:

$$\Delta\beta = \frac{2\sqrt{2}}{w_1} \tan \theta \quad (3.14)$$

which shows that the bandwidth increases with θ and decreases with w_1 . This makes sense as, for the grating period that leads to maximum radiation, the angle of radiation is double the tilt angle as given by the law of reflection [22]. This means that a smaller tilt angle will have a smaller radiation angle for maximum radiation. The light perceives the grating modulations that are along the path of the radiated beam which are in greater number when the angle of the radiated beam is smaller. The greater number of index modulations leads to the diffraction being in a more strongly defined direction which leads to a smaller bandwidth. Therefore, the bandwidth quickly decreases as the tilt angle decreases as a function of $\frac{1}{\tan \theta}$. Conversely, a large tilt angle leads to a wider bandwidth. A wider waveguide and/or input mode also increases the number of index modulations along that path and so decreases the bandwidth. Plots of Equation (3.12), where we assume $n_{core} \simeq n_{eff}$, can be seen in Figures 3.2 and 3.3 which confirm the aforementioned behaviour. Figure 3.3 also shows that, below a certain value of θ , the

efficiency of reflection starts to increase. This is due to the $\sin^2(\theta)$ term in Equation (3.12). This, together with the small bandwidth, makes small angle gratings best suited for filtering one particular frequency and radiating it out of the grating.

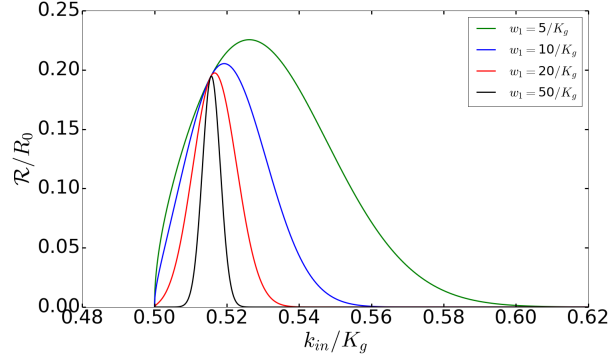


Figure 3.2: Spectral response of the grating ($\theta = 10^\circ$) for different values of $w_1 K_g$. When $w_1 K_g$ is larger, the bandwidth becomes smaller and the response more Gaussian.

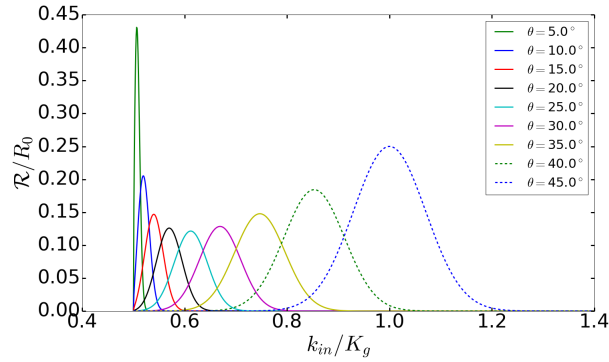


Figure 3.3: These plots show the spectral response of the grating ($w_1 K_g = 10$) for different values of θ . When θ is larger, the bandwidth becomes greater and the response more Gaussian.

3.3 Numerical Model

3.3.1 Finite element simulation

We verify the analytical solution derived in Section 3.2 by studying light scattering in this system numerically using a finite element method in COMSOL. A 2D area is divided into a mesh of very small mostly irregular triangles. The refractive index of the material is varied with position so as to create a waveguide with a tilted grating of finite length starting at a given point along z . It is given by the following equation:

$$n(z, x) = n_{clad} + \left[\delta n + \delta n_g \sin \left(2\pi \frac{z - x \tan \theta}{\Lambda_g} \right) \text{env}(z) \right] g(x) \quad (3.15)$$

where n_{clad} is the cladding refractive index, $\delta n = n_{core} - n_{clad}$ is the difference in refractive index between the centre of the core and the cladding and δn_g is the grating index contrast. The term $\text{env}(z)$ is the apodization profile of the grating. For top-hat apodization, it is given by:

$$\text{env}(z) = u(z) - u(z - L) \quad (3.16)$$

where $u(z)$ is a smoothed out Heaviside function and L is the grating length. Whereas for the super-Gaussian apodization, it is given by:

$$\text{env}(z) = \exp\left(-\frac{(z - z_0)^4}{\varsigma^4}\right) \quad (3.17)$$

where ς is the $1/e$ width of the apodized grating and $z = z_0$ is the point in z at which it is strongest. Graphs of both forms of apodization can be seen in Figure 3.4. We show a 3D schematic of the device in Figure 3.5(a). The area that is simulated is a cross section inside the core layer. Its geometry is shown in Figure 3.5(b).

At the input port on the left, a boundary mode analysis is undertaken to find the input mode(s) (TE) of the waveguide and its effective refractive index. This is done by solving Equation (2.9) in COMSOL as an eigenvalue problem. Using the fundamental mode at the input port, Equation (2.2) is integrated using a finite element method to find the electric field and the Poynting vector everywhere within the geometry of model.

Reflections from the boundary of the model are suppressed through the use of a perfectly matched layer (PML). This is a fictitious material that is anisotropic and uniaxial meaning that it has dielectric and permeability constants in the form of tensors. These tensors are diagonal matrices and have complex elements especially chosen such that the propagation constant of the wave inside the PML has the same real part as the wave incident on it (so that there is no reflection) but also has a non-zero imaginary part. This imaginary part attenuates the wave [109].

However, we are obliged to have a gap at the left end for the input port. This gap must be of minimum size so as to not distort the mode (which leads to divergence from the waveguide and thus inaccurate results). However, for radiation at a small angle, this requires that there is a certain distance between the port and the start of the grating. This is so as to make sure that the radiated light is incident upon the PML and is absorbed by it rather than being incident upon the gap in the PML used for the input port. This would lead to it being reflected by it and remaining in the system leading to inaccurate simulation results.

The mesh has a maximum size of $\frac{\lambda_0}{8n_{clad}}$ for the sides of each triangular element. This was approximately the finest mesh that could be simulated on the office desktop without running into memory limitations. Cross sections in the simulation record the power flow at every point along them. They are placed $1\mu m$ away from the PMLs so as to avoid the

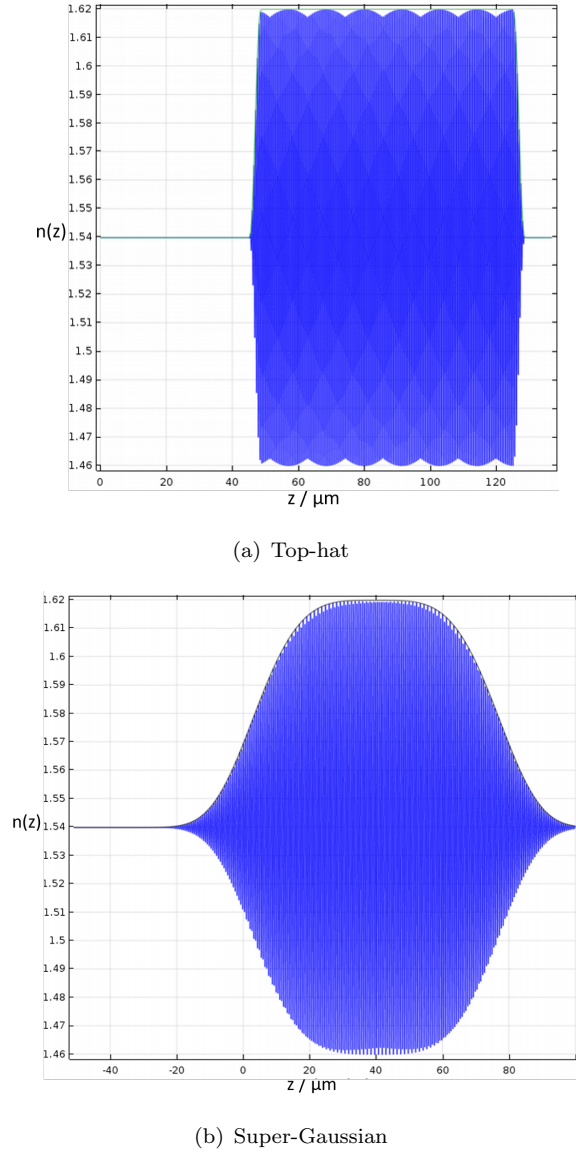
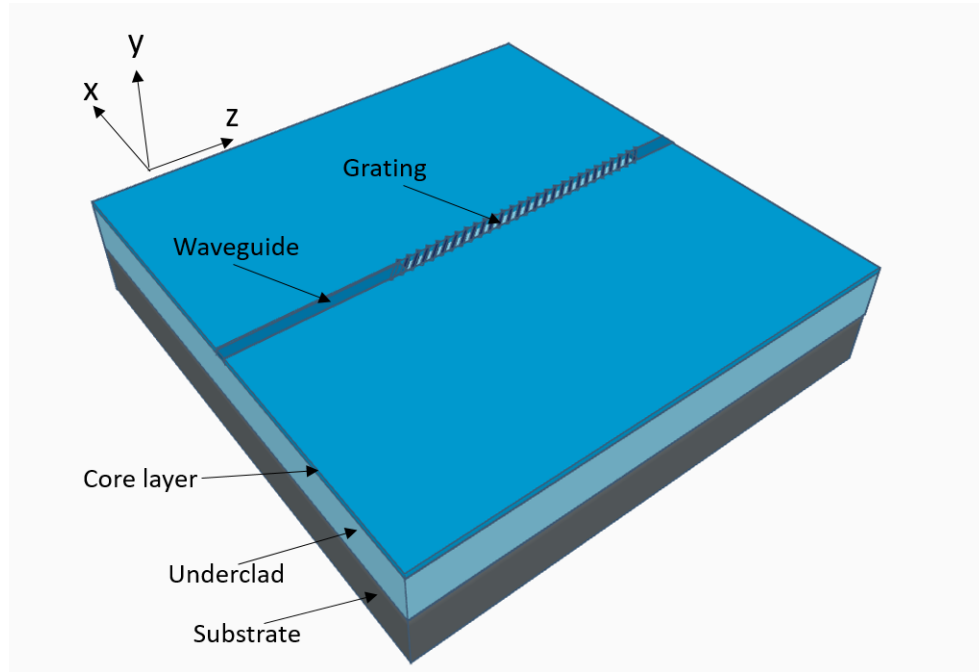


Figure 3.4: Refractive index along centre of simulated waveguide and grating in the z -dimension as shown in Figure 3.5. This is with top-hat (a, $L = 80\mu\text{m}$) and super-Gaussian (b, $\varsigma = 40\mu\text{m}$) apodization. Note, the modulations visible in (a) and to some extent in (b) are the result of undersampling.

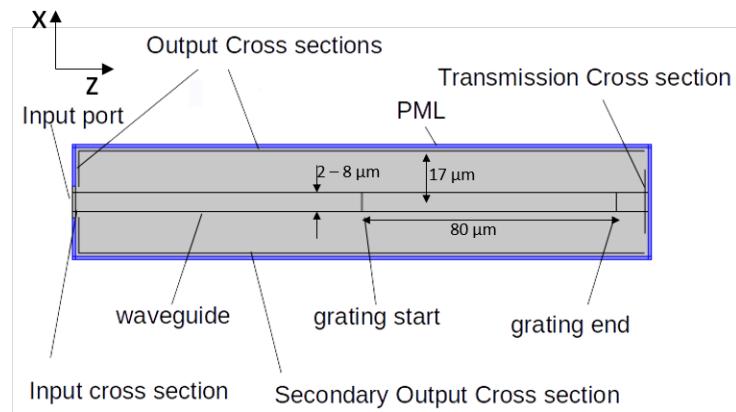
results being affected by them. The following parameters were used in the COMSOL model unless otherwise stated: $\lambda_0 = 1.55\mu\text{m}$, $n_{\text{clad}} = 1.4398$. The refractive index in the core is given by $n_{\text{core}} = n_{\text{clad}} + \delta_n$ where δ_n is the value we quote throughout this chapter.

3.3.2 Postprocessing

In order to find the reflectance out of the grating, backreflectance from the grating and transmittance through the grating, we must find the power flowing through the relevant



(a)



(b)

Figure 3.5: (a) 3D schematic of the device showing the core layer containing the waveguide and grating on top of the underclad and substrate. The overclad is not shown in this picture. (b) Geometry of the simulated model inside of the core layer, showing waveguide, start and end of grating, input port and cross sections for measurement of output power flow. Blue are the perfectly matched layers (PMLs) that act as near perfect absorbers of electromagnetic waves. Note that the waveguide width shown on the graph is 4σ or double the $1/e$ waveguide diameter.

cross sections of the model. This is defined by the Poynting vector:

$$\vec{S} = \vec{E} \times \vec{H} \quad (3.18)$$

In order to find the power P flowing through a cross section l , we must integrate the Poynting vector along it:

$$P = \int_L \vec{S} \cdot \vec{n} \, dl \quad (3.19)$$

where \vec{n} is the unit vector normal to the cross section. The reflected power P_{ref} and the transmitted power P_{trans} are both found directly using that method as well as the power flowing at the front of the waveguide P_{front} before it hits the grating. In order to find the input power, P_{front} is calculated in the absence of a grating and is defined as P_{in} . Any power that is backreflected from the grating will lead to a reduction in P_{front} from P_{in} . Thus we can find the backreflected power using the equation $P_{back} = P_{in} - P_{front}$. The reflectance, transmittance and back reflectance of the grating can thus be found:

$$R = \frac{P_{ref}}{P_{in}} \quad T = \frac{P_{trans}}{P_{in}} \quad R_{back} = \frac{P_{back}}{P_{in}} \quad (3.20)$$

The Poynting vector gives the direction of the power flow. This means that the angle in which the power is propagating at any point (x, y) can be found simply as $\alpha(x, y) = \tan^{-1}(\frac{Sy(x,y)}{Sx(x,y)})$. The angle of the reflected beam in the simulated model is found simply by taking a cross section across it and making a weighted average of the angle at each point along the cross section. The amplitude of the Poynting vector is used as a weight.

3.4 Results and Analysis

3.4.1 Mode Analysis of Gaussian Waveguide

Figure (3.6) shows that the effective refractive indices of the modes increase with the waveguide depth. For higher order modes, the real part is practically constant below the threshold (which corresponds to cladding modes) and increasing above it. The imaginary part is non-zero for cladding modes as they are delimited by the PMLs which absorb the light and make the modes lossy.

Our simulations show that the threshold waveguide depth for the second order mode is decreasing with waveguide width in a manner consistent with Equation (2.10). Defining the V-number as $V = k_0 \sigma \sqrt{n_{core}^2 - n_{clad}^2}$ shows that the threshold is $V = 1.661 \pm 0.005$.

As the fundamental modes of the waveguides are not precisely Gaussian, their width is approximated by only considering where the electric field of the mode is more than half the maximum. The reason for this is that these points are closest to the centre

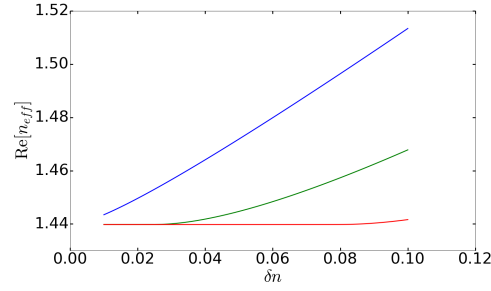


Figure 3.6: Effective refractive indices of fundamental (blue) and first (green) and second (red) higher order modes of a Gaussian waveguide of width $\sigma = 1.5\mu\text{m}$ against grating depth.

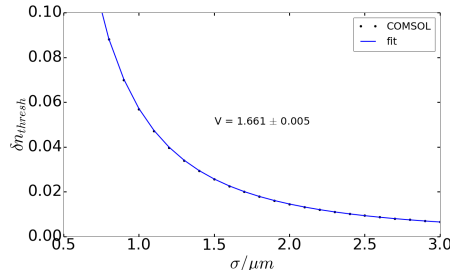


Figure 3.7: Threshold of second-order mode against waveguide width.

of the grating and as $\mathcal{R} \propto \kappa^2$ their contribution dominates the reflection. The points considered are fitted to a Gaussian using a non-linear least squares fit to find the width. Also, near the centre, a Gaussian can be approximated by a parabola; and a parabolic index waveguide is known to have a fundamental mode with a Gaussian transverse profile [3]. For this reason, the shape of the mode is expected to be near-Gaussian in the centre of the waveguide but decaying exponentially on the outside. Figure (3.8) ($\delta n = 0.01$) shows that, as the width of the waveguide is increased, the confinement improves and the shape of the mode becomes more and more similar to a Gaussian. Figures 3.8(a) and 3.8(b) clearly represent the two extremes of behaviour.

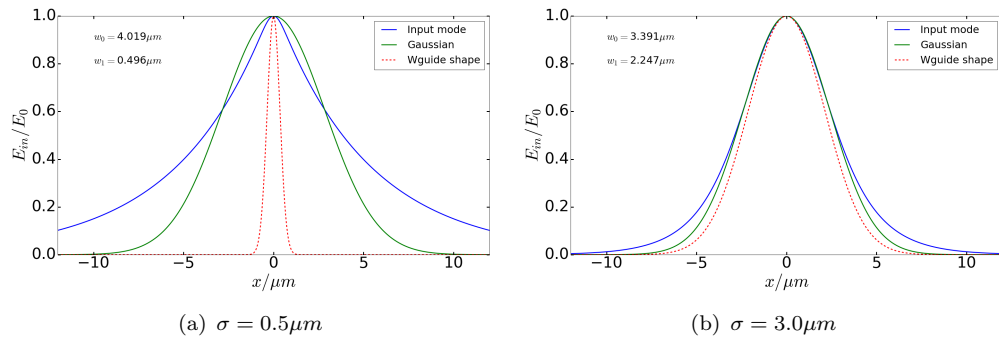


Figure 3.8: Shape of input mode with Gaussian fit and waveguide outline for various values of σ . The width of the mode w_0 and the effective width w_1 are shown on each figure. $\delta n = 0.01$.

For a well confined mode, its width increases with the width of the waveguide, however, as the waveguide width is reduced, there comes a point at which the confinement is no longer good enough and the width of the mode increases dramatically as the width of the waveguide is reduced. This behaviour is already visible in Figure 3.8 but is shown clearly on Figure 3.9(a). However, the effective width of the mode seen by the grating does not show that behaviour (Figure 3.9(b)). The reason why can be understood if we consider the equation for it (restated here as $w_1 = \frac{\sigma w_0}{\sqrt{\sigma^2 + w_0^2}}$). As the confinement becomes increasingly poor and $w_0 \rightarrow \infty$, then $w_1 \rightarrow \sigma$ and so continues to reduce with σ .

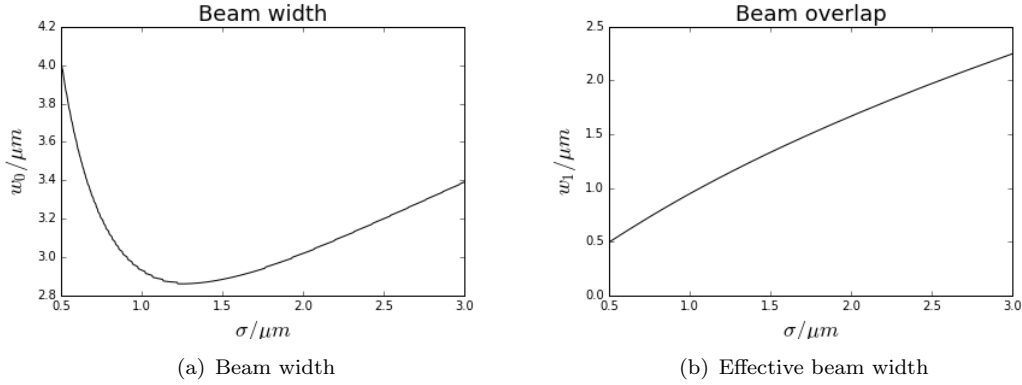


Figure 3.9: Beam width (a) and effective width (b) of mode of waveguide with Gaussian-index profile with $\delta = 0.01$ as the width of the waveguide is increased.

3.4.2 Single-mode - narrow grating

The earliest simulations were made using an index contrast of $\delta n = 0.1$ and a grating of tilt angle $\theta = 10^\circ$, depth $\delta n g = 0.08$, width $\sigma = 0.5\mu\text{m}$ (for single-mode operation), and length $L = 80\mu\text{m}$ ($\varsigma = 40\mu\text{m}$ for super-Gaussian apodization). This is not a realistic example of a grating. However, it allows us to fit a tilted grating, with a considerable amount of scattering from it in a space small enough to be simulated as the finite element method is extremely computationally expensive.

The returned electric fields throughout the entire region can be seen in Figures 3.10 for both top-hat and Super-Gaussian apodization and with a selection of grating periods. They show that the angle of propagation of the scattered light increases with the grating period as expected from Equation (3.10). It can also be seen that the grating continues to scatter a significant amount of light for a wide range of grating periods for the same wavelength which would correspond to a very large bandwidth if the wavelength were varied instead. We see also that there is a weaker secondary field scattered in the downwards direction. The effective refractive index of the waveguide mode is 1.4792.

All these effects can be understood if we consider that we are near the limit of a grating as an array of pointlike scatterers. Because the grating is so narrow, the individual reflections from each plane see a lot of divergence and this greatly enhances the efficiency of coherent scattering at angles away from the resonant $\alpha = 2\theta$. Enough of the light is scattered in the $-x$ direction to add coherently to give a reflection at an angle that is the negative of Equation (3.10).

We can also see (especially at resonance) that the light scattered from a super-Gaussian apodized grating is far more collimated than the light scattered from a top-hat grating. This is because in the latter case the majority of the light is scattered from the nearest part of the grating, and is thus emitted from a much smaller area, so it diverges more. For an apodized grating the light is scattered from a much wider section.

Figures (3.11) are graphs of the efficiency of scattering out of the grating (in both directions), back-scattering (i.e. Bragg), and transmission through the grating. They show that the response curves of the grating are highly asymmetrical. This is to be expected because of the small tilt angle which causes the resonant grating periods for outwards reflection and backreflection to be close together. As the grating period is reduced from $\Lambda_g = 540nm$ to $\Lambda_g = 530nm$ there is a sudden decrease in the outwards scattering efficiency and a corresponding increase in the efficiency for backscattering. This is because the angle of the light scattered out by the grating is no longer great enough to escape the waveguide and is instead totally internally reflected and becomes part of the backscattered light.

Super-Gaussian apodized gratings have a much sharper peak for coupling to radiation modes compared to the much more rounded peak for top-hat gratings (see Figure 3.11(a)). This is because they have a much smoother apodization function which means that the spatial Fourier components of the grating index distribution away from the grating period are suppressed. The bandwidth for back-reflection is also considerably smaller (see Figure 3.11(c)) to the point that, at resonance for reflection out of the grating, backreflection is virtually removed.

Figure 3.12 shows that the output angle given by COMSOL has very good agreement with Equation (3.10). The error bars show that, for top-hat apodization, there is a large amount of divergence in the propagation of the reflected beam which implies that it is poorly collimated. This is greatly improved with super-Gaussian apodization.

All these properties make super-Gaussian apodization far superior to top-hat apodization for any application of tilted gratings in which the efficient production of beams with a precisely defined direction and a sharp bandwidth is paramount.

Since $n_{clad} = 1.4398$ and $n_{core} = n_{clad} + \delta n = 1.5398$ we can calculate, using the equation $n_{core} \sin \theta_c = n_{clad}$ for the critical angle, that the minimum scattering angle for light scattered from the core to escape is $\alpha_{min} = 90^\circ - \theta_c = 20.8^\circ$ which considering

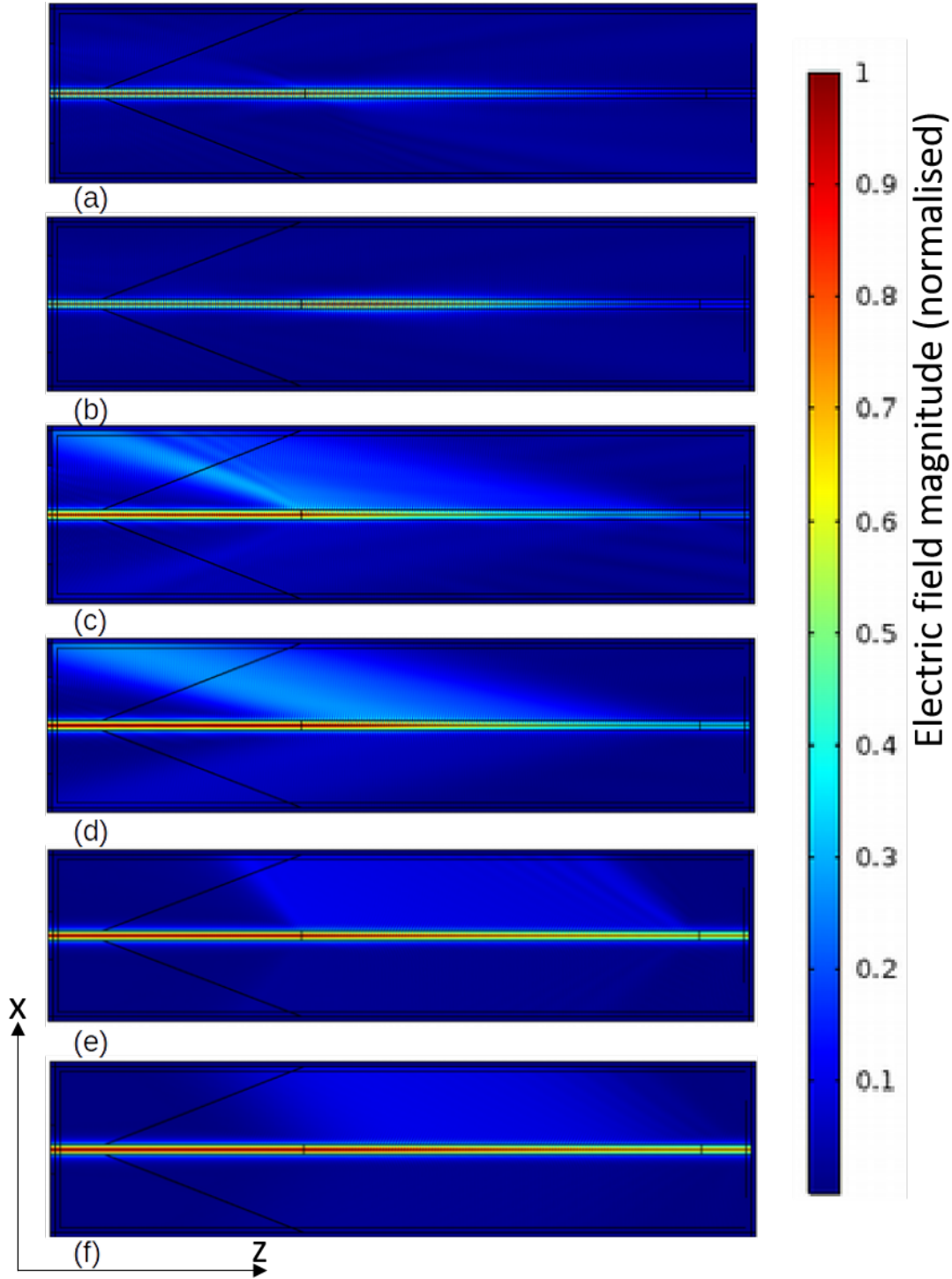


Figure 3.10: Electric field (z -component) inside the simulate area of the core layer, defined in Figures 3.5(a) and 3.5(b), of light scattered by a gratings with a selection of grating periods and apodization profiles. Here (a, b) show back-reflection into the counter-propagating waveguide mode with $\Lambda_g = 530\text{nm}$, (c, d) show scattering out of the waveguide at resonance with $\Lambda_g = 540\text{nm}$ and (e, f) show scattering off-resonance at a higher angle and with lower scattering efficiency with $\Lambda_g = 620\text{nm}$. Results using both Top-hat (a, c, e) and super-Gaussian apodization (b, d, f) are shown for comparison with better beam collimation in the latter case. The diagonal black lines are the lines along which the Poynting vector is integrated to calculate the power flowing through them. On the right shows the colour scale for the electric field strength (normalised) that applies to all figures.

Equation (3.10) will correspond to a grating period of $\Lambda_g = 531nm$ which is close to the cut-off for reflectance in Figure 3.11(a).

Equation (2.19) predicts a resonant grating period of $540nm$ which is the maximum found for Super-Gaussian apodization.

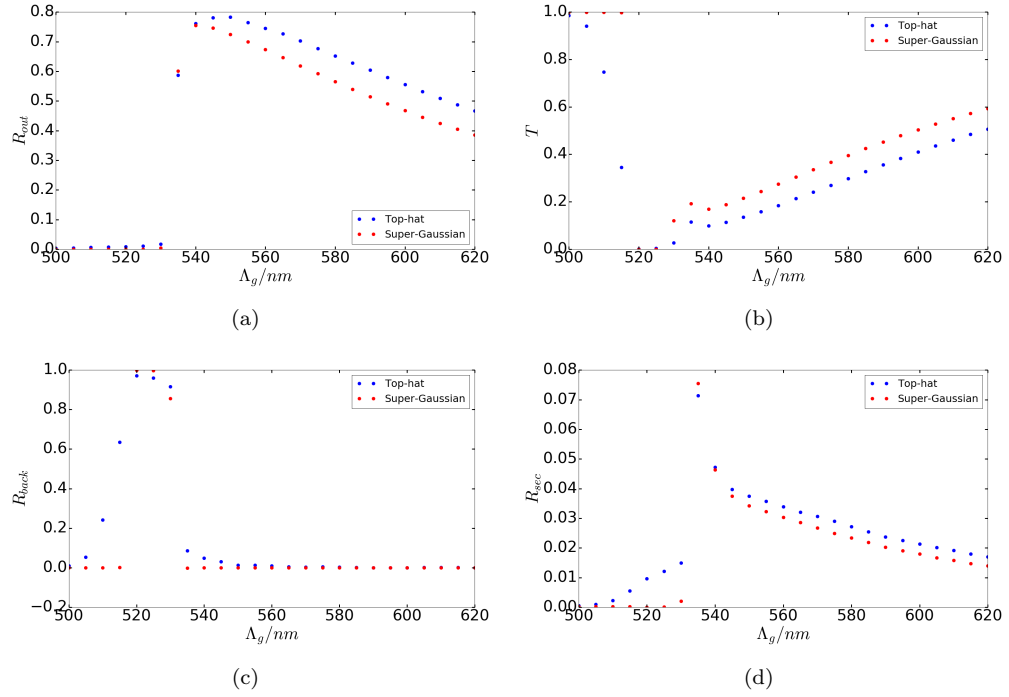


Figure 3.11: Graphs of reflectance (a), transmittance (b), back-reflectance (c) and secondary (downwards) reflectance (d) against grating period for both top-hat and Super-Gaussian apodization.

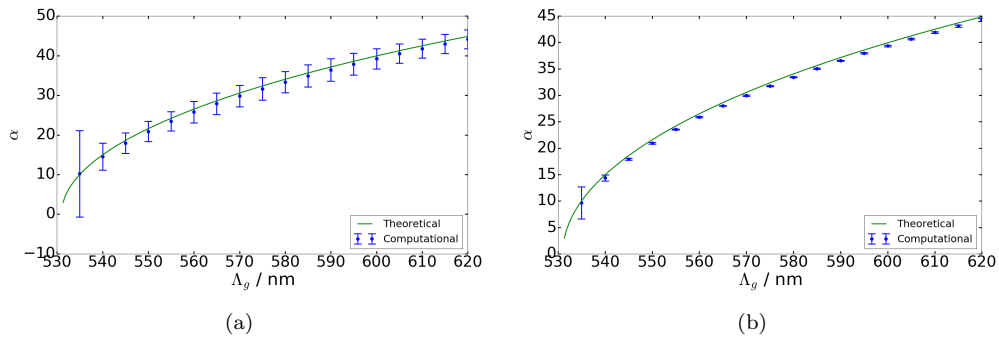


Figure 3.12: Graph of angle of scattered radiation against grating period for a top-hat (a) and super-Gaussian apodized (b) grating.

3.4.3 Parameter scans of simulations, comparison with analytical equation

Parameter scans of simulations have been made by sweeping the wavelength of the mode and one other parameter, either the grating/waveguide width or the tilt angle in order to see how well the theoretical predictions match the results of the simulations. In order to keep the parameters in the region that is comparable to waveguide gratings written in a real laboratory setting, simulations are run with a waveguide of index contrast $\delta n = 0.015$ and a grating of depth $\delta n_g = 0.012$ and period $\Lambda_g = 700\text{nm}$. We choose a grating length of $80\mu\text{m}$. These parameters also keep the simulations in the regime in which the equations derived in Section 3.2 are valid by keeping the grating depth and index contrast small and the grating wide. In these simulations, the wavelength of the input mode is varied from $\lambda_0 = 1.5\mu\text{m}$ to $\lambda_0 = 2.1\mu\text{m}$.

Simulations with a tilt angle of 20° and several different values of the width can be seen in Figure 3.13(a). They show that the equation derived, Equation (3.11), predicts the simulated behaviour of the grating reasonably well, even though the efficiency of the grating is overestimated. Figure 3.13(b) shows that the backreflectance is reduced with large grating and waveguide width. This could be because increasing the grating width leads to the grating becoming more mirror-like and thus reflecting in a more well defined direction given by $\alpha = 2\theta$. Negative backreflectances are unphysical and are due to modelling errors.

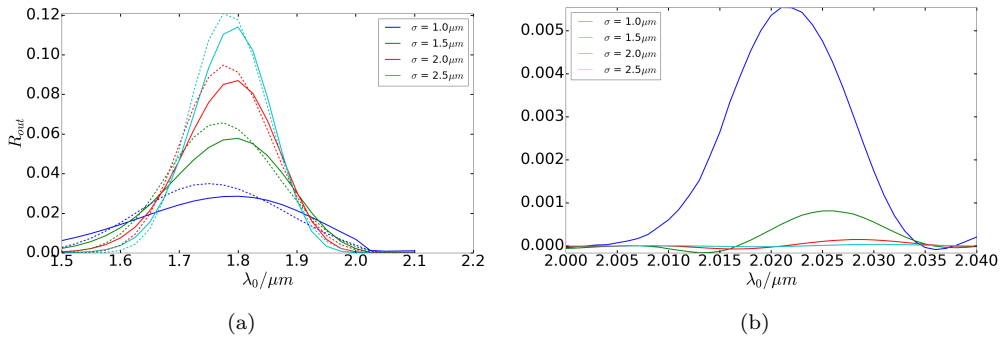


Figure 3.13: Graphs of reflectance (a) and back-reflectance (b) against input wavelength for different grating widths and constant tilt angle (20°). Solid are the computational results and dotted are the results from Equation (3.11).

More simulations were made with, this time, the width kept constant at $\sigma = 1.5\mu\text{m}$ and the tilt angle varied (Figure 3.14). They show that in the region of $\theta = 20^\circ$ the equation predicts the simulations reasonably well but as θ is reduced to 10° the theoretical and computational behaviour begin to diverge. The computational results do show a reduction in bandwidth and an increasingly asymmetrical result as expected but the location of the peak and the shape of the curve become very different from that predicted by Equation (3.11) with a larger resonance wavelength and a drop in reflectance similar to

that in Figure 3.11(a). This suggests that there are phenomena that we have not considered in our analytical derivation that become important for small angle gratings. For example, we have not considered the effect of the waveguide on light diffracted at small output angles. That light would refract more than light diffracted at higher angles and, as a result, would have a reduction in the output angle with angles small enough leading to total internal reflection and the light being backreflected. This also has the effect of decreasing the beam collimation as shown in Figure 3.12 as the refraction is highly dependent upon the angle. This in turn increases the device bandwidth and shifts the peak in radiation towards higher wavelengths where the diffracted angle is smaller. This phenomenon could explain the difference between the numerical and analytical solution for the light radiation from the grating for smaller angles shown in Figure 3.14.

Figure 3.14(b) shows that the backreflectance is reduced for greater angles. This is in part a result described in [8] where it is explained by a reduction in the "fringe visibility", i.e. the effective refractive index modulation perceived in the z direction. Another cause could be because, as the tilt angle is reduced, the angle of scattering at resonance is reduced and so a greater proportion of the scattered light will be internally reflected thus contributing to back-reflection.

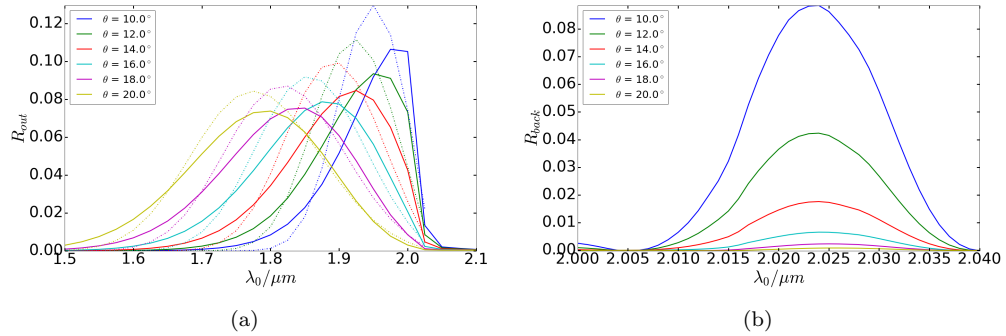


Figure 3.14: Graphs of reflectance (a) and back-reflectance (b) against input wavelength for different tilt angles and constant grating width ($\sigma = 1.5\mu m$). Solid are the computational results and dotted are the results from Equation (3.11).

3.5 Conclusion

In this chapter, we have investigated the use of tilted Bragg gratings to couple to in-chip radiation modes for small tilt angles. We have derived an equation for the light radiated by tilted Bragg gratings using an analytical beam tracing method based on that in [23] but generalised for arbitrary tilt angles. We have modelled small-angled tilted Bragg gratings using a finite element simulation in COMSOL and have reproduced the general qualitative behaviour expected by the analytical solution. Good agreement was

found between the numerical and analytical result except for small-angle tilted gratings which is most likely the result of refraction by the waveguide/cladding interface for small diffraction angles.

This work has since been expanded by Mr Dominic Ko for gratings of variable grating period and tilt angle used for focussing beams outside of the chip. He has used this analytical derivation to find an expression for the refractive index distribution needed to couple light from the waveguide to a Gaussian mode and plans to further expand that work to three dimensions.

Chapter 4

Cladding mode-based waveguide coupler

4.1 Introduction

The second sub-project investigates a grating-based waveguide coupler which is expected to be more efficient than previously developed in the OEQP group [24]. This device is designed with the fabrication method outlined in Section 2.4 in mind. It consists of a single ridge structure, fabricated by micromachining two parallel trenches, with a raised index photosensitive core layer. The ridge structure is made narrow enough such that the planar core layer supports only a limited number of modes that are well separated in terms of effective index. Using UV-writing, two identical single-mode channel waveguides are written in parallel inside the core layer simultaneously with tilted Bragg gratings. This allows light to be transferred between the two waveguides by coupling them via the modes of the core layer (see Figure 4.1). The material defined by the ridge structure, including in the core layer, acts as the cladding to the channel waveguides. Therefore, the modes of the core layer that are confined by the ridge structure are henceforth referred to as cladding modes. The modes of the channel waveguides are referred to as core modes. We show a schematic of this system in Figure 4.1 including a cross section of the device in (a) and a schematic of the waveguides, gratings and ridge structure in (b). Figure 4.1(b) also shows an overlaid ray diagram showing the two waveguide modes coupled by a cladding mode. This device is different from the long-period waveguide grating coupler presented in [37, 38] and introduced in this thesis in Section 2.3.1.3 as the device here couples using backward propagating modes using a far shorter grating period and introduces a tilt angle.

The light not transferred to the output waveguide mode by its grating will remain in the cladding modes and thus will not be lost by the system. As such, losses incurred in the system result from leakage via the end facets of the ridge structure, from absorption by

the material, or rough surfaces at the material/air interface. We show in this chapter that device parameters can be chosen such that losses from the end facets can be eliminated. The latter two sources of loss are small enough to be neglected (see [110] and [105] respectively).

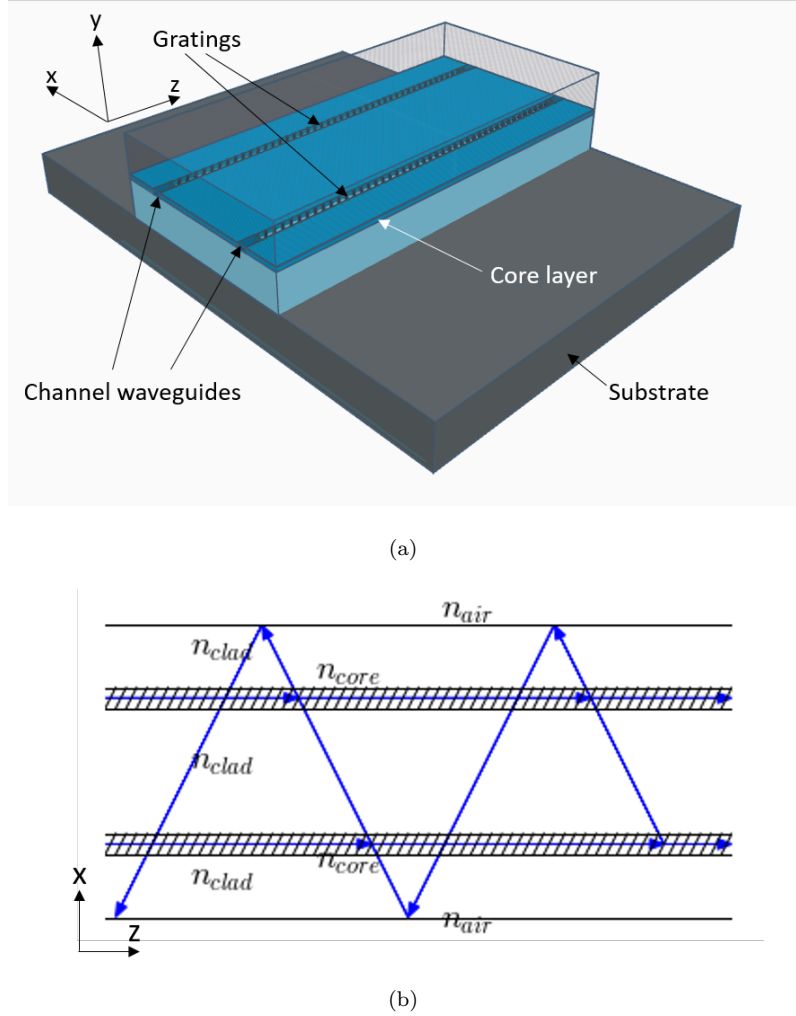


Figure 4.1: Schematics of the cladding mode-based waveguide coupler showing (a) a 3D model of the device showing the ridge structure, the photosensitive core layer and the two single-mode waveguides and gratings and (b) a cross section inside the core layer superimposed with a ray diagram of the two waveguides and gratings coupled together by a cladding mode.

At the beginning of the investigation, we thought that using backward propagating modes should greatly increase the coupling efficiency, and thus decrease device length compared to the long-period grating coupler, as a result of using gratings of shorter period to couple via backward propagating modes. However, this turned out not to be the case as our own implementation of long-period waveguide couplers in Section 6.4.3 of Chapter 6 is not longer than our implementation using short-period gratings in this chapter. As explained in Section 2.2.2, this is because the coupling coefficient between two modes co-propagating and two modes counter-propagating is the same for the same

value of the transverse grating wavevector K_t , and that the value of K_t for phase-matching is the same regardless of whether one couples to the forward or backwards propagating version of a mode. However, we have found that this device has a very narrow transmission bandwidth, that is much narrower than the long-period version, which could allow it to be used as a narrow-band frequency filter with applications such as separating the signal and the pump from a Raman amplifier or a parametric amplifier.

In this project, I used numerical methods for calculating the modes and for simulating the light propagation. First, I used inbuilt tools in COMSOL (for mode calculations) and Python. Later on, I used code that I have written myself that is considerably faster at solving the type of problem that I study in this and the following chapters. As I had already done some work using the inbuilt methods before developing the faster methods and I use different parameters for each I will discuss the results from both methods in different sections.

Throughout this thesis, in this and the following chapters, I will refer to the two waveguides as waveguides 0 and 1 where, unless stated otherwise, waveguide 0 is the one being pumped.

In Section 4.2, I introduce the analytical solution of the coupled-mode equations for the light propagation in the device using the approximation that the light is coupled entirely via a single cladding mode. In Section 4.3, I introduce the numerical models used to calculate the modes and numerically simulate the light propagation. In Section 4.4, I present the results of the simulations with the inbuilt solvers that I did in order to find parameters that coupled entirely via a single cladding mode. In Section 4.5, I present the results of the simulations made after developing my own numerical methods for simulating the device. This includes simulations showing the effect of device parameters on the device bandwidth, tolerance to fabrication parameters and temperature etc. in addition to the effect of grating apodization and grating "noise" that comes from phase error, which results from the UV-writing system as explained in Section 2.4.3. In Section 4.6, I present the simulations using parameters that members of the Optical Engineering and Quantum Photonics Group intend to use to fabricate the device including the results of simulations that would help them build it. For completeness, I also model the group delay properties of the device.

4.2 Analytical solution to the three mode problem

The aim of this section is to find an analytical solution which can then be used to greatly help the design of cladding mode-based waveguide couplers for real life applications, for example, by finding its coupling length, estimating its bandwidth or by finding parameters that achieve 100% coupling, or any other desired coupling ratio. We also derive the transfer matrices, as defined in Section 2.2.3, relating the device outputs to the inputs.

We also use this analytical solution to show how we can achieve grating induced transparency, by which light in a particular superposition of modes is transmitted through the grating structure as if it were transparent.

4.2.1 General analytical solution to the three mode problem

An analytical solution for the cladding mode-based waveguide coupler is found very similarly to that for two mode coupling in Section 2.2.2.1. Equation (2.40) is used as a starting point. The system has two forward propagating core modes of the same propagation constant $\beta_0 = \beta_1 > 0$ and one backward propagating cladding mode $\beta_2 < 0$ which means that all the cladding modes other than the one we seek to couple to are neglected. We assume that there is no evanescent coupling and so the core modes are only coupled to the cladding mode and not to each other. We also assume that the two core modes have the same coupling coefficient with the cladding mode. These are all assumptions that we justify in the later Section 4.4 where we show a set of parameters in which evanescent coupling between the waveguides and coupling to cladding modes, other than the ones we seek to couple to, are negligible and also show that the amplitude of the coupling coefficients are equal for both gratings. Defining $\Delta K = -\beta_0 + \beta_2 + K_g$ and using these approximations, Equation (2.40) can be simplified to:

$$\begin{aligned}\frac{dA_0(z)}{dz} &= -\frac{c}{2}e^{-i(\Delta K z + \phi_0)}A_2(z) \\ \frac{dA_1(z)}{dz} &= -\frac{c}{2}e^{-i(\Delta K z + \phi_1)}A_2(z) \\ \frac{dA_2(z)}{dz} &= -\frac{1}{2}\left[e^{i(\Delta K z + \phi_0)}cA_0(z) + e^{i(\Delta K z + \phi_1)}cA_1(z)\right]\end{aligned}\tag{4.1}$$

where $A_0(z)$ and $A_1(z)$ are the mode amplitudes of the core modes of waveguides 0 and 1 and $A_2(z)$ is the amplitude of the cladding mode. The variable c is the absolute value of the coupling coefficients between the core modes and the cladding mode and ϕ_0 and ϕ_1 are the coupling coefficient phases of the gratings in the respective waveguides. By substituting $\mathcal{A}_{0,1} = A_{0,1}e^{i\phi_{0,1}}$ the equations become:

$$\begin{aligned}\frac{d\mathcal{A}_0(z)}{dz} &= -\frac{1}{2}ce^{-i\Delta K z}\mathcal{A}_2(z) \\ \frac{d\mathcal{A}_1(z)}{dz} &= -\frac{1}{2}ce^{-i\Delta K z}\mathcal{A}_2(z) \\ \frac{d\mathcal{A}_2(z)}{dz} &= -\frac{1}{2}(c\mathcal{A}_0(z) + c\mathcal{A}_1(z))e^{i\Delta K z}\end{aligned}\tag{4.2}$$

for counter-propagating modes. Applying the transformations:

$$\begin{aligned}R_0(z) &= \mathcal{A}_0(z)e^{-\frac{i}{2}\Delta K z} \\ R_1(z) &= \mathcal{A}_1(z)e^{-\frac{i}{2}\Delta K z} \\ R_2(z) &= \mathcal{A}_2(z)e^{+\frac{i}{2}\Delta K z}\end{aligned}\tag{4.3}$$

allows one to derive the following equation in matrix form:

$$\frac{d}{dz} \begin{bmatrix} R_0(z) \\ R_1(z) \\ R_2(z) \end{bmatrix} = M \begin{bmatrix} R_0(z) \\ R_1(z) \\ R_2(z) \end{bmatrix} \quad (4.4)$$

where M is given by the following:

$$M = \begin{bmatrix} \frac{i}{2}\Delta K & 0 & \frac{-c}{2} \\ 0 & \frac{i}{2}\Delta K & \frac{-c}{2} \\ \frac{-c}{2} & \frac{-c}{2} & -\frac{i}{2}\Delta K \end{bmatrix} \quad (4.5)$$

Note that, unlike in other chapters, we use real and not complex values of c . The eigenvalues of the matrix are found using Mathematica to be:

$$\gamma_0 = \frac{i}{2}\Delta K \quad (4.6)$$

$$\gamma_{\pm} = \pm \frac{1}{2}\sqrt{2c^2 - \Delta K^2} \quad (4.7)$$

with the corresponding eigenvectors:

$$\eta_0 = \begin{bmatrix} -c \\ c \\ 0 \end{bmatrix} \quad \eta_{\pm} = \begin{bmatrix} c \\ c \\ i\Delta K \mp 2\gamma \end{bmatrix} \quad (4.8)$$

For a phase matched system $\Delta K = 0$, this yields the general solution of ($\gamma = \gamma_+$):

$$\begin{bmatrix} R_0(z) \\ R_1(z) \\ R_2(z) \end{bmatrix} = p_0 \begin{bmatrix} -c \\ c \\ 0 \end{bmatrix} + q_- e^{-\gamma z} \begin{bmatrix} c \\ c \\ 2\gamma \end{bmatrix} + q_+ e^{\gamma z} \begin{bmatrix} c \\ c \\ -2\gamma \end{bmatrix} \quad (4.9)$$

where p_0 , q_- and q_+ are arbitrary constants. Imposing the boundary conditions that $R_0(z=0) = 1$ and $R_1(z=0) = 0$ yields the following equations for the coefficients:

$$\begin{aligned} p_0 &= \frac{-1}{2c} \\ (q_+ + q_-) &= \frac{1}{2c} \\ (q_+ - q_-) &= 2q_+ - \frac{1}{2c} \end{aligned} \quad (4.10)$$

If we consider an infinitely long grating ($L \rightarrow \infty$) and apply the boundary condition that $R_2(z = L) = 0$ then $q_+ = 0$ and the general solution becomes very simple:

$$\begin{aligned} R_0(z) &= \frac{1}{2}(1 + e^{-\gamma z}) \\ R_1(z) &= \frac{1}{2}(-1 + e^{-\gamma z}) \\ R_2(z) &= \frac{1}{\sqrt{2}}e^{-\gamma z} \end{aligned} \quad (4.11)$$

which for $z \rightarrow \infty$ has the simple solutions for the power that $|R_1(z)|^2 = |R_0(z)|^2 = \frac{1}{4}$ whereas $|R_2(z)|^2 = \frac{1}{2}$ so it carries the remaining half of the power backwards.

Oscillations are found in the region where $\Delta K^2 > 2c^2$. By defining the oscillation frequency Ω using $\gamma = i\Omega$ the general solution can be stated as:

$$\begin{bmatrix} R_0(z) \\ R_1(z) \\ R_2(z) \end{bmatrix} = p_0 e^{\frac{i}{2}\Delta K z} \begin{bmatrix} -c \\ c \\ 0 \end{bmatrix} + q_- e^{-i\Omega z} \begin{bmatrix} c \\ c \\ i(\Delta K + 2\Omega) \end{bmatrix} + q_+ e^{i\Omega z} \begin{bmatrix} c \\ c \\ i(\Delta K - 2\Omega) \end{bmatrix} \quad (4.12)$$

and applying $R_2(z = L) = 0$ yields the following equation for q_+ :

$$q_+ = \frac{[U + iV]}{2c} \quad (4.13)$$

where U and V are decompositions of q_+ and restated from Section 2.2.2.1 as:

$$\begin{aligned} U &= \frac{\sin(\Omega L)^2 \Delta K^2 + 2\Delta K \Omega + 4 \cos(\Omega L)^2 \Omega^2}{D} \\ V &= \frac{\cos(\Omega L) \sin(\Omega L) [\Delta K^2 - 4\Omega^2]}{D} \\ D &= 2(\sin(\Omega L)^2 \Delta K^2 + 4 \cos(\Omega L)^2 \Omega^2) \end{aligned} \quad (4.14)$$

By taking the absolute value square, we find the following expressions for the power inside each mode:

$$\begin{aligned} |R_0(z)|^2 &= \frac{1}{4}(1 + B(z) + C(z)) \\ |R_1(z)|^2 &= \frac{1}{4}(1 - B(z) + C(z)) \\ |R_2(z)|^2 &= S_3 + \frac{1}{2}(C(z) - 1) \end{aligned} \quad (4.15)$$

where $B(z)$ and $C(z)$ are defined as:

$$\begin{aligned}
 B(z) &= 2 \left((1-U) \cos \left[\left(\frac{\Delta K}{2} + \Omega \right) z \right] + U \cos \left[\left(\frac{\Delta K}{2} - \Omega \right) z \right] \right. \\
 &\quad \left. - V \sin \left[\left(\frac{\Delta K}{2} + \Omega \right) z \right] + V \sin \left[\left(\frac{\Delta K}{2} - \Omega \right) z \right] \right) \\
 C(z) &= 1 + 2(U^2 + V^2 - U)(1 - \cos(2\Omega z)) - 2V \sin(2\Omega z)
 \end{aligned} \tag{4.16}$$

and $S_3 = \frac{1}{2c^2} [(\Delta K + 2\Omega)^2 - 8\Omega U(\Delta K + 2\Omega) + 16\Omega^2(U^2 + V^2)]$. $C(z)$ describes the oscillations with wavenumber 2Ω that are due to the direct coupling between the core and cladding modes that are also observed in the two mode problem. $B(z)$ describes the oscillations of power between the top and bottom waveguide modes. It contains the terms with wavenumber $\frac{\Delta K}{2} + \Omega$ and $\frac{\Delta K}{2} - \Omega$ that are due to multiplying the eigenvalue oscillation terms $e^{\pm i\Omega}$ and $e^{i\frac{\Delta K}{2}}$. It is the term $\frac{\Delta K}{2} - \Omega$ that governs the period of oscillation between the top and bottom waveguides and thus the coupling length of $L_C = \frac{\pi}{\Delta K/2 - \Omega} = \frac{2\pi}{\Delta K - \sqrt{\Delta K^2 - c_0^2 - c_1^2}}$.

From Equation (4.12), it can be derived that, just like for $\Delta K = 0$, if we have $\Delta K \neq 0$ and $\Delta K^2 < 2c^2$, we still have $|R_0(L)|^2 \rightarrow \frac{1}{4}$, $|R_1(L)|^2 \rightarrow \frac{1}{4}$ and $|R_2(0)|^2 \rightarrow \frac{1}{2}$ for $L \rightarrow \infty$.

As $\Delta K \rightarrow \infty$, that is as the phase mismatch becomes increasingly large, then $\Omega \rightarrow \frac{1}{2}\Delta K$ which means that the three oscillation frequencies tend towards: $2\Omega \rightarrow \Delta K$, $\frac{\Delta K}{2} + \Omega \rightarrow \Delta K$ and $\frac{\Delta K}{2} - \Omega \rightarrow 0$. This means that the oscillation frequency of the cladding mode becomes increasingly large as the phase mismatch is increased, whereas the oscillation frequency between the two core modes becomes increasingly small. Our equations also show that the oscillation amplitude becomes increasingly small away from phase-matching and so the amount of light that is coupled to the cladding mode, or transferred to the other waveguide, decreases, which means that an increasing amount is transmitted.

From this we can conclude that the power scattered out of the cladding mode has a nearly flat dependence on the phase-mismatch inside of the bandgap (for large L) and with side lobes of decreasing amplitude and increasing frequency as the phase-mismatch is increased. The power output of the two waveguides is also independent of phase-mismatch inside the bandgap with, on top of the increasingly fast oscillations they have in common with the cladding mode, oscillations between them that decrease in frequency as the phase-mismatch is increased. This behaviour is confirmed numerically in Section 4.5.2.

The cladding mode oscillates with a single frequency 2Ω . This means that if we want no power escaping via the cladding modes such that $R_2(0) = R_2(L) = 0$ then we need to have a device of length:

$$\Omega L = m\pi \tag{4.17}$$

where m is an integer.

This leads us to the following equations for the light amplitudes at the waveguide outputs:

$$\begin{aligned} R_0(L) &= -p_0 e^{\frac{i}{2}\Delta K L} c + (q_- + q_+) (-1)^m c \\ R_1(L) &= p_0 e^{\frac{i}{2}\Delta K L} c + (q_- + q_+) (-1)^m c \end{aligned} \quad (4.18)$$

Recall that the oscillation between the top and bottom waveguides is governed by the slow oscillation term $\frac{\Delta K}{2} - \Omega$. If we want to have complete power transfer between the two waveguides, we need to have a half oscillation between the two waveguides. That is, we need to have:

$$\left(\frac{\Delta K}{2} - \Omega \right) L = \pi \quad (4.19)$$

Rearranging for $\frac{\Delta K L}{2}$ and inserting into Equation (4.18) gets us the following outputs:

$$\begin{aligned} R_0(L) &= 0 \\ R_1(L) &= (-1)^m \end{aligned} \quad (4.20)$$

which means that all of the light is transferred from one waveguide to the other.

In general, we can achieve any rotation angle α between the two waveguides, where here "rotation" refers to a transformation between the two modes of the waveguides. For example, a rotation angle of $\alpha = \frac{\pi}{2}$ transfers all light from one waveguide to another, $\alpha = \frac{\pi}{4}$ would put light one in waveguide into an equal superposition of both waveguides, $\alpha = \pi$ would leave it into a negative of its original state and $\alpha = 2\pi$ would leave it in its original state. To achieve this we use the generalised form of Equation (4.19) which is:

$$\left(\frac{\Delta K}{2} - \Omega \right) L = 2\alpha \quad (4.21)$$

which gets us (for $\phi_0 = 0$):

$$\begin{aligned} R_0(L) &= (-1)^m e^{i\alpha} \cos(\alpha) \\ R_1(L) &= -i(-1)^m e^{i\alpha} \sin(\alpha) \end{aligned} \quad (4.22)$$

Similarly to the cases shown in Section 2.2.3, the relations between the inputs and outputs of this device with the length chosen so as to prevent light escaping via the cladding mode can be expressed in terms of a transfer matrix. We find it analytically to be given by:

$$M = (-1)^m e^{i\alpha} \begin{bmatrix} \cos(\alpha) & -i \sin(\alpha) \\ -i \sin(\alpha) & \cos(\alpha) \end{bmatrix} \quad (4.23)$$

With multiplication by a phase-shift in one of the waveguides, we are able to implement any unitary 2×2 matrix. We can also achieve this by providing a phase-difference between the coupling coefficients of the two gratings.

4.2.2 Phase-selective grating induced transparency

From the general solution (Equation 4.12) we can see that with the gratings precisely at resonance (i.e. $\Delta K = 0$), we have the first of these eigenvalues equal to 0. This implies that the device exhibits grating induced transparency [111] if it is excited by the superposition of modes given by

$$\frac{1}{\sqrt{2}} \begin{bmatrix} -1 \\ 1 \\ 0 \end{bmatrix}$$

This means that if you were to launch light in an *antisymmetric* superposition of the two waveguide modes, it would propagate through the device without any exchange of light between the modes, provided that the cladding mode is itself symmetric. For an antisymmetric cladding mode, the coupling coefficients of the two gratings are the negative of each other already which means that a *symmetric* superposition of the two waveguide modes would be transparent. Whichever mode superposition is transparent, the core mode that is perpendicular to it in vector space is completely backreflected into the cladding mode in the same way that light is backreflected from a standard Bragg grating (see Section 2.1.2). This means that the grating induced transparency is selective to the phase difference between the light in the two core modes. Light pumped into one of the waveguides is in an equal superposition of the *symmetric* and *antisymmetric* core modes. This means that half-of it is backreflected into the cladding mode whereas the other half is in an equal superposition of the two waveguide modes. This behaviour explains why we have the result in Equation (4.11).

4.3 Numerical model and methods

Our numerical model consists of three parts. First we calculate the modes of the transverse structure of the device in order to find both their effective indices and their transverse amplitude profile. Then, we calculate the coupling coefficient between each mode and every other mode as mediated by perturbative Bragg gratings. Finally, we use a coupled mode model to calculate the light propagation through our device. For both the first and last part, we have two different numerical methods that we use to implement the model.

The transverse index structure of the complete (dual core + cladding) system inside the photosensitive core layer consist of a cladding of width W and refractive index n_{clad} in

which two waveguides of Gaussian refractive index profile are written at a distance x_0 from the centre. They have a depth (index difference between centre and cladding) of δn and a $1/e$ width of σ . A grating is written in one or both of the waveguides and have identical profiles and grating depth (amplitude) of δn_g . As such, it is defined using the following equation:

$$n(x) = n_{clad} + \delta n \left[\exp \left(\frac{-(x - x_0)^2}{\sigma^2} \right) + \exp \left(\frac{-(x + x_0)^2}{\sigma^2} \right) \right] \quad (4.24)$$

inside the cladding region defined by $-\frac{W}{2} \leq x \leq \frac{W}{2}$ and $n(x) = 1$ outside of it. The envelope of the grating is defined similarly in Python as:

$$\Delta n(x) = \delta n_g \left[\exp \left(\frac{-(x - x_0)^2}{\sigma^2} \right) + \exp \left(\frac{-(x + x_0)^2}{\sigma^2} \right) \right] \quad (4.25)$$

for a grating in each waveguide and:

$$\Delta n(x) = \delta n_g \exp \left(\frac{-(x - x_0)^2}{\sigma^2} \right) \quad (4.26)$$

for a grating in only one waveguide.

We show in Figure 4.2 a plot of the transverse refractive index profile of the device in the core layer defined by Equation (4.24) showing the two waveguides inside the ridge structure.

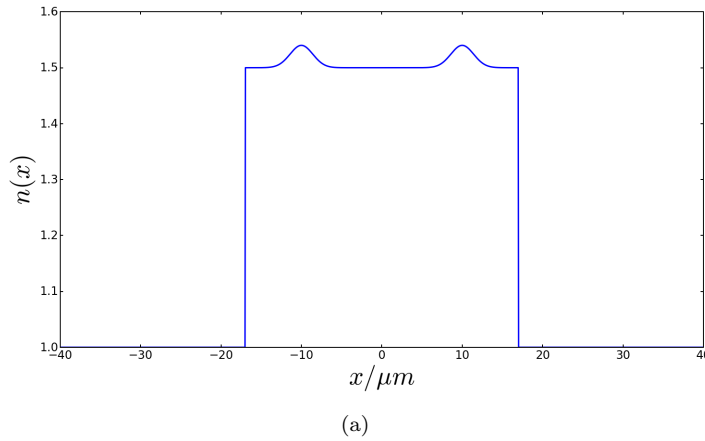


Figure 4.2: Transverse index profile inside the photosensitive core layer with two channel waveguides (waveguide depth exaggerated to make them easier to see).

In the numerical model the modes of the system are first solved numerically by solving Equation (2.9) using one of two different methods, either in COMSOL using the inbuilt finite elements method or using the finite differences method [112] in Python that we have implemented ourselves. The first two (highest effective refractive index) modes are the system's symmetric and anti-symmetric core modes. Then the modes are read into

a Python script and are normalised using Equation (2.26). Two N by N matrices (with N the number of modes) of all the coupling coefficients $d_{mn,+}$ and $d_{mn,-}$ are computed in Python using Equations (2.35) and (2.36). The full system contains both forward and backward propagating modes so two greater matrices are built up from the smaller ones using the equations: $d_{mn,+,full} = \begin{bmatrix} d_{mn,+} & -d_{mn,+} \\ d_{mn,+} & -d_{mn,+} \end{bmatrix}$ and similarly for $d_{mn,-}$. A matrix containing the difference in propagation constants between all forward and backward propagating modes is also created.

In order to simulate the light propagation through the device, we set the boundary conditions of the first two forward propagating mode amplitudes, i.e. the symmetric and antisymmetric core modes, to a value of $\frac{1}{\sqrt{2}}$ at $z = 0$ with z the longitudinal dimension. All other forward propagating modes have an amplitude of 0. The backward propagating modes all have a value of 0 at $z = L$ where L is the length of the system being simulated. This corresponds to the launching of light in one of the waveguides (waveguide 0) in the forward direction and no launching of light in the other waveguide (waveguide 1) or in any of the forward or backward propagating cladding modes.

The system is computed numerically in two different ways. In the first model, Equation (2.41) is used to represent the system and is solved as a boundary value problem to find the mode amplitudes all along z . The function `solve_bvp` [113] from the Python library SciPy is used which is based on a method similar to [114]. The step size along z is made to be considerably smaller than the grating period in order to avoid undersampling. We split the real and imaginary parts of the amplitudes into two different real variables in order to be able to use `solve_bvp`. The initial condition is used so that the $A_n(z) = 0$ for all n everywhere except at the boundaries where they are defined above. The power in the modes along z is found by adding the squares of the real and imaginary parts of the mode amplitudes after solving for them.

The second model computes the system numerically by instead solving Equation (2.42) by expressing it in matrix form with an N by N matrix and solving for the eigenvalues and eigenvectors of that matrix similarly to Equations (4.4) and (4.5) in Section 4.2.1. We express the eigenvalues as a vector γ with N entries where γ_i corresponds to the i th eigenvalue, and the eigenvectors as an N by N matrix μ whose columns μ_j correspond to the eigenvectors. We define A_j where $A_{i,j} = \mu_{i,j}$ for each forward propagating mode i and $A_{i,j} = \mu_{i,j}e^{\gamma_i L}$, where L is the device length for each backward propagating mode i . We define the boundary conditions above as a vector B where $B_0 = B_1 = \frac{1}{\sqrt{2}}$ corresponding to the forward propagating core modes and $B_i = 0$ for all other values of i . We then solve the following matrix equation $A\kappa = B$ for κ in order to find the particular numerical solution of our system, which is given by:

$$\mathcal{R}_j(z) = \sum_{j=0}^{N-1} \kappa e^{\gamma_j z} \mu_j \quad (4.27)$$

The code is tested in several ways, the first is to check that the total power flow is constant along z . This is found by taking the sum of the power in all forward propagating modes and subtracting the power in backward propagating modes. If the result does not vary along z then the law of conservation of energy is respected. If not, then there is a problem with the code. Another way is to ensure that there is no (or minimal) coupling to modes that are far from phase matched. Inappropriate coupling of modes can be the result of undersampling in the case of `solve_bvp`. Agreement between numerical and analytical solutions is also taken as validation of code.

Before plotting the results we convert the amplitudes of the symmetric (A_0) and anti-symmetric (A_1) core modes into those for the bottom and waveguide 1 using the following $A_B = \frac{1}{\sqrt{2}}(A_S + A_A)$ and $A_T = \frac{1}{\sqrt{2}}(A_S - A_A)$ where A_B and A_T are the amplitudes of the core modes in the bottom and top waveguides whereas A_S and A_A are the symmetric and antisymmetric core modes.

Except where otherwise specified the model is run using a cladding refractive index of $n_{clad} = 1.4398$ and a width, $W = 34\mu m$. The COMSOL simulation is extended to a distance of $W_a = 20\mu m$ outside the cladding in both directions when computing the modes. The waveguides are separated from the centre by a distance of $x_0 = 10\mu m$ and have width of $\sigma = 2.0\mu m$ and index contrast of $\delta n = 0.01$. We use a wavelength of the light in free space of $\lambda_0 = 1.55\mu m$.

4.4 Numerical simulations using a BVP solver

In this section, we show the results of simulations we made before we implemented the finite differences method to calculate the modes or the eigenvalue method to simulate light propagation in the device in Python. As a result, all the results presented in the section use the finite elements method in COMSOL to calculate the modes and `solve_bvp` to simulate light propagation in Python. The aims of this section are to demonstrate that we can find a set of parameters such that the light can be coupled between the waveguides via a single cladding mode without any contribution from the other cladding modes and to verify that the solutions of the numerical simulations and analytical derivations are consistent.

In Section 4.4.1 we show the results of our mode calculations and calculate the coupling coefficients between the modes and how they depend on the transverse grating wavevector K_t . In Section 4.4.2, we show the numerical results using a grating in one waveguide but not the other in order to make sure that results are the same as those already known for standard Bragg gratings and to compare with the analytical solutions in Section 2.2.2.1. In Section 4.4.2 we show the results for an identical grating in each waveguide in order to find parameters with coupling via only one cladding mode and confirm the analytical result in, and provide a motivation for, Section 4.2.

4.4.1 Mode Analysis and coupling coefficients

Solving for the modes of the above system as an eigenvalue problem using the finite element method in COMSOL yields a solution with 46 different modes. There are two core modes as expected, a symmetric and an anti-symmetric core mode. The rest are cladding modes. An assortment of several different modes are plotted in Figure 4.3.

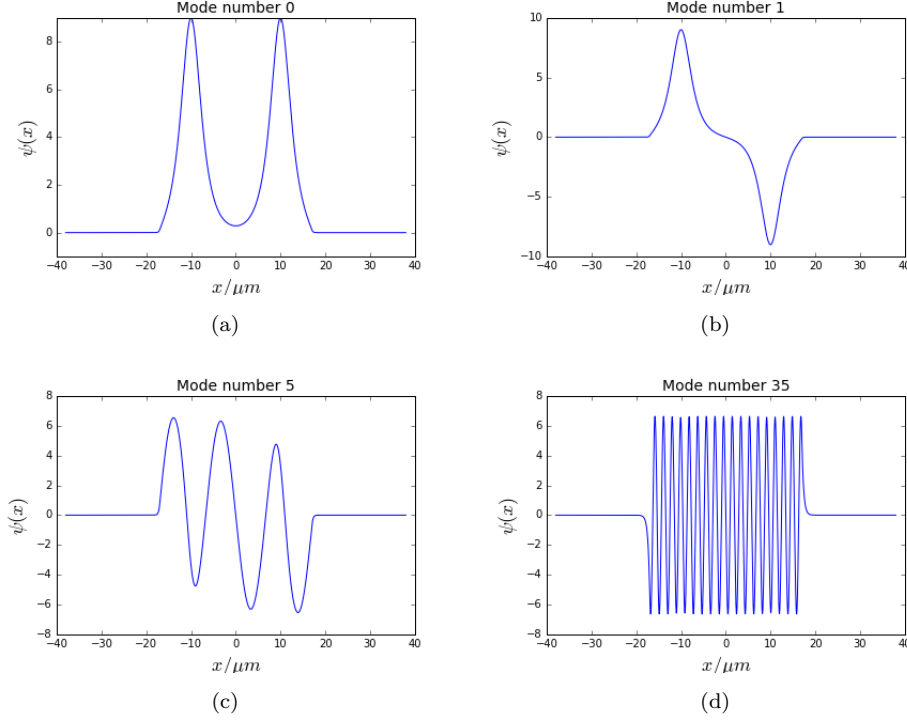


Figure 4.3: Mode plots of the device with symmetric (a) and antisymmetric (b) core modes as well as two cladding modes (c-d). The waveguides have a depth of $\delta n = 0.01$, a width of $\sigma = 2.0\mu m$, are at a distance of $x_0 = 10\mu m$ from the centre and the cladding has a width of $W = 34\mu m$.

A plot of the mode effective indices against mode number can be seen in Figure 4.4. We can see that there is a parabolic correlation and so the higher order modes are spaced further apart. This is similar to a step index waveguide [3]. This is a good reason to use a cladding mode of relatively high order for coupling, though without having an effective refractive index similar or close to that of air, as the cladding mode would then extend too far out into the air. This would increase the risk of leakage as a result of surface roughness.

The symmetric and anti-symmetric core modes have effective refractive indices of 1.479 with a difference of $2 \cdot 10^{-6}$ between them. Using Equation (2.57) this implies a beat length of around 309 mm from evanescent coupling. So long as the length of the device is kept considerably shorter than this, evanescent coupling can be safely ignored. It is easier to conceptualise the system as having two core waveguide modes guided by the

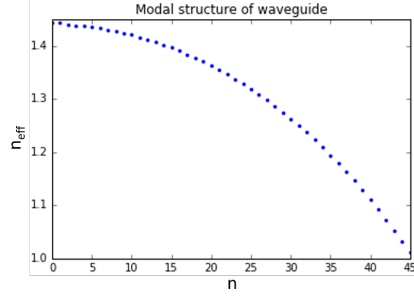


Figure 4.4: Effective refractive index against mode number with $\delta n = 0.01$, $\sigma = 2.0\mu m$, $x_0 = 10\mu m$ and $W = 34\mu m$.

bottom waveguide and the top waveguide respectively, as we do in Section 4.2, that are linear superpositions of the symmetric and antisymmetric modes. So long as we remain considerably below the beat length then this picture will yield equivalent results to that with a symmetric and antisymmetric mode.

For this reason, we convert the coupling coefficients between the core modes and other modes using the following equations:

$$\begin{aligned} d_{Bn\pm} &= \frac{1}{\sqrt{2}}(d_{0n\pm} + d_{1n\pm}) \\ d_{Tn\pm} &= \frac{1}{\sqrt{2}}(d_{0n\pm} - d_{1n\pm}) \end{aligned} \quad (4.28)$$

and the actual coupling coefficients c_{Bn} and c_{Tn} that we plot are found using Equation (2.37).

We plot the coupling coefficients as a function of the transverse wavevector K_t , as defined in the background Section 2.2.2 in Figure 4.5(a). We see that the higher the order of the mode, the greater the transverse wavevector required to couple a core waveguide mode to it. As K_t is proportional to $\tan(\theta)$ this implies that greater tilt angles are needed to couple more efficiently to higher order cladding modes. This makes sense if we understand higher order modes (and hence cladding modes) as propagating at an angle to the z axis and being reflected by the boundary.

For low-order cladding modes, there is coupling with $K_t = 0$, which corresponds to regular, non-tilted, Bragg gratings. However, the cladding modes have effective indices that are too close together so they couple to the core modes with a coupling coefficient comparable to the difference in propagation constants with neighbouring cladding modes. This leads to unwanted coupling between the core and these neighbouring modes which greatly reduces the device performance. Alternately, the coupling coefficient could be made extremely small which, in order to achieve coupling between two waveguides, requires a device that is much longer and therefore with a greatly reduced bandwidth (see Section 4.5.3) compared to the devices with parameters that we study in Sections

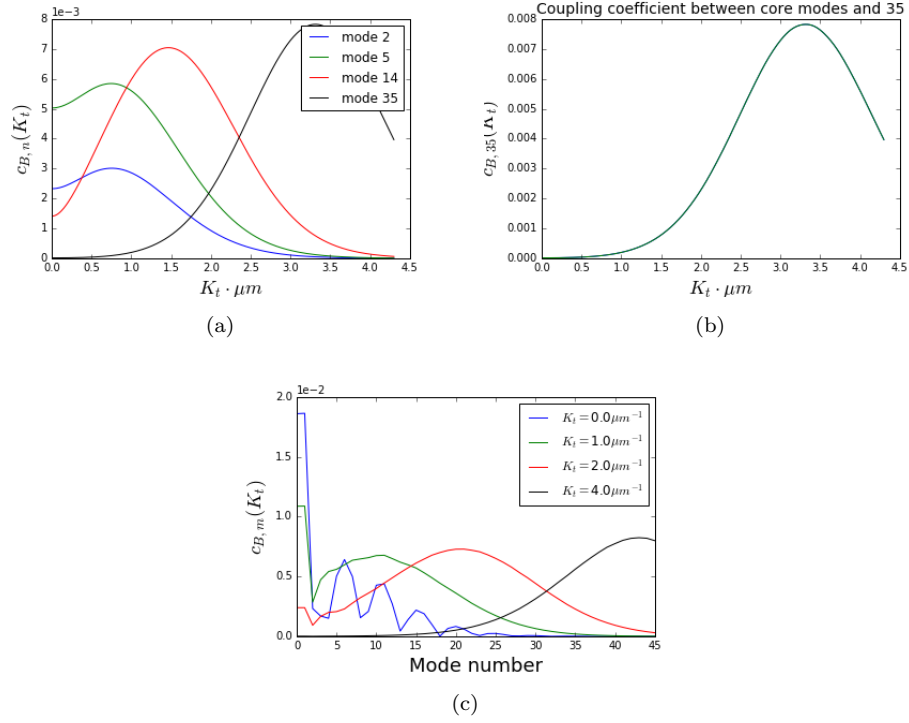


Figure 4.5: (a) Coupling coefficients of the grating in waveguide 0 between the core mode of waveguide 0 and selected cladding modes as a function of K_t . With a grating in both waveguides, overlaid coupling coefficients (b) between the two waveguides and a cladding mode (35). Curves are indistinguishable as the coupling coefficients are identical. Plots in (c) are of the coupling coefficient against mode number for different values of K_t . $\delta n = 0.01$, $\sigma = 2.0$, $x_0 = 10 \mu m$, $W = 34 \mu m$.

4.4.3 and 4.5. This renders a device with untilted gratings impractical and therefore justifies the use of tilted Bragg gratings.

Figure 4.5(b) shows that adding a grating to waveguide 1 causes coupling to waveguide 1 with a coupling coefficient that is equal to that coupling waveguide 0 to the cladding mode. This is very important as it greatly simplifies the analytical solution for the coupling of two core modes by a single cladding mode (see Section 4.2.1). Figure 4.5(c) shows the dependence of the coupling coefficient to the mode number coupled to for different values of K_t . It confirms that higher values of K_t couple more strongly to higher-order cladding modes. The oscillations on that graph for $K_t = 0$ are due to maxima in these mode profiles coinciding with the waveguide cores and thus the maxima of the core modes.

4.4.2 Coupling to cladding modes using one grating

First, the simulations are run in the presence of a grating only in one of the waveguides. This means that our system has only two modes that are coupled, the core mode of the

waveguide with the grating and the cladding mode. This allows us to test the Python code by reproducing known results for the coupling of one mode to multiple cladding modes. The expected result is that the strongest excitation is seen for the mode(s) with phase mismatch closest to zero. Some leakage to other cladding modes is expected which would make the coupling to the phase matched mode potentially weaker. These cladding modes will have a little bit of excitation and their oscillation/decay depends upon the following equation $\lambda = \frac{1}{2}\sqrt{c^2 - \Delta K^2}$ from Section 2.2.2.1 as is the case with two mode coupling.

4.4.2.1 Numerical simulations

The first step is to choose which cladding mode to couple the core modes to using the grating. Looking at Figure 4.4, mode number 35 is chosen as its effective index (1.194) is sufficiently different from that of neighbouring modes (1.179 and 1.209) to avoid unwanted coupling to them but is also not too close to the refractive index of air, which would cause leakage as explained in Section 4.4.1. From Equation (2.21), this mode is resonant with the core modes when the grating period is $587.3nm$. The value of c_{qn} for this mode peaks at $K_g \simeq 3.31$ (see Figure 4.5(a)) which for $\Lambda_g = 587.3nm$ corresponds to a grating tilt angle of $\theta = 17.19^\circ$. We will show in Section 4.5.2 how a high level of accuracy on the grating period can be achieved. We can currently achieve a precision of $0.1nm$ (preliminary value, not well characterised). In an established platform (fibre), better precisions have been achieved [115, 116, 117]. The number of decimal points in the tilt angle was chosen quite arbitrarily but is consistent with the four digit accuracy of the grating period.

We run the simulations using a grating of index contrast $\delta n_g = 0.0025$ and a device length of $L = 2000\mu m$ with 18000 grid points in the z direction. Due to memory limitations, only cladding modes in the index range 30 - 40 are simulated. We plot the power propagation in Figure 4.6. The behaviour of the mode of the bottom waveguide is dominated by an exponential decay along z . This is due to the resonant coupling with the desired mode (which also behaves exponentially). However, the core mode also has off-resonant coupling with other cladding modes that show oscillatory behaviour. This is precisely the expected behaviour and is an indication that the Python model functions and returns the correct results. We can see quite clearly in Figure 4.6 almost pure coupling between the core mode and a single cladding mode with only negligible coupling to the neighbouring cladding modes which means that the system can be reduced to only these two modes.

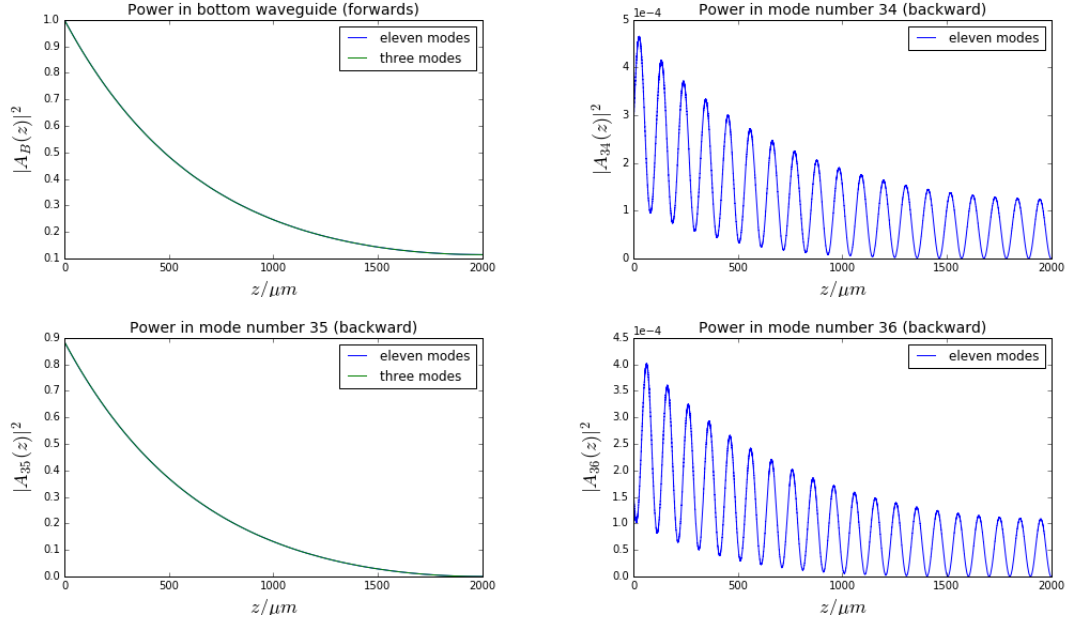


Figure 4.6: Results of numerical simulations of the reduced ("full") system with $\Lambda_g = 587.3\text{nm}$, $\theta = 17.19^\circ$ and $\delta n_g = 0.0025$ and eleven cladding modes on top of the core mode. Overlaid where applicable, results of numerical simulations with only two core modes and the resonant cladding mode of number 35. There is a near perfect match. The system is phase matched so the exponential behaviour seen here is expected.

4.4.2.2 Comparison with analytical solution to two mode coupling

Now that it has been established that it is possible to choose parameters with which we can approximate the system with a grating in one waveguide with only two modes, the next step is to evaluate how well this system can be described by the analytical solution derived in Section 2.2.2.1. This is important as the same methodology is used in Section 4.2.1 to derive the analytical solution for the coupling to two forward propagating modes (of equal n_{eff}) to one backward propagating cladding mode in order to make an analytical representation of the cladding mode-based waveguide coupler.

Figure 4.7 shows good agreement between plots of the real and imaginary parts of the bottom waveguide core mode and the cladding mode after applying the transformation in Equation (2.45) with plots of the analytical solution from Equation (2.47). This confirms two things, that the Python code works properly and returns the correct solutions and that the analytical solution is correct which implies, more importantly, that the methodology for finding the analytical solution is correct. This means that the methodology used in Section 4.2.1 must also be correct. The parameters used are $\Lambda_g = 587.0\text{nm}$, $\theta = 17.19^\circ$ and $\delta n_g = 0.005$ which couple to mode number 35.

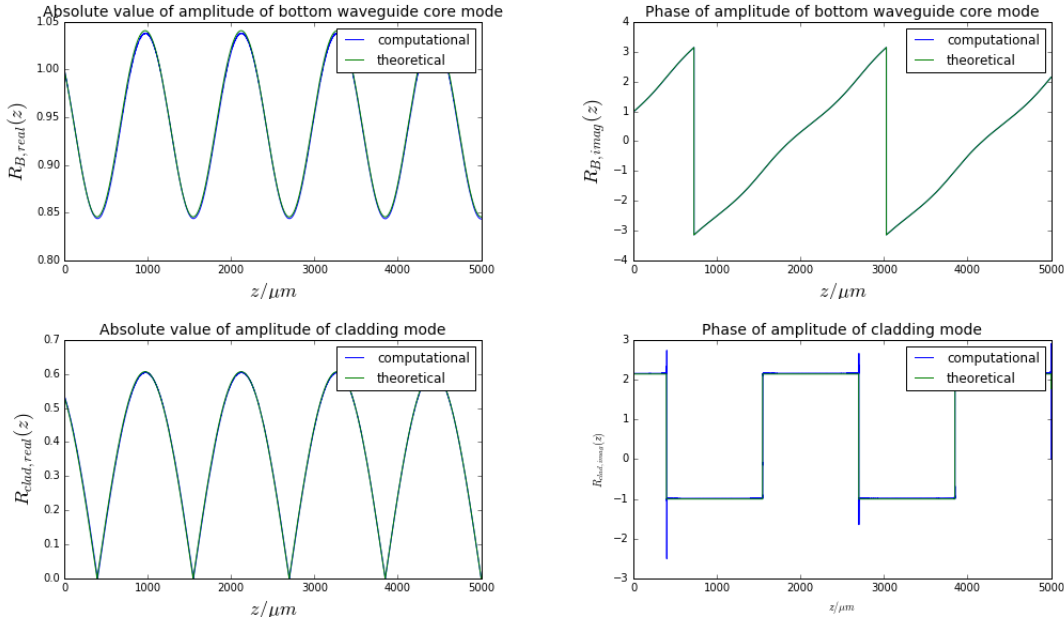


Figure 4.7: Plots of (transformed) amplitudes (left) and phases (right) of the core (top) and cladding (number 35, bottom) modes. Parameters used are $\Lambda_g = 587.0\text{nm}$, $\theta = 17.19^\circ$ and $\delta n_g = 0.005$.

4.4.3 Coupling of two waveguides by cladding modes

Now the complete system is considered that has two gratings, one in each waveguide in order to simulate the cladding-mode based waveguide coupler. The aim here is to find a regime in which the system can be described with only three modes, the two core modes and one of the cladding modes. Once that regime has been found, it is compared with the analytical solution for three mode coupling that is derived in Section 4.2.1.

4.4.3.1 Numerical simulations

Again the core modes are chosen to be coupled to the cladding mode of mode number 35. The parameters we use are $\Lambda_g = 587.3\text{nm}$, $\theta = 17.19^\circ$ and $\delta n_g = 0.0025$ so the modes (and gratings) are phase matched. Figure 4.8 shows the power approaching 25% in each waveguide and 50% in the cladding mode, in keeping with the analytical result in Section 4.2.1. It also shows that there is now a more noticeable difference between the results of the simulations with the core modes plus mode 35 and the core modes plus all cladding modes numbered from 30 to 40. This is unlike the investigations using the same parameters with only one grating for which no difference was found (Figure 4.6) which suggests that the cladding mode-based waveguide coupler is more sensitive to the presence of other modes than a simple grating. This effect is more noticeable with a slight phase mismatch using $\Lambda_g = 587.0\text{nm}$ (Figure 4.9). Nonetheless, the three mode system still shows the same general behaviour. Reducing δn_g to 0.001 we can see

that the problem can indeed be reduced to three modes. This is very important as it allows us to greatly simplify the problem and justifies the application of the analytical solution with only a single cladding mode from Section 4.2.1 in future sections. We will show in the future Section 4.5.2 that the analytical solution with a single cladding mode is indeed correct and fits with the numerical results.

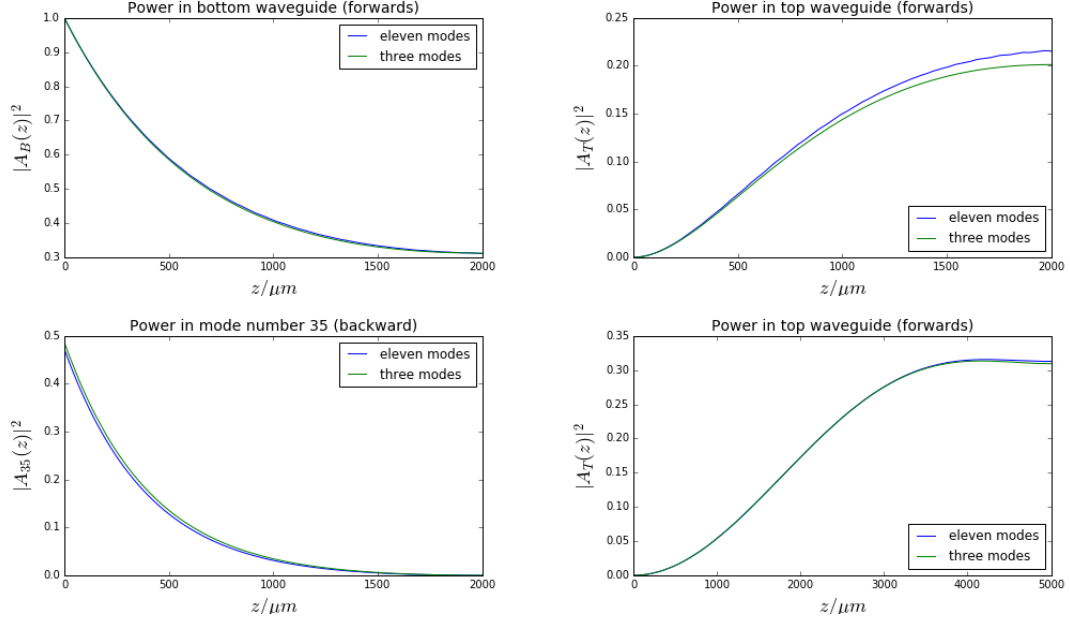


Figure 4.8: Graphs showing the amplitudes of the top and bottom waveguide modes as well as the 35th cladding mode for the "full" system with eleven cladding modes on top of the core mode as well as the system with just three modes. Parameters used are $\Lambda_g = 587.3nm$, $\theta = 17.19^\circ$ and $\delta n_g = 0.0025$. Also (bottom right) graph showing the amplitude of the top waveguide mode with $\delta n_g = 0.0001$.

Due to the use of counter-propagating modes, the device becomes a partial resonator. This means that adding up the power in all of the modes we in general achieve a power at an arbitrary point z that is greater than the input power. Instead it is the sum of power propagation in the modes travelling in one direction minus the sum of power propagation in the modes travelling in the opposite direction that is conserved along the length of the device. This is why we see the power in the core mode increase above one in Figure 4.9

However, there is a problem inherent to using `solve_bvp` which is that it takes a considerably long time to run. It takes 3.8 seconds using only the 35th cladding mode and 2 minutes and 44 seconds using the cladding modes 30 - 40 for the calculations using the following parameters: $\Lambda_g = 587.0nm$, $\theta = 17.19^\circ$, $\delta n_g = 0.0025$, $L = 2000\mu m$ with 18000 grid points along z . More importantly, because it is based on an implicit Runge-Kutta method [114], it is not guaranteed to give an exact solution. We see in Figure 4.10 that the calculated output power of waveguide 0 deviates slightly from the 25% of the input for zero phase mismatch as predicted by the analytical solution in Section 4.2.1. This

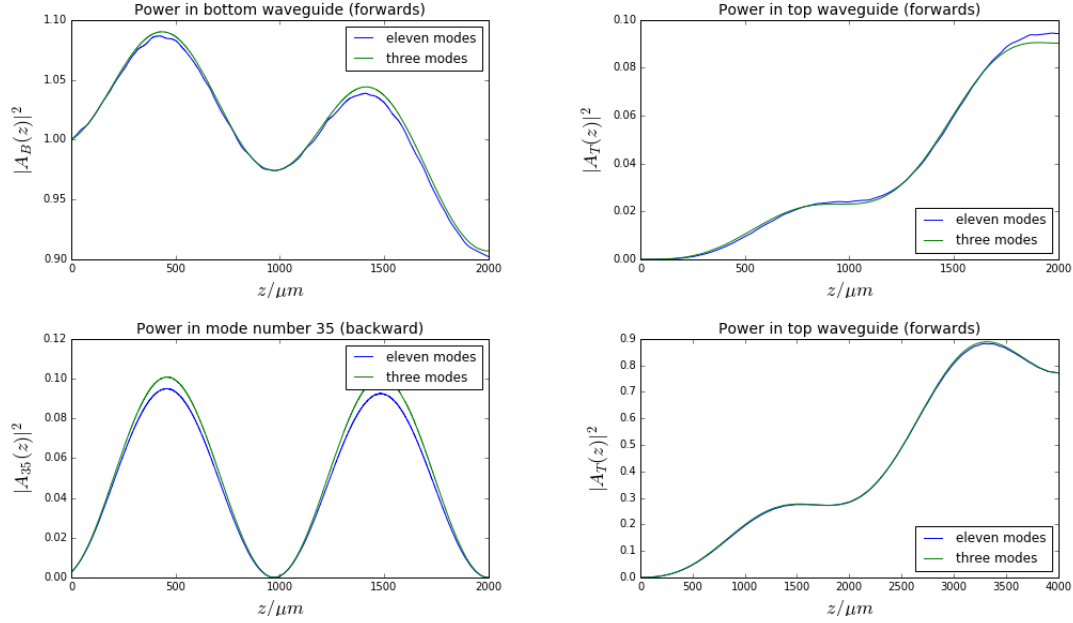


Figure 4.9: Graphs results showing the amplitudes of the top and bottom waveguide modes as well as the 35th cladding mode for the "full" system with eleven cladding modes on top of the core mode as well as the system with just three modes. Parameters used are $\Lambda_g = 587.0nm$, $\theta = 17.19^\circ$ and $\delta n_g = 0.0025$. Also (bottom right) graph showing the amplitude of the top waveguide mode with $\Lambda_g = 587.15nm$.

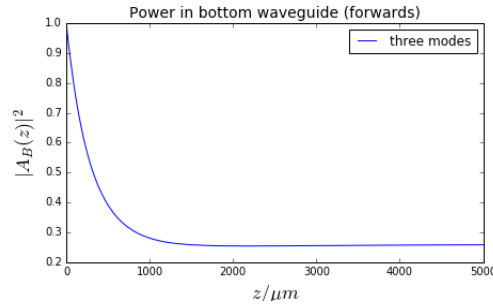


Figure 4.10: Mode amplitude in waveguide 0 with $\theta = 17.19^\circ$ and $\delta n_g = 0.005$ and $\Lambda_g = 587.3nm$. This graph shows that the output power of waveguide 0 deviates slightly from the 25% that is analytically predicted. This is a result of numerical error.

is most likely the result of numerical error. Increasing the number of grid points in the method or using more cladding modes in an attempt to improve its accuracy would exceed the memory limitations of the computer used for these simulations. This, together with the long simulation times, motivates the development of a numerical method for calculating the light propagation that is both faster and more exact.

4.4.3.2 Sensitivity of the device to its length

An apparent consequence of the $\sin(\Omega L)$ and $\cos(\Omega L)$ terms in the analytical solution (see Equation 4.14 in Section 4.2.1) is that the coupling between the waveguides is sensitive to its length. This is very important as the length of the device is one of the key fabrication parameters that must be considered. It is immediately obvious that this behaviour is periodic and so changing its length by an integer multiple of $\frac{2\pi}{\Omega}$ would lead to the same behaviour. This can be seen clearly in Figure 4.11.

In Figure 4.12, we show overlaying plots of the power in the top waveguide with 1000 different lengths. We see that at certain points along z , the power in the top waveguide does not vary at all. This is because at these points we have an integer number of cladding mode oscillations which means that we have no leakage through the cladding mode as we discuss in Section 4.2.1. As we will show in the future Section 4.5.2, these are the parameters that we choose to implement beam splitters. From this we can conclude that, for such parameters, the device would be very robust to its length.

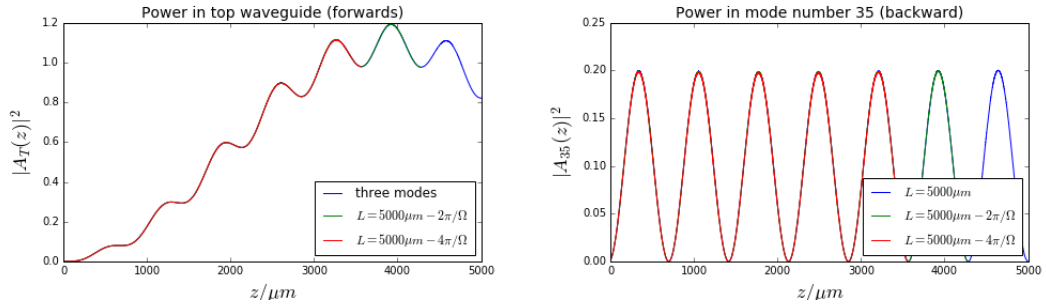


Figure 4.11: Plots of the power in the top waveguide and in the cladding for $\Lambda_g = 586.8nm$, $\theta = 17.19^\circ$ and $\delta n_g = 0.005$. The length is changed by integer multiples of the core to cladding coupling period which keeps the behaviour the same.

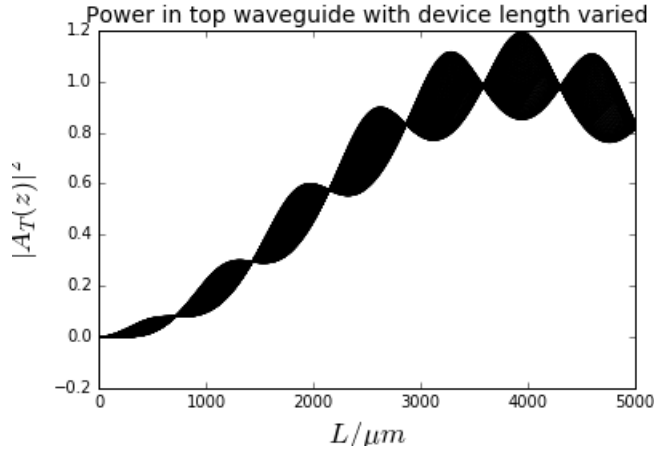


Figure 4.12: Using $\Lambda_g = 586.8\text{nm}$, $\theta = 17.19^\circ$ and $\delta n_g = 0.005$, the filled area shows the full spectrum of possible behaviours of the top waveguide as the device length is changed. This is a key result as it shows that despite the dependence on $\sin \Omega L$ and $\cos \Omega L$ of the analytical solution it is possible to design grating based waveguide couplers whose coupling properties are very stable with the device length.

4.5 Numerical simulations using an eigenvalue method

As we have shown at the end of Section 4.4.3.1, the inbuilt function `solve_bvp` is limited by both speed and the number of cladding modes and grid points in the z -direction that it is able to support. For this reason, we have developed a new numerical method based on the eigenvalue solver introduced in Section 4.3 in order to calculate the mode propagation through the device. This new method is much faster and less memory intensive and therefore allows us to calculate with the full range of cladding modes over a shorter period of time. The performance of this method is also not dependent on the number of grid points in z for accuracy, permitting the simulation of long devices, and therefore allows the reduction of grating index contrast in the simulation to the more realistic $\delta n_g = 0.001$, while still being able to simulate coupling between waveguides. This method is suitable so long as the coupling coefficient is constant (i.e. no apodization) and there are no phase shifts.

I have also moved to using the finite differences method in Python (see Section 4.3) in order to calculate the mode profiles and avoid switching between Python and COMSOL. Unless otherwise stated, all the results presented in this and the following sections will have been calculated using these two methods.

Section 4.5.1 begins by providing the standardised parameters that we use in this section. Then, in Section 4.5.2 we provide the numerical solutions using this method including a sweep of the light wavelength in order to show its bandwidth properties and showing solutions with 100% coupling between the two waveguides. We find that the device has a very narrow linewidth which could make it useful for separating a Raman pump

from the signal. In Section 4.5.3, we will show how the bandwidth is dependent on device parameters including grating index contrast, tilt angle and device length in order to show how the bandwidth can be controlled. In Section 4.5.4 we will show how the light output of the device depends on temperature and find that it has a large thermal stability. In Section 4.5.5 we will calculate the tolerances to fabrication parameters that are required in order to have a fully functioning device. In Section 4.5.6 we will show the effect of super-Gaussian apodization on the device and find that it can suppress leakage via the cladding mode. Finally, in Section 4.5.7 we will use phase shifts in order to simulate grating "noise" in the device, that results from phase-error introduced by the UV-writing system [25] or from other distortions introduced during device fabrication. We find that it is very robust to this kind of "noise".

4.5.1 Standardised parameters used

In this section, unless otherwise stated, we will use the same standardised parameters as those outlined at the end of Section 4.3. We confirm that these parameters define a device with 46 modes in total for $\lambda_0 = 1.55\mu m$. The core modes have effective indices of $n_{eff,0} \simeq n_{eff,1} = 1.4445$ and the 35th mode, that we couple to, is a cladding mode with effective index $n_{eff,35} = 1.1946$.

We use a gratings of a grating period of $587.34nm$ a tilt angle of 17.23° which, for the modes calculated using the finite differences method, provides phase-matched coupling with the highest coupling coefficient. We use a grating index contrast of 0.001, the latter of which is the maximum that can be achieved as quoted in [25] and lower than that used in Section 4.4. We use a device length of $20mm$ over which to simulate the device which is the typical length of a device [10, 50, 118, 119].

We calculate the modes using a width of $W_a = 5\mu m$ outside the waveguides in order to limit the time to calculate them. We use the finite differences method with 4001 grid points, an order of derivative of 2 and an order of accuracy of 4 as defined in [112].

4.5.2 Numerical results

We show the results of the simulations for light propagation both inside and outside of the bandgap using the eigenvalue solver on Figure 4.13 together with the predictions from the analytical solution derived in Section 4.2.1. We see that inside the bandgap, unlike in Figure 4.8 of Section 4.4.3, we have almost precisely 25% of the light at each waveguide output and 50% of the light in the cladding mode, in keeping with the analytical solution in Section 4.2.1. This shows that the eigenvalue solver is more reliable than `solve_bvp`. It is also much faster, taking 1.33 seconds to run with the full set of modes and 0.25 seconds to run with one cladding mode. As a result, it is preferable to use the eigenvalue

method unless we use grating structures that are not supported by it, such as a chirp, an apodization function or phase-shifts.

We see also very good agreement between the numerical result and the analytical solution from Section 4.2.1. As a result, we are able to verify that the analytical solution is indeed correct.

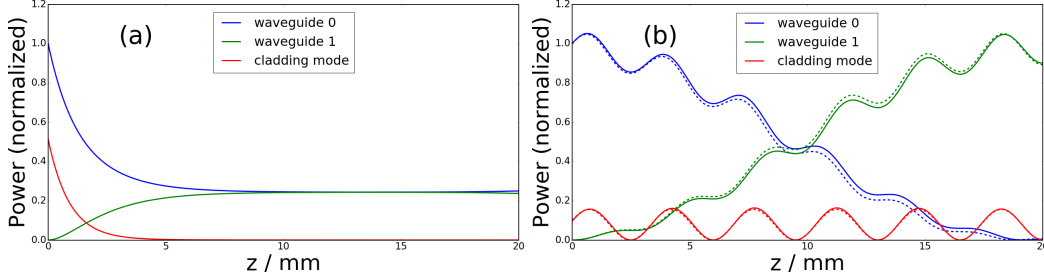


Figure 4.13: Graphs showing the power propagating through the top and bottom waveguide modes as well as the 35th cladding mode for (a) $\lambda_0 = 1.55\mu\text{m}$ (inside the bandgap) and (b) $\lambda_0 = 1.54975\mu\text{m}$ (outside the bandgap). We plot the numerical solution of the system with all cladding modes on top of the core modes (solid) alongside the results from the analytical solution (dashed).

The decrease in simulation time also allows us to make parameter sweeps in a far shorter time. We vary the light wavelength and plot the power output in Figure 4.14. We show the photonic bandgap around the phase-matching condition in which around a quarter of the power is outputted from each of the two waveguides. At either side of the bandgap, there are two peaks in which the amount of light coupled from one waveguide to the other reaches a maximum sharply before reducing back down to zero as the wavelength gets further away from resonance, and is consistent with the analytical prediction in Section 4.2.1. There are clear oscillations in the power outputs of both waveguides whose oscillations get longer and larger closer to the bandgap edge whereas they quickly become much shallower and noticeably faster away from the bandgap which are a result of the increasingly fast oscillations in the cladding mode. This is precisely what is predicted in the analytical solutions detailed in Section 4.2.1. The presence of this bandgap is one of differences between the behaviour of our device and the long-period waveguide grating coupler [37, 38] introduced in Section 2.3.1.3 in the background.

In Figure 4.15, we plot the cladding mode frequency 2Ω and the waveguide to waveguide coupling frequencies $\frac{\Delta K}{2} \pm \Omega$ with wavelength. Outside of the bandgap, these are real variables and 2Ω increases linearly with wavelength detuning in the limit where it is large. On the other hand, the frequency $\frac{\Delta K}{2} - \Omega$ is inversely proportional to the wavelength detuning which corresponds to a linear increase in the coupling length of the device. This can be understood by examining the equation $\Omega = +\frac{1}{2}\sqrt{\Delta K^2 - 2c^2}$. ΔK is the phase mismatch and is proportional to the wavelength detuning. As explained in Section 4.2.1, for $|\Delta K| \gg \sqrt{2}c$, Ω tends towards $\Delta K/2$ and is thus proportional to it, whereas

the difference tends towards zero. $\frac{\Delta K}{2} + \Omega$ is simply the sum of these frequencies and thus has a linear dependence for large phase mismatch.

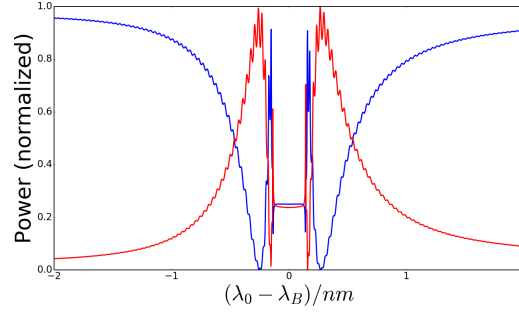


Figure 4.14: Power output of waveguide 0 (blue) and waveguide 1 (red) as the wavelength is swept around the Bragg wavelength.

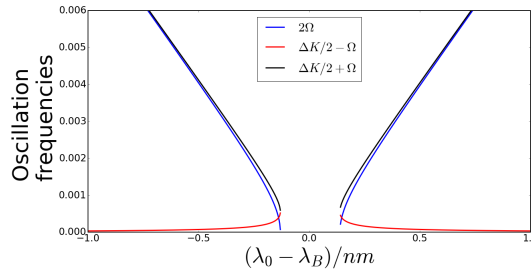


Figure 4.15: Wavelength dependence of the frequency terms 2Ω , $\Delta K/2 - \Omega$ and $\Delta K/2 + \Omega$ outside of the bandgap.

The fast cladding mode oscillations provide an obstacle to the goal of achieving 100% coupling between the waveguides. To fix this issue, we must choose parameters such that there is no backward propagating light in the cladding mode at $z = 0$. As discussed in Section 4.2.1, the oscillations of the waveguide modes are described by the term $\Delta K/2 - \Omega$. Oscillations of the cladding mode are described by 2Ω . Also, as explained in Section 4.2.1, to have complete transfer of light between the waveguides the device must not only have a length of half an oscillation of the waveguide modes but must support an integer n number of oscillations of the cladding mode. Therefore, by solving Equations (4.17) and (4.19) it is possible to find a set of parameters that allow for up to 100% power transfer between the waveguides or any desired splitting ratio.

We use Newton's method to solve Equations (4.17) and (4.19) by varying the grating period while keeping the other variables constant except for the length which is given by Equation (4.17). For $m = 1, 2$ and 3 , we find that the optimal grating periods of the device are $\Lambda_g = 587.409, 587.420$ and $587.432nm$ with lengths $L = 9.737, 12.570$ and $14.873mm$ respectively. In all of these cases we have 100% power transfer between the waveguides and we have an integer number of cladding mode power oscillations given by m . We need this level of precision in the grating period in order for the simulation to work.

As explained in Section 2.4.3 in the background, the gratings are defined by the interference pattern between two UV beams. In the experimental set-up, the two beams are created by a beam splitter. The sample is placed onto an air-bearing stage system in order to smoothly move the device with a very precisely defined speed (see Figure 2.14 in the background Section 2.4.3) [25]. This means that the grating can be defined such that it is still able to maintain a well defined phase over a long distance. How precisely a grating can be defined is a function of how many grating planes can be added sequentially along the longitudinal direction while still maintaining coherence. This is limited by the uniformity of the planar layer's width and refractive index distribution [120]. To fabricate the grating with a target grating period, we need to first know the effective index of the core layer from a previous device. Then, we can define the central wavelength, and thus grating period, to a precision of around $0.1nm$. This is a preliminary value and is not well characterised. In a fibre platform, UV-written Bragg gratings have been defined with more precise grating periods. For example, a standard fibre Bragg grating has been fabricated with a full-width half-maximum bandwidth of $0.04nm$ which implies a precision of $0.02nm$ on the grating period [115, 116] whereas the following source [117] states that fibre Bragg gratings can be manufactured to a precision better than $0.1nm$. As the fabrication method is similar, we should expect similar precisions for our gratings. Repeatability from one device to the next on separate wafers would still be quite difficult as the effective index of the planar layers of each wafer would have to be measured separately.

We show the evolution of the propagating power in each of the modes in Figure 4.16. This allows our device to be used as a wavelength selective coupler which could then form the basis of a wavelength division multiplexer. We can use the same method with Equations (4.17) and (4.21) to calculate parameters for any other splitting ratio, such as a 50 : 50 power splitter.

So as to find out how well our device works as a frequency filter, on Figure 4.17 we show the power output from the waveguides in the intermediate region between phase matching to cladding modes. We choose the parameters $\Lambda_g = 587.409\text{ nm}$, $L = 9.737\text{ mm}$ which we previously showed lead to 100% coupling at $\lambda_0 = 1.55\mu m$. We see that the modes 35 and 36 are sufficiently well separated so as to have a large region between them in which the majority of the light is transmitted in waveguide 0 and is not transferred to waveguide 1 by either of the cladding modes. We find that at a wavelength of $1.5479\mu m$ there is a minimum in the transferred power of 0.80% of the input power which corresponds to a on-off ratio of -20 dB .

4.5.3 Bandwidth Control

In certain photonics applications, such as filtering and for wavelength division multiplexing, it is useful to have control over the device bandwidth. We define the bandwidth

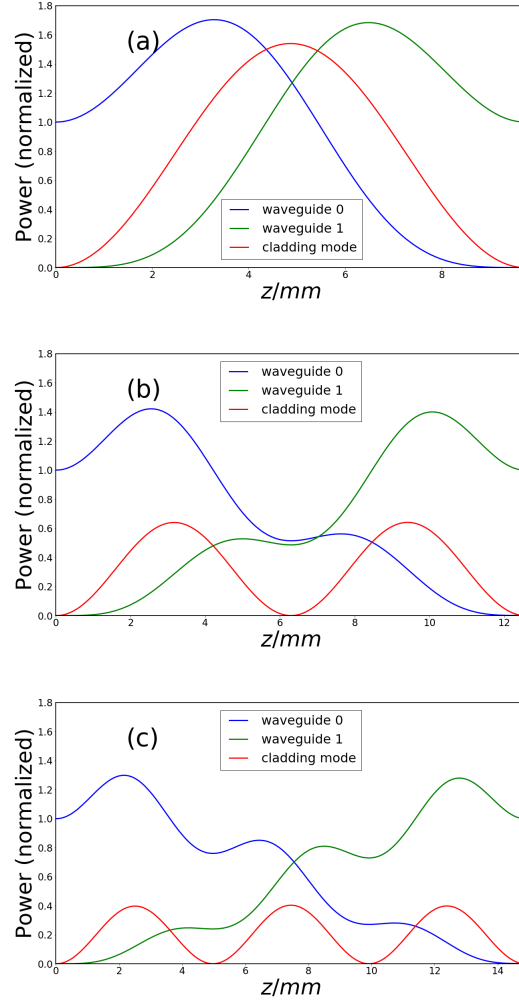


Figure 4.16: Evolution of propagating power in the two core waveguide modes and in the resonantly coupled cladding mode (35th mode) with parameters chosen such that there is as close as possible to complete transfer between the waveguides by supporting n cladding mode oscillations. Solid curves are a numerical solution including all cladding modes, dashed curves are the analytical solution including only one cladding mode. Here, the parameters are (a) $\Lambda_g = 587.409\text{nm}$, $L = 9.737\text{mm}$ (b) $\Lambda_g = 587.420\text{nm}$, $L = 12.570\text{mm}$ and (c) $\Lambda_g = 587.432\text{nm}$, $L = 14.873\text{mm}$.

here as full-width half-maximum in terms of wavelength. In this section, we show how the bandwidth is affected by different device parameters. We plot the dependence of the device bandwidth with grating index contrast, tilt angle, and on the device length in Figure 4.18. We find that the bandwidth of the devices increases with increased coupling coefficient and this causes it to increase with the grating index contrast and change with the tilt angle in accordance to how the coupling coefficient changes with the tilt angle. The bandwidth also increases with the device length.

In Figure 4.18 we can see that our device has a bandwidth of around 0.3nm for parameters of $\Lambda_g = 587.34\text{nm}$, $L = 20\text{mm}$, $\theta = 17.23^\circ$, and $\Delta n_g = 0.001$. This is far

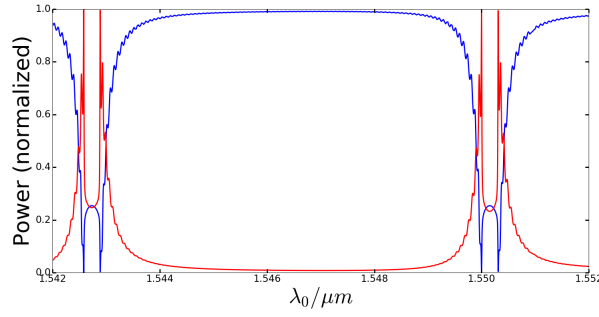


Figure 4.17: Fractional output power from waveguides 0 (blue) and 1 (red) as a function of wavelength where at the input light is launched only into waveguide 0. Parameters are $\Lambda_g = 587.409$ nm, $L = 9.737$ mm.

narrower than that reported in [39] for long-period grating waveguide couplers (20nm). By chaining our couplers together it would be possible to multiplex/demultiplex a large number of different frequency channels. This allows the application of our device in telecommunications or spectral filtering.

The reason for such a narrow bandwidth can be explained by looking at the phase mismatch term restated here as $\Delta K = K_g - \beta_0 + \beta_2$. This is because changing the wavelength causes all the propagation constants to shift in the same direction. In [37, 38, 39], both β_0 and β_2 have the same sign and so the difference between them, and thus ΔK changes more slowly with λ_0 leading to a wide bandwidth. However, in our case, β_0 and β_2 have opposite sign and so ΔK depends on their sum. This means it varies much faster with λ_0 leading to a narrow bandwidth.

We can derive approximately an expression for the bandwidth in terms of the phase mismatch rather than the wavelength. The edges of the bandwidth correspond to where the device length is roughly one quarter of the waveguide mode oscillation period. That means that the length is related to the phase mismatch and coupling frequency as $(\Delta K/2 - \Omega)L = \pi/2$ as opposed to Equation (4.19). Using Equation (4.7) we rearrange the equation to:

$$\Delta K = \frac{1}{2} \frac{\pi}{L} + c^2 \frac{L}{\pi} \quad (4.29)$$

This shows that, in terms of the phase mismatch, and thus in terms of the wavelength which is roughly proportional, the bandwidth is proportional to the coupling coefficient squared, and thus the grating index contrast squared. It is also proportional to the device length (for sufficiently large L). We make, as before, the simplifying assumption that the expression of the bandwidth in terms of wavelength is proportional to that in terms of the phase mismatch as we are looking in a narrow enough window. As a result, we are able to explain the results in Figure 4.18 which also show a dependence of the bandwidth on the square of the index contrast and a roughly linear dependence on the

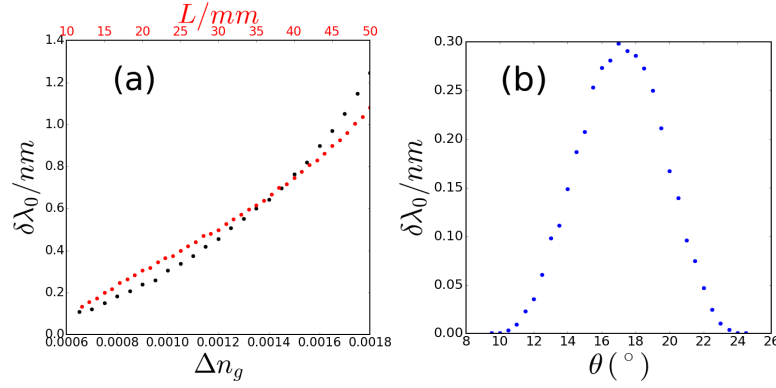


Figure 4.18: Dependence of the bandwidth of the device (full-width half maximum) on (a) the index contrast of the gratings and its length and (b) the tilt angle of the gratings.

length. This also explains the bandwidth's dependence on the tilt angle as the coupling coefficient also depends on the tilt angle with a maximum at $\theta = 17.19^\circ$.

Changing the length or grating index contrast to control the bandwidth seems more straightforward than the tilt angle. However, the former is limited as we cannot bring it past 0.001 using the current state of the art as explained in the previous section. Assuming a loss of $0.2dB/cm$ as in [71, 110], leads to around 50% loss over a length of $15cm$ which is the size of a wafer. In practice, experimentalists may desire to limit the device length below that length. Therefore, if the largest bandwidth is desired, it is advantageous to have the tilt angle at precisely the optimal value for maximum coupling.

4.5.4 Thermal stability

In this section we explore the effect of temperature on the modal structure of the device and thus the wavelength of operation. The temperature affects the device in two different ways. First, the temperature has a direct effect on the refractive index of the material; second, heating up the material causes the device dimensions to change as a result of thermal expansion.

In our device, we model the first effect using the three term temperature-dependent Sellmeier model with the parameters defined in [121] for silica to provide the index of the cladding. We assume for simplicity that the index contrasts of the waveguide and of the grating do not depend on temperature.

We assume linear thermal expansion. The thermal expansion of silica at room temperature is $\alpha_L = 5.5 \times 10^{-7}/K$ [122]. We scale all the dimension parameters of our device (cladding width, waveguide width, waveguide separation, grating period and device length) linearly assuming that the parameters $W = 34.0\text{ nm}$, $x_0 = 10.0\text{ nm}$, $\sigma = 2.0\mu m$,

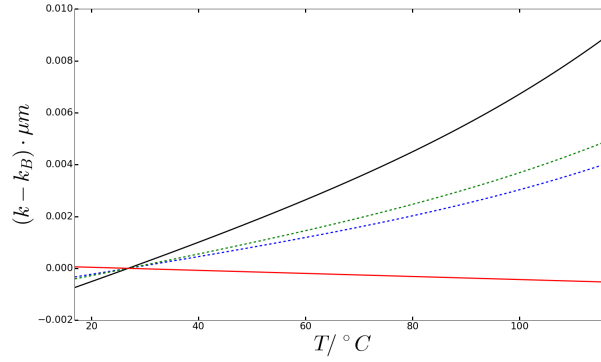


Figure 4.19: Plot of the wavevectors against temperature showing (black) the sum of the propagation constants of the core and cladding mode (blue and green, dashed) the contributions from the core and cladding mode respectively and (red), the grating wavevector. Parameters are (at $T = 300K = 26.85^\circ C$) $W = 34.0\text{ nm}$, $x_0 = 10.0\text{ nm}$, $\sigma = 2.0\text{ }\mu m$, $\Lambda_g = 585.068\text{ nm}$, $\alpha_L = 5.5 \times 10^{-7}/K$, $\lambda_B = 1.55\text{ }\mu m$ and refractive index given by [121].

$\Lambda_g = 585.068\text{ nm}$ and $L = 20\text{ mm}$ apply for a temperature of $T = 300K$. We chose these parameters so that the device is phase-matched at $T = 300K$.

In Figure 4.19 we show how the propagation constants and the grating wavevector vary with temperature. We see that the largest contribution to the phase mismatch come from the changes in propagation constant of the modes and not from the shift in grating period due to thermal expansion. The changes in propagation constant are themselves largely due to the change in index of the device and not thermal expansion.

We find that the resonant wavelength shifts from $\lambda_0 = 1.54988 - 1.55012\text{ }\mu m$ ($\Delta K = 240\text{ pm}$) as the temperature is varied from $T = 290 - 310\text{ K}$. This is considerably less than the bandwidth which means that the device is robust with temperature. This corresponds to a wavelength vs. temperature shift of $12\text{ pm}/K$ which is similar to that reported for Bragg gratings in the same material [123]. This means that our device has a much higher thermal stability compared to [38, 39]. This is unsurprising as our device is made out of silica and those in [38, 39] are made out of a polymer.

We show how the power output from the waveguides vary with temperature in Figure 4.20. We assume that the grating does not degrade as a result of annealing by high temperature. This degradation begins to happen slowly at a temperature of around $150^\circ C$ [124]. The trend shown in Figure 4.20 is mirrored in Figure 4.14 with a wide temperature "bandwidth". The consequence is that the device would have a very low tuning range if the device temperature were used for tuning.

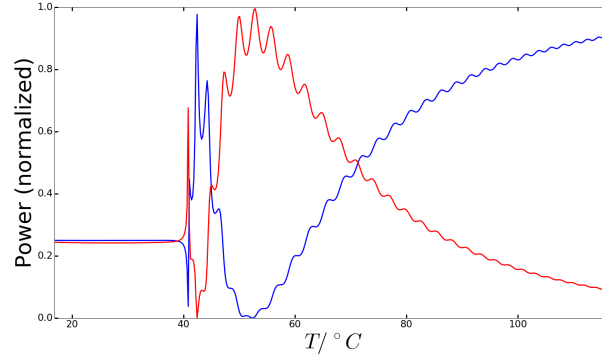


Figure 4.20: Fractional output power from waveguides 0 (blue) and 1 (red) as a function of temperature where at the input light is launched only into waveguide 0. Parameters are $\Lambda_g = 587.34$ nm, $\theta = 17.23^\circ$, $L = 20$ mm, $\delta n_g = 0.001$, $\lambda_0 = 1.55 \mu\text{m}$.

4.5.5 Tolerance to fabrication parameters

In order to be able to build a physically realizable device, we must be able to fabricate using parameters within a fabrication tolerance window. In this section, we vary different parameters in our device and then calculate the power output with these parameters in order to find out how robust our device is to imprecisions in these parameters. We vary all the parameters which includes the device width and length, waveguide separation, width and index contrast, and the grating period, index contrast and tilt angle.

Here, we use the parameters used to find the device with 100% transfer between waveguides with $m = 1$ plotted in Figure 4.16 in Section 4.5.2. That is, with the parameters in Section 4.5.1 except with $L = 9.737$ mm and $\Lambda_g = 587.409$.

We show in Figure 4.21 that the device is extremely sensitive to fabrication imprecisions in the device width. We see a reproduction of the two peak structure similar to that found in Figure 4.14. This is because changes in the width of the device leads to changes in the effective indices of the cladding modes and, as a result, changes in the wavelength at which the gratings are phase matched. There are two sources of uncertainty in the device width that arise from the micromachining process: uniformity and repeatability. Micromachining technology available in the ORC (see Section 2.4.4) can fabricate trenches so as to have a level of uniformity in the width of around $0.1 \mu\text{m}$ due to fabrication precision [107]. The uncertainty from repeatability in fabrication between different chips is on the same order. This means that, if the goal is to have a device that specifically transfers a particular wavelength ($1.55 \mu\text{m}$ in this case), the level of precision needed for that can not be achieved with the current technology available at the ORC. However, there would still be a two peak structure with 100% power transfer at a certain wavelength. We show in the later Section 4.6.2 that, by tuning the device using an external index oil, it would be possible to correct for this and return the peak power transfer to the target and so greatly improve the fabrication tolerances.

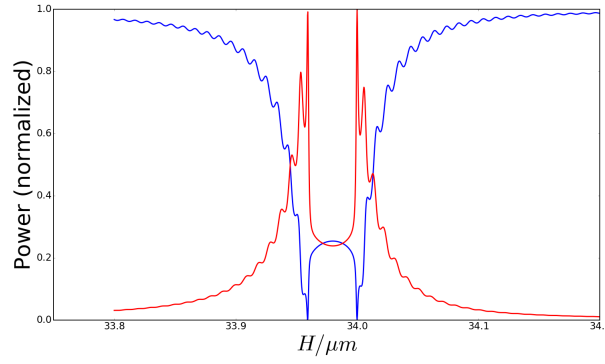


Figure 4.21: Power output of waveguides 0 (blue) and 1 (red) as a function of device width for $\Lambda_g = 587.409$ nm and $L = 9.737$ mm.

To find a physical value for the fabrication tolerances, we use parameters for 100% coupling as an initial value. Then, individually for each parameter, we use Brent's method [15] to find the point at which that parameter leads to 90% coupling, on either side of the peak. The fabrication tolerances we quote are the difference between the parameters leading to 90% coupling and that are needed for 100% coupling. We take the smallest difference and approximate it to 1 significant figure. We find the following fabrication tolerances:

$$W : 0.4nm$$

$$L : 0.9mm$$

$$x_0 : 0.3\mu m$$

$$\sigma : 2nm$$

$$\delta n : 6 \times 10^{-3}$$

$$\Lambda_g : 0.001nm$$

$$\delta n_g : 2 \times 10^{-5}$$

$$\theta : 0.9^\circ$$

Note that the fabrication tolerance on the width is a lot more stringent than it looks on Figure 4.21 as a result of the fast oscillations of frequency 2Ω discussed in Section 4.2.1 which lead to a very sharp peak at $\lambda_0 = 1.55\mu m$. These fabrication parameter tolerances are all extremely stringent except for the tolerances on the length, waveguide position and tilt angle (assuming that the device remains symmetrical). In particular, the device width requires a wide fabrication tolerance, of around $0.1 - 0.2\mu m$ as a result of the imprecision of the diamond saw used for micromachining as explained in Section 2.4.4. This fabrication tolerance is still wider than the full width half maximum of a single one of the two peaks we see in Figure 4.21. This means that, even if we used a grating

apodization function to smooth out the peak (see Section 4.5.6), the fabrication parameter tolerance would still be too stringent. Nonetheless, if more precise micromachining technology becomes available, calculating the fabrication tolerances with apodized gratings could be a useful avenue for future study. As a result, it is not currently realistic to attempt to build a device that can work out of the box without tuning. How we tune the device and the challenges involved in that will be explored in Section 4.6.2.

4.5.6 Using apodized gratings

As mentioned in the background Section 2.1.2, Apodized gratings can be used to suppress boundary effects such as side lobes [125]. We discuss in Section 4.2.1 that the high frequency oscillations of frequency 2Ω in the cladding mode and core modes are due to side lobes in the light coupled into the cladding mode. In this subsection, we investigate the outcome of using an apodization function to define our longitudinal grating index profile. We find that we suppress the side lobes and therefore the high frequency oscillations and that this leads to a much smoother wavelength dependence on the power output of the two waveguides.

We define the apodization function as a super-Gaussian in the following way:

$$a(z) = \exp \left(- \left(\frac{z - \frac{z_0}{2}}{\frac{z_0}{2}} \right)^{2n_{SG}} \right) \quad (4.30)$$

where n_{SG} is the order of the super-Gaussian and z_0 is used to define both the $1/e$ "length" of the grating as well as the centre-point of the grating at $z = \frac{z_0}{2}$. Note that the apodization profile approaches more and more that of a top hat function with $L = z_0$ as n_{SG} is increased.

This means that the grating index contrast along the z direction is given by:

$$\delta n_g(z) = \delta n_{g,0} a(z) \quad (4.31)$$

We solve the coupled mode equations using the method `solve_bvp` similarly to Section 4.4. We calculate the coupling coefficients $d_{mn,-,0}$ and $d_{mn,+,0}$ at the centre-point by inserting the value of $\delta n_{g,0}$ in Equations (2.36) and (2.35). Then we define the coupling coefficients along z as:

$$\begin{aligned} d_{mn,-}(z) &= d_{mn,-,0} a(z) \\ d_{mn,+}(z) &= d_{mn,+,0} a(z) \end{aligned} \quad (4.32)$$

We then solve Equations (2.41) using the variable coupling coefficients in Equation (4.32) and for that we use `solve_bvp`. Note that the eigenvalue method used in previous

subsections in this section is not suitable for use with variable coupling coefficient. We use the same parameters as those in Section 4.5.1 with $\delta n_{g,0} = 0.001$.

We show plots of the power propagation with apodized gratings with a selection of super-Gaussian orders in Figure 4.22. This data shows that, as the order of the super-Gaussian increases, the more the power propagation resembles that in Figure 4.13 for non-apodized gratings. This is because, as mentioned earlier, the apodization function more and more resembles a top-hat function.

In Figure 4.23, we show that with a super-Gaussian of order 4, we achieve a two-peak structure similar to that in Figure 4.14 for non-apodized gratings. However, the fringes have been eliminated and almost no light is escaping via the cladding mode outside of the bandgap. This is because the apodization function removes any side lobes in the wavelength dependence of the reflected light, as explained in the background Section 2.1.2. As mentioned in Section 4.2.1, it is these side lobes that actually cause leakage via the cladding mode outside of the bandgap.

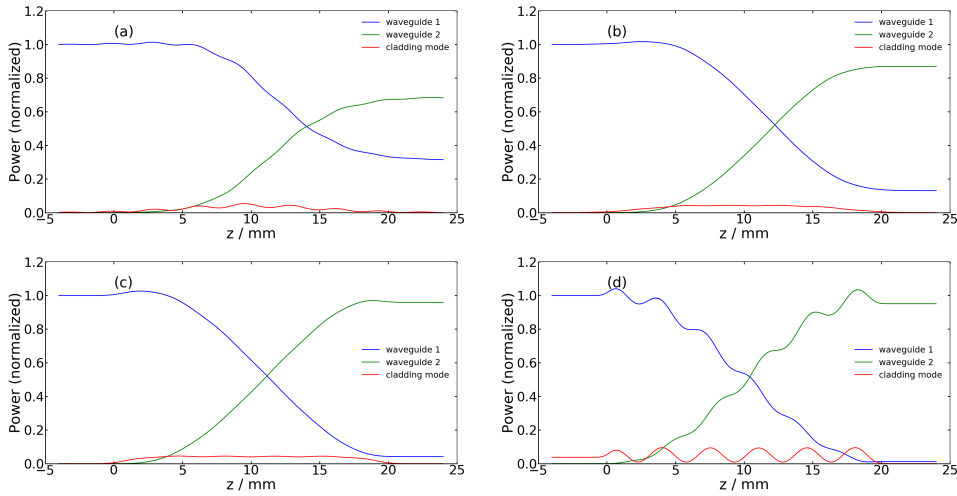


Figure 4.22: Power propagation with apodized grating index contrast defined by Equations (4.30) and (4.31) in text with $\delta n_{g,0} = 0.001$ and $z_0 = 20\text{mm}$. We use super-Gaussian orders $n_{SG} = 1$ (a), 2 (b), 4 (c) and 10 (d)

4.5.7 Using phase-shifts to simulate grating "noise"

In this subsection, we simulate the effect of "noise" in the gratings by modelling them as grating phase-shifts. This "noise" is the result of imperfections defined during fabrication. We model it by defining the gratings as having a large number of evenly separated phase shifts generated by a random number generator. The refractive index perturbation provided by the gratings is thus given by:

$$\delta n(x, z) = \delta n_g \sin \left(2\pi \frac{(z - x \tan \theta + \delta \phi(z))}{\Lambda_g} \right) \exp \left(\frac{-(x - x_0)^2}{\sigma^2} \right) \quad (4.33)$$

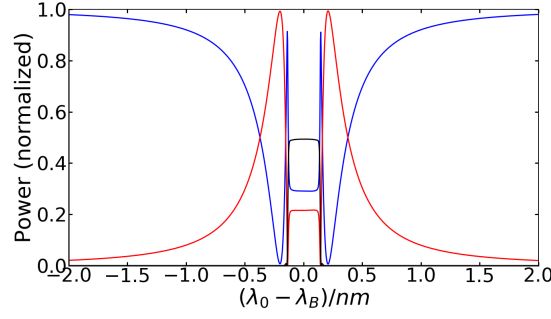


Figure 4.23: Power output of waveguide 0 (blue), waveguide 1 (red) and the backwards propagating cladding mode (black) as the wavelength is swept around the Bragg wavelength. We use the same parameters as Figure 4.22 with $n_{SG} = 2$.

for each grating, where $\delta\phi(z)$ is the additional grating phase along z and is defined by:

$$\delta\phi(z) = \begin{cases} \phi_{r,n} & \text{for } \frac{nL}{N} < z < \frac{(n+1)L}{N} \end{cases} \quad (4.34)$$

where N is the number of segments in which a random phase is added, such that $N - 1$ is the number of phase-shifts, $\phi_{r,n}$ is the random phase added at each segment and n is the segment index and ranges from 0 to $N - 1$. The random numbers generated representing the phases of the segments have a Gaussian distribution and a standard deviation of σ_ϕ , which we will henceforth call the noise amplitude.

In our simulations we calculated the coupling coefficients in the same way as in the previous subsections and as outlined in Section 4.3. We then use the following expression for the variation of the coupling coefficients against z :

$$c_{mn}(z) = d_{mn,+} \sin(K_g z + \delta\phi(z)) + d_{mn,-} \cos(K_g z + \delta\phi(z)) \quad (4.35)$$

which we insert into the coupled mode equations:

$$\frac{dA_m(z)}{dz} = -i \sum_n e^{i(\beta_m - \beta_n)z} A_n(z) c_{mn}(z) \quad (4.36)$$

where if $\delta\phi(z) = 0$ the above equation is the same as Equation (2.41). We use the function `solve_bvp` similarly to Sections 4.4 and 4.5.6 with Equations (4.36) to numerically simulate the device.

For simulating grating "noise" that is defined using fabrication we use the same values of $\phi_{r,n}$ for every wavelength for which the light propagation is simulated. This noise could result from unwanted phase shifts resulting from the UV-writing system as explained in Section 2.4.3. This occurs approximately once every grating period. Noise can also result from fluctuations in the power output of the laser. Fast fluctuations lead to noise variations along the propagation direction of size equal to the spot size. Slower

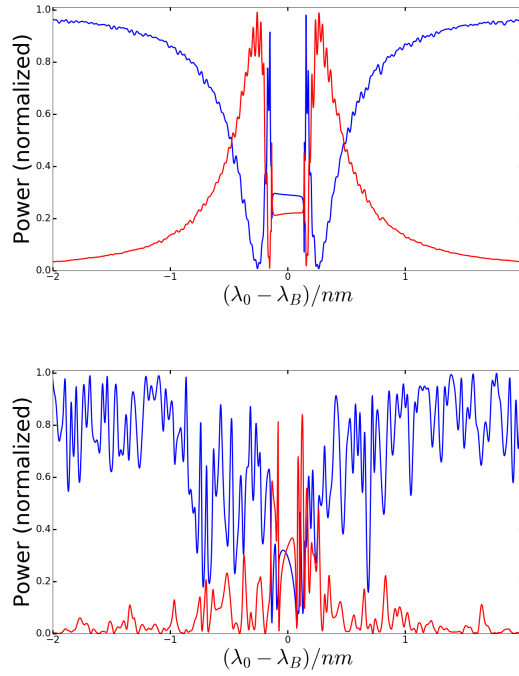


Figure 4.24: Power output from both waveguide with "noisy" gratings composing of $N = 100$ segments with a noise amplitude of $\sigma_\phi = 0.1$ (top) and $\sigma_\phi = 1.2$ (bottom). Both sets of noise have been generated from the same seed.

fluctuation can lead to longer variations. Variations smaller than $1\mu m$ may also result from defects in the substrate. Noise can also result from variations in the thickness and refractive index of the planar layer fabricated via FHD.

For the sake of repeatability, we state that the random numbers have been generated using `numpy.random.normal` in Python version 2.7.12 using a seed of 1.

We first plot on Figure 4.24 the results of simulations of the device with $N = 100$ segments all of the same size. This leads to a segment size of $200\mu m$ which is far greater than the light wavelength. This corresponds to gratings that have been crumpled, in the sense of having large segments with phase-shifts between them, during fabrication, most likely as a result of translation errors during UV-writing. We plot the power output of the two waveguides and find, as expected, that the device becomes more noisy as the noise amplitude is increased. The bandwidth structure becomes more and more distorted and then unrecognisable from its original two peak structure as σ_ϕ increases. This is because the light is able to build constructively interfering reflections over the long segments which then interfere destructively with light reflected from other segments.

We then plot simulation results for a device with $N = 40000$ segments in Figure 4.25. This leads to a segment size of $0.5\mu m$ which is just under the order of one Bragg period. This segment size could result from the unwanted phase-shifts as mentioned before as they typically occur each grating period. We find that the noise has practically no

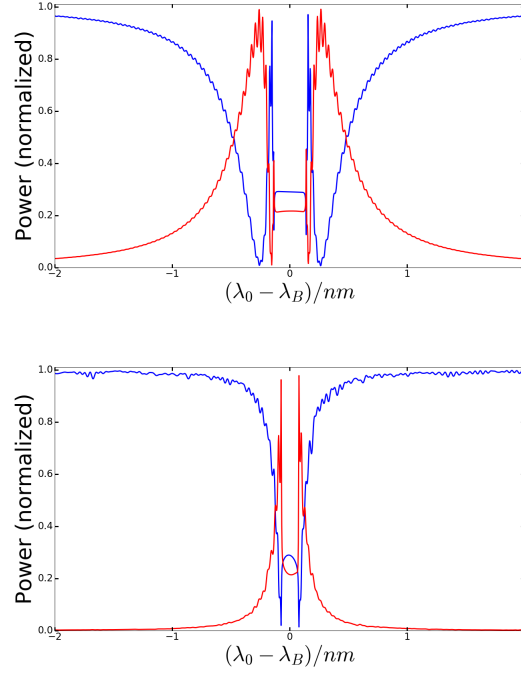


Figure 4.25: Power output from both waveguide with "noisy" gratings composing of $N = 40000$ segments with a noise amplitude of $\sigma_\phi = 0.1$ (top) and $\sigma_\phi = 1.2$ (bottom). Both sets of noise have been generated from the same seed.

noticeable effect with an amplitude of $\sigma_\phi = 0.1$ compared to $\sigma_\phi = 0$ (see Figure 4.14). Increasing the amplitude further, we see the size of the bandgap shrinking. This is because the segment size is now smaller than the light wavelength and so the light needs to build up constructive interference over a large number of segments with different phase-shifts between them. This means that the light sees an average "effective" coupling coefficient along the grating that is smaller than the local coupling coefficient at a point along the grating. The decrease in "effective" coupling coefficient leads to a reduction in the width of the bandgap as it is proportional to the coupling coefficient (see Section 4.2.1). We still see an increase in the measured noise in the output light however as there is still a countable number of segments per light wavelength and so there are still local variations in the average coupling coefficient. Nonetheless, there is less measured noise in the simulations with $N = 40000$ segments than in the simulations with $N = 100$ because of the smaller segment size.

We also show the results of simulations with a $N = 4000$ segments in Figure 4.26. These results are interesting because they have a segment size of $5\mu m$ which is similar to the spot size used to write the gratings. Variations on the order of the spot size typically result from fast variations in the power output of the UV laser. These typically lead to errors in the phase as well as index contrast though we consider only phase-error here. The results we find are intermediate between those we find with a very small (Figure 4.25) and very large (Figure 4.24) segment size as they have a higher level of noise in

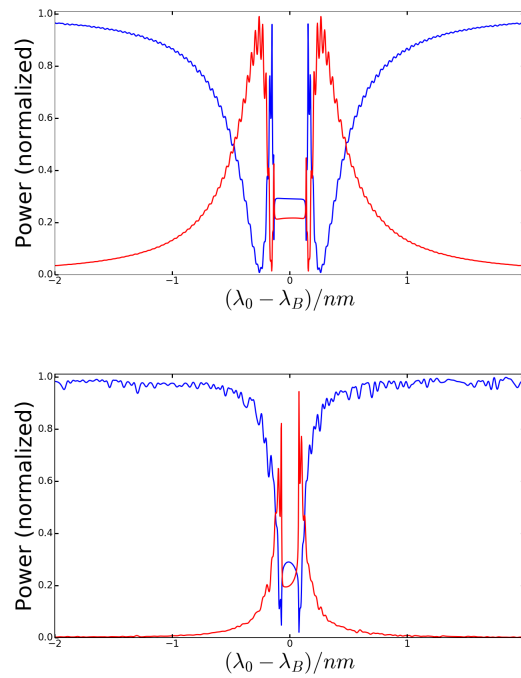


Figure 4.26: Power output from both waveguide with "noisy" gratings composing of $N = 4000$ segments with a noise amplitude of $\sigma_\phi = 0.1$ (top) and $\sigma_\phi = 1.2$ (bottom). Both sets of noise have been generated from the same seed.

the output than Figure 4.25 (though it is still not noticeable for $\sigma_\phi = 0.1$). The output for a higher noise amplitude is distorted (like in Figure 4.24) but still has a recognisable two peak structure with a smaller bandwidth (like in Figure 4.25).

4.6 Using parameters intended for device fabrication and tuning

In this section, we present the collaborative work together with members of the Optical Engineering and Quantum Photonics Group (OEQP), particularly Mr James Field but also Dr James Gates and Dr Rex Bannerman in finding a set of physically realisable parameters in which to build the device with realistic fabrication tolerances.

As we can see in Section 4.5.5, the fabrication tolerances for the device built with the set of parameters used in that section are too stringent. As stated in that section, we need a way to tune the device. In Section 4.5.4, we showed that the device is very robust to temperature which makes changing the temperature unsuitable for tuning the device. In this section, we introduce the use of an external oil that we pour into the two trenches used to fabricate the ridge of the device. It has a refractive index that can be adjusted in a certain range. As the electric fields of the cladding modes, but not the core modes, extend outside of the device (see Figure 4.3 in Section 4.4.1), they will now extend into the index oil. This means that changing the refractive index of the external index oil will now change the effective indices of the cladding modes but not the core modes and so will change the grating period needed for phase-matched coupling between the core modes and the desired cladding mode and therefore tune the device.

Mr James Field provided the dimensions of two physical silica wafers constructed by the OEQP group as well as the $1/e^2$ width of laser writing beam, together with the maximum waveguide and grating index contrasts that can be achieved. I then found a set of parameters within these restrictions in which this device can be fabricated. Section 4.6.1 presents the set of fabrication parameters I have found with which to build this device. In Section 4.6.2, I show the effect of varying the external oil and how that can be used to tune the device. I also calculate a new value of the fabrication tolerance on the device width to show how using an external oil greatly improves the fabrication tolerances. In Section 4.6.3, I show the effect of the asymmetries in the position and index contrasts in the two waveguides and quote values for the fabrication tolerances for these. Finally, in Section 4.6.4, I present the group delay properties of a pulse propagating through the device.

Mr James Field and other members of the OEQP group intended to fabricate the device with the parameters used in this section. Unfortunately, they could not as a result of the lockdown imposed in response to the coronavirus pandemic.

4.6.1 Standardised parameters used

The transverse profile of the wafers used is plotted on Figure 4.27. We choose to use the wafer labelled NB15 on account of its higher index contrast leading to a better

Wafer NB12	Wafer NB15
Clad 18.11 μm 1.4447	Clad 18.11 μm 1.4447
Core 6.17 μm 1.4545	Core 3.80 μm 1.4568
THOX 16.5 μm 1.445	THOX 16.5 μm 1.445
Silicon Substrate	Silicon Substrate

Figure 4.27: Dimensions and refractive indices of the wafers available that could be used for fabricating the device. We chose the wafer NB15 on the right.

confined mode. We calculate the effective index of the fundamental mode of the wafer core confined in the y direction (up and down on Figure 4.27) by solving Equations (2.11, 2.12, 2.13, 2.14) in the Background Section 2.1.1.1 using Brent's method. We find an effective index of 1.4521. Now, we solve this device using the eigenvalue method outlined in Section 4.3 using this effective index as the value of the cladding index.

Mr. James Field provided me with the following constraints to work within. The available wafers had a length of $L = 20\text{mm}$ which provided a maximum length for the device. The UV-writing laser emitted a Gaussian beam of a $1/e^2$ half-width of $\sqrt{2}\sigma = 2.5\mu\text{m}$ and could create waveguides and Bragg gratings of index contrasts of $\delta n = 0.005$ and $\delta n_g = 0.0009$. The refractive index oil used to tune the device was available with indices in the range $1.30 - 1.40$.

This leads the following additional difficulties compared to the parameters used in Section 4.5.1. The reduced index contrast and increased width of the waveguide mean that the fundamental waveguide mode is less confined by the waveguide and so has a higher modal width. This means that the two waveguides need to be further apart in order to avoid evanescent coupling. This means that device width also needs to be larger which leads to there being more cladding modes and thus brings their effective indices closer together. In addition, the use of the external index oil means that any cladding modes of effective index lower than that of the external oil no longer exist. This means that we must use a cladding mode of higher effective index than the external oil. The cladding modes in this region are also closer together in terms of effective indices than the high order cladding modes we would otherwise be able to use.

Nonetheless, we are still able to simulate a device of acceptable performance. We choose a device of width $W = 60.0\mu m$ in order to have waveguides of distance $a = 16.0\mu m$ from the centre. We assume that the waveguide index profile is equal to the intensity profile of the UV-writing beam and so we have waveguides with a Gaussian index profile with a $1/e$ half-width of $\sigma = \frac{2.5}{\sqrt{2}}\mu m$. We choose to find parameters at which the device operates with an external oil index of $n_{out} = 1.35$. We use gratings of period $\Lambda_g = 0.5489\mu m$ and tilt angle $\theta = 9.65^\circ$ and a device length of $L = 19.076mm$. This device has 42 modes in total and couples between the two waveguides via the 37th mode with an effective index of 1.3705. The waveguide core modes have an effective index of 1.4537.

4.6.2 Effect of the external oil

We plot the effect of varying the external oil in Figure 4.28 for three different cladding modes. We find that the closer the external oil index gets to the cladding mode index, the more sensitive the cladding mode index becomes to the external oil. This means that sensitivity of the power output of the device is greater if we use a higher order cladding mode of index close to that at which the device is designed to operate (1.35 in this case). We show this using the 33rd mode with an effective index of 1.3871 and the 40th mode with an effective index of 1.3569. The grating periods and tilt angles used to couple to the 33rd mode are $\Lambda_g = 545.652nm$ and $\theta = 8.60^\circ$ and to couple to the 40th mode they are $\Lambda_g = 551.456nm$ and $\theta = 10.42^\circ$.

The oil is available with refractive indices in increments of 0.1. Any refractive index in the range of 1.3 – 1.4 can be achieved by mixing together oil from two different pots. This mixing is done largely prior to pouring the oil into the trenches. However, some oil may be added later for fine tuning. As tuning needs to be done individually for each device so it would not be possible to mass produce, rendering it impractical for a commercial device. The trenches may be sealed prior to delivery, however, in order to avoid oil leakage.

Now, we need to show how this is able to greatly increase the fabrication parameter tolerances. We choose to look at the fabrication tolerance in the device width as it was the most extreme tolerance calculated in Section 4.5.5. Recall that the way we increase the tolerances is by varying the refractive index oil within a certain range. However, this range is also limited by the index of the cladding mode which is cut-off above a certain external oil index. We can see in Figure 4.28 where this cut-off point is for the various cladding modes used as no light is coupled to the other waveguide above it. For the 37th cladding mode, it is just above 1.37. This limits the tuning range of the oil for this cladding mode to 1.30 – 1.37.

In order to calculate the fabrication tolerances of this device to the width, we calculate the waveguide modes with an external oil index of 1.3 and 1.37 and either increase or

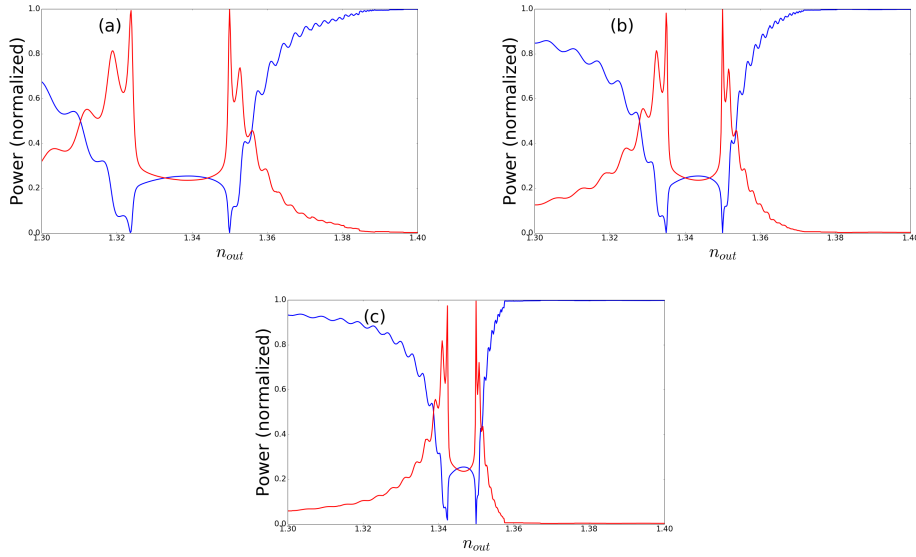


Figure 4.28: Waveguide outputs with external oil index varied. In (a), $\Lambda_g = 545.652\text{nm}$, $\theta = 8.60^\circ$ and $L = 19.167\text{mm}$ and the 33rd cladding mode is used. In (b), $\Lambda_g = 548.861\text{nm}$, $\theta = 9.65^\circ$ and $L = 19.076\text{mm}$ and the 37th cladding mode is used. Finally, in (c) $\Lambda_g = 551.518\text{nm}$, $\theta = 10.42^\circ$ and $L = 19.058\text{mm}$ and the 40th cladding mode is used.

decrease the device width respectively until the phase mismatch is the same as with an external oil index of 1.35. For both the 37th and 40th cladding mode, we achieve a fabrication tolerance on the width of $0.3\mu\text{m}$. This is a massive improvement of around three orders of magnitude on the value of 0.4nm that we achieve without an external index oil in Section 4.5.5. This is within the fabrication tolerance required to micromachine the device and so should be possible to produce.

We find that, although the device becomes more sensitive to the external oil for a cladding mode of effective index closer to the oil index, this does not translate to a significant increase in the fabrication parameter tolerances when coupling via the cladding mode of order 40 compared to 37. This is most likely because, while the modal structure of the device becomes more sensitive to the external oil index it also becomes more sensitive to the device width and the two effects cancel each other out.

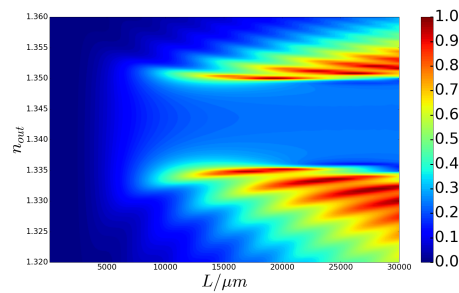


Figure 4.29: Output power of waveguide 1 as a function of external index oil and device length.

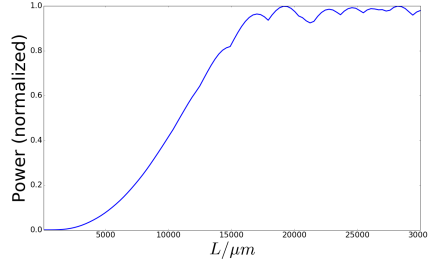


Figure 4.30: Maximum output power of waveguide 1 as a function of device length that can be achieved for any external oil index within the range 1.32 – 1.36.

We also want to show how tunable the device is to imprecisions in the length. To do that, we make a 2D plot of the power output of the device sweeping both the device length and the external oil index, which we show on Figure 4.29. We then take the maximum coupling ratio achieved for a certain length for any external oil index and plot it against the length in Figure 4.30 in order to find out how well the device performance can be recuperated by changing the external oil index. We find that, for any length greater than around $L = 15\text{mm}$ we can achieve a coupling ratio greater than 90%. However, if we want very good coupling of at least 98%, we still need just as much precision in the device length during fabrication than without the external oil. Fortunately, the fabrication tolerance of 0.9mm quoted in Section 4.5.5 for the parameters in Section 4.5.1 is unlikely to be significantly changed with current parameters and is not too stringent.

4.6.3 Fabrication tolerances to waveguide asymmetries

However, we also need to consider fabrication tolerances to asymmetries in the device. We consider two types of asymmetry, asymmetry in the waveguide position and in the waveguide index contrast. The latter can occur if UV-writing the first waveguide causes the photosensitivity of the surrounding region to change and, as a result, the same level of UV exposure no longer causes the same amount of refractive index change when fabricating the second waveguide [126]. This is known as the proximity effect.

We plot the power outputs of the device with asymmetric waveguide position on Figure 4.31. We fix the distance between the centre of the device and waveguide 0 at $a_0 = 16\mu\text{m}$ and vary the distance between waveguide 1 and the centre which we label a . We find a wide fabrication parameter tolerance of $3.5\mu\text{m}$. We do similarly with the device index contrast in Figure 4.32 with a fixed index contrast for waveguide 0 of $\delta n_{g,0} = 0.005$ and the index contrast for waveguide 1 varied. We find the far more stringent fabrication parameter tolerance of 7×10^{-6} . Fortunately, the difference in fabricated index contrast resulting from the proximity effect reduces fast with distance from the previously fabricated region and is no longer measurable with a spacing of more than $13.5\mu\text{m}$ [126], which is much less than our waveguide separation of $32\mu\text{m}$.

As a result, the proximity effect is unlikely to cause a major issue when fabricating our device.

4.6.4 Group delay

In realistic optical setups, the light used to pump the device will not be purely monochromatic or of continuous amplitude and frequency, also known as continuous wave or CW. As such, it is necessary to know the chromatic and pulse properties of the light pumped through this device. In this last subsection, we calculate group delay, which is the amount of time the pulse takes to propagate through the device, and group velocity dispersion (GVD), which governs its chromatic dispersion and pulse broadening, of a pulse propagating through the device. As these quantities are relatively easy to measure experimentally, we include the results of calculations in this section.

The group delay is defined by the following equation:

$$\tau_g(\omega) = -\frac{d\phi(\omega)}{d\omega} \quad (4.37)$$

where $\phi(\omega)$ is the phase of the electric field at the waveguide output as a function of light frequency $\omega = \frac{2\pi c}{\lambda_0}$ where c is the speed of light and λ_0 is the light wavelength. It

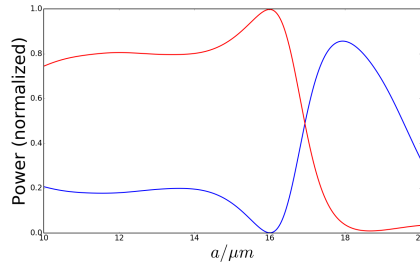


Figure 4.31: Power output of waveguide 0 (blue) and waveguide 1 (red) against the position of waveguide 1 (labelled a here) where $a_0 = 16\mu m$ is the position of waveguide 0.

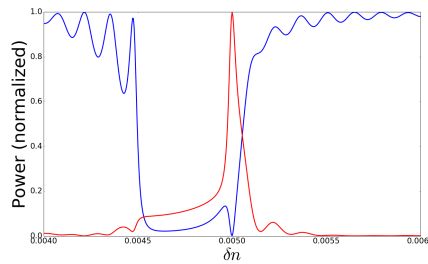


Figure 4.32: Power output of waveguide 0 (blue) and waveguide 1 (red) against the index contrast of waveguide 1 (labelled δn here) where $\delta n_0 = 16\mu m$ is the index contrast of waveguide 0.

is closely related to the optical length as follows:

$$L_O(\omega) = \tau_g(\omega)c \quad (4.38)$$

The GVD is given by the following equation:

$$\text{GVD}(\omega) = \frac{d^2\beta(\omega)}{d\omega^2} \quad (4.39)$$

where $\beta(\omega)$ is the propagation constant as a function of ω and so is related to the phase of the electric field as $\phi(\omega) = \beta(\omega)L$. This allows us to express the GVD as a function of group delay as:

$$\text{GVD}(\omega) = -\frac{1}{L} \frac{d\tau_g(\omega)}{d\omega} \quad (4.40)$$

The pulse broadening is governed by GVD. It is related to the dispersion length which is the propagation length required for the length of the pulse to increase by $\sqrt{2}$. For a Gaussian pulse and for constant GVD, this is given by:

$$L_D = \frac{\tau_0^2}{|\text{GVD}|} \quad (4.41)$$

where τ_0 is half the $1/e^2$ pulse half-width in terms of time.

By taking the Fourier transform of a Gaussian, the pulse width is related to the linewidth via the uncertainty relation:

$$\tau_0 \geq \frac{1}{2\pi} \frac{\lambda_0^2}{c\delta\lambda} \quad (4.42)$$

where $\delta\lambda$ is the pulse linewidth (same measure as for τ_0) and K is a factor that depends on the shape of the pulse.

We plot on Figure 4.33 the group delay against wavelength at both waveguide outputs for a narrow wavelength window around the wavelength at which all light gets transferred from waveguide 0 to waveguide 1. We find that for waveguide 1, we have a group delay

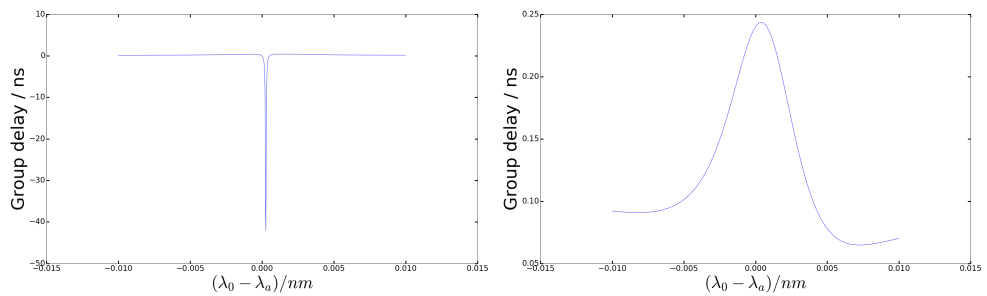


Figure 4.33: Group delay at outputs of waveguide 0 (left) and waveguide 1 (right).

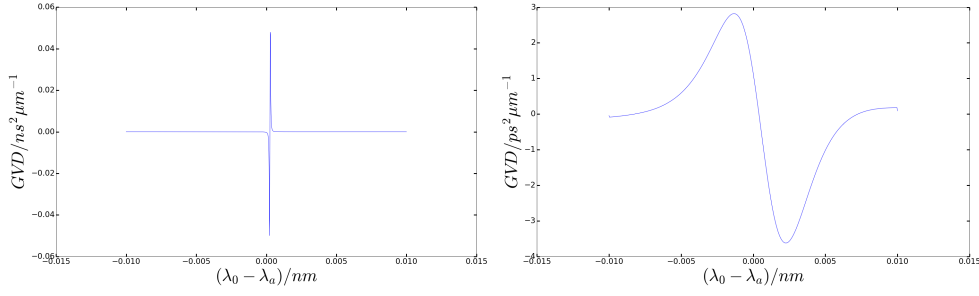


Figure 4.34: GVD outputs of waveguide 0 (left) and waveguide 1 (right).

of $0.243ns$ which correspond to an optical length of $7.31cm$. This means that the grating structure slows down the light by more than two times. We see that for waveguide 0, we have a negative group delay of less than $-45ns$. This corresponds to a large group speed-up and is due to the beginning of the pulse not building up enough coherent reflections and so not being coupled by the grating. The rest of the pulse does get coupled to the cladding mode and so the mean position of the pulse moves forward sharply which gives the impression of the pulse speeding up.

In Figure 4.34 we see the GVD of the pulse going through it. For the light outputted from waveguide 0, we see a very large GVD. This means that, if the pulse is of long enough duration and thus has a narrow enough linewidth that it fits inside the region with high GVD in Figure 4.34 (left), where the vast majority of the pulse is transferred to waveguide 1, what remains of the pulse in waveguide 0 will undergo a very large amount of pulse broadening and a very large chirp as the different wavelengths propagate at different velocities and thus become spatially separated. On Figure 4.34(b) we see that, in order to be affected by the chirp, the beam needs to have a linewidth of maximum around $0.05pm$. For a Gaussian pulse, this means its temporal width needs to be at least $25ns$ long according to Equation (4.42). The GVD in the waveguide 0 peaks at around $0.08ns^2/\mu m$. Inserting that into Equation (4.41) leads to a dispersion length of $8mm$. Over a length of $19.076mm$, we therefore have around 2 dispersion lengths which means that the pulse broadens by around 3 times which is large. Note that this is approximate as the equation assumes that GVD is constant across the pulse spectrum, which is not the case. This calculation is only an estimate and I expect it to be correct to around an order of magnitude. This results from the fact that the vast majority of the incident pulse is transferred to the other waveguide. Away from that point, the GVD approaches zero, which means that there is no pulse broadening.

For the light transferred to waveguide 1, the GVD is a lot more moderate and peaks at around $3ps^2/\mu m$, but the wavelength range with high GVD is larger. This means that, although the amount of chromatic dispersion and thus pulse broadening/chirping is not as high as for the output of waveguide 0, it affects shorter pulses with a larger (though still narrow) linewidth of up to around $4\delta\lambda = 5pm$. From Equation (4.42), this is equivalent to a pulse duration of at around $1ns$. As such, we now have a dispersion

length of around $0.3m$ as per Equation (4.41). For a length of $19.076mm$, we therefore have around 0.06 dispersion lengths which leads to a pulse broadening of around 0.09 times. In this case, we have normal dispersion when the wavelength is smaller than that at which all light is transferred and anomalous dispersion when it is larger whereas the opposite was the case for the output of waveguide 0. Again, this is only an approximate solution correct to around an order of magnitude. Nonetheless, this suggests a more moderate amount of pulse broadening.

4.7 Conclusion

In this chapter we have investigated a novel device for coupling waveguides. I have learned that the cladding mode-based waveguide coupler is theoretically capable of 100% coupling between two waveguides without having to bring the waveguides physically together. I have derived a simplified analytical solution for the waveguide power transfer and verified it numerically. I found that this device exhibited grating induced transparency which could be used as a phase comparator between two beams.

I have developed an algorithm for calculating the parameters for which we achieve 100% coupling and have calculated the fabrication tolerances on these parameters. I have found that, without the use of an external oil to tune it, the device has a good tolerance on its length, to temperature and to grating "noise" but is extremely sensitive to other parameters such as the device width, which makes it hard to fabricate. I have also found that apodizing the device gratings greatly reduces the amount of light reflected into the cladding mode to near zero.

In collaboration with members of the Optical Engineering and Quantum Photonics Group, we have found a set of parameters that can be used to fabricate the device with the addition of an external oil to tune it. Then, I have calculated a far more usable fabrication tolerance as well as fabrication tolerances on waveguide asymmetries. I have also calculated pulse properties of light propagating through the device such as group delay and GVD.

In future Chapters, I will investigate generalisations of this device to a greater number of inputs and outputs.

Chapter 5

Mode division multiplexing, interferometry and power splitting

5.1 Introduction

In this Chapter, we study a generalisation of the system in Chapter 4 with two waveguides, each supporting two modes, as opposed to single-mode waveguides. Tilted Bragg gratings are inscribed into each of the waveguides, potentially superimposed, in order to couple each of the core modes to a cladding mode in order to transfer light between the core modes similarly to Chapter 4. This leads to a device with four input and output ports. In this Chapter we will show how this device can be used as a mode division multiplexer (MDM), how it can be used to achieve any arbitrary splitting ratio between the core modes, and how, by chaining multiple MDMs together, it can be used to implement universal linear optics with four modes.

In Section 5.2 we present the results of a mode analysis of the device with two-mode waveguides. Using the results from the mode analysis, we present the standardised parameters we use in this Section in 5.3. In Section 5.4 we show how our device can be used as an MDM. Section 5.5 shows how the device can be used as a 4×4 power splitter both analytically (Section 5.5.1) and numerically (Section 5.5.2). In Section 5.6 we show how our device can be used to implement any unitary matrix or quantum gate. Finally, in Section 5.7, we present the conclusions of this section including any limitations that this device may have.

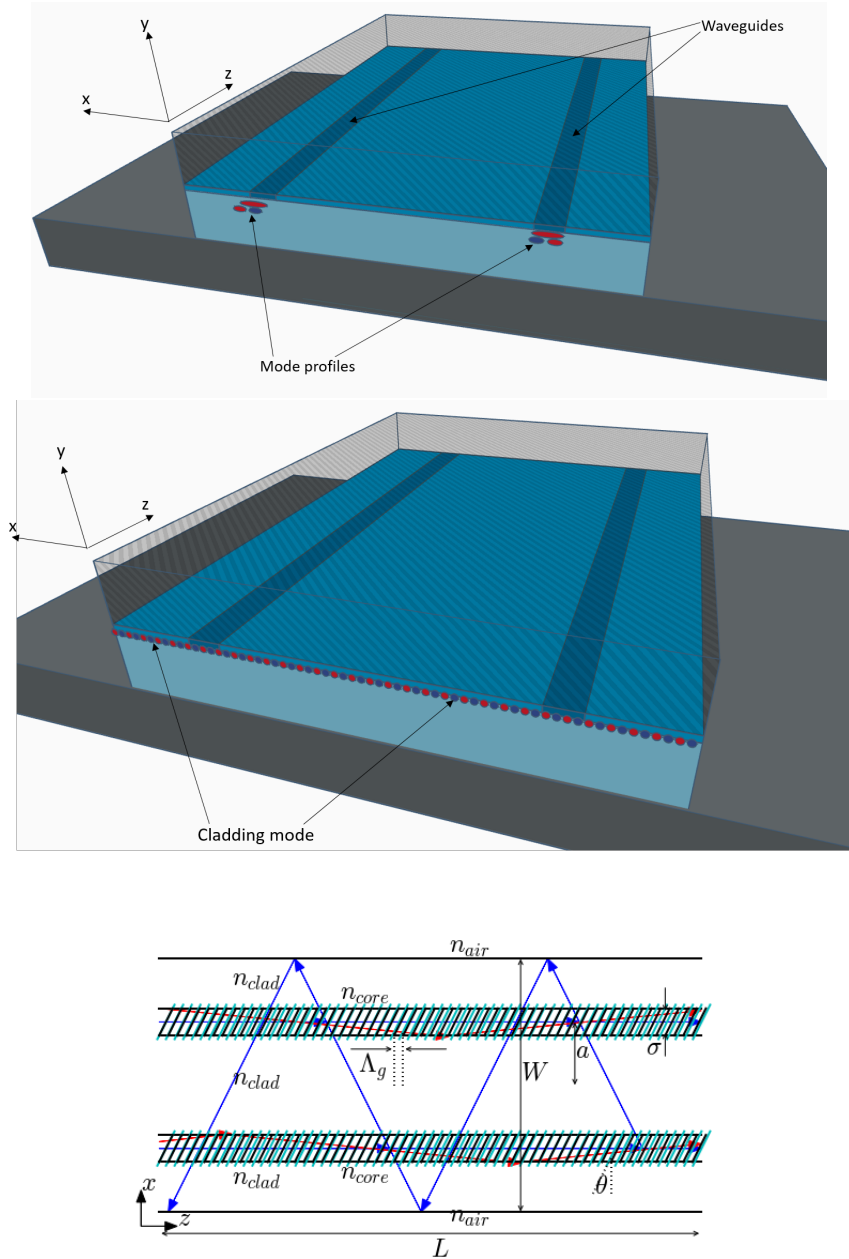


Figure 5.1: (top) 3D model of the device including, ridge structure, core layer and channel waveguides. Also, fundamental and high-order core modes. The superimposed gratings aren't shown here. (middle) Same as top left but showing the cladding mode instead of the core modes. (bottom) Cross section of device inside the core layer, showing waveguides and superimposed Bragg gratings with ray diagram of light in both modes, with (as an example) the fundamental mode of waveguide 0 coupled to the cladding mode and the higher-order mode of waveguide 0 transmitted.

5.2 Mode analysis with two-mode waveguides

In order to support two modes in each waveguide, there are multiple adjustments that need to be made to the parameters compared to those stated in Section 4.5.1 of Chapter 4. First, we need to increase either the width or index contrast of the waveguides so that they can support two modes each. As the index contrast is already $\delta n = 0.01$ for the device in Chapter 4 and this is approximately the maximum that can be fabricated on this platform with hydrogenisation as explained in Section 2.4.3 we are left with only the choice to increase the waveguide width. However, in this section, we will also show that if the remaining parameters are the same as in Section 4.5.1 then there is unwanted evanescent coupling between the higher order waveguide modes and that we need to increase the device width and waveguide separation to avoid this.

We will show that with a waveguide with a width of $\sigma = 4\mu m$, position of $x_0 = 20\mu m$ and a device width of $W = 54\mu m$ we are able to define two two-mode waveguides and avoid evanescent coupling between the higher order waveguide modes. In order to justify using these parameters, we will plot the results of mode analysis using parameter sweeps. We will sweep the waveguide width at and around $x_0 = 10\mu m$ and $W = 34\mu m$ as in Section 4.5.1 in order to show that we need a waveguide width of $\sigma = 4\mu m$ to support two two mode waveguides. We will then plot a parameter sweep of the waveguide separation and device width simultaneously in order to show that we need $x_0 = 20\mu m$ and $W = 54\mu m$ in order to avoid evanescent coupling between higher order modes.

We plot the effective indices of the system against waveguide width in Figure 5.2 for both sets of width and waveguide separation. We use 501 transverse grid points instead of the usual 4001 in order to save computation time. As a result, the effective indices calculated are only approximately correct but are sufficient for finding a set of parameters for our device. The dotted line at $n_{eff} = n_{clad}$ in Figure 5.2 represents the threshold effective index between the mode types, with modes above the dotted line being core modes and those below, cladding modes. We see, therefore, that for a waveguide width of $\sigma = 4.0\mu m$ the system is able to support four core modes in total, corresponding to two modes each in two waveguides, for both sets of parameters.

However, we can also see that for, $W = 34\mu m$, $x_0 = 10\mu m$, there is a visible gap between the effective indices of the 2nd and 3rd core mode, numbered from zero. These correspond to symmetric and antisymmetric superposition of the higher order core modes of the waveguides. This means that there will be evanescent coupling between them. This necessitates the increase in waveguide separation in order to reduce this evanescent coupling.

In Figure 5.3, we plot the effective indices against waveguide separation x_0 with the device width increased in tandem as $W = 2x_0 + 14\mu m$. We need to increase the device width in tandem with the waveguide separation or else the waveguides become too close

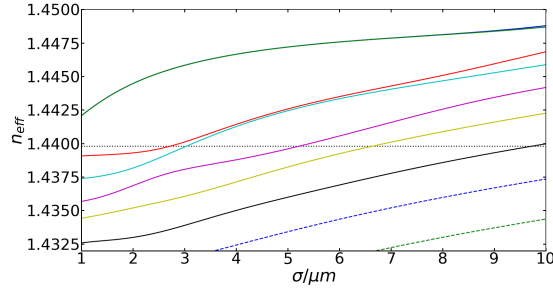


Figure 5.2: Effective indices against waveguide width. Here $W = 34\mu m$, $x_0 = 10\mu m$. The different colours represent the different modes with blue and green (who are close together) representing the 0th and 1st modes, i.e. the symmetric and anti-symmetric superpositions of the fundamental waveguide modes. Red, cyan, violet, yellow, black, blue (dashed) and green (dashed) represent, in order, modes 2 to 8.

to the boundary between the material and the air. If this occurs, the waveguide modes will become distorted by it and so there will still be a large difference between the symmetric and antisymmetric superposition of the higher-order waveguide mode and thus evanescent coupling. The waveguide separation we need will not fit in a device of width $W = 34\mu m$. We plot on Figure 5.4 the difference between the symmetric and anti-symmetric core modes for both the fundamental and higher order waveguide modes. We find that for $x_0 = 20\mu m$ and $W = 54\mu m$ we are able to achieve a small difference between the symmetric and anti-symmetric higher order waveguide modes of 7.3×10^{-7} which corresponds to an evanescent coupling length of $1.05m$.

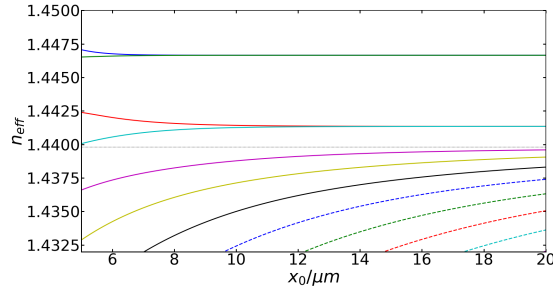


Figure 5.3: Effective indices against waveguide distance from center. $W = 2x_0 + 14\mu m$, $\sigma = 4\mu m$. The colours represent the same modes as Figure 5.2 with the addition of modes 9 and 10 in red (dashed) and cyan (dashed).

For that reason we choose a device of width $W = 54\mu m$, with waveguides of width $\sigma = 4.0\mu m$ and a distance $x_0 = 20\mu m$ from the centre. This system has 73 modes in total with the effective indices of the fundamental and higher-order core modes being 1.4466 and 1.4413 respectively. We choose to couple to the 55th cladding mode with effective index 1.2032. We use gratings of period 584.947nm or 586.121nm to couple either the fundamental core modes or higher order modes respectively. We plot the coupling coefficient against tilt angle for both gratings and their respective waveguide modes on Figure 5.5. We see that for the higher order mode, there are two peaks in

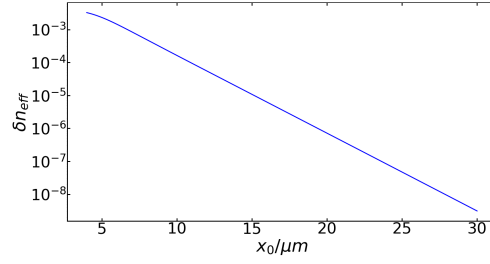


Figure 5.4: Difference between effective indices of both waveguides against waveguide distance from center for the higher order waveguide modes, 2 and 3. $W = 2x_0 + 14\mu\text{m}$, $\sigma = 4\mu\text{m}$.

the coupling coefficient with no coupling in the middle. This can be understood by considering the fact that when the grating tilt angle is chosen such that the grating is phase-matched to a cladding mode, the product of the transverse grating index profile at any point along z to the transverse profile of the cladding mode is itself symmetric. When coupling from the fundamental waveguide mode, which is also symmetric, the integral along the transverse direction of the product of the modes together with the grating is the largest possible which leads to the greatest amount of coupling possible. However, the first higher order mode is antisymmetric, which means that integral of the product of the modes together with the grating is instead zero. This leads to the minimum we see in Figure 5.5. When we move away from the transverse phase matching condition, the product of the transverse index profile becomes no longer symmetric and so the coupling coefficient from the higher-order cladding mode becomes non-zero.

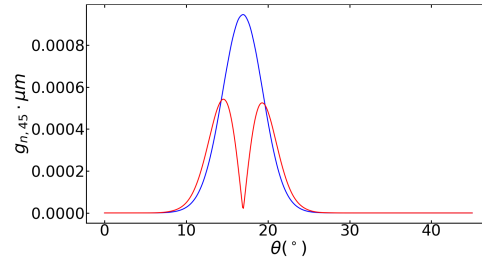


Figure 5.5: Coupling coefficient vs tilt angle between the fundamental (blue) and higher-order (red) waveguide modes and a selection of cladding modes. Here we use $W = 54\mu\text{m}$, $\sigma = 4.0\mu\text{m}$, $x_0 = 20\mu\text{m}$ and $\Lambda_g = 584.947\text{nm}$ (blue) and $\Lambda_g = 586.121\text{nm}$ (red).

5.3 Standardised parameters

Throughout this Chapter we will be using the following parameters unless stated otherwise: a ridge of width $W = 54\mu\text{m}$ with waveguides of width $\sigma = 4.0$, index contrast $\delta n = 0.01$ and of distance $x_0 = 20\mu\text{m}$ from the centre. The two waveguide modes

will be coupled to the 55th cladding mode using gratings of period of either (or both) $584.947nm$ and $586.121nm$, of index contrast of 0.001, and of tilt angle 14.27° . These parameters are chosen so as to have the same coupling coefficient with the same index contrast for both gratings.

5.4 Mode division multiplexing

We first examine the usefulness of our device as a mode division multiplexer. We begin by using the eigenvalue method outlined in Section 4.3 of Chapter 4. We plot the power outputs of waveguide 1 against wavelength on Figure 5.6 using two different grating periods and pump both the fundamental and higher-order modes. We find that, for a grating period of $\Lambda_g = 584.947nm$ we are able to nearly purely couple light between the fundamental modes of each waveguide while coupling only 0.17% of the light from the higher order mode. For a grating period of $\Lambda_g = 586.121nm$, we can couple between the higher order modes while coupling only 0.43% of the light in the fundamental mode. As we can see from Figure 5.5, with a tilt angle of 17.0° , we can have strong coupling between the fundamental modes and eliminate unwanted coupling between the higher order core modes. Similarly, we can couple between the higher-order waveguide modes while eliminating coupling between the fundamental waveguide modes by using a tilt angle sufficiently lower than 14.27° . In the latter case, it leads to a lower coupling coefficient for the higher-order modes as well as the fundamental modes and therefore requires a device of longer length.

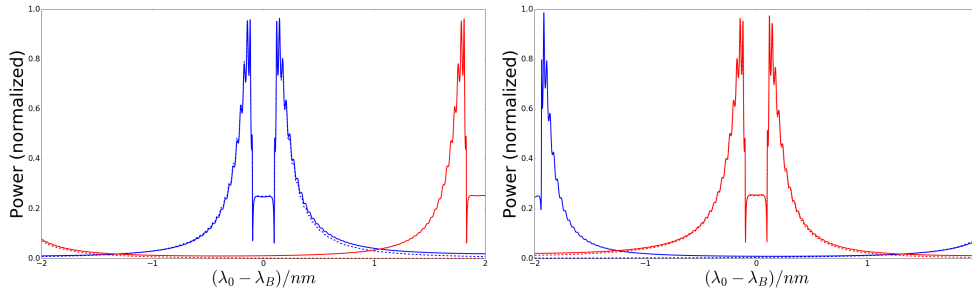


Figure 5.6: Power output of waveguide 1 against wavelength with fundamental (blue) and higher-order (red) mode of waveguide 0 pumped with gratings in both waveguide of period $\Lambda_g = 584.947nm$ (a) and $\Lambda_g = 586.121nm$ (b).

In order to couple light from the fundamental mode of one waveguide to the higher order mode of the other, and vice versa, we need to use gratings of different grating period in the two waveguides. Unfortunately, the eigenvalue solver, as outlined in Section 4.3, is not suitable for solving problems of this sort with different grating periods as the assumption of a constant grating period is used to derive Equation (2.42) in the background Section 2.2.2. Also, the method `solve_bvp` does not seem to work with devices of asymmetric grating period and is therefore unable to compute this problem.

The reason for this is at present unclear. As a result, we have been unable to confirm that we can achieve pure coupling from one mode of one waveguide and the other mode of the other waveguide without affecting the remaining mode. However, the spacing between the phase-matching conditions is not likely to be much different in this case compared to coupling the fundamental or higher-order modes to each other and so it is unlikely for there to be much unwanted coupling in this system. If unwanted coupling does occur, it can be fixed by carefully selecting the tilt angles so as to tune the coupling coefficients prior to fabrication.

5.5 Four-port interference device

In this section, we extend this analysis to a device composed of superimposed gratings in each waveguide. By superimposing gratings of period $\Lambda = 584.947nm$ and $\Lambda = 586.121nm$ in the same waveguide, we are able to couple both modes of the waveguide to the same cladding mode simultaneously. With two grating in each waveguide, we couple all four core modes to a cladding mode and we can achieve a wide variety of transformations.

In Section 5.5.1, we solve the coupled mode equations analytically for this system and show how we can achieve any arbitrary power splitting ratio between the waveguides by deriving an equation expressing the power outputs in terms of the coupling coefficients. In Section 5.5.2, we verify this numerically for a selection of splitting ratios and provide the parameters that achieve them and plot the power propagation.

5.5.1 Analytical Solution for five-mode problem

From Equation (2.40), and using the same method used to derive Equations (4.4) and (4.5) in Section 4.2.1 of Chapter 4, we derive the following coupled mode equations to describe the system:

$$\frac{d}{dz} \begin{bmatrix} R_0(z) \\ R_1(z) \\ R_2(z) \\ R_3(z) \\ R_4(z) \end{bmatrix} = M \begin{bmatrix} R_1(z) \\ R_2(z) \\ R_3(z) \\ R_4(z) \\ R_5(z) \end{bmatrix} \quad (5.1)$$

where:

$$M = \begin{bmatrix} \frac{i\Delta K}{2} & \cdot & \cdot & \cdot & -\frac{1}{2}c \\ \cdot & \frac{i\Delta K}{2} & \cdot & \cdot & -\frac{1}{2}d \\ \cdot & \cdot & \frac{i\Delta K}{2} & \cdot & -\frac{1}{2}e \\ \cdot & \cdot & \cdot & \frac{i\Delta K}{2} & -\frac{1}{2}f \\ -\frac{1}{2}\bar{c} & -\frac{1}{2}\bar{d} & -\frac{1}{2}\bar{e} & -\frac{1}{2}\bar{f} & -\frac{i\Delta K}{2} \end{bmatrix} \quad (5.2)$$

We denote as $R_m(z)$ the electric field amplitudes in mode m , where: $m = 0, 1$ are the fundamental modes of waveguides 0 and 1; $m = 2, 3$ are the corresponding higher-order waveguide modes; and $m = 4$ is the cladding mode. Here c and d are the coupling coefficients of the gratings coupling the fundamental modes of waveguide 0 and 1 to the cladding mode, e and f are those for the gratings coupling the respective higher-order waveguide modes to the cladding mode. Here, we assume that the phase mismatches are identical. That is $\Delta K = \beta_4 - \beta_0 + K_{g,0} = \beta_4 - \beta_2 + K_{g,1}$ and $\beta_0 = \beta_1$, $\beta_2 = \beta_3$. Here β_n are the propagation constants in mode n . $K_{g,0}$ and $K_{g,1}$ are the grating periods of the superimposed gratings.

From this we compute the following eigenvalues:

$$\begin{aligned}\lambda_0 = \lambda_1 = \lambda_2 &= \frac{i\Delta K}{2} \\ -\lambda_3 = \lambda_4 &= \gamma\end{aligned}\tag{5.3}$$

where:

$$\gamma = \frac{1}{2}\sqrt{|c|^2 + |d|^2 + |e|^2 + |f|^2 - \Delta K^2}\tag{5.4}$$

We compute also the corresponding eigenvectors:

$$\eta_0 = \begin{bmatrix} -\bar{f} \\ \cdot \\ \cdot \\ \bar{c} \\ \cdot \end{bmatrix} \quad \eta_1 = \begin{bmatrix} -\bar{e} \\ \cdot \\ \bar{c} \\ \cdot \\ \cdot \end{bmatrix} \quad \eta_2 = \begin{bmatrix} -\bar{d} \\ \bar{c} \\ \cdot \\ \cdot \\ \cdot \end{bmatrix} \quad \eta_3 = \begin{bmatrix} c \\ d \\ e \\ f \\ i\Delta K + \gamma \end{bmatrix} \quad \eta_4 = \begin{bmatrix} c \\ d \\ e \\ f \\ i\Delta K - \gamma \end{bmatrix}\tag{5.5}$$

Which allows us to find the general solution:

$$\begin{bmatrix} R_0(z) \\ R_1(z) \\ R_2(z) \\ R_3(z) \\ R_4(z) \end{bmatrix} = \begin{bmatrix} -(p_0\bar{f} + p_1\bar{e} + p_2\bar{d}) \\ p_2\bar{c} \\ p_1\bar{c} \\ p_0\bar{c} \\ \cdot \end{bmatrix} e^{\frac{i\Delta K}{2}z + q_-} \begin{bmatrix} c \\ d \\ e \\ f \\ i(\Delta K + \Omega) \end{bmatrix} e^{-i\Omega z + q_+} \begin{bmatrix} c \\ d \\ e \\ f \\ i(\Delta K - \Omega) \end{bmatrix} e^{i\Omega z}\tag{5.6}$$

where $\gamma = i\Omega$

We then impose the boundary conditions $R_0(0) = 1$ and $R_1(0) = R_2(0) = R_3(0) = 0$ in order to yield the following relations:

$$\begin{aligned}
 p_0 &= -fq_0 \\
 p_1 &= -eq_0 \\
 p_2 &= -dq_0 \\
 (|f|^2 + |e|^2 + |d|^2 + |c|^2)q_0 &= 1 \\
 q_0 &= \frac{q_- + q_+}{\bar{c}}
 \end{aligned} \tag{5.7}$$

This simplifies the solution to:

$$\begin{bmatrix} R_0(z) \\ R_1(z) \\ R_2(z) \\ R_3(z) \\ R_4(z) \end{bmatrix} = q_0 \begin{bmatrix} |f|^2 + |e|^2 + |d|^2 \\ -d\bar{c} \\ -e\bar{c} \\ -f\bar{c} \\ \cdot \end{bmatrix} e^{\frac{i\Delta K}{2}z + q_-} \begin{bmatrix} c \\ d \\ e \\ f \\ i(\Delta K + 2\Omega) \end{bmatrix} e^{-i\Omega z + q_+} \begin{bmatrix} c \\ d \\ e \\ f \\ i(\Delta K - 2\Omega) \end{bmatrix} e^{i\Omega z} \tag{5.8}$$

Much like in Section 4.2.1 of Chapter 4, there are three frequencies of oscillation: 2Ω , $\frac{\Delta K}{2} - \Omega$, $\frac{\Delta K}{2} + \Omega$. This means that, similarly to Chapter 4, we can choose parameters such that $R_2(0) = 0$ and there is only one oscillation in the cladding mode which means our solution must satisfy Equations (4.17) and (4.19) in that section. This then simplifies our problem down to:

$$\begin{bmatrix} R_0(L) \\ R_1(L) \\ R_2(L) \\ R_3(L) \end{bmatrix} = \frac{(-1)^m}{|f|^2 + |e|^2 + |d|^2 + |c|^2} \begin{bmatrix} |c|^2 - |d|^2 - |e|^2 - |f|^2 \\ 2d\bar{c} \\ 2e\bar{c} \\ 2f\bar{c} \end{bmatrix} \tag{5.9}$$

This allows us to come up with an algorithm for obtaining any unit vector, which is a vector of magnitude 1. By setting:

$$\begin{bmatrix} R_0(L) \\ R_1(L) \\ R_2(L) \\ R_3(L) \end{bmatrix} = \begin{bmatrix} a_0 \\ a_1 \\ a_2 \\ a_3 \end{bmatrix} \tag{5.10}$$

and defining $G = \frac{|d|^2 + |e|^2 + |f|^2}{|c|^2}$ we get $R_{00}(L) = \frac{1-G}{1+G} = a_0$ which rearranging gives:

$$G = \frac{1 - a_0}{1 + a_0} \tag{5.11}$$

We define the ratios of coupling coefficients as $h_1 = \frac{d}{c}$, $h_2 = \frac{e}{c}$ and $h_3 = \frac{f}{c}$. In terms of a_n these are given by

$$h_n = \frac{1 - G}{2} \frac{a_n}{a_0} \quad (5.12)$$

for $n = 1, 2$ or 3 .

The algorithm can then provide all the coupling coefficients required to obtain the target values of a_n . The first step is to calculate G using Equation (5.11) and then the values of h_n from the Equation (5.12). From an arbitrarily value of any of the coupling coefficients we can then calculate the other three.

Generalising Equation (??) for all the remaining boundary conditions yields the following matrix equation:

$$\begin{bmatrix} R_0(L) \\ R_1(L) \\ R_2(L) \\ R_3(L) \end{bmatrix} S = \begin{bmatrix} R_0(0) \\ R_1(0) \\ R_2(0) \\ R_3(0) \end{bmatrix} \quad (5.13)$$

where:

$$S = \frac{(-1)^m}{|c|^2 + |d|^2 + |e|^2 + |f|^2} \cdot \begin{bmatrix} |c|^2 - |d|^2 - |e|^2 - |f|^2 & 2c\bar{d} & 2c\bar{e} & 2c\bar{f} \\ 2d\bar{c} & -|c|^2 + |d|^2 - |e|^2 - |f|^2 & 2d\bar{e} & 2d\bar{f} \\ 2e\bar{c} & 2e\bar{d} & -|c|^2 - |d|^2 + |e|^2 - |f|^2 & 2e\bar{f} \\ 2f\bar{c} & 2f\bar{d} & 2f\bar{e} & -|c|^2 - |d|^2 - |e|^2 + |f|^2 \end{bmatrix} \quad (5.14)$$

In a way that is mathematically identical to [40], by choosing m to be odd and $-c = d = e = f$, we arrive at the following:

$$S = \frac{1}{2} \begin{bmatrix} 1 & 1 & 1 & 1 \\ 1 & 1 & -1 & -1 \\ 1 & -1 & 1 & -1 \\ 1 & -1 & -1 & 1 \end{bmatrix} \quad (5.15)$$

which is a Walsh-Hadamard gate.

In general we can set: $\Omega L = m\pi$, $(\frac{\Delta K}{2} - \Omega)L = \alpha$ for $\alpha \neq \pi$. Then we get the following transformation matrix:

$$S = \frac{(-1)^m}{|c|^2 + |d|^2 + |e|^2 + |f|^2} \cdot \begin{bmatrix} |c|^2 + (|d|^2 - |e|^2 - |f|^2)e^{i\alpha} & (-e^{i\alpha} + 1)c\bar{d} & (-e^{i\alpha} + 1)c\bar{e} & (-e^{i\alpha} + 1)c\bar{f} \\ (-e^{i\alpha} + 1)d\bar{c} & -|c|^2 + |d|^2 - |e|^2 - |f|^2 & (-e^{i\alpha} + 1)d\bar{e} & (-e^{i\alpha} + 1)d\bar{f} \\ (-e^{i\alpha} + 1)e\bar{c} & (-e^{i\alpha} + 1)e\bar{d} & -|c|^2 - |d|^2 + |e|^2 - |f|^2 & (-e^{i\alpha} + 1)e\bar{f} \\ (-e^{i\alpha} + 1)f\bar{c} & (-e^{i\alpha} + 1)f\bar{d} & (-e^{i\alpha} + 1)f\bar{e} & -|c|^2 - |d|^2 - |e|^2 + |f|^2 \end{bmatrix} \quad (5.16)$$

We see that the relative powers at each output are only affected by the absolute value of the coupling coefficients, and not by their phases, which only affects the output phases.

5.5.2 Four-way power splitting

In order to compute this system numerically with super-imposed gratings, we solve a system of equations similar to Equation (5.1) only with the following matrix M solved as an eigenvalue/eigenvector problem:

$$M = \begin{bmatrix} \frac{i(\Delta K_0 - \Delta K_1)}{2} & \cdot & \cdot & \cdot & -\frac{1}{2}c \\ \cdot & \frac{i(\Delta K_1 - \Delta K_0)}{2} & \cdot & \cdot & -\frac{1}{2}d \\ \cdot & \cdot & \frac{i(\Delta K_0 - \Delta K_1)}{2} & \cdot & -\frac{1}{2}e \\ \cdot & \cdot & \cdot & \frac{i(\Delta K_1 - \Delta K_0)}{2} & -\frac{1}{2}f \\ -\frac{1}{2}\bar{c} & -\frac{1}{2}\bar{d} & -\frac{1}{2}\bar{e} & -\frac{1}{2}\bar{f} & -\frac{i(\Delta K_0 + \Delta K_1)}{2} \end{bmatrix} \quad (5.17)$$

The power output of all four modes against wavelength with all four gratings equal to 0.001 is shown in Figure 5.7, and displays a two peak structure similar to that found in Section 4.5.2. We find that, at a certain wavelength away from phase-matching, we have close to 25% power output in each waveguide. This is as close to what we expect from Equation (5.15) for equal coupling coefficient. Any deviation is likely the result of the effective indices of the two waveguide modes varying unequally with light wavelength which leads to the phase-mismatch of the two different gratings being slightly different.

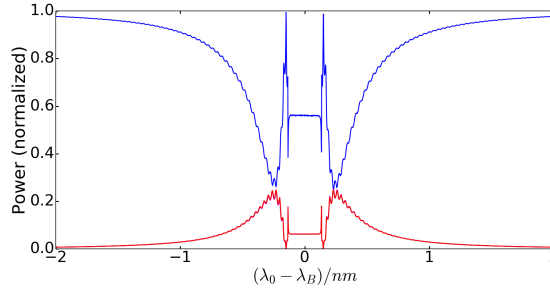


Figure 5.7: Power output of mode 0 of waveguide 0 (blue) and all three other modes (red) against light wavelength with all four gratings of index contrast $\delta n_g = 0.001$ and therefore of equal coupling coefficient ($c = d = e = f$).

In the remainder of this section, we show that we can achieve any power splitting ratio between the outputs of the waveguide modes. We show a selection of splitting ratios as examples. We use the algorithm outlined in Section 5.5.1 based on Equations (5.11) and (5.12) to calculate all the ratios of coupling coefficients needed to achieve the desired splitting ratios. We then calculate the grating index contrasts needed to achieve these coupling coefficients normalised such that the largest index contrast is equal to 0.001. We then solve for the grating periods and device length needed to achieve the power splitting without leakage into the cladding mode using Equations (4.17) and (4.19) similarly to how we do in Section 4.5.2. In each case, we use a negative value of a_0 as defined in Equation (5.10) as this leads to smaller oscillations and a shorter device compared to a positive a_0 .

Figure 5.8 shows the power propagation through the device with parameters that lead to equal power splitting. We find using the method outlined above that we need superimposed gratings each of equal coupling coefficient in each waveguide of $\delta n_g = 0.001$ and with grating periods of $\Lambda_g = 585.014nm$ and $586.189nm$ and a device length of $L = 10.190mm$. We show in Figure 5.9 a wavelength sweep with these parameters.

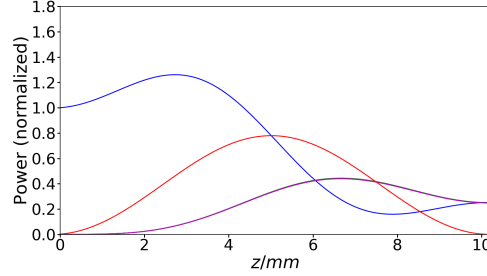


Figure 5.8: Power propagation through device in mode 0 of waveguide 0 (blue), all other waveguide modes (violet) and backward propagating cladding mode (red). Here we have superimposed gratings in each waveguide of periods $\Lambda_g = 585.014nm$ and $586.189nm$, grating index contrast of $\delta n_g = 0.001$ and device length of $L = 10.190mm$.

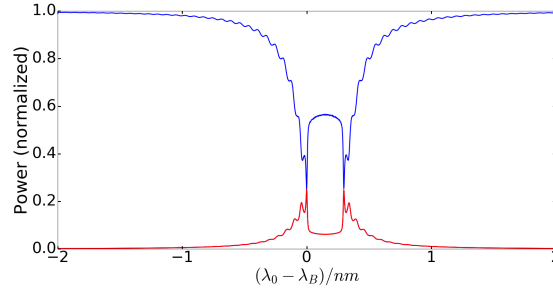


Figure 5.9: Power output of mode 0 of waveguide 0 (blue) and every other core mode (red) as wavelength is swept. Here we have superimposed gratings in each waveguide of periods $\Lambda_g = 585.014nm$ and $586.189\mu m$, grating index contrast of $\delta n_g = 0.001$ and device length of $L = 10.190mm$.

In Figure 5.10 we show the power propagation through the modes of the device for the parameters required to achieve a selection of splitting ratios that we have found using the method outlined above. We do this in order to demonstrate that we can achieve any arbitrary power splitting ratio in our device. We also include in the plots the ratios of coupling coefficients with the actual parameters in the Table 5.1.

5.6 Implementation of any arbitrary 4×4 unitary matrix

In this section, we investigate the usefulness of this platform in implementing any 4×4 unitary transformation between the electric fields at the four input and output ports of our device.

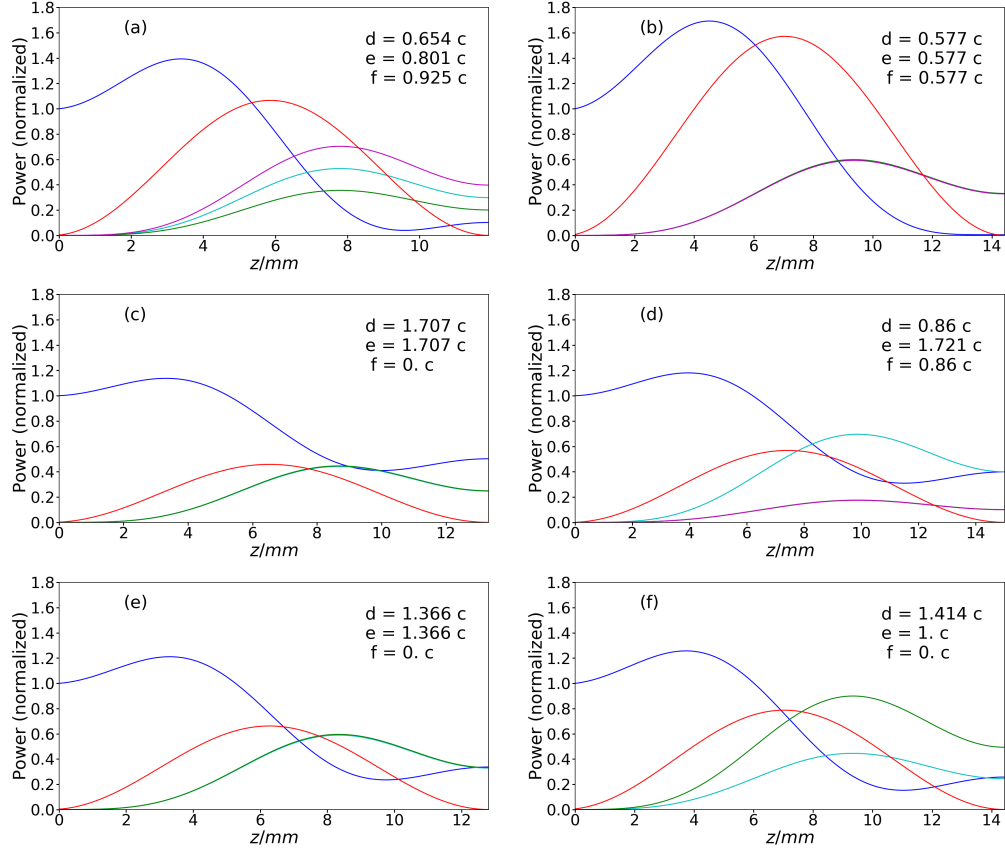


Figure 5.10: Power propagation through device in mode 0 of waveguide 0 (blue), in mode 1 of waveguide 0 (cyan), mode 0 of waveguide 1 (green), in mode 1 of waveguide 1 (magenta) and the backward propagating cladding mode (red). The device parameters for the respective plots are found in Table 5.1

Plot label	$\Lambda_{g,0}$	$\Lambda_{g,1}$	$\delta n_{g,0}$	$\delta n_{g,1}$	$\delta n_{g,2}$	$\delta n_{g,3}$	L
(a)	585.004nm	586.179nm	0.001	0.000654	0.000801	0.000925	11.916mm
(b)	584.994nm	586.169nm	0.001	0.000577	0.000577	0.000577	14.428mm
(c)	584.998nm	586.173nm	0.00058579	0.001	0.001	0.0000	13.322mm
(d)	584.992nm	586.167nm	0.00058114	0.0005	0.001	0.0005	15.015mm
(e)	585.000nm	586.175nm	0.000732	0.001	0.001	0.0000	12.809mm
(f)	584.994nm	586.169nm	0.000707	0.001	0.000707	0.0000	14.437mm

Table 5.1: Parameters used to produce the plots in Figure 5.10. Here, the entries in the rows for plot labels (n) refer to the parameters used to produce Figure 5.10(n). $\Lambda_{g,0}$ and $\Lambda_{g,1}$ refer to the grating periods of the superimposed gratings that exist in each of the waveguides. The parameters $\delta n_{g,0}$ and $\delta n_{g,1}$ refer to the index contrast of the gratings of period $\Lambda_{g,0}$ and $\Lambda_{g,1}$ in waveguide 0 whereas $\delta n_{g,2}$ and $\delta n_{g,3}$ refer to the respective index contrasts in waveguide 1. L is the device length.

Recall from the background Section 2.3.4 that any $N \times N$ unitary transfer matrix can be implemented in an integrated photonics platform. In particular, these implementations use a network of directional couplers in order to decompose any $N \times N$ unitary transformation into a product of 2×2 transformations. In this section, we show how this can be achieved using our device for 4×4 unitary transforms.

As noted in Section 2.3.4, in order to achieve an $N \times N$ unitary transform we need to decompose it into $\frac{N(N-1)}{2}$ 2×2 unitary transforms. As in our case $N = 4$, this means we need to implement 6 mutually independent transfer matrices in our device.

In Section 4.2.1 of Chapter 4, we found that, by using a cladding mode-based waveguide coupler with the addition of a phase-shift, we are able to achieve any arbitrary 2×2 unitary matrix that we showed in Equation (4.23). This can be generalised to 2×2 transfer matrices between each of the four core modes in our device. We show the four transfer matrices transforming between each of the core modes of waveguide 0 and each of the core modes of waveguide 1 below:

$$\begin{aligned}
 S_1(\alpha_0) &= (-1)^{m_1} e^{i\alpha_0} \begin{bmatrix} \cos(\alpha_0) & -i \sin(\alpha_0) & \cdot & \cdot \\ -i \sin(\alpha_0) & \cos(\alpha_0) & \cdot & \cdot \\ \cdot & \cdot & 1 & \cdot \\ \cdot & \cdot & \cdot & 1 \end{bmatrix} \\
 S_2(\alpha_0) &= (-1)^{m_1} e^{i\alpha_0} \begin{bmatrix} 1 & \cdot & \cdot & \cdot \\ \cdot & 1 & \cdot & \cdot \\ \cdot & \cdot & \cos(\alpha_2) & -i \sin(\alpha_2) \\ \cdot & \cdot & -i \sin(\alpha_2) & \cos(\alpha_2) \end{bmatrix} \\
 S_3(\alpha_1) &= (-1)^{m_2} e^{i\alpha_1} \begin{bmatrix} \cos(\alpha_1) & \cdot & \cdot & -i \sin(\alpha_1) \\ \cdot & 1 & \cdot & \cdot \\ \cdot & \cdot & 1 & \cdot \\ -i \sin(\alpha_1) & \cdot & \cdot & \cos(\alpha_1) \end{bmatrix} \\
 S_4(\alpha_1) &= (-1)^{m_2} e^{i\alpha_1} \begin{bmatrix} 1 & \cdot & \cdot & \cdot \\ \cdot & \cos(\alpha_3) & -i \sin(\alpha_3) & \cdot \\ \cdot & -i \sin(\alpha_3) & \cos(\alpha_3) & \cdot \\ \cdot & \cdot & \cdot & 1 \end{bmatrix}
 \end{aligned} \tag{5.18}$$

For coupling two modes of the same waveguide, we use long-period waveguide gratings to couple directly between them without the intermediary of a cladding mode. In our implementation, these gratings have a grating period of $291.905 \mu\text{m}$ and a slight tilt angle of $\theta = 3.26^\circ$ to lift the anti-symmetry that leads to zero coupling at $\theta = 0.0$. Using a similar method to that used to find Equation (2.56) only for co-propagating waveguide

modes, we find:

$$\begin{aligned}
 S_5(\phi_{\lambda,0}) &= \begin{bmatrix} \cos(\phi_{\lambda,0}) & \cdot & \sin(\phi_{\lambda,0}) & \cdot \\ \cdot & 1 & \cdot & \cdot \\ -\sin(\phi_{\lambda,0}) & \cdot & \cos(\phi_{\lambda,0}) & \cdot \\ \cdot & \cdot & \cdot & 1 \end{bmatrix} \\
 S_6(\phi_{\lambda,1}) &= \begin{bmatrix} 1 & \cdot & \cdot & \cdot \\ \cdot & \cos(\phi_{\lambda,1}) & \cdot & \sin(\phi_{\lambda,1}) \\ \cdot & \cdot & 1 & \cdot \\ \cdot & -\sin(\phi_{\lambda,1}) & \cdot & \cos(\phi_{\lambda,1}) \end{bmatrix}
 \end{aligned} \tag{5.19}$$

We can also phase-shift any of the four modes by coupling them to a cladding mode with a long-period grating. For example, for phase-shifting mode 0 of waveguide 0:

$$\mathbf{S} = \begin{bmatrix} e^{i\varphi} & \cdot & \cdot & \cdot \\ \cdot & 1 & \cdot & \cdot \\ \cdot & \cdot & 1 & \cdot \\ \cdot & \cdot & \cdot & 1 \end{bmatrix} \tag{5.20}$$

As noted at the end of Section 4.2.1, by phase-shifting the coupling coefficients of one of the gratings that form a single coupler, we can achieve unitary 2×2 matrices that we can use in lieu of phase shifts.

This gives us the 6 basis transfer matrices which, together with phase-shifts, we can use to build up to any 4×4 unitary matrix as outlined in Section 2.3.4. By concatenating them together in a chip, we are able to guide light through a sequence of transformations and achieve any arbitrary 4×4 unitary matrix.

5.7 Conclusion

By using two two-mode waveguides in a single ridge structure, we are able to build a mode division multiplexer. We show also that, by superimposing gratings together, we are able to achieve any arbitrary power splitting in our device. We also show that we can build up to any 4×4 unitary matrix. This we achieve by concatenating individual MDMs together with long-period gratings coupling between the two core-modes of the same waveguide.

However, our device does have a weakness in that it is difficult to launch into the higher-order core mode of a waveguide without loss. This motivates the work in Chapter 6 in which we use both directions of two single-mode waveguides to provide the four

core modes and therefore four input and output ports rather than using unidirectional propagation with two two-mode waveguides.

Chapter 6

Four-port device based on counter-propagating waveguide modes

6.1 Introduction

As we mentioned in Chapter 5, the problem with the device in that chapter is that it is difficult to couple light into higher-order modes of multimode waveguides without loss. In this Chapter, we explore a possible solution to this and another scheme to couple four modes to each other. Instead of using two two-mode waveguides to build up a system with four different modes, we use two single-mode waveguides and exploit both propagation directions, in order to have four modes in the system in total.

Similarly to the devices in Chapters 4 and 5, we inscribe both waveguides parallel in an integrated photonics chip consisting of a single ridge structure with multiple modes. We again call the waveguide modes core modes and the modes of the ridge structure cladding modes. We use tilted gratings of both long-period and short-period as defined in Section 2.1.2 in order to couple light between the core modes and a single cladding mode.

Recall that the short-period gratings couple between counter-propagating modes whereas the long-period gratings couple between co-propagating modes. The gratings may be super-imposed, with one grating of each type in each waveguide leading to a maximum of four gratings. Similarly to Chapters 4 and 5, we carefully select the grating period to achieve longitudinal phase-matching and the tilt angle to maximise the coupling coefficient. This tilt angle is close to that predicted for mirror reflection from the core mode into the cladding mode (see Section 2.1.2.1). For short-period gratings, it would be much smaller than 45° whereas for long-period gratings, it would be greater than

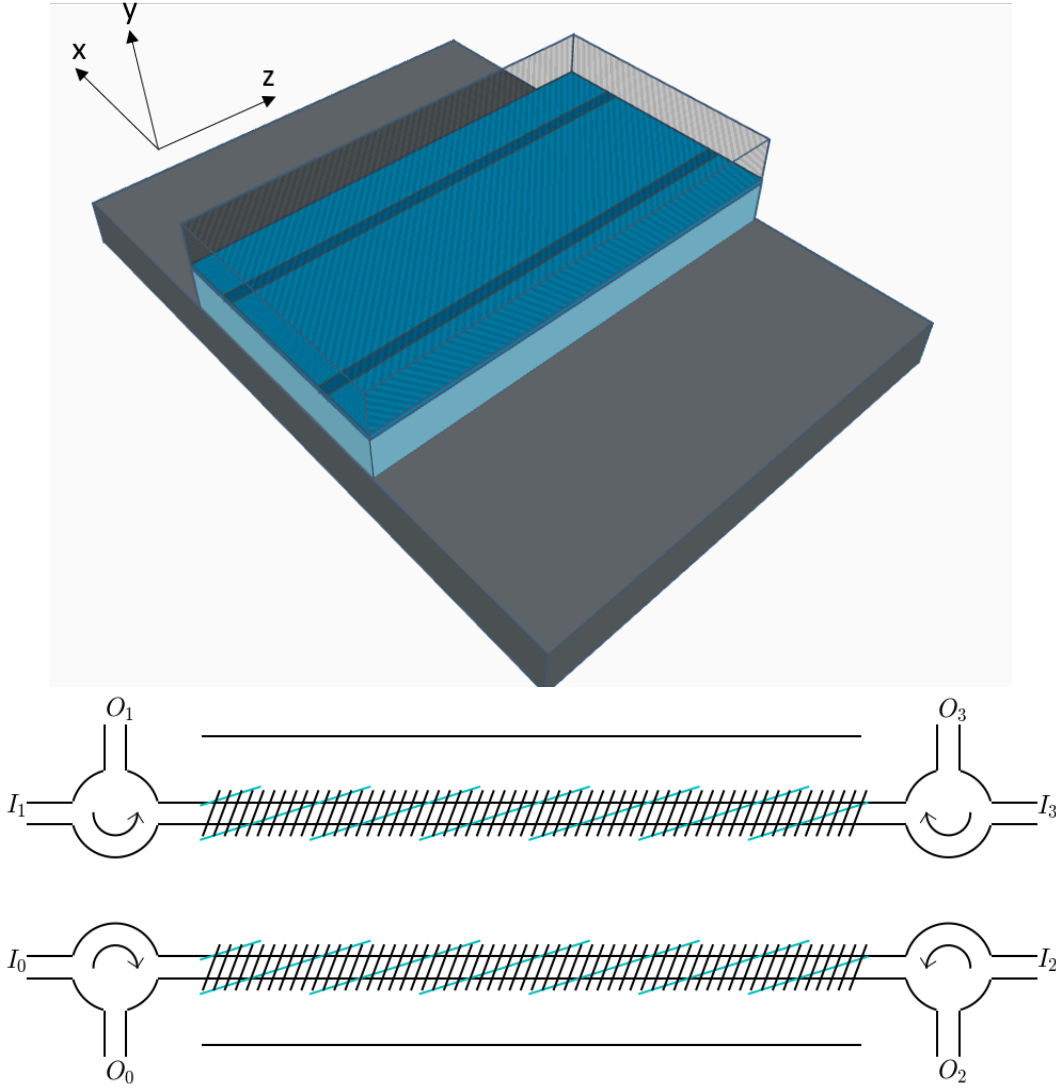


Figure 6.1: (a) 3D Schematic of integrated four-port waveguide coupler exploiting both directions of propagation (superimposed gratings and circulators not shown). (b) Cross section and ray diagram of coupler inside the core layer including superimposed long- and short-period gratings and the circulators. We colour the tilted long- and short-period gratings in cyan and black respectively and label the inputs and outputs of the circulators.

45° . In our simulations, in the case of the long-period gratings, we choose a tilt angle slightly different from that leading to maximum coupling coefficient. This detuning of the tilt angle is such that the two types of grating have the same coupling coefficient with the same index contrast.

By connecting circulators at the ends of each waveguide, as seen in Figure 6.1, we are able to separate the light going into and coming out of the device and therefore have a device with four input ports and four output ports. We can express the field amplitudes at the outputs in terms of those at the inputs using a transfer matrix as we discuss in the background (Section 2.2.3) and have used in Sections 4.2.1 and 5.6 in the previous

two chapters. We describe in this chapter a set of simple individual transformations that can be implemented in this platform using one or two gratings. We show that, by concatenating them together, we can build up to any transfer matrix that is both symmetric and unitary.

We label the inputs and outputs as shown on Figure 6.1 and define waveguide 0 as the one with the inputs and outputs I_0, I_2, O_0, O_2 and waveguide 1 as the one with I_1, I_3, O_1, O_3 .

6.2 Numerical device model

We simulate this device by calculating the light propagation in multiple modes. We must first derive a set of differential equations we can use to simulate the system numerically. As with Chapters 4 and 5, we start from the coupled-mode equations, Equation (2.40). We can expand the Equation (2.40) to involve gratings of two different grating periods:

$$\begin{aligned} \frac{dA_m(z)}{dz} = & -\frac{1}{2} \sum_n \left[\left(e^{i[(\beta_m - \beta_n + K_g)z + \phi_{mn}]} - e^{i[(\beta_m - \beta_n - K_g)z - \phi_{mn}]} \right) A_n(z) c_{mn} \right. \\ & \left. + \left(e^{i[(\beta_m - \beta_n + K_h)z + \phi_{mn,h}]} - e^{i[(\beta_m - \beta_n - K_h)z - \phi_{mn,h}]} \right) A_n(z) c_{mn,h} \right] \end{aligned} \quad (6.1)$$

Here the symbols mean the same as in Equation (2.40). K_h refers to the grating period of the long-period grating and $c_{mn,h}$ and $\phi_{mn,h}$ refer to its coupling coefficient amplitudes and phases when coupling together modes m and n . We consider the problem with the forward and backward propagating directions of two core modes and one cladding mode, leading to six modes in total. We label the forward propagating core modes as 0 and 1 and the backward propagating core modes as 2 and 3. And we label the forward and backward propagating cladding modes as 4 and 5 respectively. We assume that the two core modes in each direction are identical. The propagation constants of the modes are $\beta_0 = \beta_1 = -\beta_2 = -\beta_3$ and $\beta_4 = -\beta_5$.

Each of the core modes are coupled with each of the cladding modes using superimposed gratings of two different grating periods. We end up with six coupled mode equations:

$$\begin{aligned}
\frac{dA_0(z)}{dz} &= \frac{1}{2} \left(e^{i[-\Delta K z - \phi_{05}]} A_5(z) c_{05} + e^{i[\Delta K_h z - \phi_{04h}]} A_4(z) c_{04h} \right) \\
\frac{dA_1(z)}{dz} &= \frac{1}{2} \left(e^{i[-\Delta K z - \phi_{15}]} A_5(z) c_{15} + e^{i[\Delta K_h z - \phi_{14h}]} A_4(z) c_{14h} \right) \\
\frac{dA_2(z)}{dz} &= \frac{1}{2} \left(-e^{i[-\Delta K_h z + \phi_{25h}]} A_5(z) c_{25h} - e^{i[\Delta K z + \phi_{24}]} A_4(z) c_{24} \right) \\
\frac{dA_3(z)}{dz} &= \frac{1}{2} \left(-e^{i[-\Delta K_h z + \phi_{35h}]} A_5(z) c_{35h} - e^{i[\Delta K z + \phi_{34}]} A_4(z) c_{34} \right) \\
\frac{dA_4(z)}{dz} &= \frac{1}{2} \left(-e^{i[-\Delta K_h z + \phi_{40h}]} A_0(z) c_{40h} - e^{i[-\Delta K_h z + \phi_{41h}]} A_1(z) c_{41h} \right. \\
&\quad \left. + e^{i[-\Delta K z - \phi_{42}]} A_2(z) c_{42} + e^{i[-\Delta K z - \phi_{43}]} A_3(z) c_{43} \right) \\
\frac{dA_5(z)}{dz} &= -\frac{1}{2} \left(e^{i[\Delta K z + \phi_{50}]} A_0(z) c_{50} + e^{i[\Delta K z + \phi_{51}]} A_1(z) c_{51} \right. \\
&\quad \left. - e^{i[\Delta K_h z - \phi_{52h}]} A_2(z) c_{52h} - e^{i[\Delta K_h z - \phi_{53h}]} A_3(z) c_{53h} \right)
\end{aligned} \tag{6.2}$$

Here, we define the phase mismatch for the short-period and long-period gratings as $\Delta K = -\beta_0 - \beta_4 + K_g$ and $\Delta K_h = \beta_0 - \beta_4 - K_h$. In the above equation, we use the rotating wave approximation to neglect non-resonant terms as explained in Section 2.2.2.1.

Now, we have up to only four gratings. Many of the above relations are mediated by the same grating. This is because the same grating that couples light between modes in one direction, must also couple between the same modes propagating in the opposite direction. We can thus equate the coupling coefficient amplitudes as:

$$\begin{aligned}
c_{05} = c_{50} &= c_{24} = c_{42} = c_0 \\
c_{15} = c_{51} &= c_{34} = c_{43} = d_0 \\
c_{25h} = c_{52h} &= c_{04h} = c_{40h} = e_0 \\
c_{35h} = c_{53h} &= c_{14h} = c_{41h} = f_0
\end{aligned} \tag{6.3}$$

and the phases:

$$\begin{aligned}
\phi_{05} - \pi = \phi_{50} &= \phi_{24} = \phi_{42} - \pi = \phi_c \\
\phi_{15} - \pi = \phi_{51} &= \phi_{34} = \phi_{43} - \pi = \phi_d \\
\phi_{25h} - \pi = \phi_{52h} - \pi &= \phi_{04h} = \phi_{40h} = \phi_e \\
\phi_{35h} - \pi = \phi_{53h} - \pi &= \phi_{14h} = \phi_{41h} = \phi_f
\end{aligned} \tag{6.4}$$

Now, let us define the complex coupling coefficients as $c = c_0 e^{-i\phi_c}$ and their complex conjugate as $\bar{c} = c_0 e^{+i\phi_c}$. We can then make the following substitutions:

$$\begin{aligned}
 R_0(z) &= A_0(z) \\
 R_1(z) &= A_1(z) \\
 R_2(z) &= e^{-i(\Delta K - \Delta K_h)} A_2(z) \\
 R_3(z) &= e^{-i(\Delta K - \Delta K_h)} A_3(z) \\
 R_4(z) &= e^{i\Delta K_h z} A_4(z) \\
 R_5(z) &= e^{-i\Delta K z} A_5(z)
 \end{aligned} \tag{6.5}$$

We can simplify even further to:

$$\begin{aligned}
 \frac{dR_0(z)}{dz} &= \frac{1}{2} (-R_5(z)c + R_4(z)e) \\
 \frac{dR_1(z)}{dz} &= \frac{1}{2} (-R_5(z)d + R_4(z)f) \\
 \frac{dR_2(z)}{dz} &= \frac{1}{2} (R_5(z)\bar{e} - R_4(z)\bar{c}) - i(\Delta K - \Delta K_h)R_2(z) \\
 \frac{dR_3(z)}{dz} &= \frac{1}{2} (R_5(z)\bar{f} - R_4(z)\bar{d}) - i(\Delta K - \Delta K_h)R_3(z) \\
 \frac{dR_4(z)}{dz} &= -\frac{1}{2} \left(R_0(z)\bar{e} + R_1(z)\bar{f} \right. \\
 &\quad \left. + R_2(z)c + R_3(z)d \right) + i\Delta K_h R_4(z) \\
 \frac{dR_5(z)}{dz} &= -\frac{1}{2} \left(R_0(z)\bar{c} + R_1(z)\bar{d} \right. \\
 &\quad \left. + R_2(z)e + R_3(z)f \right) - i\Delta K R_5(z)
 \end{aligned} \tag{6.6}$$

which we can express in matrix form:

$$\frac{d\underline{R}(z)}{dz} = M \underline{R}(z) \tag{6.7}$$

where:

$$\underline{R}(z) = \begin{bmatrix} R_0(z) \\ R_1(z) \\ R_2(z) \\ R_3(z) \\ R_4(z) \\ R_5(z) \end{bmatrix} \tag{6.8}$$

and

$$M = \begin{bmatrix} \cdot & \cdot & \cdot & \cdot & \frac{1}{2}e & -\frac{1}{2}c \\ \cdot & \cdot & \cdot & \cdot & \frac{1}{2}f & -\frac{1}{2}d \\ \cdot & \cdot & -i(\Delta K - \Delta K_h) & \cdot & -\frac{1}{2}\bar{c} & \frac{1}{2}\bar{e} \\ \cdot & \cdot & \cdot & -i(\Delta K - \Delta K_h) & -\frac{1}{2}\bar{d} & \frac{1}{2}\bar{f} \\ -\frac{1}{2}\bar{e} & -\frac{1}{2}\bar{f} & -\frac{1}{2}c & -\frac{1}{2}d & i\Delta K_h & \cdot \\ -\frac{1}{2}\bar{c} & -\frac{1}{2}\bar{d} & -\frac{1}{2}e & -\frac{1}{2}f & \cdot & -i\Delta K \end{bmatrix} \quad (6.9)$$

Just as for Equation (2.46) in Section 2.2.2.1 and as used in Sections 4.2.1 and 5.5.1, this can be computed as an eigenvalue/eigenvector equation. Its solution for non-zero phase mismatch is too complicated for us to derive analytically. This means that, in order to calculate the behaviour of the device away from the phase matching condition, so as to, for example, find the device bandwidth or its fabrication tolerances, it is better to use a numerical method.

6.3 Analytical solutions to the six-mode problem and transfer matrices

In this section, we show how we can solve Equation (6.7) analytically for $\Delta K = \Delta K_h = 0$. In the first subsection (Section 6.3.1), we begin by finding a general analytical solution to the six-mode problem. Then, in Section 6.3.2, we derive a set of transfer matrices relating the outputs to the inputs that we can construct in this platform. We show how to transform these matrices into matrices that express the inputs and outputs at one end of the device to the other in Section 6.3.3. We demonstrate how we can achieve a general 4×4 symmetric unitary matrix in Section 6.3.4 with examples in Section 6.3.5. Finally, we show that by superimposing long- and short-period gratings we can achieve complex transformations in a single short device and we give the example of a compact Walsh-Hadamard transform.

6.3.1 General analytical solution to the six-mode problem

For $\Delta K = 0$, $\Delta K_h = 0$, we are able to simplify the matrix in Equation (6.7) as

$$M = \begin{bmatrix} \cdot & \cdot & \cdot & \cdot & -\frac{1}{2}\bar{e} & -\frac{1}{2}c \\ \cdot & \cdot & \cdot & \cdot & -\frac{1}{2}\bar{f} & -\frac{1}{2}d \\ \cdot & \cdot & \cdot & \cdot & -\frac{1}{2}\bar{c} & -\frac{1}{2}e \\ \cdot & \cdot & \cdot & \cdot & -\frac{1}{2}\bar{d} & -\frac{1}{2}f \\ \frac{1}{2}e & \frac{1}{2}f & -\frac{1}{2}c & -\frac{1}{2}d & \cdot & \cdot \\ -\frac{1}{2}\bar{c} & -\frac{1}{2}\bar{d} & \frac{1}{2}\bar{e} & -\frac{1}{2}\bar{f} & \cdot & \cdot \end{bmatrix} \quad (6.10)$$

In which we have substituted $e \rightarrow -\bar{e}$, $f \rightarrow -\bar{f}$.

The eigenvalues are given by:

$$\lambda_0 = \lambda_1 = 0 \quad -\lambda_2 = -\lambda_3 = \lambda_4 = \lambda_5 = \gamma \quad (6.11)$$

The eigenvectors are given by:

$$\mu_0 = \begin{bmatrix} |f|^2 - |d|^2 \\ d\bar{c} - e\bar{f} \\ \cdot \\ f\bar{c} - e\bar{d} \\ \cdot \\ \cdot \end{bmatrix} \quad \mu_1 = \begin{bmatrix} f\bar{e} - c\bar{d} \\ |c|^2 - |e|^2 \\ f\bar{c} - e\bar{d} \\ \cdot \\ \cdot \\ \cdot \end{bmatrix} \quad \mu_2 = \begin{bmatrix} c \\ d \\ e \\ f \\ \cdot \\ 2\gamma \end{bmatrix} \quad \mu_3 = \begin{bmatrix} \bar{e} \\ \bar{f} \\ \bar{c} \\ \bar{d} \\ 2\gamma \\ \cdot \end{bmatrix} \quad \mu_4 = \begin{bmatrix} c \\ d \\ e \\ f \\ \cdot \\ -2\gamma \end{bmatrix} \quad \mu_5 = \begin{bmatrix} \bar{e} \\ \bar{f} \\ \bar{c} \\ \bar{d} \\ -2\gamma \\ \cdot \end{bmatrix} \quad (6.12)$$

Here γ is equal to:

$$\gamma = \frac{1}{2} \sqrt{|c|^2 + |d|^2 - |e|^2 - |f|^2} \quad (6.13)$$

So, the general solution for the propagation of mode amplitudes is given by:

$$\begin{bmatrix} R_0(z) \\ R_1(z) \\ R_2(z) \\ R_3(z) \\ R_4(z) \\ R_5(z) \end{bmatrix} = p_0 \begin{bmatrix} |f|^2 - |d|^2 \\ d\bar{c} - e\bar{f} \\ \cdot \\ f\bar{c} - e\bar{d} \\ \cdot \\ \cdot \end{bmatrix} + p_1 \begin{bmatrix} f\bar{e} - c\bar{d} \\ |c|^2 - |e|^2 \\ f\bar{c} - e\bar{d} \\ \cdot \\ \cdot \\ \cdot \end{bmatrix} + q_0 \begin{bmatrix} c \\ d \\ e \\ f \\ \cdot \\ 2\gamma \end{bmatrix} e^{-\gamma z} + q_1 \begin{bmatrix} \bar{e} \\ \bar{f} \\ \bar{c} \\ \bar{d} \\ 2\gamma \\ \cdot \end{bmatrix} e^{-\gamma z} \\ + q_2 \begin{bmatrix} c \\ d \\ e \\ f \\ \cdot \\ -2\gamma \end{bmatrix} e^{\gamma z} + q_3 \begin{bmatrix} \bar{e} \\ \bar{f} \\ \bar{c} \\ \bar{d} \\ -2\gamma \\ \cdot \end{bmatrix} e^{\gamma z} \quad (6.14)$$

Now, we have two regimes of behaviour. Recall from Section 2.2.2.1 that short-period gratings, that couple together counter-propagating modes, have a photonic bandgap, but the long-period gratings coupling together co-propagating modes do not have a bandgap. For $|c|^2 + |d|^2 - |e|^2 - |f|^2 > 0$, the effect of the short-period gratings dominates over that of the long-period gratings. All of the eigenvalues are real, so we have an exponentially decaying solution which, similarly to Section 2.2.2.1 and Chapters 4 and 5, defines a photonic bandgap. For $|c|^2 + |d|^2 - |e|^2 - |f|^2 < 0$, all of the eigenvalues are imaginary which leads to the fields inside the device oscillating with frequency defined by $\gamma = i\Omega$. Some solutions exist for which $|c|^2 + |d|^2 - |e|^2 - |f|^2 = 0$. In these cases, the eigenvalues are degenerate and are all zero. We find that in these cases, the electric fields vary

linearly with z and we need a device of length that approaches infinity in order achieve complete power transfer between waveguide modes.

In our device, we do not launch any light into the cladding mode at either end, this means that we set the following boundary conditions:

$$\begin{aligned} R_4(0) &= 0 \\ R_5(L) &= 0 \end{aligned} \quad (6.15)$$

We also want device parameters in which no light escapes via the cladding mode at the opposite end. This means that the amplitude of the cladding modes at both ends of the device must be zero. Therefore, what we want is the special case where:

$$\begin{aligned} R_4(L) &= 0 \\ R_5(0) &= 0 \end{aligned} \quad (6.16)$$

This requires that:

$$\gamma L = in\pi \quad (6.17)$$

which means that the solution must be oscillatory and so the device must have a set of coupling coefficients for the gratings such that the effect of the long-period gratings dominates, i.e. $|c|^2 + |d|^2 - |e|^2 - |f|^2 < 0$.

We get the following relations between some of the coefficients of the general solution (Equation 6.14):

$$\begin{aligned} q_3 &= q_1 = q_+ \\ q_2 &= q_0 = q_- \end{aligned} \quad (6.18)$$

This means we can greatly simplify the solution for the propagation of mode amplitudes to:

$$\begin{bmatrix} R_0(z) \\ R_1(z) \\ R_2(z) \\ R_3(z) \end{bmatrix} = p_0 \begin{bmatrix} |f|^2 - |d|^2 \\ d\bar{c} - e\bar{f} \\ \cdot \\ f\bar{c} - e\bar{d} \end{bmatrix} + p_1 \begin{bmatrix} f\bar{e} - c\bar{d} \\ |c|^2 - |e|^2 \\ f\bar{c} - e\bar{d} \\ \cdot \end{bmatrix} + 2 \left(q_- \begin{bmatrix} c \\ d \\ e \\ f \end{bmatrix} + q_+ \begin{bmatrix} \bar{e} \\ \bar{f} \\ \bar{c} \\ \bar{d} \end{bmatrix} \right) \cos(\Omega z) \quad (6.19)$$

for the core modes and:

$$\begin{aligned} R_4(z) &= -2iq_- \Omega \sin(\Omega z) \\ R_5(z) &= -2iq_+ \Omega \sin(\Omega z) \end{aligned} \quad (6.20)$$

for the cladding modes.

However, in order to achieve a transfer matrix other than the identity matrix, we also need the output field amplitudes to be different from the input field amplitudes. This requires that n is an odd number, so a half-integer number of oscillations of our system with $\cos(\Omega L) = \cos(n\pi) = -1$. With n even, that is with a full-integer number of oscillations, the system returns to its original state.

So our solution at the boundaries becomes:

$$\begin{bmatrix} R_0(0) \\ R_1(0) \\ R_2(0) \\ R_3(0) \end{bmatrix} = p_0 \begin{bmatrix} |f|^2 - |d|^2 \\ d\bar{c} - e\bar{f} \\ \cdot \\ f\bar{c} - e\bar{d} \end{bmatrix} + p_1 \begin{bmatrix} f\bar{e} - c\bar{d} \\ |c|^2 - |e|^2 \\ f\bar{c} - e\bar{d} \\ \cdot \end{bmatrix} + 2 \left(q_- \begin{bmatrix} c \\ d \\ e \\ f \end{bmatrix} + q_+ \begin{bmatrix} \bar{e} \\ \bar{f} \\ \bar{c} \\ \bar{d} \end{bmatrix} \right) \quad (6.21)$$

And:

$$\begin{bmatrix} R_0(L) \\ R_1(L) \\ R_2(L) \\ R_3(L) \end{bmatrix} = p_0 \begin{bmatrix} |f|^2 - |d|^2 \\ d\bar{c} - e\bar{f} \\ \cdot \\ f\bar{c} - e\bar{d} \end{bmatrix} + p_1 \begin{bmatrix} f\bar{e} - c\bar{d} \\ |c|^2 - |e|^2 \\ f\bar{c} - e\bar{d} \\ \cdot \end{bmatrix} - 2 \left(q_- \begin{bmatrix} c \\ d \\ e \\ f \end{bmatrix} + q_+ \begin{bmatrix} \bar{e} \\ \bar{f} \\ \bar{c} \\ \bar{d} \end{bmatrix} \right) \quad (6.22)$$

Unlike for the general solution expressing the mode propagation of the devices in Chapters 4 and 5 (Section 5.5.1), we cannot find analytically a set of expressions that relates any desired symmetric unitary matrix to the coupling coefficients of the gratings required to achieve them. This is the result of terms in Equations (6.21) and (6.22) consisting of a product of two coupling coefficients.

In order to achieve any desired symmetric unitary matrix, we must instead decompose our matrix into a set of individual "fundamental" transfer matrices that can easily be achieved on this platform. To derive the "fundamental" matrices we need analytically, we consider the simplest devices we can fabricate, consisting of either one or two gratings, and vary only one parameter consisting of a combination of the coupling coefficients of the two gratings (or of the coupling coefficient and length of one grating). Using the methods outlined in the above paragraph will be the focus of the following subsections from Section 6.3.2 to 6.3.5.

We also found some more complex transformations using superimposed gratings, such as those in Section 6.3.6 including the Walsh-Hadamard transform. We show how we can numerically achieve a range of transformations using superimposed gratings in Section 6.7.

If we are only interested in finding the coupling coefficients to achieve a particular power splitting ratio, however, this can be achieved numerically by using Newton's method or the basin-hopping method to minimize the difference between the output powers of the device and the target output power. Again, this method is not entirely reliable and not

all splitting ratios can be converged to using this method, either due to a limitation in the numerical methods used or because no solution achieving these splitting ratios exist.

6.3.2 Analytical derivations of "fundamental" transformations with transfer matrices

Here, we show how we can achieve four different "fundamental" transfer matrices which can be concatenated together to achieve any arbitrary symmetric unitary matrix on this platform. The transfer matrices we seek to achieve relate the outputs of the device to the inputs, which we define as:

$$\begin{bmatrix} I_0 \\ I_1 \\ I_2 \\ I_3 \end{bmatrix} = \begin{bmatrix} R_0(0) \\ R_1(0) \\ R_2(L) \\ R_3(L) \end{bmatrix}, \quad \begin{bmatrix} O_0 \\ O_1 \\ O_2 \\ O_3 \end{bmatrix} = \begin{bmatrix} R_2(0) \\ R_3(0) \\ R_0(L) \\ R_1(L) \end{bmatrix} \quad (6.23)$$

such that the transfer matrices S are given by:

$$\begin{bmatrix} O_0 \\ O_1 \\ O_2 \\ O_3 \end{bmatrix} = S \begin{bmatrix} I_0 \\ I_1 \\ I_2 \\ I_3 \end{bmatrix} \quad (6.24)$$

6.3.2.1 Standard Bragg gratings in either waveguides

The first two transfer matrices simply consist of a standard Bragg grating coupling the forward and backward propagating modes in either waveguide. Expanding from Equation (2.56) in Section (2.2.3), we get the following two equations for each grating (for $\phi = 0$):

$$\begin{bmatrix} R_0(L) \\ R_1(L) \\ R_2(0) \\ R_3(0) \end{bmatrix} = \begin{bmatrix} \text{sech}(\phi_{\kappa,0}) & \cdot & -\tanh(\phi_{\kappa,0}) & \cdot \\ \cdot & 1 & \cdot & \cdot \\ \tanh(\phi_{\kappa,0}) & \cdot & \text{sech}(\phi_{\kappa,0}) & \cdot \\ \cdot & \cdot & \cdot & 1 \end{bmatrix} \begin{bmatrix} R_0(0) \\ R_1(0) \\ R_2(L) \\ R_3(L) \end{bmatrix} \quad (6.25)$$

for a grating in waveguide 0 and

$$\begin{bmatrix} R_0(L) \\ R_1(L) \\ R_2(0) \\ R_3(0) \end{bmatrix} = \begin{bmatrix} 1 & \cdot & \cdot & \cdot \\ \cdot & \text{sech}(\phi_{\kappa,1}) & \cdot & -\tanh(\phi_{\kappa,1}) \\ \cdot & \cdot & 1 & \cdot \\ \cdot & \tanh(\phi_{\kappa,1}) & \cdot & \text{sech}(\phi_{\kappa,1}) \end{bmatrix} \begin{bmatrix} R_0(0) \\ R_1(0) \\ R_2(L) \\ R_3(L) \end{bmatrix} \quad (6.26)$$

for a grating in waveguide 1. Here $\phi_{\kappa,0} = \frac{|g_0|L}{2}$ and $\phi_{\kappa,1} = \frac{|g_1|L}{2}$ where g_0 and g_1 are the coupling coefficients of a standard Bragg grating in waveguides 0 and 1 respectively.

In the form given by Equation (6.24) they are given by:

$$\begin{aligned} S_0 &= \begin{bmatrix} -\tanh(\phi_{\kappa,0}) & \cdot & \text{sech}(\phi_{\kappa,0}) & \cdot \\ \cdot & \cdot & \cdot & 1 \\ \text{sech}(\phi_{\kappa,0}) & \cdot & \tanh(\phi_{\kappa,0}) & \cdot \\ \cdot & 1 & \cdot & \cdot \end{bmatrix} \\ S_1 &= \begin{bmatrix} \cdot & \cdot & 1 & \cdot \\ \cdot & -\tanh(\phi_{\kappa,1}) & \cdot & \text{sech}(\phi_{\kappa,1}) \\ 1 & \cdot & \cdot & \cdot \\ \cdot & \text{sech}(\phi_{\kappa,1}) & \cdot & \tanh(\phi_{\kappa,1}) \end{bmatrix} \end{aligned} \quad (6.27)$$

6.3.2.2 Long-period waveguide-to-waveguide couplers

The third transfer matrix we achieve uses a long-period waveguide-to-waveguide coupler previously introduced in [37, 38, 39] and mentioned in the background Section 2.3.1.3. The only difference is that we provide a wide tilt angle ($> 45^\circ$) to the gratings in order to maximise the coupling to high-order cladding modes. This does not change the maths however. We set $c = 0, d = 0, f = -a\epsilon$ which represents two long-period waveguide gratings, one in each waveguide with an arbitrary ratio of coupling coefficients. However, simply inserting this condition into Equations (6.21) and (6.22) causes us to have an incomplete set of equations as two of the equations are degenerate.

To solve this problem, we need to find the eigenvalues of the matrix in Equation (6.10) from scratch. This leads to the following transfer matrix:

$$\begin{bmatrix} R_0(L) \\ R_1(L) \\ R_2(0) \\ R_3(0) \end{bmatrix} = \frac{1}{1 + |\alpha|^2} \begin{bmatrix} -1 + |\alpha|^2 & 2\bar{\alpha} & \cdot & \cdot \\ 2\alpha & 1 - |\alpha|^2 & \cdot & \cdot \\ \cdot & \cdot & -1 + |\alpha|^2 & 2\alpha \\ \cdot & \cdot & 2\bar{\alpha} & 1 - |\alpha|^2 \end{bmatrix} \begin{bmatrix} R_0(0) \\ R_1(0) \\ R_2(L) \\ R_3(L) \end{bmatrix} \quad (6.28)$$

We can then make the following substitution: $\cos(\phi) = \frac{1 - |\alpha|^2}{1 + |\alpha|^2}$ and $\sin(\phi) = \frac{2|\alpha|}{1 + |\alpha|^2}$ so the above transfer matrix becomes:

$$\begin{bmatrix} R_0(L) \\ R_1(L) \\ R_2(0) \\ R_3(0) \end{bmatrix} = \begin{bmatrix} -\cos(\phi) & \sin(\phi) & \cdot & \cdot \\ \sin(\phi) & \cos(\phi) & \cdot & \cdot \\ \cdot & \cdot & -\cos(\phi) & \sin(\phi) \\ \cdot & \cdot & \sin(\phi) & \cos(\phi) \end{bmatrix} \begin{bmatrix} R_0(0) \\ R_1(0) \\ R_2(L) \\ R_3(L) \end{bmatrix} \quad (6.29)$$

which in the form defined in Equation (6.24) is given by:

$$S_2 = \begin{bmatrix} \cdot & \cdot & -\cos(\phi) & \sin(\phi) \\ \cdot & \cdot & \sin(\phi) & \cos(\phi) \\ -\cos(\phi) & \sin(\phi) & \cdot & \cdot \\ \sin(\phi) & \cos(\phi) & \cdot & \cdot \end{bmatrix} \quad (6.30)$$

6.3.2.3 Counter-directional coupler based on a long- and a short-period grating in different waveguides

The next transfer matrix is implemented through the use of gratings of two different types in the two waveguides. In one waveguide, we have a long-period grating coupling light from that waveguide to a co-propagating cladding mode. And in the other waveguide, we have a short-period grating coupling light from that cladding mode into the core mode of that waveguide travelling in the counter-propagating direction. As such, the device couples some of the light from one waveguide into the other waveguide in the counter-propagating direction.

For this, we set $d = \epsilon e$, $c = 0$ and $f = 0$. This time, we are able to substitute these conditions directly into Equations (6.21) and (6.22). They become:

$$\begin{bmatrix} R_0(0) \\ R_1(0) \\ R_2(0) \\ R_3(0) \end{bmatrix} = p_0 \begin{bmatrix} -\epsilon^2 |e|^2 \\ \cdot \\ \cdot \\ -\epsilon |e|^2 \end{bmatrix} + p_1 \begin{bmatrix} \cdot \\ -|e|^2 \\ -\epsilon |e|^2 \\ \cdot \end{bmatrix} + 2 \left(q_- \begin{bmatrix} \cdot \\ \epsilon e \\ e \\ \cdot \end{bmatrix} + q_+ \begin{bmatrix} \bar{e} \\ \cdot \\ \cdot \\ \epsilon \bar{e} \end{bmatrix} \right) \quad (6.31)$$

And:

$$\begin{bmatrix} R_0(L) \\ R_1(L) \\ R_2(L) \\ R_3(L) \end{bmatrix} = p_0 \begin{bmatrix} -\epsilon^2 |e|^2 \\ \cdot \\ \cdot \\ -\epsilon |e|^2 \end{bmatrix} + p_1 \begin{bmatrix} \cdot \\ -|e|^2 \\ -\epsilon |e|^2 \\ \cdot \end{bmatrix} - 2 \left(q_- \begin{bmatrix} \cdot \\ \epsilon e \\ e \\ \cdot \end{bmatrix} + q_+ \begin{bmatrix} \bar{e} \\ \cdot \\ \cdot \\ \epsilon \bar{e} \end{bmatrix} \right) \quad (6.32)$$

which leads to:

$$\begin{bmatrix} R_0(L) \\ R_1(L) \\ R_2(0) \\ R_3(0) \end{bmatrix} = \frac{1}{1 + \epsilon^2} \begin{bmatrix} \epsilon^2 - 1 & \cdot & \cdot & 2\epsilon \\ \cdot & -\epsilon^2 + 1 & 2\epsilon & \cdot \\ \cdot & 2\epsilon & \epsilon^2 - 1 & \cdot \\ 2\epsilon & \cdot & \cdot & -\epsilon^2 + 1 \end{bmatrix} \begin{bmatrix} R_0(0) \\ R_1(0) \\ R_2(L) \\ R_3(L) \end{bmatrix} \quad (6.33)$$

Again, we can simplify this equation by setting $\epsilon = \tanh(\phi/2)$. Re-arranging into the form given by Equation (6.24) gets us the following transfer matrix:

$$S_3 = \begin{bmatrix} \cdot & \tanh(\phi) & -\operatorname{sech}(\phi) & \cdot \\ \tanh(\phi) & \cdot & \cdot & \operatorname{sech}(\phi) \\ -\operatorname{sech}(\phi) & \cdot & \cdot & \tanh(\phi) \\ \cdot & \operatorname{sech}(\phi) & \tanh(\phi) & \cdot \end{bmatrix} \quad (6.34)$$

6.3.2.4 Phase shifts

Phase shifts are very easy to implement in this platform and to express in matrix form. They are implemented by changing the path length along one of the waveguides. One way to implement this would be to physically increase the length of the waveguide by making it go along a curved path. However, this is difficult to write and would lead to loss as the light propagates round the bend [127]. A better idea is to keep the waveguide in a straight line but to change the propagation constant of the fundamental mode along it. This can be achieved either by changing the waveguide index contrast or the waveguide width. It can also be achieved dynamically with a heater. As such, this would lead to a phase difference accumulating between the waveguides that can be expressed as a phase shift along a waveguide. Since we use both directions of propagation in our device, it is impossible to have a different phase shift along the two directions of a waveguide. We thus achieve the following two matrices for the phase shifts for the two waveguides respectively:

$$\begin{aligned} \Phi_0(\varphi_0) &= \begin{bmatrix} \cdot & \cdot & \exp(i\varphi_0) & \cdot \\ \cdot & \cdot & \cdot & 1 \\ \exp(i\varphi_0) & \cdot & \cdot & \cdot \\ \cdot & 1 & \cdot & \cdot \end{bmatrix} \\ \Phi_1(\varphi_1) &= \begin{bmatrix} \cdot & \cdot & 1 & \cdot \\ \cdot & \cdot & \cdot & \exp(i\varphi_1) \\ 1 & \cdot & \cdot & \cdot \\ \cdot & \exp(i\varphi_1) & \cdot & \cdot \end{bmatrix} \end{aligned} \quad (6.35)$$

These phase-shifts can also be achieved by using a long-period grating to couple to a cladding mode with a slight phase-mismatch and having an integer number of half-oscillations.

6.3.3 Transforming the matrices into unidirectional form

Now, we need to find a way in which we can use the building blocks we derive in Section 6.3.2 in order to achieve as wide a range of matrices as possible. The form of the matrices

given by Equation (6.24) is not suitable for achieving this goal. In order to achieve this goal, we must re-express these matrices such that they give the mode amplitudes on one side of the device in terms of the other, such that:

$$\begin{bmatrix} O_2 \\ O_3 \\ I_2 \\ I_3 \end{bmatrix} = \Sigma \begin{bmatrix} I_0 \\ I_1 \\ O_0 \\ O_1 \end{bmatrix} \quad (6.36)$$

Throughout this thesis, we will call this form of matrix the unidirectional form.

To do that we must re-express the matrices S in terms of four 2×2 submatrices:

$$S = \begin{bmatrix} S_{00} & S_{01} \\ S_{10} & S_{11} \end{bmatrix} \quad (6.37)$$

which allows us to find the submatrices of Σ as:

$$\Sigma = \begin{bmatrix} S_{10} - S_{11}S_{01}^{-1}S_{00} & S_{11}S_{01}^{-1} \\ -S_{01}^{-1}S_{00} & S_{01}^{-1} \end{bmatrix} \quad (6.38)$$

which means that any transformation matrix that is physically realisable on our platform, that is expressed as Equation (6.24), can be re-expressed in unidirectional form provided that the submatrix S_{01} is not singular. If the submatrix S_{01} is singular, then the length of the device represented by this transfer matrix is infinite and can not be precisely physically realized (though such devices can be realized approximately, as we will show in future sections). The matrix in Σ form becomes undefined and the behaviour on the right hand side of the device becomes independent of the left hand side.

Taking Equations (6.27) that represent standard Bragg gratings and expressing them in this form gets us:

$$\begin{aligned} \Sigma_0(\phi) &= \begin{bmatrix} \cosh(\phi) & \cdot & \sinh(\phi) & \cdot \\ \cdot & 1 & \cdot & \cdot \\ \sinh(\phi) & \cdot & \cosh(\phi) & \cdot \\ \cdot & \cdot & \cdot & 1 \end{bmatrix}, \\ \Sigma_1(\phi) &= \begin{bmatrix} 1 & \cdot & \cdot & \cdot \\ \cdot & \cosh(\phi) & \cdot & \sinh(\phi) \\ \cdot & \cdot & 1 & \cdot \\ \cdot & \sinh(\phi) & \cdot & \cosh(\phi) \end{bmatrix} \end{aligned} \quad (6.39)$$

In the case of long-period waveguide grating couplers, they only couple unidirectionally in the first place so expressing them in unidirectional form only leads to the swapping

of rows in Equation (6.30):

$$\Sigma_2(\phi) = \begin{bmatrix} -\cos(\phi) & \sin(\phi) & \cdot & \cdot \\ \sin(\phi) & \cos(\phi) & \cdot & \cdot \\ \cdot & \cdot & -\cos(\phi) & \sin(\phi) \\ \cdot & \cdot & \sin(\phi) & \cos(\phi) \end{bmatrix} \quad (6.40)$$

In the case of a coupler consisting of both a long and a short grating, we re-express Equation (6.34) as:

$$\Sigma_3(\phi) = \begin{bmatrix} -\cosh(\phi) & \cdot & \cdot & \sinh(\phi) \\ \cdot & \cosh(\phi) & -\sinh(\phi) & \cdot \\ \cdot & \sinh(\phi) & -\cosh(\phi) & \cdot \\ -\sinh(\phi) & \cdot & \cdot & \cosh(\phi) \end{bmatrix} \quad (6.41)$$

We find that there is no way of multiplying any two or three of the above matrices together that would achieve the third or fourth matrix which implies that they are mutually independent.

The phase shifts in unidirectional form are very easy to derive from Equation (6.35) and are:

$$\begin{aligned} \Theta_0(\varphi) &= \begin{bmatrix} \exp(i\varphi) & \cdot & \cdot & \cdot \\ \cdot & 1 & \cdot & \cdot \\ \cdot & \cdot & \exp(-i\varphi) & \cdot \\ \cdot & \cdot & \cdot & 1 \end{bmatrix} \\ \Theta_1(\varphi) &= \begin{bmatrix} 1 & \cdot & \cdot & \cdot \\ \cdot & \exp(i\varphi) & \cdot & \cdot \\ \cdot & \cdot & 1 & \cdot \\ \cdot & \cdot & \cdot & \exp(-i\varphi) \end{bmatrix}. \end{aligned} \quad (6.42)$$

In Section 2.3.2.2 we mentioned that the having a π phase shift in the centre of a standard back-reflecting Bragg grating with equal lengths and coupling coefficients on both sides of the grating leads to transparency at the phase-matching condition. We confirm this analytically on our platform with:

$$\begin{aligned} \Sigma_0(\phi) \cdot \Theta(\pi) \cdot \Sigma_0(\phi) &= I \\ \Sigma_1(\phi) \cdot \Theta(\pi) \cdot \Sigma_1(\phi) &= I \end{aligned} \quad (6.43)$$

We mention in Section 6.3.1 that when coupling via cladding modes, a full number of oscillations in the system leads to input light returning to its original state. Since the device operates with a half-integer number of oscillations, doubling the length should

lead to transparency. We confirm this analytically with:

$$\begin{aligned}\Sigma_2(\phi) \cdot \Sigma_2(\phi) &= I \\ \Sigma_3(\phi) \cdot \Sigma_3(\phi) &= I\end{aligned}\tag{6.44}$$

In the case of Σ_2 and Σ_3 , phase-shifting the gratings relative to each other has the same effect as providing phase-shifts before and after the operation. Generalising the derivations in Section 6.3.2 for complex coupling coefficients, which is equivalent to phase-shifting the grating, confirms this.

6.3.4 Construction of an arbitrary symmetric unitary matrix

In this section, we show that we can achieve any arbitrary matrix relating the output ports to the input ports on this platform that is both unitary and symmetric. That is, any matrix that satisfies the following conditions:

$$\begin{aligned}S^\dagger \cdot S &= I \\ S &= S^T\end{aligned}\tag{6.45}$$

where T and \dagger are the conjugate and the conjugate transpose, respectively. By inserting the above equations into Equation (6.38), we can achieve any unidirectional matrix of the form:

$$\Sigma = \begin{bmatrix} P & \bar{Q} \\ Q & \bar{P} \end{bmatrix}\tag{6.46}$$

subject to the following independent conditions which represent conservation of energy for matrices written in unidirectional form: $\sigma_{0,0}^2 + \sigma_{1,0}^2 - \sigma_{2,0}^2 - \sigma_{3,0}^2 = 1$, $\sigma_{0,1}^2 + \sigma_{1,1}^2 - \sigma_{2,1}^2 - \sigma_{3,1}^2 = 1$, $\bar{\sigma}_{0,0}\sigma_{0,1} + \bar{\sigma}_{1,0}\sigma_{1,1} - \bar{\sigma}_{2,0}\sigma_{2,1} - \bar{\sigma}_{3,0}\sigma_{3,1} = 0$ and $\sigma_{0,0}\sigma_{2,1} + \sigma_{1,0}\sigma_{3,1} - \sigma_{2,0}\sigma_{0,1} - \sigma_{3,0}\sigma_{1,1} = 0$, with $\sigma_{m,n}$ referring to the individual elements of Σ .

We see in Equation (6.46) that the matrix Σ has only 8 distinct elements and is subject to 4 additional independent conditions. We make the assumption that, for a real-valued matrix, the number of degrees of freedom is equal to the number of distinct elements minus the number of additional independent conditions. This means that the subset of matrices Σ with only real-valued elements has 4 degrees of freedom. Recall also that we find 4 "fundamental" transformations in Equations (6.39), (6.40) and (6.41) and that these transformations are independent of one another. This means that they provide 4 degrees of freedom, which is equal to the number of degrees of freedom in the real-valued subset of Σ which means that by multiplying Equations (6.39), (6.40) and (6.41) together, we can build any unitary matrix defined by Equation (6.46). To generalise for complex values, we use the phase-shift matrices in Equation (6.42). Notice that, here, the equivalent entries along the diagonal (that are two columns and two rows apart) are the complex conjugate of each other. Using such phase-shifts at any point during the

construction will lead to a global phase being applied to column m where $m = 1$ or 2 in Equation (6.46) and the complex conjugate of that phase being applied to column $m + 2$.

Now, we will present a recipe for building any arbitrary symmetric unitary matrix. As we have shown above, any such matrix can be expressed in the form of Equation (6.46) provided that the submatrix S_{01} is not singular. We take advantage of the fact that making one of the values zero in one half of the matrix Σ must also make the corresponding value zero in the other half. First, let us consider real valued matrices.

Starting off with an arbitrary matrix in the form given by Equation (6.47):

$$\Sigma = \begin{bmatrix} * & * & * & * \\ * & * & * & * \\ * & * & * & * \\ * & * & * & * \end{bmatrix} \quad (6.47)$$

, with $*$ representing arbitrary matrix elements, we apply a long-period grating waveguide-to-waveguide coupler represented by a transfer matrix, $\Sigma_2(\phi)$ in Equation (6.40), with the correct value of ϕ . Therefore with the correct ratio of coupling coefficients and the correct length, we multiply $\Sigma_2(\phi)$ with Σ in Equation (6.47) to set the entry 10 to zero. For a real-valued matrix, this is always possible by using $\phi = \tan^{-1}(\frac{\sigma_{10}}{\sigma_{00}})$. This necessarily also sets the entry 32 to zero. So the matrix becomes:

$$\Sigma_2(\phi_\alpha) \cdot \Sigma = \begin{bmatrix} * & * & * & * \\ \cdot & * & * & * \\ * & * & * & * \\ * & * & \cdot & * \end{bmatrix} \quad (6.48)$$

where “ \cdot ” indicates a zero matrix element.

Applying a standard Bragg grating in waveguide 0 to set the entry 20 to zero, which also sets element 02 to zero and without changing any of the zeros in Equation (6.48), gets us:

$$\Sigma_0(\phi_{\gamma,0}) \cdot \Sigma_2(\phi_\alpha) \cdot \Sigma = \begin{bmatrix} * & * & \cdot & * \\ \cdot & * & * & * \\ \cdot & * & * & * \\ * & * & \cdot & * \end{bmatrix} \quad (6.49)$$

Then, we apply the coupler we introduced in Section 6.3.2.3 with a long-period grating in one waveguide and a short-period grating in the other. Using it to set the entry at 30 to zero not only does the same to 12, but as all entries in column 0 are zero except for 00 then so must all the remaining entries in row 0 be zero. This is because of the conservation of energy equations just after Equation 6.46. This, in turn, requires the

entries 21 and 23 to also be zero. Applying that coupler therefore leads us to:

$$\Sigma_3(\phi_\epsilon) \cdot \Sigma_0(\phi_{\gamma,0}) \cdot \Sigma_2(\phi_\alpha) \cdot \Sigma = \begin{bmatrix} * & \cdot & \cdot & \cdot \\ \cdot & * & \cdot & * \\ \cdot & \cdot & * & \cdot \\ \cdot & * & \cdot & * \end{bmatrix} \quad (6.50)$$

This means, that in the end, we only need to apply the remaining block which is a grating in waveguide 1, chosen to set the entry at 31 to be zero, which also sets the entry at 13 to zero, again this does not change the elements previously set to zero:

$$\Sigma_1(\phi_{\gamma,1}) \cdot \Sigma_3(\phi_\epsilon) \cdot \Sigma_0(\phi_{\gamma,0}) \cdot \Sigma_2(\phi_\alpha) \cdot \Sigma = \begin{bmatrix} * & \cdot & \cdot & \cdot \\ \cdot & * & \cdot & \cdot \\ \cdot & \cdot & * & \cdot \\ \cdot & \cdot & \cdot & * \end{bmatrix} \quad (6.51)$$

where each element of the diagonal matrix is ± 1 and also $\sigma_{00} = \sigma_{22}$ and $\sigma_{11} = \sigma_{33}$. This means that, as needed, we may also add a π phase shift in either waveguide to achieve the identity matrix:

$$\Theta_0(m_0\pi) \cdot \Theta_1(m_0\pi) \Sigma_1(\phi_{\gamma,1}) \cdot \Sigma_3(\phi_\epsilon) \cdot \Sigma_0(\phi_{\gamma,0}) \cdot \Sigma_2(\phi_\alpha) \cdot \Sigma = \begin{bmatrix} 1 & \cdot & \cdot & \cdot \\ \cdot & 1 & \cdot & \cdot \\ \cdot & \cdot & 1 & \cdot \\ \cdot & \cdot & \cdot & 1 \end{bmatrix} \quad (6.52)$$

$$\text{where } m_{0,1} = \begin{cases} 0 \\ 1 \end{cases}.$$

Of course, for a symmetric unitary matrix with complex entries, we are also required to use the phase shifts in Equations (6.42) as needed between each of the steps described above. We can also build up to a wider set of matrices if we use phase shifts on the outside of the circulators.

We show on Figure 6.2 a diagram of the concatenated device showing all the fundamental blocks that are used to implement an arbitrary symmetric unitary matrix. The blocks and phase shifts between them are concatenated in the reverse order to that in which the individual transformations are multiplied together. By carefully selecting the parameters of the gratings and of the phase-shifts between the couplers, it is possible to implement any transformation on the light inputs that is both symmetric and unitary. As explained in Section 6.1, circulators are connected to each waveguide end facet in order to separate the input and output fields.

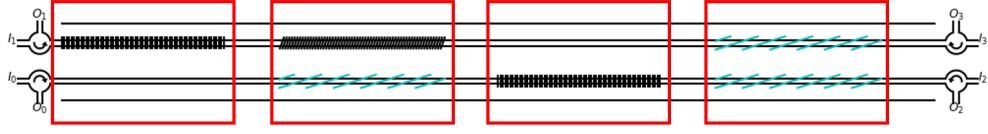


Figure 6.2: Concatenated coupler used to implement any arbitrary symmetric unitary matrix. In the red boxes we show the individual couplers that make up the device including, from left to right, a standard Bragg grating in waveguide 1, a counter-directional coupler of the sort we introduced in Section 6.3.2.3 consisting of a long-period grating in waveguide 0 and a short-period grating in waveguide 1, a standard Bragg grating in waveguide 0 and a long-period waveguide-to-waveguide coupler. The phase shifts between the individual blocks are not shown. Shown also are the circulators connected to the waveguide that are used to separate the input and output light fields.

6.3.5 Symmetric unitary matrix examples

We give the example of how to construct a Walsh-Hadamard gate in the form:

$$H = \frac{1}{2} \begin{bmatrix} 1 & 1 & 1 & 1 \\ 1 & -1 & 1 & -1 \\ 1 & 1 & -1 & -1 \\ 1 & -1 & -1 & 1 \end{bmatrix} \quad (6.53)$$

In unidirectional form, this is given by:

$$\Sigma_H = \begin{bmatrix} 1 & 1 & 1 & \cdot \\ 1 & -1 & \cdot & 1 \\ 1 & \cdot & 1 & 1 \\ \cdot & 1 & 1 & -1 \end{bmatrix} \quad (6.54)$$

By applying the following transformations to it, we arrive at the identity matrix:

$$\begin{aligned} & \Theta_1(\pi) \cdot \Sigma_1(\operatorname{arctanh}(\frac{1}{2})) \cdot \Sigma_3(-\operatorname{arctanh}(\frac{1}{\sqrt{3}})) \\ & \cdot \Sigma_0(-\operatorname{arctanh}(\frac{1}{2})) \cdot \Sigma_2(-\frac{\pi}{4}) \cdot \Sigma_W = I \end{aligned} \quad (6.55)$$

where I is the 4×4 identity matrix.

This means that the Walsh-Hadamard matrix can be constructed using:

$$\begin{aligned} \Sigma_H = & \Sigma_2\left(-\frac{\pi}{4}\right) \cdot \Sigma_0\left(\operatorname{arctanh}\left(\frac{1}{2}\right)\right) \cdot \Sigma_3\left(-\operatorname{arctanh}\left(\frac{1}{\sqrt{3}}\right)\right) \\ & \cdot \Sigma_1\left(-\operatorname{arctanh}\left(\frac{1}{2}\right)\right) \cdot \Theta_1(\pi) \end{aligned} \quad (6.56)$$

Similarly, the 4×4 Quantum Fourier Transform (QFT):

$$QFT = \frac{1}{2} \begin{bmatrix} 1 & 1 & 1 & 1 \\ 1 & i & -1 & -i \\ 1 & 1 & 1 & -1 \\ 1 & -i & -1 & i \end{bmatrix} \quad (6.57)$$

is expressed in unidirectional form as:

$$\Sigma_{QFT} = \begin{bmatrix} 1+i & 1-i & -i & 1+i \\ -1+i & 1-i & 1-i & i \\ i & 1-i & 1-i & 1+i \\ 1+i & -i & -1-i & 1+i \end{bmatrix} \quad (6.58)$$

so following the steps above gets us the following decomposition for the QFT:

$$\begin{aligned} \Sigma_{QFT} = & \Theta_0\left(\frac{\pi}{4}\right) \cdot \Theta_1\left(-\frac{\pi}{4}\right) \cdot \Sigma_2\left(\frac{\pi}{4}\right) \cdot \Theta_0\left(\frac{\arctan(\frac{1}{3})}{2}\right) \\ & \cdot \Sigma_0\left(-\operatorname{arctanh}\left(\frac{\sqrt{10}}{4}\right)\right) \cdot \Theta_0\left(\frac{-\arctan(\frac{1}{3})}{2}\right) \\ & \cdot \Theta_1\left(-\frac{\pi}{4}\right) \cdot \Sigma_3\left(\operatorname{arctanh}\left(\frac{1}{\sqrt{3}}\right)\right) \cdot \Theta_1\left(-\frac{\pi}{4}\right) \\ & \cdot \Sigma_1\left(\operatorname{arctanh}\left(\frac{1}{2}\right)\right) \cdot \Theta_1\left(\frac{\pi}{4}\right) \end{aligned} \quad (6.59)$$

Creating a C-NOT transform, using the waveguide the light is in as control, that is, a C-NOT transform in this form:

$$S_0(\phi \rightarrow \infty) = \begin{bmatrix} -1 & 0 & 0 & 0 \\ 0 & 0 & 0 & 1 \\ 0 & 0 & 1 & 0 \\ 0 & 1 & 0 & 0 \end{bmatrix} \quad (6.60)$$

is achieved by using a standard-Bragg grating (in this case in waveguide 0) and tending its length towards infinity. The -1 at the entry s_{00} can be corrected by using a π phase shift at either the input port I_0 or the output port O_0 on the outside of the circulators, or alternately, by having a $\frac{\pi}{2}$ phase-shift within the chip just before that end facet that would apply in both directions, that is, as a $\frac{\pi}{2}$ phase-shift to both the input and the output port. As such, it becomes:

$$S_{\text{CNOT},1} = \begin{bmatrix} 1 & 0 & 0 & 0 \\ 0 & 0 & 0 & 1 \\ 0 & 0 & 1 & 0 \\ 0 & 1 & 0 & 0 \end{bmatrix} \quad (6.61)$$

So far in this thesis, we have been assuming classical light fields. However, here we will briefly consider how our implementation of a C-NOT transform can be used as a quantum gate. As mentioned in the background Section 2.3.4, a photon can be in a superposition of different states which makes it ideal for encoding qubits. To use this implementation as a C-NOT gate for quantum computing, we must encode both qubits in a single photon. This means that our photon is, in general, in a superposition of four different states. This is rather than two if it were used to encode a single qubit. The photon is in a superposition of both waveguides and in a superposition of both propagation directions. As a result, when the photon enters or exits the device, it is in general in a superposition of states. When detectors are placed at the device outputs, the photon has different probabilities of being detected at the various outputs. In this implementation of a C-NOT gate, we encode the qubits in the following way. The first qubit is encoded in whether the photon enters/exits the device on the left or the right hand side whereas the other is encoded in which waveguide the photon is in. As such, qubit $|00\rangle$ represents a photon entering at input I_0 or exiting at output O_0 , $|0q\rangle$ is at port I_1 or O_1 , $|10\rangle$ is at I_2 or O_2 and $|11\rangle$ represents a photon inputted at I_3 or detected at O_3 . We show a 3D schematic of this implementation in Figure 6.3 alongside a truth table, which represents the states of the output qubits in terms of the input qubits. On the surface this looks like a far simpler implementation compared of a C-NOT gate compared to those discussed in Section 2.3.4 in the background and also has the advantage that it functions 100% of the time. However, if it were to be used in quantum information processing, the fact that both qubits are encoded in a single photon would make it very difficult to scale as encoding additional qubits into a single photon would require an exponentially larger number of waveguides. The method used by mainstream implementations (Section 2.3.4 and [58]) encodes each qubit in individual photons which requires only a linearly increasing number of waveguides.

Another C-NOT transform can be achieved of the form:

$$S_{CNOT,2} = \begin{bmatrix} 1 & 0 & 0 & 0 \\ 0 & 1 & 0 & 0 \\ 0 & 0 & 0 & 1 \\ 0 & 0 & 1 & 0 \end{bmatrix} \quad (6.62)$$

which can be achieved by using the combination of a short- and long-period grating-based waveguide coupler and a standard Bragg grating in sequence, each with 100% coupling to the target mode, that is, with:

$$\Sigma_3(\phi \rightarrow \infty) \cdot \Sigma_0(\phi \rightarrow \infty) \quad (6.63)$$

as well as a π phase shift at the input I_0 or output O_0 as before. Note that in both the C-NOT transforms we achieve above, the matrix S_{01} is singular which means that no transformation to a unidirectional matrix Σ is possible. These transforms cannot be

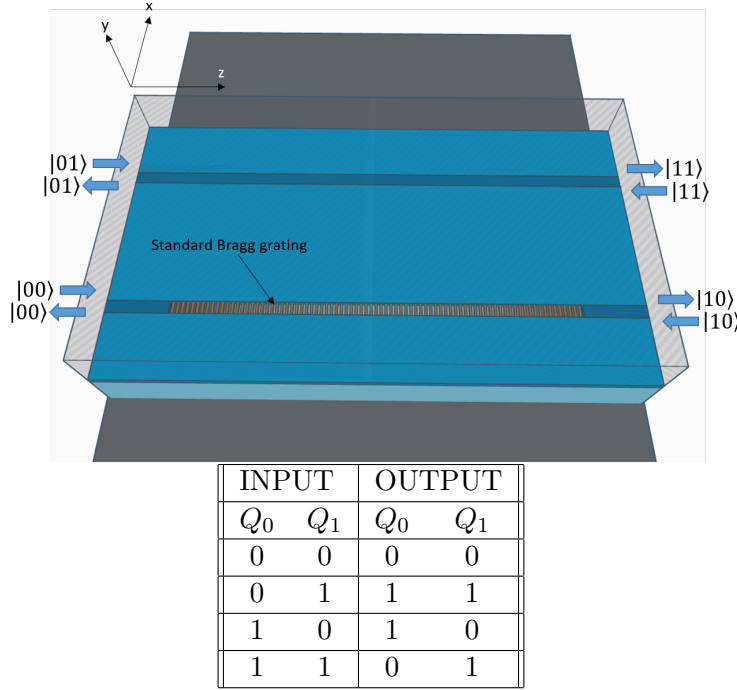


Figure 6.3: (top) 3D schematic of a CNOT gate implemented on this platform (external phase shift not shown). It consists of a single Bragg grating in waveguide 0. (bottom) Truth table of the quantum gate. The two left columns represents the states of the qubits at input whereas the right column represents their states at the outputs. Qubit Q_0 is implemented in at which side of the device the photon is inputted or detected, qubit Q_1 is implemented in which waveguide the photon is.

achieved exactly as they require that the length of the gratings tends towards infinity. However, with finite length they can be achieved with negligible transmission through the gratings. This also leads to a negligible but non-zero determinant of S_{01} which means that the matrix in unidirectional form actually exists, albeit with very large entries.

6.3.6 Compact transformations using superimposed gratings

Rather than having a long device made out of four different blocks with six gratings, by overlapping long- and short-period gratings, we can achieve the many of the same transformations in a single short device with only up to four, and in some cases only three, gratings. This makes these transformations a lot easier to fabricate than by concatenating "fundamental" transformations as fewer Bragg gratings would need to be written, thereby reducing the number of independent grating parameters, and because it allows the device to be shorter and therefore easier to have a constant effective refractive index of the core and cladding modes along the entire device.

However, this method has a disadvantage over the method presented in Section 6.3.4 in that there is no evidence that every symmetric unitary matrix can be achieved in

this way in a single block. Also, as mentioned at the end of Section 6.3.1, there is no reliable method for achieving a desired power splitting ratio in this compact platform. The transformation matrices that we catalogue in this subsection we have found either through chance or with an educated guess. This is of course, not a reliable method. Note also that the solutions found using this method are also not necessarily unique and multiple compact implementations of the same transformation can be found.

To demonstrate this, we present multiple examples of how a compact Walsh-Hadamard transform can be implemented using this method. We show the derivation for one of them but also the parameters for two others in order to demonstrate that there is no unique way of implementing it.

The first solution requires that all of the gratings have the same coupling coefficient amplitude with one another except for one of the long-period waveguide gratings which has a coupling coefficient three times as high. The two short-period gratings must be in phase with each other and the two long-period gratings must be out of phase (or the other way around). That means they must satisfy any of the following sets of equations:

$$\begin{aligned} c &= d = ee^{i\psi} \\ f &= -3e \end{aligned} \tag{6.64}$$

,

$$\begin{aligned} c &= d = fe^{i\psi} \\ e &= -3f \end{aligned} \tag{6.65}$$

,

$$\begin{aligned} \mp c &= \pm d = ee^{i\psi} \\ f &= -3e \end{aligned} \tag{6.66}$$

or,

$$\begin{aligned} \mp c &= \pm d = fe^{i\psi} \\ e &= -3f \end{aligned} \tag{6.67}$$

where ψ is an arbitrary phase difference between the short- and long-period gratings.

In this section, we consider the solution in Equation (6.64) with $\psi = 0$. We find, using the same method as in Section 6.3.1 the following transfer matrix:

$$S_M = \frac{1}{2} \begin{bmatrix} 1 & -1 & 1 & 1 \\ -1 & -1 & 1 & -1 \\ 1 & 1 & 1 & -1 \\ 1 & -1 & -1 & -1 \end{bmatrix}. \tag{6.68}$$

which is both unitary and symmetric.

By providing a π phase shift at the output O_3 and at the input I_1 , on the outside of the circulators, and by switching round the inputs I_0 and I_2 by re-labelling them, we can achieve a Walsh-Hadamard transform in the following form:

$$\Upsilon_{O,3} \cdot S_M \cdot \Upsilon_{I,1} \Lambda_{I,02} = \frac{1}{2} \begin{bmatrix} 1 & 1 & 1 & 1 \\ 1 & 1 & -1 & -1 \\ 1 & -1 & 1 & -1 \\ 1 & -1 & -1 & 1 \end{bmatrix} \quad (6.69)$$

where:

$$\begin{aligned} \Upsilon_{O,3} &= \begin{bmatrix} 1 & \cdot & \cdot & \cdot \\ \cdot & 1 & \cdot & \cdot \\ \cdot & \cdot & 1 & \cdot \\ \cdot & \cdot & \cdot & -1 \end{bmatrix}, & \Upsilon_{I,1} &= \begin{bmatrix} 1 & \cdot & \cdot & \cdot \\ \cdot & -1 & \cdot & \cdot \\ \cdot & \cdot & 1 & \cdot \\ \cdot & \cdot & \cdot & 1 \end{bmatrix}, \\ \Lambda_{I,02} &= \begin{bmatrix} \cdot & \cdot & 1 & \cdot \\ \cdot & 1 & \cdot & \cdot \\ 1 & \cdot & \cdot & \cdot \\ \cdot & \cdot & \cdot & 1 \end{bmatrix}. \end{aligned} \quad (6.70)$$

We more recently found another implementation of the Walsh-Hadamard gate. This time, employing only three gratings and using either of the following sets of parameters:

$$\begin{aligned} e &= 2|f|e^{i\phi_0} \\ d &= |f|e^{i\phi_1} \\ f &= |f|e^{i\phi_2} \\ c &= 0 \end{aligned} \quad (6.71)$$

or,

$$\begin{aligned} f &= 2|e|e^{i\phi_0} \\ c &= |e|e^{i\phi_1} \\ e &= |e|e^{i\phi_2} \\ d &= 0 \end{aligned} \quad (6.72)$$

We also found an implementation of the Walsh-Hadamard transform with $c = d = e = f$. However, we find that this leads to a device that is highly sensitive to grating parameters such as the grating periods. This is because, as we see from Equation (6.13), all of the eigenvalues are equal to zero and we are therefore between the oscillatory and exponential regimes of behaviour.

6.4 Long-period wide-angle tilted waveguide gratings

In this section, we numerically simulate our own implementation of the long-period waveguide grating coupler that we have investigated analytically in Section 6.3.2.2. Apart from the fact that we use a silica, rather than polymer, platform, the main difference between our implementation and the ones in [38, 39] is that we provide a wide tilt angle ($\gg 45^\circ$) in order to maximise coupling to higher order modes. Just as in general with tilted UV-written Bragg gratings, the gratings can be described as the waveguides following a sinusoidal path.

Unless otherwise stated, in this and the following sections, we use the same parameters for our device as in Section 4.5.1 for the device coupling using short-period gratings with the addition of the following parameters for the long-period gratings, a grating period of $6.2021\mu\text{m}$ and a tilt angle of 72.936° . We launch the light at input I_0 as marked in Figure 6.1. We show a contour plot of the refractive index distribution of a long-period waveguide grating in Figure 6.4.

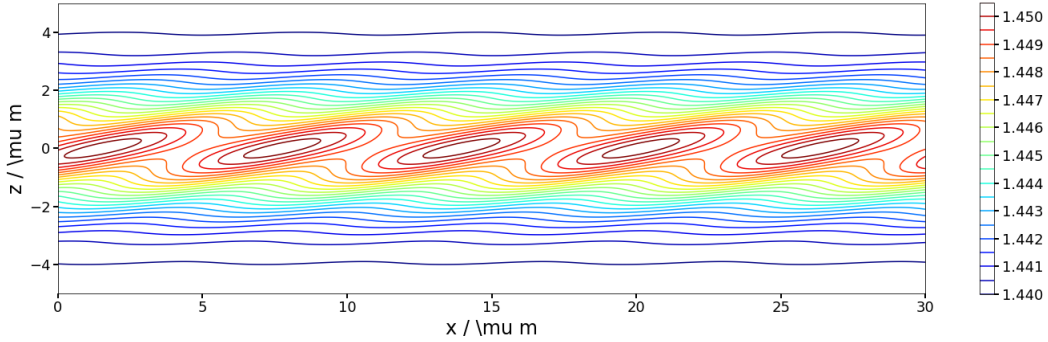


Figure 6.4: Refractive index distribution of a waveguide and long-period waveguide grating against propagating direction (horizontal) and transverse direction (vertical). Axes show position in μm . The colour bar shows refractive index levels.

This section is divided between three subsections. In Section 6.4.1, we begin by calculating the coupling coefficient of a long-period waveguide grating as we change the tilt angle for coupling to different cladding modes. In Section 6.4.2, we show numerically the behaviour of a tilted long-period waveguide grating coupling to a particular high-order cladding mode and in Section 6.4.3, we simulate our implementation of the long-period waveguide-to-waveguide coupler which is one of the "fundamental" transformations that we use in our four-port platform based on bidirectional propagation.

6.4.1 Coupling coefficients vs tilt angle

We show in Figure 6.5 how the coupling coefficient depends on the tilt angle for a selection of cladding modes. In each case the grating period is chosen so as to lead

to phase-matching. We find that for coupling to low order cladding modes, there is no need to tilt the gratings as there is already a lot of coupling for a tilt angle of 0° and little dependence of the coupling coefficient on the tilt angle until it approaches 90° . However, the greater the order of the cladding mode that is coupled to, the lower the coupling coefficient for an untilted grating and the stronger the dependence of the coupling coefficient on the tilt angle. It is easy to see that, according to the law of reflection, the tilt angle needed for the most efficient coupling is in the region of 45° - 90° . This is confirmed in Figure 6.5 where we find that the most efficient tilt angle is close to that given by the law of reflection.

As previously discussed in Section 2.2.2, coupled mode theory predicts that the coupling coefficient for a grating coupling to forward propagating modes is the same as for a grating coupling to backwards propagating modes as long as the transverse wavevector $K_t = K_g \tan(\theta)$ is the same. A long-period grating simply requires a far greater θ due to smaller K_g . We confirm that this is the case.

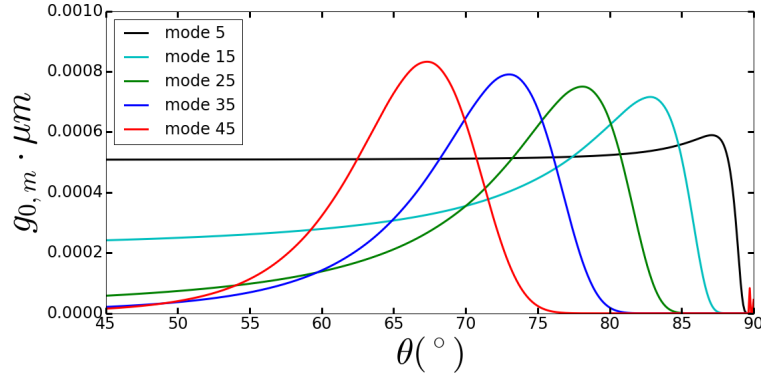


Figure 6.5: Coupling coefficient of long-period waveguide grating for a selection of cladding modes as the tilt angle is varied. Grating period is different for each cladding mode that coupled to in order that the gratings are always longitudinally phase-matched and is given by $117\mu m$ for mode 5, $32.1\mu m$ for mode 15 and $12.3\mu m$, $6.20\mu m$ and $3.56\mu m$ for modes 25, 35 and 45 respectively.

6.4.2 Coupling to cladding modes

As we show in Figure 6.6, with a long-period waveguide grating in one waveguide but not the other, we reproduce the expected result (see end of Section 2.2.2.1). We get an oscillatory solution with complete power exchange between the core mode and the cladding mode. With a slight phase mismatch, in this case caused by a detuning in the light wavelength, we see a reduction in the amplitude of the oscillations, such that there is now only partial power exchange, and an increase in the exchange frequency. Making a wavelength sweep of the results, as seen in Figure 6.7 confirms this. We see a large peak at the phase-matching condition at $\lambda_0 = 1.55\mu m$ and smaller peaks with increased frequency as the wavelength moves away from phase matching.

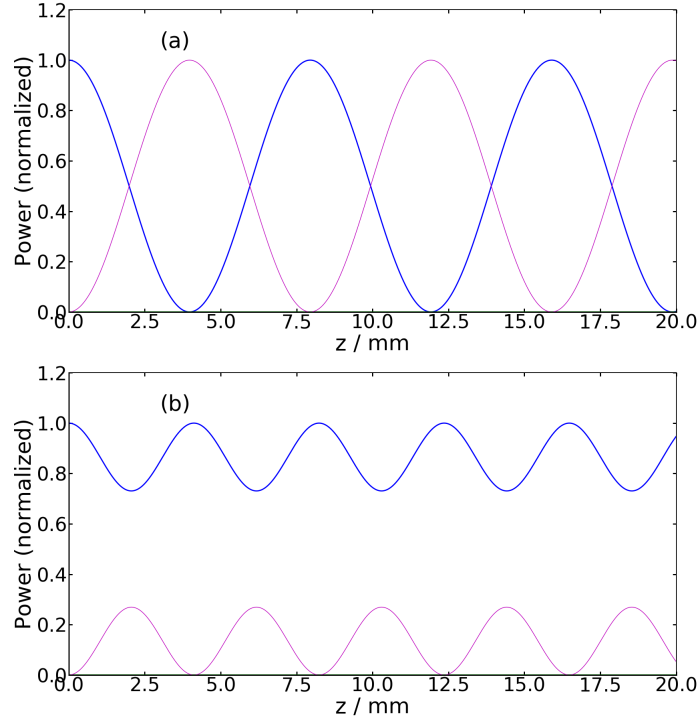


Figure 6.6: Power propagation in core mode (blue) and forward propagating cladding mode (magenta) for a device with a single long-period waveguide grating in one of the waveguides. Here, $\lambda_0 = 1.55\mu\text{m}$ (a) and $\lambda_0 = 1.548\mu\text{m}$ (b).

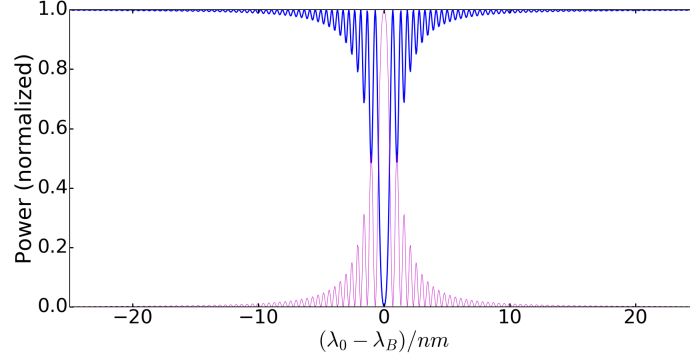


Figure 6.7: power output of core mode and cladding mode for a device with a single long-period waveguide grating in one of the waveguides.

6.4.3 Tilted long-period waveguide grating couplers

By coupling two long-period gratings via a cladding mode, we find similar results to those found in [37]. The main difference is that, unlike in [37] we use long-period gratings with a tilt angle which increases the coupling coefficient we can achieve and so significantly reduces the device length. With gratings of equal coupling coefficient, we are also able to achieve 100% power transfer between the waveguides regardless of the phase-mismatch. We report the figures with our own parameters in order to provide comparison with our device in Chapter 4. Just like the coupling using short-period gratings via backward

propagating modes (see Chapter 4), we have three oscillation frequencies for the power propagation, 2Ω , $\frac{\Delta K}{2} + \Omega$ and $\frac{\Delta K}{2} - \Omega$. Only here, $\Omega = \frac{1}{2}\Delta K^2 + |e|^2 + |f|^2$ where e and f are the coupling coefficients of the long-period gratings. As such, just like the coupler using short-period gratings, we have fast oscillations of spacial frequency 2Ω between the core modes and the cladding mode and long oscillations of frequency $\frac{\Delta K}{2} - \Omega$ between the two core modes. The former oscillations become faster as the phase mismatch is increased and the latter become slower. We plot the power propagation along the two core modes and the cladding mode for equal coupling coefficients in Figure 6.8 and a wavelength sweep of the power output of the device on Figure 6.9. We also find that the oscillations in the two core modes are identical with a π phase shift regardless of the length or phase mismatch of the device.

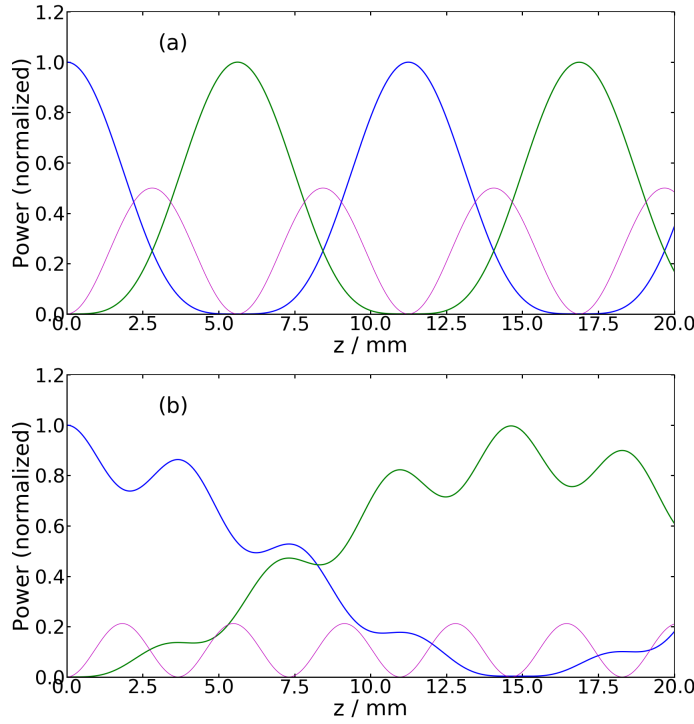


Figure 6.8: Power propagation in core modes of waveguide 0 (blue) and 1 (green) and forward propagating cladding mode (magenta) for a device with identical long-period waveguide grating in each waveguides. Here, $\lambda_0 = 1.55 \mu\text{m}$ (a) and $\lambda_0 = 1.548 \mu\text{m}$ (b).

We see in Figures 6.8 and 6.9 two main differences between this set-up and the device studied in Chapter 4. They are the lack of a bandgap at the phase-matching condition and the much broader bandwidth. The latter is because the core and cladding modes propagate in the same direction which means that, as the light wavelength is varied, the propagation constants of the core and cladding modes change in the same direction which means that the difference between them, and thus the phase mismatch, changes much more slowly. In Figure 6.9(b) we show that, for a length of 5.623 mm , we can achieve complete power transfer.

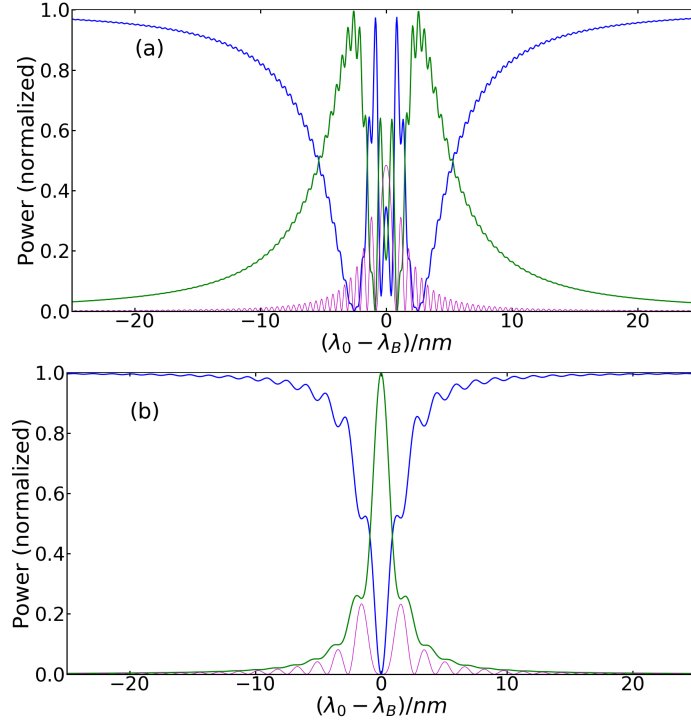


Figure 6.9: Power output of core modes (blue and green for waveguide 0 and 1, respectively) and cladding mode (magenta) for a device with identical long-period waveguide grating in each waveguide. In the two devices the length is $L = 20mm$ (a) and $L = 5.623mm$ (b).

We show also the behaviour of our device with tilted Bragg gratings of different coupling coefficients. Using Equation (6.40) in Section 6.3.2.2 we find that in order to have a 50 : 50 beam splitter we need to have one of the waveguides with a coupling coefficient that is 0.4142 times that of the other one. We plot the power propagation of such a beam splitter in Figure 6.10. We find that the core mode oscillations are no longer phase-shifted versions of one another. We also find that the power propagation through the device is now different depending on whether the waveguide with the stronger or weaker grating is pumped. Nonetheless, the propagation periods remain the same in both cases and we achieve a 50 : 50 waveguide coupler at a length of $7.346mm$ that is identical no matter which waveguide is pumped.

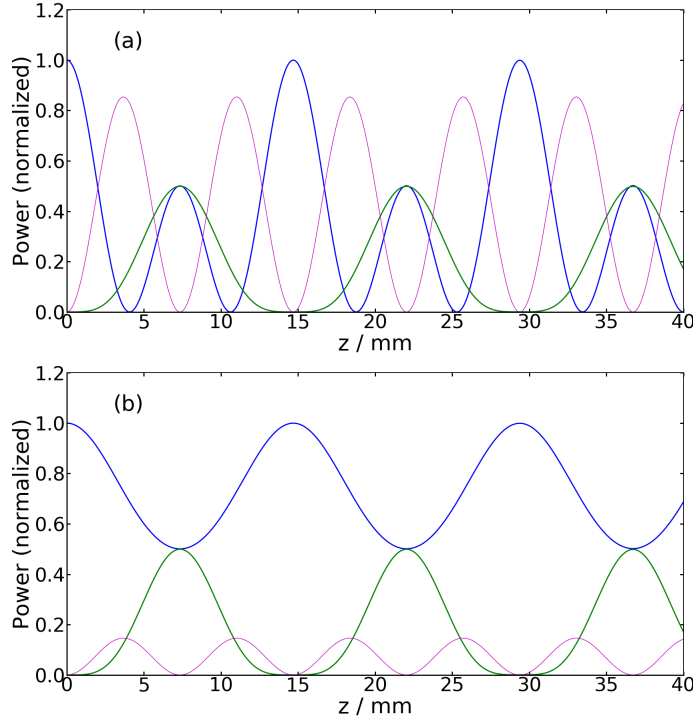


Figure 6.10: Power propagation in core mode of waveguide 0 (blue), of waveguide 1 (green), and forward propagating cladding mode (magenta) for a device with one long-period waveguide grating in each waveguides. The gratings in waveguides 0 and 1 have $\delta n_g = 0.001$ and $\delta n_g = 0.0004142$ respectively in (a) and switched round in (b). Here, $L = 40\text{mm}$.

We vary the wavelength of the light pumped through the device and show the results in Figure 6.11. We find that the full-width half-maximum bandwidth of the transferred light is identical whether the waveguide with the stronger or weaker grating is pumped and we calculate it to be 0.637nm .

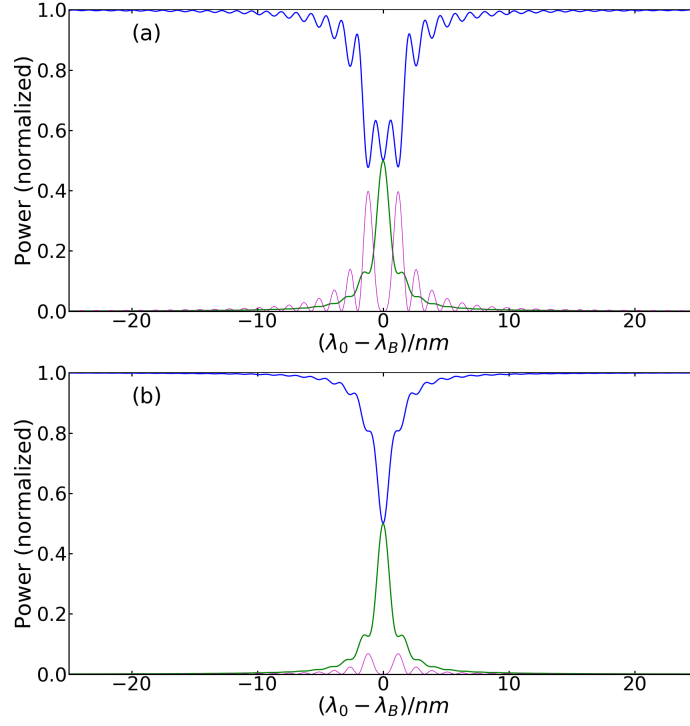


Figure 6.11: Power output of core mode and cladding mode for a device with a long-period waveguide grating in each waveguide. Here, we have the same parameters as in Figure 6.10 except with $L = 7.346mm$.

As we demonstrated in Section 6.3.2.2 we are able to achieve any coupling ratio between the two waveguides by using the correct ratio between the coupling coefficients of the gratings and the correct device length. In Figure 6.12, we plot the ratio of grating index contrast and the device length, on different axes, showing the ability to achieve any desired power splitting. We find that we are able to achieve any splitting ratio with a device length of between around $5.6mm - 8.0mm$ which is short and therefore easier to fabricate.

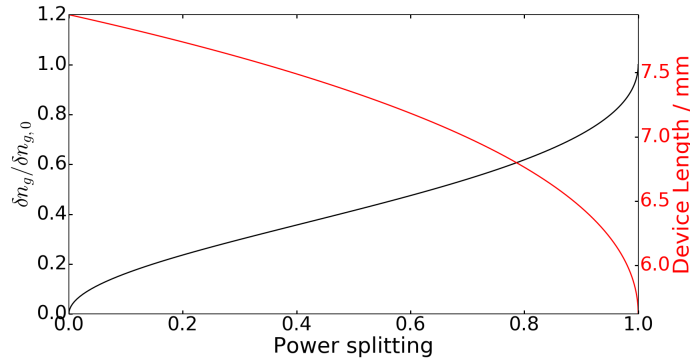


Figure 6.12: Grating index contrast ratio and device length required to achieve any desired power splitting with a long-period waveguide-to-waveguide coupler. Here, $\delta n_{g,0} = 0.001$ is the grating index contrast of one of the gratings and δn_g is the grating index contrast of the other.

6.5 Counter-directional waveguide-to-waveguide coupling using both long- and short-period waveguide gratings

In this section, we simulate numerically the new type of waveguide-to-waveguide coupler that we introduced in Section 6.3.2.3. As explained in that section, it couples light from one waveguide to the counter-propagating mode of the other. By keeping the coupling coefficient of the short-period grating smaller than that of the long-period grating so that, for zero phase-mismatch, we stay in the oscillatory regime. Using this strategy we may choose the length of the device such that part of the light is coupled to the other waveguide in the counter-propagating direction, with no light escaping via the cladding mode.

In Section 6.5.1, we begin by simulating numerically the light propagation through this device in order to confirm the analytical predictions in Section 6.3.2.3, and show how we can construct a beam splitter with this device. Then, we plot the power output against wavelength in order to find the bandwidth of the beam splitter.

A disadvantage of this device is that, as the gratings have different grating periods and tilt angles, the UV-writing system needs to be adjusted separately before fabricating each grating. This means that there are now two additional parameters for which imprecision in defining them during fabrication negatively affect the device performance. This makes the device more difficult to build. We show in Section 6.5.2 how the device output is affected by fabrication tolerances in the grating periods by varying the grating periods, and thus the phase mismatch, of the two gratings individually.

6.5.1 Propagation properties and bandwidth

6.5.1.1 Gratings of equal coupling coefficients

In Equation (6.41), we find that to have complete power transfer from one waveguide to the other propagating in the opposite direction we need to have equal coupling coefficients for the long- and short-period gratings. We can see from Equation (6.13) that for such a system the eigenvalues describing the light propagation are zero. This means, as explained in Section 6.3.1, that an infinite length is required to completely transfer light from one waveguide to the other. However, for finite lengths we are able to couple a fraction of light approaching 100%. We show on Figure 6.13 that a length of 50mm is sufficient to couple 98.97% of the light but that 1.03% leaks into the cladding mode. Although this can be fabricated, this is longer than the length of a typical device [10, 50, 118, 119, 128] and we will need to take into account chip curvature when fabricating it (see Section 2.4.3). For a typical length of 20mm (see Figure 6.13) we are

able to couple 93.88% of the light. These values do not depend on which waveguide is pumped.

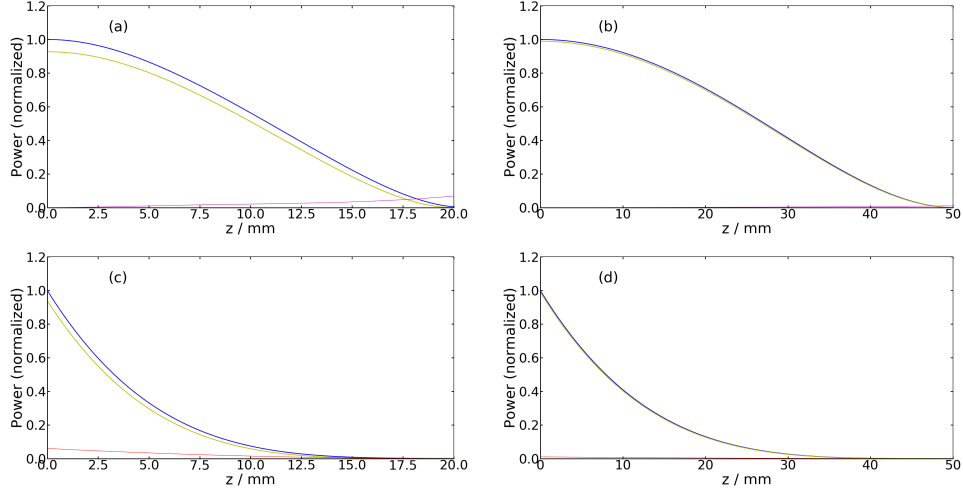


Figure 6.13: Power propagation of the forward propagating core mode of waveguide 0 (blue), the backward propagating core mode of waveguide 1 (yellow) and either the forward (magenta) or backward (red) propagating cladding mode a device with a long-period waveguide grating in one waveguide and a short-period grating in the other. With a long-period grating in waveguide 0 and a short-period grating in waveguide 1, we present the numerical results with a length of $L = 20\text{mm}$ (a) and $L = 50\text{mm}$ (b). With the gratings swapped we present the results with a length of $L = 20\text{mm}$ (c) and $L = 50\text{mm}$ (d).

As the wavelength is varied away from that required for phase-matching, the phase-mismatch for the short-period grating will vary at a different rate as that for the long-period grating. As a result, the oscillation frequencies of the device will not only be unequal but will also not be, in general, integer multiples of each other. As a result, the oscillations of the device will, in general, not be self repeating. We show an example of this device pumped away from resonance in Figure 6.14 and show in more detail in Section 6.5.2 how the phase-mismatch of the individual gratings affect the device performance.

We show the transmission curve of the device on Figure 6.15. We show that we have a single peak at the phase-matching condition which decays sharply away from phase-matching. At a certain wavelength on either side of the phase-matching condition which correspond to the same phase mismatch in both cases, the power output abruptly starts behaving in an oscillatory fashion with light propagation through the device similar to Figure 6.14. At some point when the light wavelength is sufficiently off-resonance, the phase-mismatch is too large for the short-period grating and the light essentially ignores it entirely. This leads to it behaving either as a solitary long-period grating or as a transparent device depending on which waveguide is pumped.

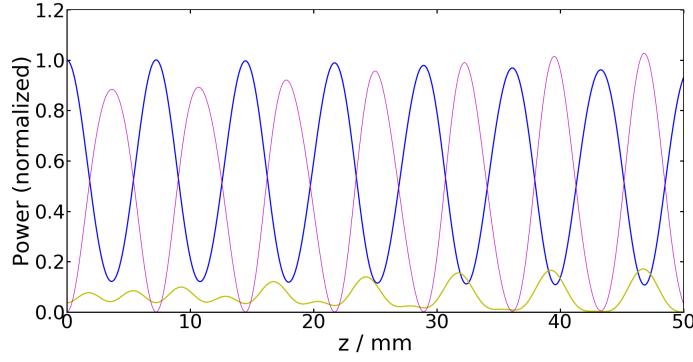


Figure 6.14: Power propagation in forward propagating core mode of waveguide 0 (blue), the backward propagating core mode of waveguide 1 (yellow) and forward propagating cladding mode (magenta) for a device with a long-period waveguide grating in one waveguide and a short-period grating in the other. We use a light wavelength of $\lambda_0 = 1.5498\mu m$ in order to show the behaviour away from phase-matching. We pump waveguide 0 in the forward propagating direction. With a long-period grating in waveguide 0 and a short-period grating in waveguide 1, we present the numerical results with a length of $L = 50mm$.

We see, in Figure 6.15(b), an exclusion band in which no power is transmitted through the grating when the waveguide with the short-period grating is pumped. This is consistent with the bandgap property of short-period gratings as all of the light is coupled from the launching mode to the cladding mode. As we move away from the phase-matching condition, we see a decay in light coupled by the long-period grating to the other waveguide as the long-period grating does not have a bandgap and instead couples a decreasing amount of light as the phase-mismatch is increased. However, when the waveguide with the long-period grating is pumped then, away from phase-matching, only some of the light is transferred from the launching mode to the cladding mode and then into the other waveguide. This means that some of the light remains in the launching mode with some coupled into the cladding mode.

6.5.1.2 Short-period grating weaker than the long-period grating

However, if we use a short-period grating with a coupling coefficient that is less than that of the long-period grating, we have an oscillatory system. From Equations (6.13) and (6.17) from Section 6.3.1, we find that the length required to have an integer number of cladding mode oscillations is:

$$\Omega = \frac{1}{2} \sqrt{|e|^2 - |d|^2} \quad (6.73)$$

$$\Omega L = n\pi$$

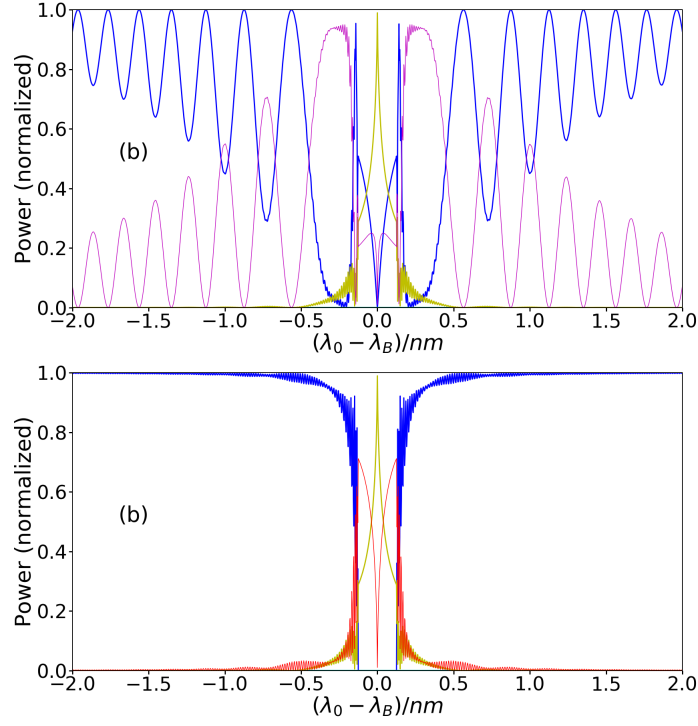


Figure 6.15: Power output of core mode and cladding mode for a device with a period waveguide grating in one waveguide and a short period grating in the other. Here, blue is the power output of the core mode of waveguide 0 in the forward direction, yellow is that of waveguide 1 in backwards direction, and magenta and red are that of the cladding mode in the forwards and backwards direction respectively where applicable. In both cases, we use a length is $L = 50mm$. In (a) we pump the waveguide with the long-period grating and in (b) the waveguide with the short-period grating.

with a long-period grating in waveguide 0 and a short-period grating in waveguide 1 or

$$\Omega = \frac{1}{2} \sqrt{|f|^2 - |c|^2} \quad (6.74)$$

$$\Omega L = n\pi$$

with the gratings swapped.

As discussed in Section 6.3.1, as for the long-period waveguide coupler (Section 6.4.3), for odd integer n we get beam splitter properties whereas for even n we return the system to its original state. However, in this device, not all the modes propagate in the same direction. As a result, the propagation of the light through the device is sensitive to its length. However, increasing the length by $L' = L + \frac{2n\pi}{\Omega}$ leads to the same power output and the same light propagation through the device.

We next present the results for a 50 : 50 beam splitter. We see in Equations (6.34) and (6.73) that this requires a grating index contrast of 0.001 for the long-period grating and 0.0004142 for the short-period grating and a length of 8.7336mm or any odd-integer multiple. We present the 50:50 beam splitters with these parameters in Figure 6.16. We

can see that the oscillations in the cladding mode and the launching core mode are of far greater amplitude when we pump the waveguide with the long-period grating than the one with the short-period grating. This is because the long-period grating has a greater coupling coefficient. All of the light is incident upon it when the waveguide with the long-period grating is pumped but far less light per unit length is incident upon it when the waveguide with the short-period grating is pumped. This means that oscillation amplitude resulting from the effect of the long-period grating is smaller in the latter case.

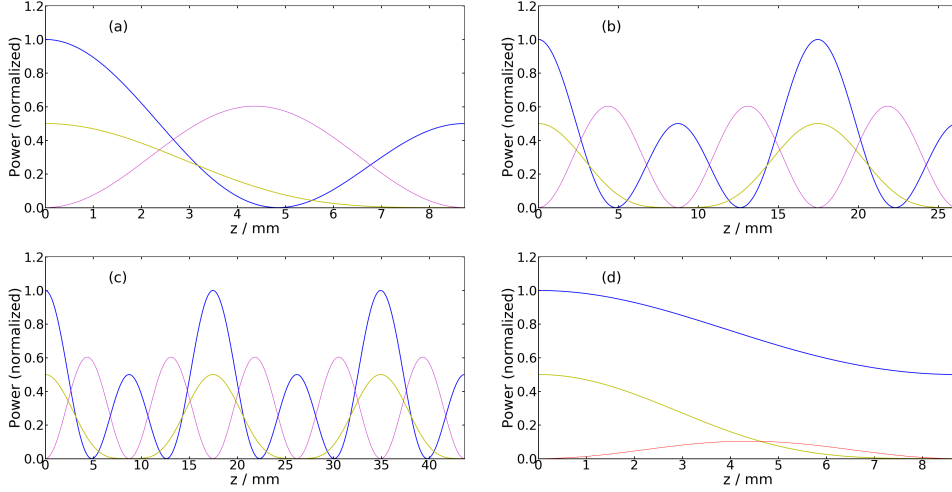


Figure 6.16: Power propagation in forward propagating core mode of waveguide 0 (blue), the backward propagating core mode of waveguide 1 (yellow) and forward propagating cladding mode (magenta) for a device with a long-period waveguide grating in one waveguide and a short-period grating in the other. The long-period grating has a grating index contrast of 0.001, whereas the short-period grating has a grating index contrast of 0.0004142. With a long-period grating in waveguide 0 and a short-period grating in waveguide 1, we present the numerical results with a length of $L = 8.734\text{mm}$ (a), $L = 26.200\text{mm}$ (b) and $L = 43.668\text{mm}$ (c). With the gratings swapped we present the results with a length of $L = 8.7336\text{mm}$ (d).

We show a wavelength sweep of the device used as a 50 : 50 beam splitter on Figure 6.17. We show that similarly to the long-period waveguide-to-waveguide coupler, we have a solitary peak in power transfer at the phase-matching condition. We find that the full-width half-maximum bandwidth of the device is 0.0533nm .

The bandwidth of our coupler using long- and short-period gratings is considerably smaller than our coupler using only long-period gratings. This can be understood quite easily by considering how the modal structure changes with wavelength. As the wavelength increases, the propagation constants of all the modes increase. Recall that, when coupling between modes propagating in the same direction using a long-period waveguide grating, the phase mismatch is given by $\Delta K_h = \beta_{core} - \beta_{clad} - K_h$. This means that changing the light wavenumber leads to a much smaller change in the phase mismatch

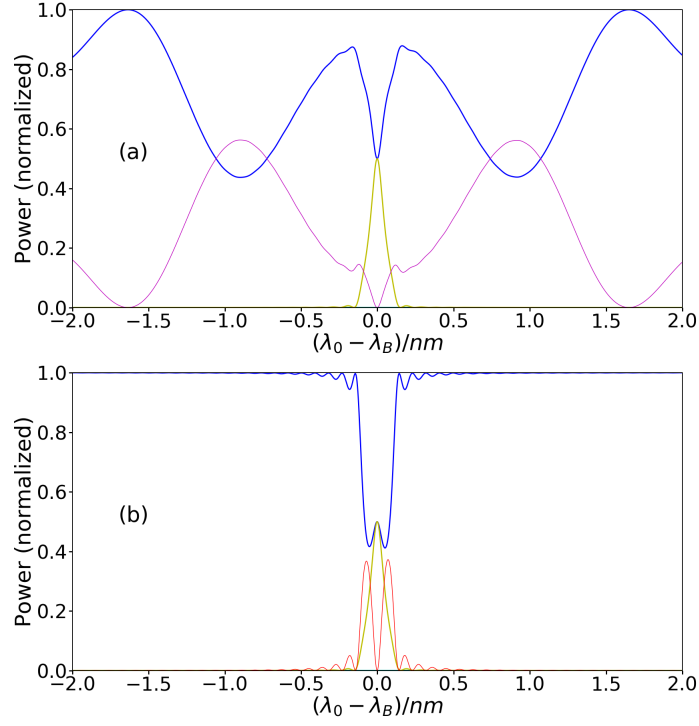


Figure 6.17: Power output of core modes and cladding mode for a device with a long-period waveguide grating in one waveguide and a short period grating in the other. The device parameters are the same as in Figure 6.16. The length of the device is $L = 17.467\text{mm}$. In (a) we pump the waveguide with the long-period grating and in (b) the waveguide with the short period grating.

as most of the change in propagation constant cancels out, leading to a wide bandwidth. The opposite is true when coupling between modes in the opposite direction with a short-period grating. The phase mismatch in this case is given by $\Delta K = -\beta_{core} - \beta_{clad} + K_g$, the changes in the propagation constants as the light wavenumber is varied add up. This translates into a reduction in the bandwidth.

Again, much like with the long-period waveguide grating coupler, we can achieve any coupling ratio with this device. The grating parameters we need to achieve any coupling ratio are calculated analytically in Section 6.3.2.3 and plotted in Figure 6.18. We find that the length of this device is necessarily longer than that of the long-period grating coupler with the same coupling coefficients and is in the region of around $8\text{mm} - 20\text{mm}$ for any splitting ratio of up to 99 : 1 to the other waveguide. This means that the majority of couplers of this type can be UV-written without needing to take into account chip curvature (see Section 2.4.2).

6.5.2 Effect of grating phase mismatch

This device uses two gratings that are phase-matched at different grating periods. This means that, after fabricating one of the gratings, the UV-writing system needs to be

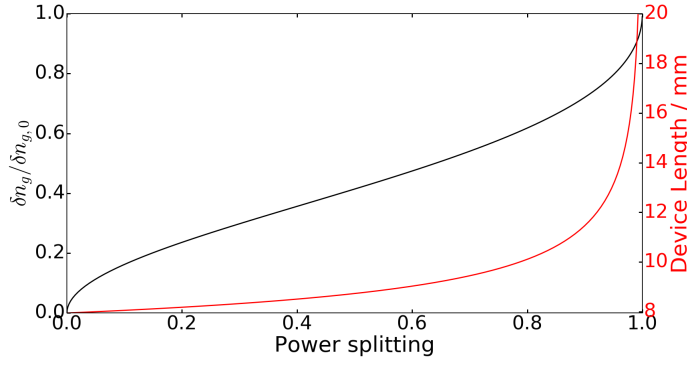


Figure 6.18: Grating index contrast ratio and device length required to achieve any desired power splitting with a waveguide-to-waveguide coupler consisting of a long-period grating in one waveguide and a short-period grating in the other. Here, we use $\delta n_{g,0} = 0.001$ as the grating index contrast of the long-period grating and define δn_g to be the index contrast of the short-period grating.

very carefully re-adjusted before fabricating the other grating to make sure that they are both phase-matched at the same wavelength.

We show 2D contour plots of how the performance of the device is affected by the deviations of both grating periods from those required for phase-matching on Figures 6.19 and 6.20 for the devices with equal (Section 6.5.1.1) and unequal (Section 6.5.1.2) coupling coefficients respectively. We see that the device is far more sensitive to imprecisions in the grating period of the short-period grating than to that of the long-period grating. This is because the phase-mismatch is directly proportional to both the relative inaccuracy in the grating period as well as the reciprocal of the grating period. As the long-period grating has a grating period of around one order of magnitude greater than the short-period grating, this requires an inaccuracy in the long-period grating that is two orders of magnitude above that required for the short-period grating to achieve the same phase-mismatch. As a result, the device is much less sensitive to the period of the long-period grating. The plots in Figures 6.19 and 6.20 support this explanation.

For the case with equal coupling coefficients, there is a very narrow band of grating periods which lead to efficient coupling. In terms of the grating period of the short-period grating, we can see that the half-width half-maximum "bandwidth", i.e. fabrication tolerance is about $0.02nm$, which is a lot less than the current estimated precision achieved at the ORC of $0.1nm$. It also does not take into account the very sharp peak we see in Figure 6.15 which leads to a device that is far more sensitive than this. We can see however, on the top left and bottom right corners of Figure 6.19(b), that providing a carefully chosen slight detuning to both of the gratings allows us to find a solution that is more robust to changes in the grating period. We also see that for non-equal coupling coefficients, we have a far more rounded peak which also makes our device more robust to imprecisions in the grating period. Nonetheless, we still have the fabrication tolerance of about $0.02nm$ which requires highly precise optical engineering. How sharply the

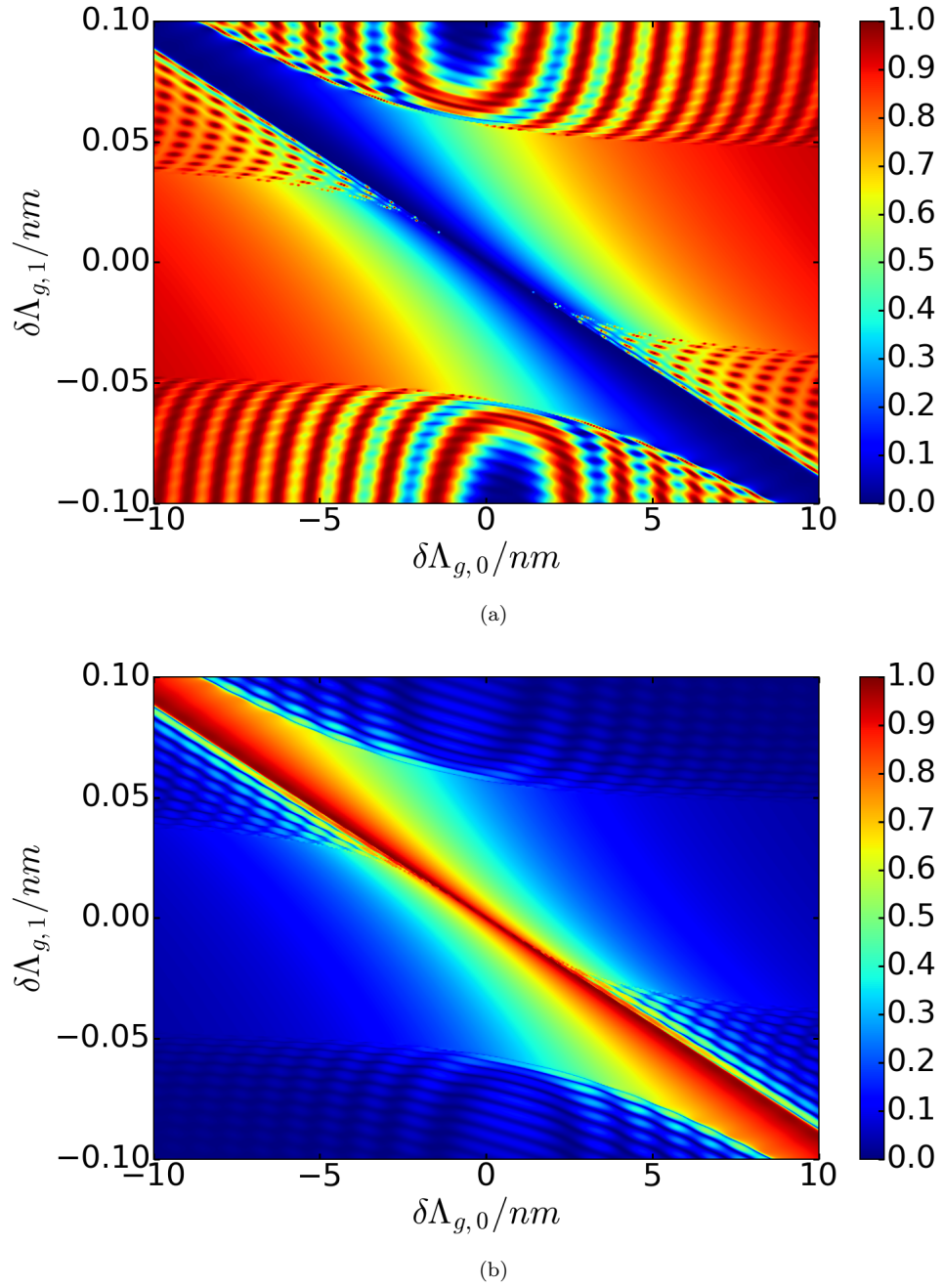


Figure 6.19: Power output of waveguide 0 in the co-propagating direction (a) and waveguide 1 in the counter-propagating direction (b) for a device with a long-period grating in one waveguide and a short period grating in the other. The gratings have equal index contrast.

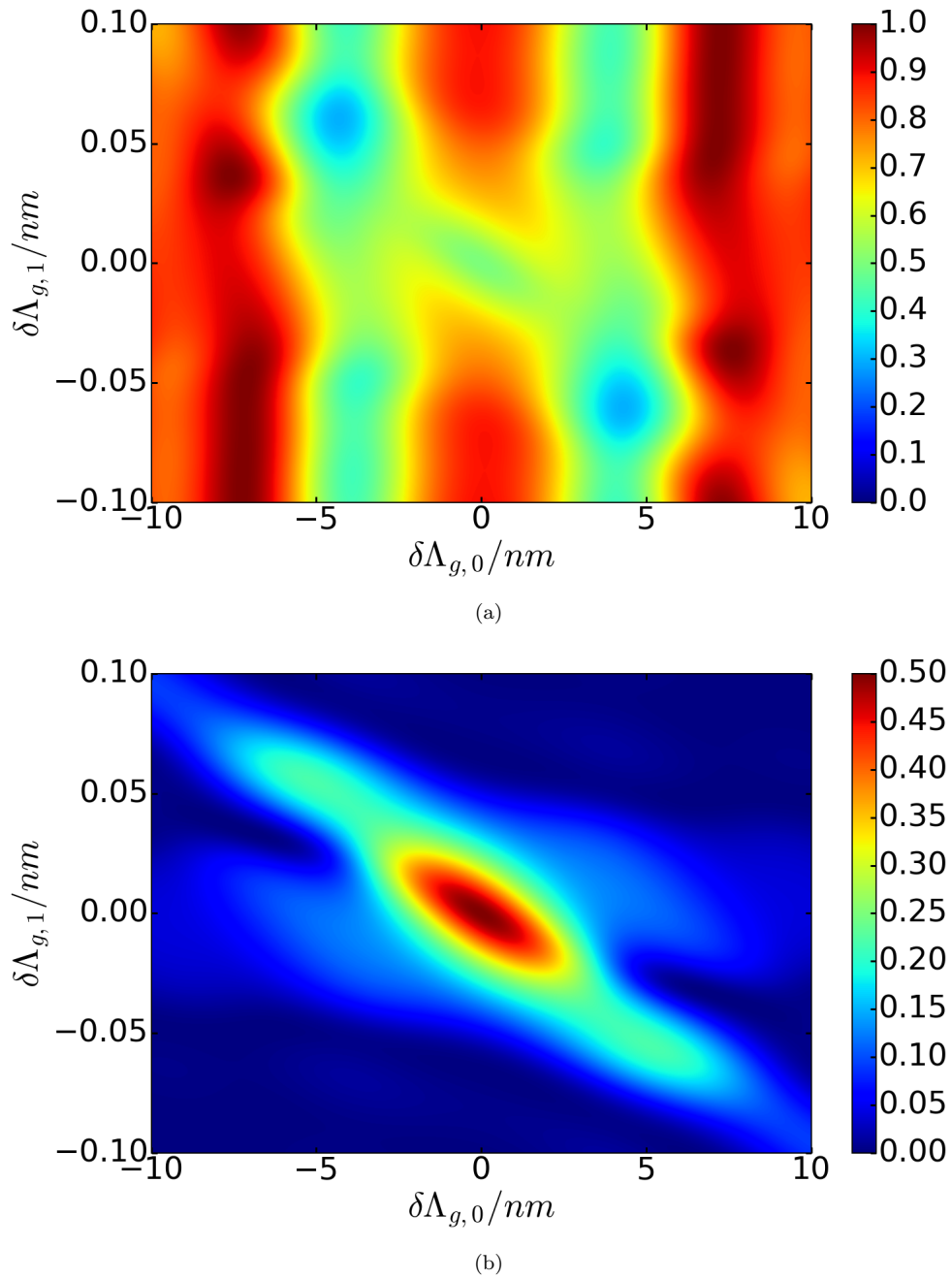


Figure 6.20: Power output of waveguide 0 in the co-propagating direction (a) and waveguide 1 in the counter-propagating direction (b) for a device with a long-period grating in one waveguide and a short period grating in the other. Here, the gratings have unequal index contrast and the parameters are the same as in Figure 6.16

grating period can be defined is limited by the uniformity of the width and refractive index distribution of the planar core layer [120]. Therefore, to fabricate this device will require it to be very uniform.

6.6 Compact Walsh-Hadamard transform

In this section, we numerically simulate a compact implementation of the Walsh-Hadamard transform that we have demonstrated analytically in Section 6.3.6. Here, we choose to simulate the first implementation we introduce in that Section.

In our device, we have superimposed long- and short-period gratings in both of the waveguides. As explained in 6.3.6, all gratings have equal coupling coefficients except for one of the long-period gratings, whose coupling coefficient is three times that of the other gratings. Also, the two long-period waveguide gratings are π out of phase whereas the short-period gratings are in phase, (we can also do it the other way around). We plot the mode propagation coupling the light input in each of the waveguides in Figure 6.21 and numerically confirm that we get a quarter of the power at each output as predicted for every input. As explained in Section 6.3.6, by applying external phase-shifts, we get a Walsh-Hadamard transform.

Note that in general for super-imposed long- and short-period gratings, the power propagation through the device is sensitive to grating phase. We therefore set the grating phase by default to be 1.108 and 2.037 for the short-period gratings in the waveguides 0 and 1, respectively, and 1.277 and -1.278 for the respective long-period gratings. These gratings phases lead to grating coupling coefficients of equal phase and any grating phase quoted in this or the following section are in addition to the phases quoted above.

In this section, we use short-period gratings with an index contrast of 0.003 and long-period gratings with an index contrast of 0.003 and 0.009 in waveguides 0 and 1 respectively. We use a device length of $L = 9.364mm$.

We show the outcome of a wavelength sweep on Figures 6.22. We find that the bandwidth is equal to $0.0480nm$ which is quite limited. It is worth noting that the power transferred to both the forward and backward propagating modes of the opposite waveguide are the same regardless of which waveguide is pumped.

6.6.1 Effect of grating phase mismatch

Sweeping the grating periods of both the long- and short-period gratings independently we find that, just like with the coupler based on a long and short-period grating (Section 6.5), the device is far more sensitive to imperfections in the short-period gratings than the long-period gratings. We plot the outcome of grating sweeps at all of the output

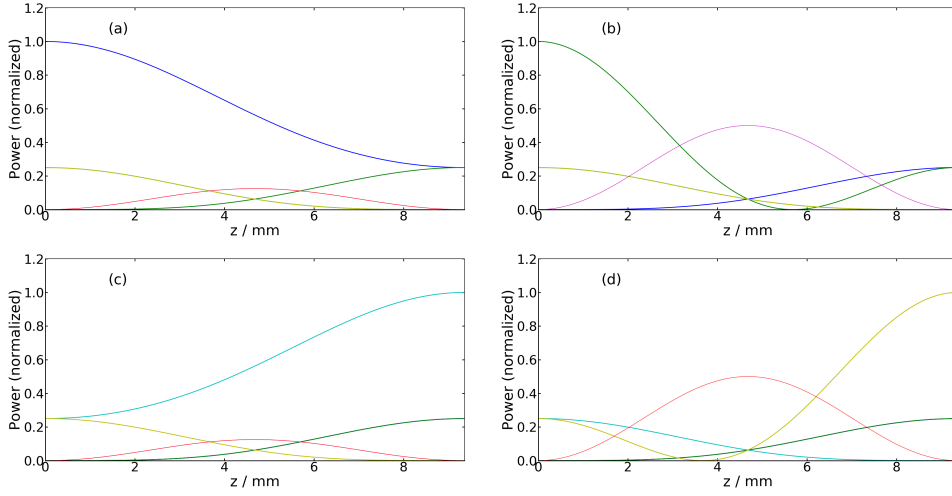


Figure 6.21: Power propagation in forward and backward propagating core mode of waveguide 0 (blue and cyan, respectively), the forward and backward propagating core mode of waveguide 1 (green and yellow, respectively) and forward and backward propagating cladding mode (magenta and red, respectively) for a device with superimposed long- and short period waveguide gratings in each waveguide. The parameters are given in text. We present the results pumping the device at inputs I_0 (a), I_1 (b), I_2 (c) and I_3 (d).

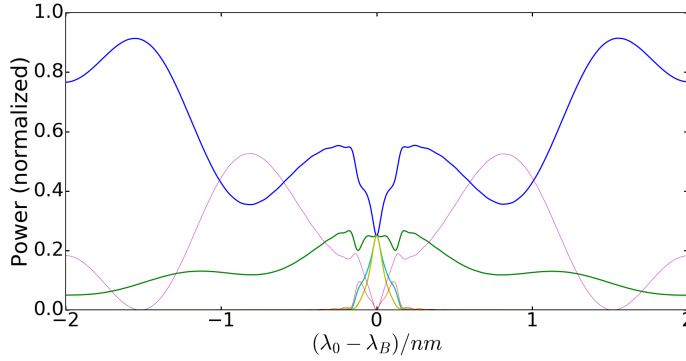


Figure 6.22: Power output against wavelength of core modes and cladding mode for a device with superimposed long- and short period waveguide gratings in each waveguide with the parameters are defined in text.

ports on Figure 6.23. Looking at the power output of the backward propagating modes (Figures 6.23(a) and 6.23(b)), we see a fabrication tolerance (half-width half-maximum) of around $0.02nm$. As previously mention at the end of Section 6.5.2, this is beyond the limit currently achieved with the UV-writing technology available at the ORC which is currently estimated to be $0.1nm$. (This is a preliminary value, see Section 4.5.2, but better precisions have been achieved in a fibre platform [115, 116, 117].)

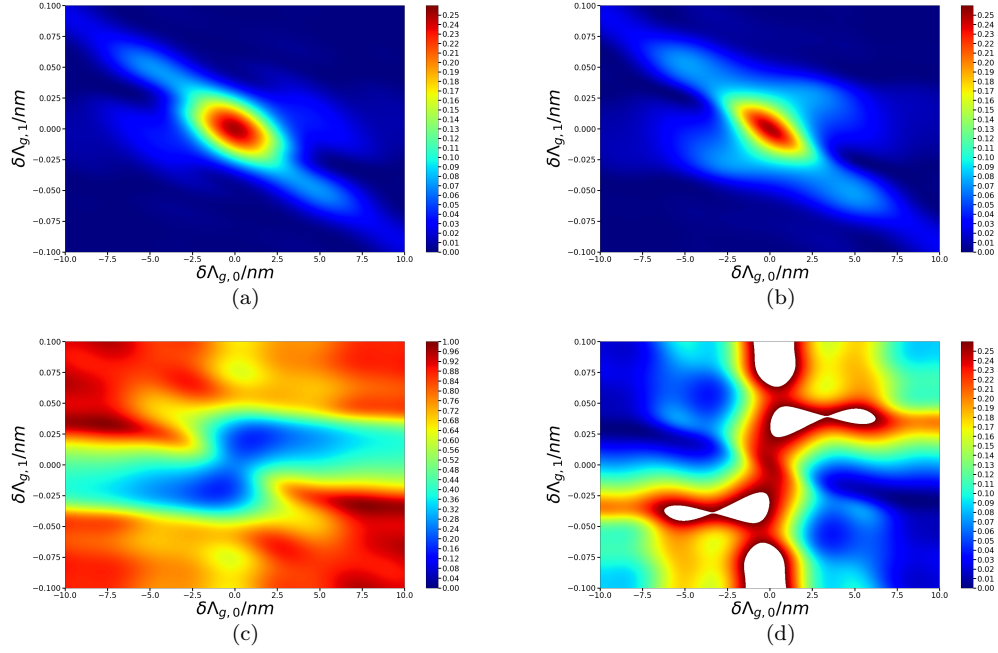


Figure 6.23: Power output against grating period at outputs O_0 (a), O_1 (b), O_2 (c) and O_3 (d) for a device with superimposed long- and short period waveguide gratings in each waveguide with parameters defined in text.

6.7 Numerical method for finding compact transformations

In this section we present and evaluate a numerical method for finding compact power splitters that can be implemented in this platform. We choose a set of output powers that we want to achieve. We assume superimposed long- and short-period gratings in each waveguide, leading to four gratings in total. We fix the coupling coefficient of one of the gratings and we start with an initial value for the coupling coefficients of the rest of the gratings. We use Newton's method to converge to values of the coupling coefficients (amplitude plus phase) of the other gratings that achieve the target power splitting by minimising the value of:

$$g_{tot} = g_0^2 + g_1^2 + g_2^2 + g_3^2 \quad (6.75)$$

where

$$g_n = P_n - P_{n,target} \quad (6.76)$$

where P_n is the power at output port O_n and $P_{n,target}$ is the output power we want to achieve.

This method is not always reliable and does not converge for many output powers. Nonetheless, we have found a selection of power outputs that we can achieve. We normalise the coupling coefficients such that the strongest grating has an index contrast

of 0.001 which was, as mentioned in the Background (Section 2.4.3), the highest coupling coefficient that could be achieved according to [25] so far in this platform.

From an input amplitude of 1 at input O_0 we find that we can achieve any of the following compact power splittings:

$$\begin{bmatrix} P_0 \\ P_1 \\ P_2 \\ P_3 \end{bmatrix} = \begin{bmatrix} b_0 b_1 \\ b_0(1 - b_1) \\ (1 - b_0)(1 - b_1) \\ (1 - b_0)b_1 \end{bmatrix} \quad (6.77)$$

Notice that we have two independent variables determining the set of output powers, b_0 and b_1 which correspond to 2 degrees of freedom. In general, the power output of a 1-to-4 beam splitter will have 3 such independent variables. However, our device is constrained as it must act in the same way in both propagation directions. This provides an additional constraint and so reduces the number of degrees of freedom by determining the output powers by 1 down to 2. Note that not all splitting ratios that can be achieved by concatenating individual blocks (see Section 6.3.4) are among those defined by Equations (6.77). This means that the transformations we can achieve in a single block with super-imposed gratings are a subset, but not the full set, of symmetric unitary matrices.

We confirm that the minimised value of g_{tot} is practically zero for all b_0 and b_1 as defined by Equation (6.77). This means that for all the power splittings defined by Equation (6.77) we are able to converge to a set of coupling coefficients (amplitude plus phase) that achieve the desired power output. We also present plots of the power propagation through the device to achieve the power splittings defined in Equations (6.77) with $b_0 = \frac{1}{3}$, $b_1 = \frac{1}{2}$ and $b_0 = \frac{1}{3}$, $b_1 = \frac{1}{3}$ in Figure 6.24, together with the coupling coefficients (amplitude and phase) found to achieve them in the figure caption.

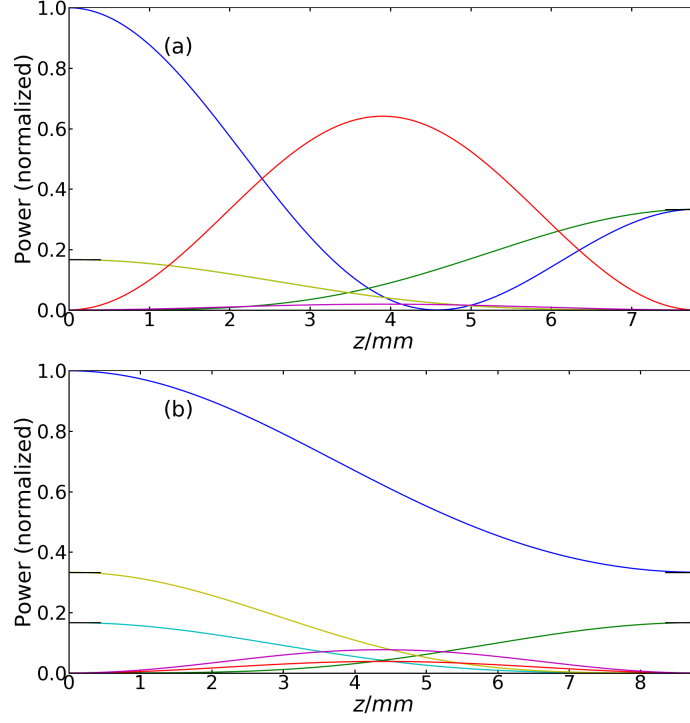


Figure 6.24: Device found numerically to achieve a certain power-splitting. Here, the blue and cyan are the forward and backward propagating modes of waveguide 0, green and yellow are the respective modes of waveguide 1 and magenta and red are the forwards and backwards propagating cladding modes. For (a), we target the output powers defined by $b_0 = \frac{1}{3}$ and $b_1 = \frac{1}{2}$. We achieve this with a grating index contrast of 0.001 and 0.0004126 for the long-period gratings in waveguides 0 and 1 and of 0.0001850 and 0.0003179 for the respective short-period grating. The grating phases respectively are 1.377 and 3.339 for the long-period gratings and 0.1968 and 0 for the short-period gratings. The length of the device is $7.182 mm$. For (b), we target the output powers defined by $b_0 = \frac{1}{2}$ and $b_1 = \frac{1}{3}$. The grating index contrasts used to achieve that are 0.0004635 and 0.001 for the long-period gratings in waveguides 0 and 1, 0.0005273 and 0.0003443 for the respective short-period gratings and the grating phases respectively are 1.8848 and 2.8275 for the long-period gratings and -0.3147 and 0 for the short-period gratings. The length of the device is $8.788 mm$.

Chapter 7

Conclusions and Future Work

7.1 Conclusion

I have theoretically investigated the capabilities of tilted Bragg grating technology for light manipulation in a planar photonics platform.

In Chapter 2, I have provided the background knowledge to this thesis including an overview of the physics of waveguides and Bragg gratings and into the analytical and numerical methods used for investigating their behaviour as well as an overview of existing devices. I have provided motivation for why I choose a silica platform for which to design the devices investigated in this thesis together with an overview of the fabrication method available at the ORC with which they are intended to be fabricated.

In Chapter 3, I computed the modes of a waveguide of Gaussian index profile, which is expected to be the approximate profile of a waveguide in our platform, and found that they could be approximated by a Gaussian mode profile for certain realistic parameters. Then, I derived an analytical solution for the behaviour of tilted Bragg gratings of arbitrary angle using an analytical beam tracing method. I found that it had good agreement with existing theory and with COMSOL finite element simulations for a wide range of realistic parameters. This analytical solution could be used as a basis for finding the analytical behaviour of more complex grating-based devices that couple to radiation modes.

In the following chapters, I investigate a new class of grating based devices for coupling waveguide inputs and outputs in our platform. These devices consist of a single ridge structure with two waveguides in parallel. They were studied both analytically and numerically using coupled mode theory with good agreement between the two methods. In Chapter 4, I used two single-mode waveguides coupled together via a backward propagating mode of the ridge. Results show that this device has a bandwidth structure in terms of the wavelength with two narrow peaks that could be used in certain

applications such as separating the signal from the pump from a Raman amplifier. I found analytically that, for certain parameters, we can achieve 100% coupling efficiency between the two waveguides and it exhibited grating induced transparency which could be used as the basis of a phase comparator between two beams. I then showed how the bandwidth could be controlled during fabrication. It was found that the device had good robustness to temperature and to noise based on phase-error but a high sensitivity to certain fabrication parameters, especially the device width. This sensitivity can be reduced in two different ways. Using an apodization function to define our grating index contrasts eliminates any leakage via the cladding mode and greatly smoothens the sharp peaks of the spectral response. However, the relaxation of fabrication tolerances was not enough to be easy to fabricate with micromachining technology currently available (though it could be in the future). The second method is by using an external index oil. I collaborated with members of Peter Smith's group in order to find a set of parameters with which the device could be fabricated with an external index oil. I found that the relaxation of fabrication tolerances is enough for this device to be fabricated using technology available at the ORC. I calculated pulse properties including the group delay and GVD for these parameters and estimated the amount of pulse broadening that would be expected.

I then considered a device with two two-mode waveguides in Chapter 5. By increasing the waveguide width, device width and waveguide separation it is able to accommodate two modes in each waveguide while avoiding unwanted evanescent coupling between the higher order modes. As such, this device can function as a mode division multiplexer coupling one of the modes of one waveguide to the other with, I find, only an acceptable level of coupling ($< 1\%$) for the other mode. I found analytically and confirmed numerically that we could use superimposed gratings to couple each waveguide mode to a single ridge mode and, in doing so, achieve an arbitrary four-way power splitter between the modes. With the addition of long-period gratings coupling directly between waveguide modes, I have shown that we can implement a full basis with which to achieve any 4×4 unitary matrix.

Finally, in Chapter 6 I investigate a new device that exploits both propagation directions of two single-mode waveguides, leading a system consisting of four modes in total. As such, our system can have four input and output ports if we connect circulators to the waveguide end facets. I've found that there are four fundamental transformations that can be achieved in this device, each with their own physical implementations. I have found that, by concatenating them together, we can achieve any transfer matrix that is both symmetric and unitary. I found an algorithm that allows us to decompose any arbitrary such matrix into a product of these fundamental transfer matrices, which I can then express as a combination of these "fundamental" couplers. Not only that, but I find that by super-imposing long- and short-period gratings, we can achieve an entire

class of transformations in a simple and compact way and I give the example of a Walsh-Hadamard transform that is more compact than previously existing implementations. I show numerical simulations of two of my "fundamental" couplers including a long-period waveguide grating coupler with tilted gratings that could be easily implemented using the fabrication method available at the ORC. I also show the implementation of a new type of coupler and show the effect of imprecisions in the grating period.

7.2 Future Directions for Research

The most obvious way to build on the work in this thesis would be to fabricate the devices that we have theoretically investigated so far. I have already made the simulations of one of our devices using parameters intended for fabrication. The reason this device has not been fabricated so far is as a result of the lockdown imposed as a result of the coronavirus pandemic. Fabrication of this device would represent a new achievement demonstrating the capabilities of the ORC's planar photonics platform, as would fabricating the long-period and "mixed" couplers and the compact Walsh-Hadamard transform in Chapter 6.

Another avenue of research would be to investigate in more detail the effect of grating apodization. The analytical behaviour of the devices in Chapters 4 and 6 could be derived for super-Gaussian apodization to aid in device fabrication. One could see how much relaxation of the fabrication parameters one would be able to achieve. If very precise micromachining technology becomes available, it could be possible to fabricate a device without requiring tuning with an external oil.

Another possibility would be to derive a full version of the analytical solutions including also evanescent coupling between the waveguides. This would allow for the design of devices implementing transfer matrices with lower waveguide separations with the evanescent coupling aiding, rather than hindering, the device performance. One could then fit a larger number of waveguides in the device expanding the range of transformations that can be achieved. The use of evanescent coupling could also shorten the devices that we study. Devices could also be shortened by increasing the index contrasts of the gratings beyond the values considered in this thesis, with a grating index contrast up to $\delta n_g = 0.002$ believed to be achievable.

Finally, the possibility of implementing more complex gates on this platform could be explored. Such a device could implement multiple qubits in individual photons with their state encoded by pairs of waveguides [58]. It could be uni-propagating based on multiple waveguides close together as described above. Alternatively, we could extend the work in Chapter 6 and attempt to implement multiphoton quantum gates such as C-NOT gates exploiting bi-directional propagation.

If these proposed devices could be achieved, they would be highly compact and frequency selective compared to existing devices. For example, we mentioned in Section 6.3.6 that we can achieve a highly compact Walsh-Hadamard transform consisting of only three gratings and two waveguides which is more compact than the previously proposed implementation using four waveguides and four gratings [40]. The frequency selectiveness could pose either an advantage, if this property were desired, or a disadvantage, as it would make them harder to fabricate. The main disadvantages of the devices explored in this thesis is that they would require very precise and uniform manufacturing of the ridge width and of the core layer properties.

As previously mention in Section 2.4.1, the use of the silica UV-writing platform developed at the ORC [13] greatly improves the quality of gratings that we can produce compared to other platforms such as those employing etched gratings. This means that our implementation of the long-period waveguide grating coupler should be of higher quality and thus greater maximum coupling efficiency compared to those in [38, 39] that are constructed in a polymer platform. This also another advantage that our proposed implementation of Walsh-Hadamard transform would have over that in [40]. This also makes this platform more suitable for implementing the more complex devices investigated in Chapter 4 using gratings.

Compared to existing implementations of universal linear optics and quantum gates (see Section 2.3.4), our proposed devices have the advantage that they do not need to couple only between waveguides that are immediately adjacent. Unlike existing implementations, they are not, for now, dynamically reconfigurable. However, the possibility of using thermo-optic phase shifters in order to change this could be explored. For the concatenated device we introduce in Section 6.3.4 of Chapter 6, these phase-shifters would have to be strategically placed for it to be made completely reconfigurable. Where standard Bragg gratings are employed, a gap would have to be placed in the centre in which a tunable phase-shift would be used to achieve any level of transmission. For the long-period waveguide grating coupler, it could be constructed with 100% coupling at resonance but a heat source could be placed under one of gratings in order to bring it away from resonance and so reduce the coupling ratio. Alternatively, two 50% waveguide-to-waveguide couplers could be constructed with a thermo-optic phase shifter between them in order to achieve any coupling ratio. The coupler based on both long-period and short-period grating, however, would have to be tuned by a heat source underneath the short-period grating. After each fundamental block, the phase-shifts could be implemented thermo-optically. We show a thermally reconfigurable version of our device in Figure 7.1.

Another disadvantage of our devices is that optical information processing arises their small bandwidth. This has the effect of making them harder to fabricate. Evanescent couplers by comparison are a lot more broadband [129] and so existing implementations of universal linear optics [7] and quantum gates [58] are easier to fabricate. However,

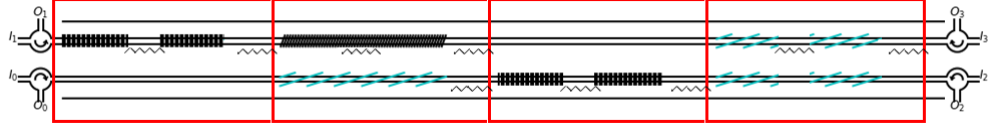


Figure 7.1: Thermally reconfigurable 4×4 coupler based on bidirectional propagation implementing any arbitrary symmetric unitary matrix. Thermo-optic phase shifters (zig-zag lines) are placed in strategic locations in order to achieve thermal reconfigurability. Each box represents a part of the device that can be used to implement the most general form of the fundamental.

we could make our unidirectional couplers in Chapter 5 a lot easier to fabricate by entirely employing long-period gratings instead of short-period gratings as these are not as narrow-band. Then, we could use multiple long-period gratings in parallel to achieve a wide range of compact transformations similarly to Section 5.5.2. This compactness would therefore provide an advantage for our devices compared to those based on directional couplers in [7] by reducing the length of a device needed to make the desired transformations. As mentioned previously, we could place more gratings in parallel if we are able to model evanescent coupling at the same time as coupling via gratings. This would provide a limited level of scalability.

Appendix A

Publications

Mathias J. Weisen, Matthew T. Posner, James C. Gates, Corin B. E. Gawith, Peter G. R. Smith, and Peter Horak, "Planar waveguide coupler based on tilted Bragg gratings and a discrete cladding mode", In: SPIE Photonics Europe 2018, Strasbourg, France (2018)

Mathias J. Weisen, Matthew T. Posner, James C. Gates, Corin B. E. Gawith, Peter G. R. Smith, and Peter Horak, "Planar waveguide coupler based on tilted Bragg gratings and a discrete cladding mode", J. Opt. Soc. Am. B, Vol. 35, pp. 1783-1791 (2019)

Mathias J. Weisen, James C. Gates, Corin B. E. Gawith, Peter G. R. Smith, and Peter Horak, "Four-Port Interference Device on an Integrated Photonics Platform Based on Tilted Bragg Gratings", In: CLEO/Europe-EQEC, Munich, Germany (2019)

Peter Horak, **Mathias J. Weisen**, James C. Gates, Corin B. E. Gawith, and Peter G. R. Smith, "Tilted Bragg Gratings as an Efficient Platform for Integrated Multimode Interference Devices", In: 21st International Conference on Transparent Optical Networks (ICTON) (2019)

Mathias J. Weisen, James C. Gates, Corin B. E. Gawith, Peter G. R. Smith, and Peter Horak, "Four-port integrated waveguide coupler exploiting bidirectional propagation of two single-mode waveguides (Conference Presentation)" In:, Nanophotonics VIII. vol. 11345, SPIE Photonics Europe, (2020)

Mathias J. Weisen, James C. Gates, Corin B. E. Gawith, Peter G. R. Smith, and Peter Horak, "4-by-4 integrated waveguide coupler based on bi-directional propagation in two single-mode waveguides", IEEE. Photon. J. (accepted 2020)

References

- [1] G. Lifante. *Integrated Photonics: Fundamentals*. John Wiley & Sons Inc., Chichester (2003)
- [2] Kuphaldt. *Lessons In Industrial Instrumentation*, chap. Ch. 5. Control Automation, San Fransisco, second edn. (2019)
- [3] A. K. Ghatak and K. Thyagarajan. *Introduction to fiber optics*. Cambridge University Press, New Dehli (1999)
- [4] K. Okamoto. *Fundamentals of optical waveguides*. Elsevier, Amsterdam, second edn. (2008)
- [5] J. Capmany and D. Pérez. *Programmable Integrated Photonics*. Oxford University Press, Oxford (2020)
- [6] J. Wang and Y. Long. *On-chip silicon photonic signaling and processing: a review*. Sci. Bull., 63 pp. 268–273 (2018)
- [7] J. Carolan et al. *Universal Linear Optics*. Science, 349 pp. 711–716 (2015)
- [8] T. Erdogan. *Fiber grating spectra*. J. Light. Technol., 15 pp. 1277–1294 (1997)
- [9] L. Cheng et al. *Grating Couplers on Silicon Photonics: Design Principles, Emerging Trends and Practical Issues*. Micromachines, 11. 666 (2020)
- [10] M. T. Posner et al. *Integrated polarizer based on 45° tilted gratings*. Optics Express, 27 pp. 11174–11181 (2019)
- [11] J. W. Field et al. *Highly-chirped Bragg gratings for integrated silica spectrometers*. Opt. Express, 28 pp. 21247–21259 (2020)
- [12] C. Holmes et al. *Planar waveguide tilted Bragg grating refractometer fabricated through physical micromachining and direct UV writing*. Opt. Express, 19 pp. 12462–12468 (2011)
- [13] C. Sima et al. *Ultra-wide detuning planar Bragg grating fabrication technique based on direct UV grating writing with electro-optic phase modulation*. Opt. Express, 21 pp. 15747–15754 (2013)

- [14] I. J. G. Sparrow. *Developement and Applications of UV Written Waveguides*. Ph.D. thesis, University of Southampton (2005)
- [15] R. P. Brent. *Algorithms for Minimization Without Derivatives*, chap. Ch. 3-4. Prentice Hall, Englewood Cliffs, New Jersey (1973)
- [16] D. P. Hand and P. S. J. Russell. *Photoinduced refractive-index changes in germanosilicate fibers*. Optics Letters, 15 pp. 102–104 (1990)
- [17] K. S. Chiang et al. *Widely Tunable Long-Period Gratings Fabricated in Polymer-Clad Ion-Exchanged Glass Waveguides*. IEEE Photonic. Tech. L., 15 pp. 1094–1096 (2003)
- [18] S. Honda et al. *Largely-tunable wideband Bragg gratings fabricated on SOI rib waveguides employed by deep-RIE*. Electron. Lett., 43 pp. 630–631 (2007)
- [19] P. S. J. Russell et al. *Fibre gratings*. Phys. World, 6 pp. 41–46 (1993)
- [20] T. Erdogan and J. Sipe. *Tilted fiber phase gratings*. J. Opt. Soc. Am. A: Opt. Image Sci. Vis., 13 pp. 296–313 (1996)
- [21] K. S. Lee. *Mode coupling in tilted planar waveguide gratings*. Appl. Opt., 39 pp. 2–7 (2000)
- [22] Y. Li et al. *Volume current method for analysis of tilted fiber gratings*. J. Light. Technol., 19 pp. 1580–1591 (2001)
- [23] T. Yoshino. *Theoretical analysis of a tilted fiber grating polarizer by the beam tracing approach*. J. Opt. Soc. Am. B, 29 pp. 2478–2483 (2012)
- [24] M. T. Posner et al. *Integrated polarizing coupler based on tilted gratings*. In: *Integrated Photonics Research, Silicon and Nanophotonics*. Vancoover, Canada (2016)
- [25] C. Sima. *Integrated Planar Bragg Grating Devices for Advanced Optical Communication Systems*. Ph.D. thesis, University of Southampton (2013)
- [26] O. R. González and A. G. Kelkar. *3 - Robust Multivariable Control*. In: W.-K. CHEN (ed.), *The Electrical Engineering Handbook*, pp. 1037 – 1047. Academic Press, Burlington (2005)
- [27] C. C. Katsidis and D. I. Siapkas. *General transfer-matrix method for optical multilayer systems with coherent, partially coherent, and incoherent interference*. Appl. Opt., 41 pp. 3978–3987 (2002)
- [28] B. Yurke et al. *SU(2) and SU(1,1) interferometers*. Phys. Rev. A, 33 pp. 4033–4054 (1986)

- [29] M. Reck et al. *Experimental Realization of Any Discrete Unitary Operator*. Phys. Rev. Lett., 73 pp. 58–63 (1994)
- [30] L. Q. et al. *Transfer matrix method for simulation of the fiber Bragg grating in polarization maintaining fiber*. Opt. Commun., 452 pp. 185–188 (2019)
- [31] J. Jin. *The finite element method in electromagnetics*. John Wiley & Sons, New York, second edn. (2002)
- [32] U. Kiran et al. *GPU-warp based finite element matrices generation and assembly using coloring method*. J. Comput. Des. Eng., 6 pp. 705–718 (2019)
- [33] B. Archambeault et al. *EMI/EMC computational modeling handbook*. Springer Science+Business Media, New York (1998)
- [34] W.-P. Huang. *Coupled-mode theory for optical waveguides: an overview*. J. Opt. Soc. Am. A, 11 pp. 963–983 (1994)
- [35] D. Marcuse. *Directional Couplers Made of Nonidentical Asymmetric Slabs. Part II: Grating-Assisted Couplers*. J. Light. Technol., 5 pp. 268–273 (1987)
- [36] J. L. Archambault et al. *Grating-frustrated coupler: a novel channel-dropping filter in single-mode optical fiber*. Opt. Lett., 19 p. 180 (1994)
- [37] Y. Bai and K. S. Chiang. *Analysis and Design of Long-Period Waveguide-Grating Couplers*. J. Light. Technol., 23 pp. 4363–4373 (2005)
- [38] Y. Bai et al. *Widely tunable long-period waveguide grating couplers*. Opt. Express, 14 pp. 2595–2597 (2006)
- [39] K. C. Chow et al. *UV-written long-period waveguide grating coupler for broadband add/drop multiplexing*. Opt. Commun., 282 pp. 378–381 (2009)
- [40] S.-Y. Tseng. *Synthesis of a 4×4 Walsh–Hadamard Transformer Using Long-Period Waveguide Grating Arrays*. IEEE Photon. Technol. Lett., 21 pp. 972–974 (2009)
- [41] M. P. Posner. *Optical integrated circuits for large-scale quantum networks*. Ph.D. thesis, University of Southampton (2017)
- [42] H. L. Rogers et al. *Experimental observation of coupling between physically separated planar waveguides utilising tilted Bragg grating structures*. In: *Conference: European Conference on Integrated Optics (ECIO)*. Stiges, Spain (2012)
- [43] N. Podoliak et al. *Optical beam splitting and switching based on arrays of tilted Bragg gratings in planar waveguides*. In: *Opto-Electronics and Communications Conference (OECC) and Photonics Global Conference (PGC)*. Singapore, Singapore (2017)

- [44] L. B. Soldano and E. C. M. Pennings. *Optical Multi-Mode Interference Devices Based on Self-Imaging : Principles and Applications*. J. Light. Technol., 13 pp. 615–627 (1995)
- [45] K. Cooney and F. H. Peters. *Analysis of multimode interferometers*. Opt. Express, 24 pp. 22481–22515 (2016)
- [46] M. Rajarajan et al. *A Rigorous Comparison of the Performance of Directional Couplers with Multimode Interference Device*. J. Lightwave Technol., 17 pp. 243–248 (1999)
- [47] S.-Y. Lee et al. *Transformation between directional couplers and multi-mode interferometers based on ridge waveguides*. Opt. Express, 12 pp. 3079–3085 (2004)
- [48] L. Yang et al. *Transformation between directional couplers and multi-mode interferometers based on ridge waveguides*. Appl. Phys. Lett., 93. 203304 (2008)
- [49] M. T. Hill et al. *Optimizing Imbalance and Loss in 2×2 3-dB Multimode Interference Couplers via Access Waveguide Width*. J. Lightwave Technol., 21 pp. 2305–2313 (2003)
- [50] C. K. Madsen et al. *Planar waveguide optical spectrum analyzer using a UV-induced grating*. IEEE J. Sel. Top. Quantum Electron., 4 pp. 925–929 (1998)
- [51] K. K. Mehta and R. J. Ram. *Precise and diffraction-limited waveguide-to-free-space focusing gratings*. Sci. Rep. (2017)
- [52] K. K. Mehta et al. *Integrated optical addressing of an ion qubit*. Nat. Nanotechnol., 11 pp. 1–7 (2016)
- [53] C. Sima et al. *Terahertz bandwidth photonic Hilbert transformers based on synthesized planar Bragg grating fabrication*. Opt. Lett., 38 pp. 3448–3451 (2013)
- [54] M. Jiang et al. *Ultralong π -phase shift fiber Bragg grating empowered single-longitudinal mode DFB phosphate fiber laser with low-threshold and high-efficiency*. Sci. Rep., 8. 13131 (2018)
- [55] B. A. Møller et al. *Silica-Waveguide Thermo-optic Phase Shifter with Low Power Consumption and Low Lateral Heat Diffusion*. IEEE Photonic. Tech. L., 5 pp. 1415–1418 (1993)
- [56] M. Jacques et al. *Optimization of thermo-optic phase-shifter design and mitigation of thermal crosstalk on the SOI platform*. Opt. Express, 27 pp. 10456–10471 (2019)
- [57] K. P. Zetie et al. *How does a Mach–Zehnder interferometer work?* Phys. Educ., 35 pp. 46–48 (2000)
- [58] A. Politi et al. *Integrated Quantum Photonics*. IEEE J. Sel. Top. Quant. Electron., 15 pp. 1673–1684 (2009)

- [59] M. R. Watts et al. *Adiabatic thermo-optic Mach–Zehnder switch*. Opt. Lett., 5 pp. 1415–1418 (1993)
- [60] C.-K. Li et al. *Decomposition of Unitary Matrices and Quantum Gates*. Int. J. Quantum. Inf., 11. 1350015 (2013)
- [61] W. R. Clements et al. *Optimal design for universal multiport interferometers*. Optica, 3 pp. 1460–1465 (2016)
- [62] T. W. Hughes et al. *Training of photonic neural networks through in situ back-propagation and gradient measurement*. Optica, 5 pp. 864–871 (2018)
- [63] F. Flamini et al. *Photonic quantum information processing: a review*. Rep. Prog. Phys., 82. 016001 (2019)
- [64] M. G. Thompson et al. *Integrated waveguide circuits for optical quantum computing*. IET Circ. Devices Syst., 5 pp. 94–102 (2011)
- [65] F. Flamini et al. *Thermally reconfigurable quantum photonic circuits at telecom wavelength by femtosecond laser micromachining*. Light. Sci. Appl., 4. E354 (2015)
- [66] N. M. A. and I. L. Chuang. *Quantum Computation and Quantum Information*. Cambridge University Press, Cambridge, first edn. (2000)
- [67] A. Crespi et al. *Integrated photonic quantum gates for polarization qubits*. Nat. Commun., 2. 556 (2011)
- [68] X. Qiang et al. *Large-scale silicon quantum photonics implementing arbitrary two-qubit processing*. Nat. Photon., 12 pp. 543–539 (2018)
- [69] A. Crespi et al. *Suppression law of quantum states in a 3D photonic fast Fourier transform chip*. Nat. Commun., 7. 10469 (2016)
- [70] N. C. Harris et al. *Quantum transport simulations in a programmable nanophotonic processor*. Nat. Photonics, 11 pp. 447–452 (2017)
- [71] H. L. Rogers et al. *In situ loss measurement of direct UV-written waveguides using integrated Bragg gratings*. Opt. Lett., 35 pp. 2849–2851 (2010)
- [72] P. C. Gow et al. *Direct UV-written integrated waveguides using 213nm light (Conference Presentation)*. In: *Integrated Optics: Devices, Materials, and Technologies XXII*, 105350M. San Francisco, United States (2018)
- [73] M. Kawachi. *Silica waveguides on silicon and their application to integrated-optic components*. Opt. Quant. Electron., 22 pp. 391–416 (1990)
- [74] Y. P. Li and C. H. Henry. *Silica-based optical integrated circuits*. IEE Proc. Optoelectron., 143 pp. 263–280 (1996)

- [75] T. E. Murphy et al. *Fabrication and Characterization of Narrow-Band Bragg-Reflection Filters in Silicon-on-Insulator Ridge Waveguides*. J. Light. Technol., 19 pp. 1938–1942 (2001)
- [76] S. LaRochelle and A. D. Simard. *Silicon photonic Bragg grating devices*. In: *2017 Optical Fiber Communications Conference and Exhibition (OFC)*, 16930162. Los Angeles, CA, United States (2017)
- [77] J. H. Schmid et al. *Subwavelength Grating Structures in Silicon-on-Insulator Waveguides*. Adv. Opt. Technol., 2008. 685489 (2008)
- [78] C. L. R. et al. *Subwavelength Grating Waveguide Devices for Telecommunications Applications*. IEEE J. Sel. Top. Quantum Electron., 25. 8200111 (2019)
- [79] J. M. Luque-González et al. *Tilted subwavelength gratings: controlling anisotropy in metamaterial nanophotonic waveguides*. Opt. Lett., 43 pp. 4691 – 4694 (2018)
- [80] J. M. Luque-González et al. *Polarization splitting directional coupler using tilted subwavelength gratings*. Opt. Lett., 45 pp. 3398 – 3401 (2020)
- [81] R. Marchetti et al. *Coupling strategies for silicon photonics integrated chips [Invited]*. Photonics Res., 7 pp. 201 – 239 (2019)
- [82] O. A. J. Gordillo et al. *Plug-and-play fiber to waveguide connector*. Opt. Express, 27 pp. 20305 – 20310 (2019)
- [83] L. Eldada et al. *Advanced polymer systems for optoelectronic integrated circuit applications*. In: *Optoelectronic Integrated Circuits*. San Jose, CA, United States (1997)
- [84] J.-S. Koo et al. *UV written waveguides using crosslinkable PMMA-based copolymers*. Opt. Matter., 23 pp. 583–592 (2003)
- [85] M.-C. Oh et al. *Polymeric wavelength filters with polymer gratings*. Appl. Phys. Lett., 72 pp. 1559–1561 (1998)
- [86] K. S. Chiang et al. *Long-Period Waveguide Gratings*. Jpn. J. Appl. Phys., 43 pp. 5690–5696 (2004)
- [87] K. P. Lor et al. *UV-Written Long-Period Gratings on Polymer Waveguides*. IEEE Photonic. Tech. L., 17 pp. 594–596 (2005)
- [88] X. Xu et al. *Circular-core single-mode polymer waveguide for high-density and high-speed optical interconnects application at 1550 nm*. Opt. Express, 25 pp. 25689–25696 (2017)
- [89] J. Halldorsson et al. *High index contrast polymer waveguide platform for integrated biophotonics*. Opt. Express, 18 pp. 16217–16226 (2010)

- [90] M. Kawachi et al. *Fabrication of SiO₂-TiO₂ glass planar optical waveguides by flame hydrolysis deposition*. Electron. Lett., 19 pp. 594–596 (1983)
- [91] S. P. Watts. *Flame hydrolysis deposition of photosensitive silicate layers for the definition of waveguiding structures through direct ultraviolet writing*. Ph.D. thesis, University of Southampton (2001)
- [92] D. L. Williams et al. *Enhanced UV photosensitivity in boron codoped germanosilicate fibres*. Electron. Lett., 29 pp. 45–47 (1993)
- [93] M. Huang. *Thermal stresses in optical waveguides*. Opt. Lett., 28 pp. 2327–2329 (2003)
- [94] K. O. Hill et al. *Photosensitivity in optical fiber waveguides: Application to reflection filter fabrication*. Appl. Phys. Lett., 32 pp. 647–649 (1978)
- [95] G. Meltz et al. *Formation of Bragg gratings in optical fibers by a transverse holographic method*. Optics Letters, 14 pp. 823–825 (1989)
- [96] M. Douay et al. *Densification Involved in the UV-Based Photosensitivity of Silica Glasses and Optical Fibers*. J. Light. Technol., 15 pp. 1329–1342 (1997)
- [97] K. O. Hill et al. *Photosensitivity in optical fibres*. Annu. Rev. Mater. Sci., 23 pp. 125–157 (1993)
- [98] P. J. Lemaire et al. *High pressure H₂ loading as a technique for achieving ultrahigh UV photosensitivity and thermal sensitivity in GeO₂ doped optical fibres*. Electron. Lett., 29 pp. 1191–1193 (1993)
- [99] P. C. Gow et al. *Integrated Waveguides and Bragg Gratings UV Written with 213Nm Light*. In: *2019 Conference on Lasers and Electro-Optics Europe & European Quantum Electronics Conference (CLEO/Europe-EQEC)*, 19148141. Munich, Germany (2019)
- [100] Y.-J. Rao. *In-fibre Bragg grating sensors*. Meas. Sci. Technol., 8 pp. 355–375 (1997)
- [101] M. Svalgaard et al. *Direct UV writing of buried singlemode channel waveguides in Ge-doped silica films*. Electronics Letters, 30 pp. 1401–1403 (1994)
- [102] G. D. Emmerson et al. *Fabrication of directly UV-written channel waveguides with simultaneously defined integral Bragg gratings*. Electronics Letters, 38 pp. 1531–1532 (2002)
- [103] S. L. Jantzen et al. *Superstructure and superimposed fiber Bragg gratings fabricated through small spot direct UV writing*. In: *CLEO Pacific Rim 2020*. Sydney, Australia (2020)

- [104] C. Holmes et al. *Excitation of Surface Plasmons Using Tilted Planar-Waveguide Bragg Gratings*. IEEE Photonics J., 3 pp. 777–788 (2011)
- [105] S. Ambran et al. *Fabrication of a Multimode Interference Device in a Low-Loss Flat-Fiber Platform Using Physical Micromachining Technique*. J. Lightwave Technol., 30 pp. 2870–2875 (2012)
- [106] L. G. Carpenter et al. *Ductile dicing of LiNbO₃ ridge waveguide facets to achieve 0.29 nm surface roughness in single process step*. Electron. Lett., 53 pp. 1672–1674 (2017)
- [107] A. C. Gray et al. *Investigation of PPLN Waveguide Uniformity via Second Harmonic Generation Spectra*. IEEE Photon. Technol. Lett., 32 pp. 63–66 (2020)
- [108] L. Riviere et al. *Properties of single-mode optical planar waveguides with Gaussian index profile*. J. Light. Technol., 3 pp. 368–377 (1985)
- [109] S. D. Gedney. *An anisotropic perfectly matched layer-absorbing medium for the truncation of FDTD lattices*. IEEE Trans. Antennas and Propag., 44 pp. 1630–1639 (1996)
- [110] P. C. Gow et al. *Direct UV written integrated planar waveguides using a 213 nm laser*. Opt. Express, 27 pp. 29133–29137 (2019)
- [111] H.-C. Liu and A. Yariv. *Grating induced transparency (GIT) and the dark mode in optical waveguides*. Opt. Express, 17 pp. 11710–11718 (2008)
- [112] B. Fornberg. *Generation of Finite Difference Formulas on Arbitrarily Spaced Grids*. Math. Comput., 51 pp. 699–706 (1988)
- [113] SciPy.org. *scipy.integrate.solvebvp*
URL https://docs.scipy.org/doc/scipy-0.18.1/reference/generated/scipy.integrate.solve_bvp.html
- [114] J. Kierzenka and L. F. Shamane. *A BVP Solver Based on Residual Control and the Matlab PSE*. ACM Trans. Math. Softw., 27 pp. 299–316 (2001)
- [115] T. Komukai et al. *An Efficient 0.04-nm Apodized Fiber Bragg Grating and Its Application to Narrow-Band Spectral Filtering*. IEEE Photonic. Tech. L, 9 pp. 934–936 (1997)
- [116] P. S. et al. *Multi-Wavelength Narrow Linewidth Random Fiber Laser Based on Fiber Bragg Grating Fabry-Perot Filter*. In: *10th International Conference on Information Science and Technology*. Bath, United Kingdom (2020)
- [117] O. A. et al. *Fibre Bragg Gratings*. In: H. Venghaus (ed.), *Wavelength Filters in Fibre Optics*. Springer, Berlin, Heidelberg (2006)

- [118] D. Mechin et al. *Add – Drop Multiplexer With UV-Written Bragg Gratings and Directional Coupler in SiO₂ – Si Integrated Waveguides*. J. Lightw. Technol., 19 pp. 1282–1286 (2001)
- [119] H. Rogers. *Direct UV-written Bragg gratings for waveguide characterisation and advanced applications*. Ph.D. thesis, University of Southampton (2013)
- [120] J. C. Gates et al. Private communication (2020)
- [121] D. B. Leviton and B. J. Frey. *Temperature-dependent absolute refractive index measurements of synthetic fused silica*. In: *Optomechanical Technologies for Astronomy*. Orlando, United States (2006)
- [122] Accuratus. *Fused Silica, SiO₂ Glass Properties* (<https://www accuratus.com/fused.html> (accessed 28/03/2019))
URL <https://www accuratus.com/fused.html>
- [123] C. Holmes et al. *150 GHz of thermo-optic tuning in direct UV written silica-on-silicon planar Bragg grating*. Electron. Lett., 45 pp. 954–956 (2009)
- [124] K. E. Chisholm et al. *Effects of thermal annealing on Bragg fibre gratings in boron/germanio-doped fibre*. J. Phys. D: Appl. Phys., 31 pp. 61–64 (1998)
- [125] S. R. Abdullina and A. A. Vlasov. *Suppression of Side Lobes in the Fiber Bragg Grating Reflection Spectrum*. Optoelectron. Instrum. Data Process., 50 pp. 75–86 (2014)
- [126] F. R. M. Adikan. *Direct UV-Written Waveguide Devices*. Ph.D. thesis, University of Southampton (2007)
- [127] P. Bienstman et al. *Calculation of Bending Losses in Dielectric Waveguides Using Eigenmode Expansion and Perfectly Matched Layers*. IEEE Photonic. Tech. L., 14 pp. 164 – 166 (2002)
- [128] C. Holmes. *Direct UV Written Planar Devices for Sensing and Telecommunication Applications*. Ph.D. thesis, University of Southampton (2009)
- [129] M. Olivero and M. Svalgaard. *Direct UV-written broadband directional planar waveguide couplers*. Opt. Express, 13 pp. 8390–8399 (2005)

Planar waveguide coupler based on tilted Bragg gratings and a discrete cladding mode

Mathias J. Weisen, Matthew T. Posner, James C. Gates, Corin B. E. Gawith, Peter G.R. Smith, Peter Horak
Optoelectronics Research Centre, University of Southampton, Southampton, UK
m.j.weisen@soton.ac.uk

Abstract

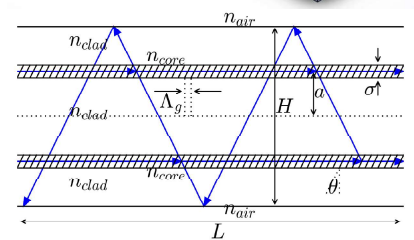
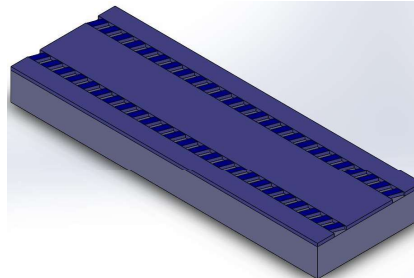
A new type of planar waveguide to waveguide coupler is presented based on two parallel single-mode waveguides written in the same ridge structure. Identical tilted gratings are used to couple light between the waveguide using the modes of the ridge. The bandwidth of the device can be controlled by varying the length. A transfer efficiency approaching 100 % is shown to be possible in this system.

Introduction

- We have recently developed tilted Bragg grating technology for use in planar photonics [1].
- Can be used to couple light efficiently between waveguide and radiation/cladding modes.
- An integrated coupler based on two 45° tilted gratings has already been demonstrated [2], but with large losses due to **leakage into radiation modes**.

We simulate a new device that overcomes this limitation:

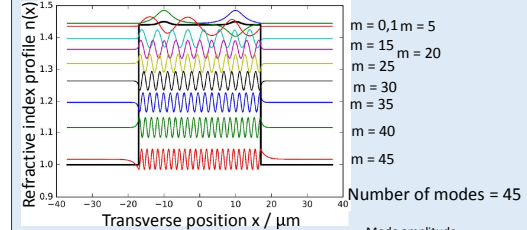
- Single ridge structure containing two parallel waveguides.
- Identical tilted gratings in each waveguide to couple to cladding modes.
- Parameters chosen to couple to a single backward propagating cladding mode.
- Power transfer between waveguides forms a coupler.
- **Bandwidth controlled by grating parameters.**



Δn : waveguide index contrast, Δn_g : grating index contrast
 λ_0 : Free space wavelength, λ_B : Bragg wavelength

Model

Transverse refractive index of structure and modes:



Coupled mode theory [3]:

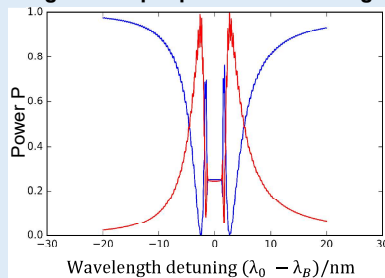
$$\frac{dR_m(z)}{dz} = i \left[\frac{K_g}{2} - \beta_m \right] R_m + \frac{1}{2} \sum_n R_n c_{mn} e^{-i\varphi_{mn}}$$

Grating period Mode propagation constant Coupling coefficient

- c_{mn} found using an overlap integral.
 - Solved numerically as an eigenvalue problem.
- Equation considers only coupling between counter-propagating modes.

Results

Waveguide output power vs wavelength



$H = 34 \mu\text{m}$, $n_{\text{clad}} = 1.4398$,
 $a = 10 \mu\text{m}$, $\sigma = 2.0 \mu\text{m}$,
 $\Delta n = 0.01$, $\Delta n_g = 0.001$,
 $\lambda_B = 1.55 \mu\text{m}$, $\lambda_g = 586.6 \text{ nm}$,
 $\theta = 17.19^\circ$, $L = 20 \text{ mm}$

Couples to mode 35

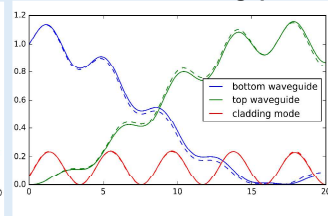
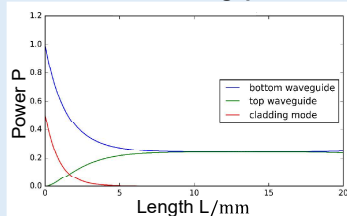
Power at bottom (blue) and top (red) waveguide outputs.

Wavevector phase mismatch
 $\Delta K = K_g + \beta_z - \beta_0$

- With one cladding mode, eigenvalues are $\gamma_0 = \frac{i\Delta K}{2}$, $\gamma_{\pm} = \pm \sqrt{2c^2 - \Delta K^2}$
- Photonic bandgap found in region where $\Delta K < \sqrt{2}c$, γ_{\pm} real:
 - One quarter of the light in each waveguide,
 - Remaining half in cladding mode (exponential behaviour).

Inside bandgap

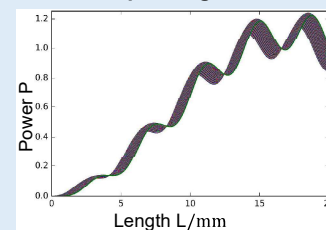
Outside bandgap



- Outside of bandgap, $\gamma_{\pm} = \pm i\Omega$ imaginary:
 - Oscillatory behaviour, beating between eigenfrequencies.
 - Cladding mode oscillates with frequency 2Ω .
 - Power transfer between waveguides approaches 100 %. Oscillation of lower frequency $\frac{\Delta K}{2} - \Omega$.

Selective transference of particular frequencies means that the device can be used as a wavelength division multiplexer (WDM).

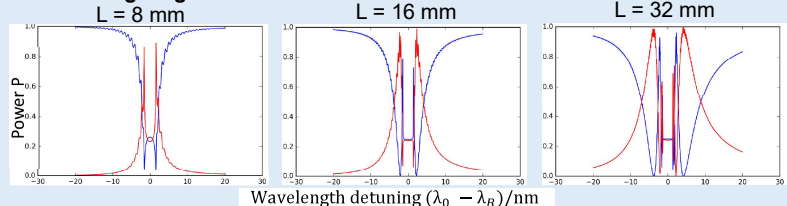
Power in top waveguide for different device lengths



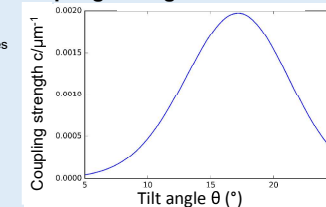
Top waveguide: points at which power does not depend on device length.

High fabrication tolerance with device length

Increasing length increases bandwidth



Coupling strength between waveguide and cladding mode vs tilt angle

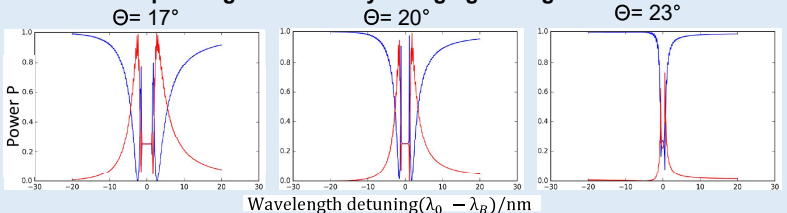


Peak at tilt angle expected by geometric optics.

Highest bandwidth at peak

That's why we need tilted gratings!

Control of operating bandwidth by changing tilt angles



Conclusions

We presented a new type of waveguide coupler that can couple light very efficiently between two waveguides. The use of tilted gratings allows for bandwidth control of the coupler which adds a new functionality in planar photonics. This could therefore be used as a flexible platform for the fabrication of new wavelength division multiplexers (WDM) or frequency filters.

[1] C. Sima et al., *Ultra-wide detuning planar Bragg grating fabrication technique based on direct UV grating writing with electro-optic phase modulation*, Optics Express, Vol. 21, 15747 (2013)

[2] M. T. Posner et al., *Integrated polarizing coupler based on tilted gratings*, In: Integrated Photonics Research, Silicon and Nanophotonics. Vancouver, Canada (2016)

[3] K. Okamoto, *Fundamentals of optical waveguides*, Elsevier, Amsterdam, second edn. (2008)

Low-loss wavelength-selective integrated waveguide coupler based on tilted Bragg gratings

MATHIAS J. WEISEN^{1,*}, MATTHEW T. POSNER¹, JAMES C. GATES¹, CORIN B. E. GAWITH¹, PETER G. R. SMITH¹, AND PETER HORAK¹

¹Optoelectronics Research Centre, University of Southampton, Southampton SO17 1BJ, United Kingdom

*Corresponding author: m.j.weisen@soton.ac.uk

Compiled May 22, 2019

We propose and investigate numerically a new kind of integrated optical waveguide coupler. Two waveguides with tilted Bragg gratings couple selectively to a discrete counter-propagating cladding mode which acts as an intermediary to transfer power between the waveguides. This gives a highly versatile platform that can act as a low-loss coupler with arbitrary coupling ratio between 0 and 100%, as a narrow-bandwidth wavelength filter, and as a phase-selective switch that transmits two light waves of a fixed relative phase but reflects the orthogonal phase within a single device. © 2019 Optical Society of America

<http://dx.doi.org/10.1364/ao.XX.XXXXXX>

1. INTRODUCTION

Directional couplers are a key component in planar photonics circuits as well as in optical fiber networks. Traditionally, coupling is achieved by bringing two waveguides close together in order to cause a spatial overlap between their modes [1]. Variations on this scheme utilize Bragg gratings to assist phase matched coupling between asymmetric waveguides [2], frustrate coupling at a particular frequency [3] or to form add-drop multiplexers [4]. Similar devices have also been realized in non-silica material platforms, e.g., grating assisted wavelength selective couplers [5] and wavelength division multiplexers [6, 7] have been demonstrated in silicon photonics.

By tilting the grating planes of a Bragg grating away from perpendicular to the propagation direction of the waveguides the full spatial degrees of freedom of light propagation in the device can be exploited, which opens up a host of novel device functionalities. Such tilted gratings work by not only phase matching modes in the forward propagation direction, but also matching the propagation constants in the transverse direction to achieve efficient coupling of waveguides to unbound radiation modes [8] or to higher order guided or cladding modes [9] in analogy to blazed diffraction gratings. While such tilted Bragg gratings offer significant potential benefits in efficiency and tunability of waveguide devices, only a few applications have been demonstrated so far, such as in spectrometry [10], waveguide division multiplexing [11], out of plane coupling to a Gaussian mode [12], and refractometry [13].

Here we investigate a new design of a directional coupler based on tilted Bragg gratings where the two waveguides sit on a common ridge structure cut into the substrate. The ridge structure only supports a limited number of discrete cladding

modes, and thus by tailoring the grating parameters it is possible to design an optical coupler utilizing only a single cladding mode as intermediary between the waveguides. This allows for low-loss waveguide coupling with arbitrary coupling efficiency up to 100%. By using a *counter-propagating* cladding mode the coupling becomes highly wavelength selective and the device acts as a narrowband coupler and/or wavelength filter. We also show that the device can operate as a phase-sensitive switch: if light is coupled simultaneously into both waveguides, then depending on the relative phase of the two waves they can either be transmitted through the device by a grating induced transparency [14] or completely reflected.

Apart from applications as filters and wavelength division multiplexers in optical telecommunication systems, the wide range of potential functionalities and low loss of our device will make it a powerful component in quantum information networks. For example, it could enhance multiphoton quantum interference devices [15, 16] by allowing photon coupling between waveguides beyond nearest neighbors, or act as a narrow-band filter to separate entangled photons generated by frequency conversion from the strong pump field [17].

Fabrication of such devices is feasible using direct UV writing, a laser fabrication technique for the simultaneous definition of waveguides and gratings through the exposure of photosensitive silica layers to UV radiation [18]. It offers excellent phase stability and control of grating properties, low cost and low insertion loss [18, 19]. Polarizers [20] and polarizing waveguide to waveguide couplers [21] based on this technology were fabricated. However, these devices exploited a continuum of substrate modes as intermediaries to couple light between waveguides, which led to very low coupling efficiencies compared

to those achievable if a discrete set of cladding modes is used [22–24].

This paper is structured as follows. In Sec. 2 we describe the geometry of the coupler and give an overview of the coupled mode theory we use to simulate the device. We then derive an analytical solution of the coupled mode model in the limit where only one cladding mode is coupled effectively to the waveguides in Sec. 3 and discuss grating induced transparency in Sec. 4. In Sec. 5 we show that the numerical and analytical models are consistent and we discuss some main properties of the device. In Sec. 6 we investigate the parameter dependence of the device operation bandwidth and in Sec. 7 its temperature sensitivity. Finally, we summarize and conclude our findings in Sec. 8.

2. DEVICE GEOMETRY AND THEORETICAL DESCRIPTION

A cross section schematic of the proposed device is shown in Fig. 1(a). Using direct UV writing, two parallel single-mode channel waveguides are fabricated, simultaneously with two identical tilted Bragg gratings, into a photosensitive raised refractive index core layer that forms part of a ridge structure. The ridge can be created by physically micro-machining two trenches on either side using the same fabrication method as [13, 25]. The narrow core layer confines light to a single transverse mode in the vertical (y) direction, while the ridge structure provides confinement in the x -direction and thus only allows for a finite number of discrete modes in the core layer with well separated modal effective indices. This structure therefore maximizes overlap and coupling between the waveguide modes and the cladding modes within this core layer. Fig. 1(b) shows a schematic of the refractive index profile in the x -direction inside the core layer and three of the modes guided in this core layer, calculated by a finite element method (FEM) using Comsol Multiphysics® for a core layer of thickness $2.0\ \mu\text{m}$ and a refractive index of 1.4468 and overlaid and underclad layers with a refractive index of 1.4368.

Our design features Bragg gratings with a short period and a small tilt angle in order to couple the waveguide modes to the backward propagating cladding modes of the ridge to allow for efficient coupling and short device lengths. The cladding modes are then used as an intermediary between the two waveguides as shown in Fig. 1(c). All light remains within the modal structure of the waveguides and the cladding and so, unlike in a system exploiting the continuum of substrate modes as intermediaries [21], there is in theory no loss of light from coupling to unbounded modes. There is also no need to bring the waveguides physically close together as in evanescent field couplers.

For clarity we use a simplified theoretical model of the device in the following. First, we only consider a two-dimensional model, i.e., we ignore the thin core layer that provides confinement in the y -direction and assume an infinitely extended structure in this direction instead. Second, we only consider the transverse electric (TE, or y -polarized) modes of the device. In this case the modes exhibit only one component of the electric field which satisfies the wave equation

$$\frac{d^2\psi(x)}{dx^2} + k_0^2[n^2(x) - n_z^2]\psi(x) = 0 \quad (1)$$

where $\psi(x)$ is the transverse profile of the mode, $n_z = \beta_z/k_0$ is the effective refractive index in the z -direction, k_0 is the free space wavenumber of the light and β_z is the z -component of the propagation constant for this mode. $n(x)$ is the transverse

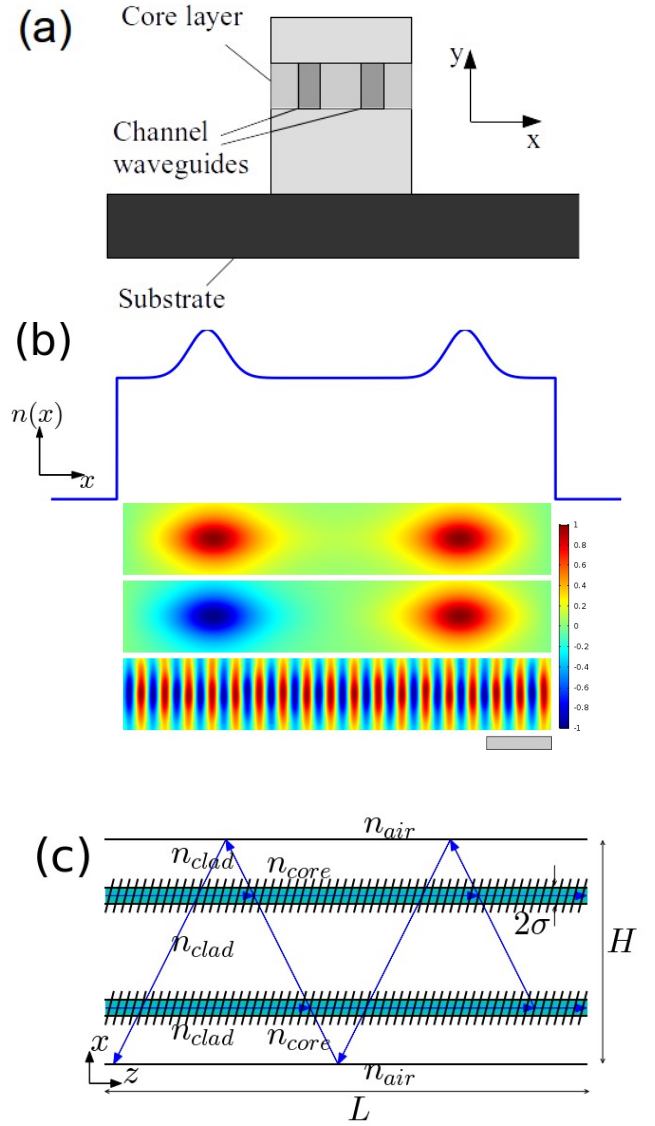


Fig. 1. (a) 2D cross section of the cladding-mode based waveguide coupler. (b) Schematic of the refractive index profile across the core layer and FEM calculations of the symmetric core mode, antisymmetric core mode, and a higher order cladding mode, all confined within the core layer. The grey scalebar corresponds to $5\ \mu\text{m}$. (c) Top view of the structure inside the core layer, where the waveguides are indicated in cyan and the tilted gratings by the diagonal grid lines, with definition of system parameters and ray diagram of coherently scattered light from the gratings.

refractive index profile of the cladding and the waveguides and is defined as

$$n(x) = n_{\text{clad}} + \Delta n \rho(x) \quad (2)$$

$$\rho(x) = \exp\left(\frac{-(x-x_0)^2}{\sigma^2}\right) + \exp\left(\frac{-(x+x_0)^2}{\sigma^2}\right) \quad (3)$$

inside the region $|x| \leq H/2$ and $n(x) = 1$ outside of it; $\rho(x)$ is the transverse profile of the waveguides. This defines two waveguides of refractive index contrast Δn and of $1/e$ width σ that are placed at a distance of $\pm x_0$ from the center of the ridge. The ridge itself has a width of H and a refractive index of n_{clad} . We choose Δn to be sufficiently small such that the waveguides support only a single mode. The eigenmodes $\psi_n(x)$ of the wave equation (1) with the refractive index profile (2) are then calculated numerically using a finite differences method.

Without the use of Bragg gratings the waveguide modes would remain decoupled from each other. The gratings act as a perturbation to the original waveguide structure leading to coupling between the waveguide modes and the cladding modes. The perturbation from the Bragg gratings is defined by

$$\delta n(x) = \Delta n_g \rho(x) \sin[K_g(z - x \tan \theta)] \quad (4)$$

where Δn_g is the refractive index modulation of the gratings, K_g is the longitudinal wave vector of the grating, θ is the tilt angle, and the transverse profile $\rho(x)$ is the same as for the waveguides themselves, Eq. (3).

Applying standard coupled mode theory [19], we can then calculate the coupling coefficients between modes ψ_n and ψ_m of the device,

$$d_{mn+} = \frac{k_0}{2c\mu_0} \text{sign}(m) \times \int n(x) \Delta n_g \cos(K_t x) \rho(x) \psi_m^*(x) \psi_n(x) dx \quad (5)$$

and

$$d_{mn-} = -\frac{k_0}{2c\mu_0} \text{sign}(m) \times \int n(x) \Delta n_g \sin(K_t x) \rho(x) \psi_m^*(x) \psi_n(x) dx \quad (6)$$

where c is the speed of light and $K_t = K_g \tan \theta$ is the transverse wavevector and we have introduced the notation that $m > 0$ denotes forward propagating modes and $m < 0$ backward propagating modes. The two components $d_{mn\pm}$ can be rewritten as an amplitude and phase,

$$g_{mn} = \sqrt{d_{mn+}^2 + d_{mn-}^2}, \quad (7)$$

$$\phi_{mn} = \tan^{-1}\left(\frac{d_{mn-}}{d_{mn+}}\right). \quad (8)$$

The dynamics of the electric field amplitudes $A_m(z)$ propagating in modes m along the device are then given by the coupled mode equations [19]

$$\frac{dA_m(z)}{dz} = -\frac{1}{2} \sum_n \left(e^{i[(\beta_m - \beta_n + K_g)z + \phi_{mn}]} - e^{i[(\beta_m - \beta_n - K_g)z - \phi_{mn}]} \right) A_n(z) g_{mn} \quad (9)$$

where $\beta_m = \beta_z$ for mode m .

In this paper we assume short period Bragg gratings that couple only modes traveling in opposite directions. This allows us to greatly simplify the problem and only consider the two forward propagating waveguide modes and the backward propagating cladding modes. Eq. (9) can then be rewritten as

$$\frac{d\mathcal{R}_m(z)}{dz} = i\left(\frac{K_g}{2} - \beta_m\right)\mathcal{R}_m(z) + \frac{1}{2} \sum \mathcal{R}_{-n}(z) g_{mn} e^{-i\phi_{mn}} \quad (10)$$

where $\mathcal{R}_m(z) = A_m e^{iK_g z/2}$ and $\mathcal{R}_{-m}(z) = A_{-m} e^{-iK_g z/2}$.

Eq. (10) is then solved numerically as follows. First, the eigen solutions of this linear set of equations are found. Next, the boundary conditions are applied, which in our case are that light is launched at $z = 0$ into only one waveguide, whereas the other waveguide is empty at $z = 0$. Additionally, the backward propagating cladding modes are all empty at the output, $z = L$, where L is the device length. These boundary conditions give a linear set of equations for the amplitudes of the eigen solutions of (10), which is solved easily and thus contains the full system dynamics along z . A full analytical solution in the special case where only a single cladding mode is involved is given below in Sec. 3.

We consider a cladding of refractive index $n_{\text{clad}} = 1.4398$ and width $H = 34 \mu\text{m}$. Two waveguides of refractive index depth $\Delta n = 0.01$ and width $\sigma = 2.0 \mu\text{m}$ are written at $x_0 = 10 \mu\text{m}$ from the center of the device, and the light wavelength is $\lambda_0 = 1.55 \mu\text{m}$. To ensure accurate computation of modes, we use 4001 grid points in the ridge region including one at each interface and include $5 \mu\text{m}$ of air on either side in the simulation. The finite differences method is computed with an accuracy level of 4 as defined in [26]. For these parameters, 46 waveguide and cladding modes have been found as shown in Fig. 2. We see that the two waveguide modes have near identical n_z which implies that evanescent coupling between them is very weak. Higher order modes are spaced increasingly further apart, as expected for a step-index profile. In Fig. 3 we show the transverse mode profiles of the 0th, 1st and 35th modes which we mainly use in our discussions below.

In Fig. 4 we show the coupling coefficients of the cladding modes to the waveguide modes for different values of the transverse wave vector of the grating $K_t = K_g \tan \theta$. For $K_t = 0$, i.e. with grating planes perpendicular to the waveguides, coupling is strongest to the low order modes which only have a small transverse propagation constant. Higher order modes, on the other hand, with a larger transverse propagation constant are not phase matched in the transverse direction and are therefore only weakly coupled. By introducing a tilt angle, i.e. increasing K_t , efficient coupling to increasingly higher order cladding modes is observed. Because of the finite physical width of the grating, its transverse index profile has Fourier components at wavenumbers other than K_t which allows for coupling to a relatively broad range of cladding modes. This implies that the device is relatively robust to the fabrication tolerance of the tilt angle. Oscillations in the $K_t = 0.0 \mu\text{m}^{-1}$ curve in Fig. 4 are a result of changing overlap between the cladding mode and the waveguides. If a maximum (or minimum) of the electric field of a mode coincides with a waveguide, this leads to a larger (or smaller) coupling coefficient.

3. ANALYTICAL SOLUTION

If the cladding modes have sufficiently different values of n_z , the grating properties can be chosen such that only a single (backward propagating) cladding mode is phase matched to

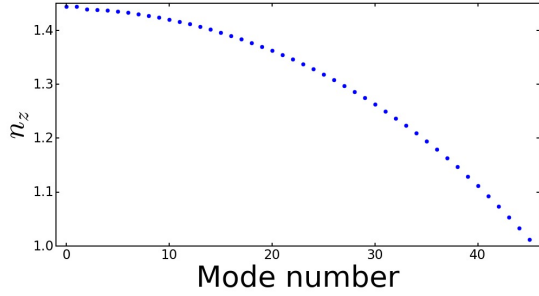


Fig. 2. Value of n_z against mode number with $\Delta n = 0.01$, $\sigma = 2.0 \mu\text{m}$, $x_0 = 10 \mu\text{m}$ and $H = 34 \mu\text{m}$.

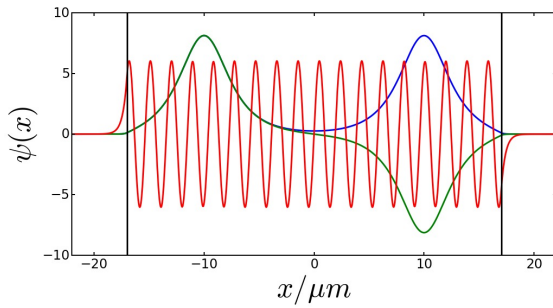


Fig. 3. Transverse profile of modes 0 (blue), 1 (green) and 35 (red) which are the symmetric and anti-symmetric core modes and a cladding mode, respectively. The vertical lines indicate the interface between the ridge structure and the surrounding air.

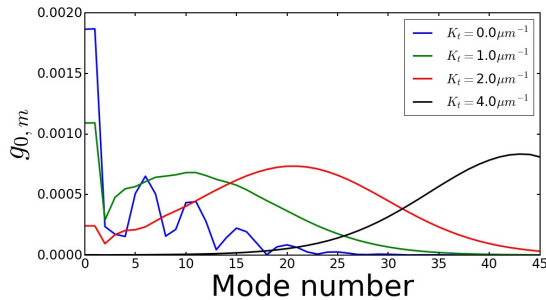


Fig. 4. Coupling coefficients of the waveguide modes to the cladding modes for different values of K_t . $\Delta n = 0.01$, $\sigma = 2.0 \mu\text{m}$, $x_0 = 10 \mu\text{m}$, $H = 34 \mu\text{m}$, $\Delta n_g = 0.001$.

the two waveguide modes in the limit of long device lengths. In this case the system dynamics effectively reduce to three coupled modes and the coupled mode equations (9) can be solved analytically, as shown in the following.

Here we assume that the two waveguide modes have the same propagation constant ($\beta_0 = \beta_1 > 0$) and assign $\beta_2 < 0$ to the cladding mode. The waveguide modes are assumed to couple to the cladding mode with coupling coefficients $ge^{i\phi_0}$ and $ge^{i\phi_1}$ i.e., with the same amplitude but different phases. With the phase mismatch defined as $\Delta K = K_g - \beta_0 + \beta_2$, Eq. (9) becomes

$$\frac{d}{dz} \begin{bmatrix} R_0(z) \\ R_1(z) \\ R_2(z) \end{bmatrix} = \frac{1}{2} \begin{bmatrix} i\Delta K & 0 & -g \\ 0 & i\Delta K & -g \\ -g & -g & -i\Delta K \end{bmatrix} \begin{bmatrix} R_0(z) \\ R_1(z) \\ R_2(z) \end{bmatrix} \quad (11)$$

where

$$\begin{aligned} R_0(z) &= A_0(z)e^{i\phi_0}e^{-\frac{i}{2}\Delta Kz} \\ R_1(z) &= A_1(z)e^{i\phi_1}e^{-\frac{i}{2}\Delta Kz} \\ R_2(z) &= A_2(z)e^{+\frac{i}{2}\Delta Kz}. \end{aligned} \quad (12)$$

Note that the transformed amplitudes R_n are defined slightly differently than \mathcal{R}_n in Eq. (10). Upon diagonalizing the linear Eq. (11) the general solution can be written as a superposition of its eigensolutions,

$$\begin{bmatrix} R_0(z) \\ R_1(z) \\ R_2(z) \end{bmatrix} = p_0 e^{\frac{i}{2}\Delta Kz} \begin{bmatrix} -g \\ g \\ 0 \end{bmatrix} + q_- e^{-\gamma z} \begin{bmatrix} g \\ g \\ i\Delta K + 2\gamma \end{bmatrix} + q_+ e^{+\gamma z} \begin{bmatrix} g \\ g \\ i\Delta K - 2\gamma \end{bmatrix} \quad (13)$$

where $\gamma = \frac{1}{2}\sqrt{2g^2 - \Delta K^2}$ is one of the eigenvalues and p_0 , q_- and q_+ are arbitrary constants. We apply the boundary conditions $R_0(z=0) = 1$, $R_1(z=0) = 0$ and $R_2(z=L) = 0$ which corresponds to light at the input port of only one of the waveguides and no light launched into the cladding mode. This yields a linear set of equations that determine the values of p_0 , q_- and q_+ as

$$\begin{aligned} p_0 &= -\frac{1}{2g} \\ q_+ &= \frac{Y^2 \Delta K^2 + 2\Delta K\Omega + 4X^2\Omega^2 + iXY[\Delta K^2 - 4\Omega^2]}{g(Y^2 \Delta K^2 + 4X^2\Omega^2)} \\ q_- &= \frac{1}{2g} - q_+ \end{aligned} \quad (14)$$

where $X = \cos(\Omega L)$, $Y = \sin(\Omega L)$.

We can distinguish two different regimes of behavior. Close to phase-matching, in the region where $|\Delta K| \leq \sqrt{2}g$, γ is real and the last two terms of Eq. (13) exhibit exponential behavior. For a long device ($L \gg 1/\gamma$), we can easily show that the constant $q_+ \rightarrow 0$ and so:

$$\begin{aligned} R_0(z) &= \frac{1}{2}(e^{i\Delta Kz} + e^{-\gamma z}) \\ R_1(z) &= \frac{1}{2}(-e^{i\Delta Kz} + e^{-\gamma z}) \\ R_2(z) &= \frac{1}{\sqrt{2}}e^{-\gamma z}. \end{aligned} \quad (15)$$

Thus, for $z \gg 1/\gamma$ the power in the device (proportional to $|R_n|^2$) tends towards one quarter in each waveguide, the remaining half being reflected backwards into the cladding mode.

Outside of the bandgap (i.e. for $|\Delta K| > \sqrt{2}g$), all eigenvalues in Eq. (13) are imaginary and we have an oscillatory solution of the amplitudes of the light fields in the three modes. The three spatial eigenfrequencies are $\Delta K/2$ and $\pm\Omega$ where $\Omega = \frac{1}{2}\sqrt{\Delta K^2 - 2g^2} = -i\gamma$. The propagating power in each mode is again given by $|A_n(z)|^2$. This results in a beating between the spatial oscillation frequencies, such that the power in the two waveguide modes has the following frequency terms: 2Ω , $\Delta K/2 + \Omega$, $\Delta K/2 - \Omega$. A comparison of the analytic solutions (13) with a numerical solution of Eq. (10) including all cladding modes will be discussed in Sec. 5, as well as a more detailed investigation of the device behavior.

4. PHASE-SELECTIVE GRATING INDUCED TRANSPARENCY

Equation (13) shows that our system allows for a specific superposition of light fields inside the two waveguides to be transmitted without loss through the device through grating induced transparency [14]. Specifically, light launched into the eigenvector

$$\begin{bmatrix} -g \\ g \\ 0 \end{bmatrix},$$

i.e. in an antisymmetric superposition of light in the two waveguides, will be transmitted without ever coupling light into the cladding mode because of destructive interference of the coupling from the two individual waveguides. On the other hand, light launched into a symmetric superposition of fields in the two waveguides will couple strongly to the cladding mode and therefore, within the grating band gap $|\Delta K| \leq \sqrt{2}g$, will be totally reflected into the cladding mode. Thus, if light is launched simultaneously into both waveguides with the same amplitude the device can act as a phase-sensitive switch, i.e. transmitting or reflecting all light with 100% efficiency depending on the relative phase between the waveguides.

This result also explains the finding of Eq. (15) where one quarter of the light power, proportional to $|R_n|^2$ ($n = 0, 1$), is transmitted in each waveguide when light is launched into a single waveguide within the grating bandgap: Coupling light into a single waveguide at the input is equivalent to launching 50% into the symmetric and 50% into the antisymmetric superposition mode of the two waveguides. Thus, 50% of the power is reflected into the backward propagating cladding mode and the remaining power is within the antisymmetric forward propagating waveguide superposition mode and therefore 25% of the power is in each waveguide.

We note that while in the discussion above we assumed equal coupling strengths of the two waveguides to the cladding mode, this is not in fact essential and an equivalent fully transmitted superposition mode exists also in the general case of the two waveguides coupling with different strengths and different relative phases to the cladding mode. In this case, the transmitted superposition mode contains unequal light power in the two waveguides.

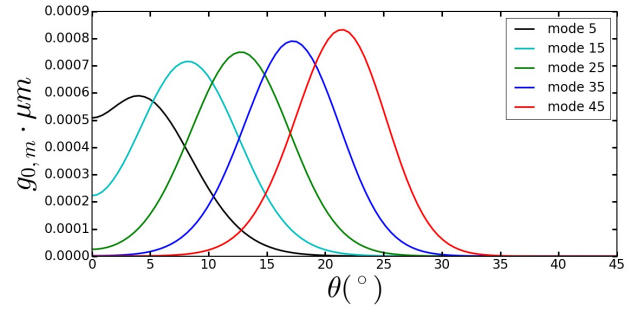


Fig. 5. Coupling coefficient between the core waveguide mode and a selection of backward propagating cladding modes as a function of tilt angle. $\Lambda_g = 587.34$ nm and $\Delta n_g = 0.001$.

5. NUMERICAL RESULTS

For numerical simulations we pick a particular cladding mode to couple to the core modes. Specifically, in the following we choose mode number 35 with $n_z = 1.1946$. The difference in n_z from the nearest neighboring cladding mode is 0.0148 and thus the difference in propagation constant $0.0599 \mu\text{m}^{-1}$ is larger than the coupling constants of order $10^{-3} \mu\text{m}^{-1}$ for the parameters used below, which ensures that coupling of the waveguide modes will be predominantly with this one cladding mode for appropriately chosen grating periods. With $n_z = 1.4445$ for the core waveguide modes, we find a grating period of $\Lambda_g = 587.34$ nm to achieve phase matching between the waveguide modes and this cladding mode. A grating depth of $\Delta n_g = 0.001$ is used in the following [18].

In Fig. 5, we plot the coupling coefficient between the waveguide core mode and a selection of cladding modes, including the 35th mode, as a function of tilt angle as calculated from Eqs. (5)-(7). We find a strong dependence on the tilt angle. In the vicinity of $\theta = 0^\circ$ which corresponds to regular, non-tilted, Bragg gratings there is very little coupling between the waveguide core mode and the higher order cladding modes. Non-tilted gratings can therefore only be used to couple to some low order modes. However, the n_z difference between low order modes is small, see Fig. 2, and therefore several cladding modes will be approximately phase matched with the grating simultaneously, thereby degrading the performance of the device. Reducing the grating strength will reduce this unwanted coupling to neighboring cladding modes but requires the use of unfeasible long devices.

Alternatively, higher order modes can be exploited which have much larger differences of n_z between them and thus a single mode can be isolated to couple efficiently to the grating. To achieve strong coupling with realistic grating strengths and thus short device lengths tilted gratings are then required as shown in Fig. 5. This is the main driver for our device design based on tilted Bragg gratings and the use of higher order modes. The coupling coefficient with mode 35 is found to be greatest for a tilt angle of 17.23° .

For these parameters and a device length of 20 mm, we show the evolution of the propagating power in the system as a function of distance in Fig. 6 obtained numerically including all cladding modes and compare the results with the analytic solution involving only three modes from Sec. 3. Here, we denote the waveguide that receives the input "waveguide 1" and the other "waveguide 2".

In agreement with the discussion of Sec. 3, inside the bandgap, Fig. 6(a) shows the power asymptotically approach-

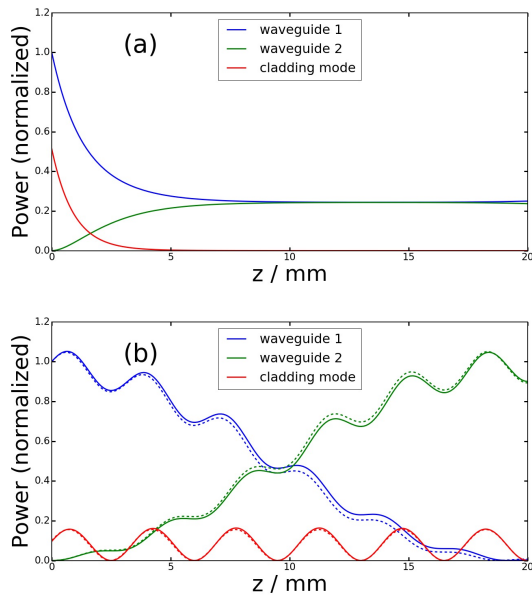


Fig. 6. Evolution of normalized propagating power in the two core waveguide modes and in the resonantly coupled cladding mode (35th mode) (a) inside the bandgap ($\lambda_0 = 1.55 \mu\text{m}$) and (b) outside the bandgap ($\lambda_0 = 1.54975 \mu\text{m}$). Solid curves are a numerical solution including all cladding modes, dashed curves are the analytical solution including only the 35th cladding mode. Parameters used are $\Lambda_g = 587.34 \text{ nm}$, $\theta = 17.23^\circ$ and $\Delta n_g = 0.001$.

ing one quarter of the input power in each waveguide with the remaining half back-reflected in the cladding mode. Outside the bandgap, Fig. 6(b), oscillatory behavior is found as expected. We chose the device length such that the majority of the light is coupled from one waveguide to the other, demonstrating its potential as a wavelength selective coupler. In both situations, the numerical results using the full set of cladding modes and the three-mode analytical solution using only the one cladding mode that is phase matched to the grating are in excellent agreement. Note that in Fig. 6(b), the power is normalized to the input power; as the core and cladding modes are counter-propagating, the device acts as a partial resonator and the local power in a mode can exceed unity. This shows that we can theoretically couple light between the two waveguides using the intermediary of one cladding mode without unwanted influence of other cladding modes. This justifies the analysis in Sec. 3 and allows us to greatly simplify the problem for further analysis.

In Fig. 7 we show how the output power in each of the two waveguides varies when light is launched into a single waveguide at the input as a function of wavelength. Close to the Bragg wavelength we find a photonic bandgap and the output power in both waveguides approaches one quarter of the input power, as discussed above. On either side of the bandgap we find two peaks where the maximum amount of power is transferred from one waveguide to the other. Far away from the bandgap, i.e., for a large phase mismatch, coupling between the waveguide and the cladding modes becomes inefficient and light is transmitted through the waveguide unchanged.

As the wavelength is varied, we can see oscillations in the output power of the waveguides. To understand these oscillations in more detail, we consider again the spatial oscilla-

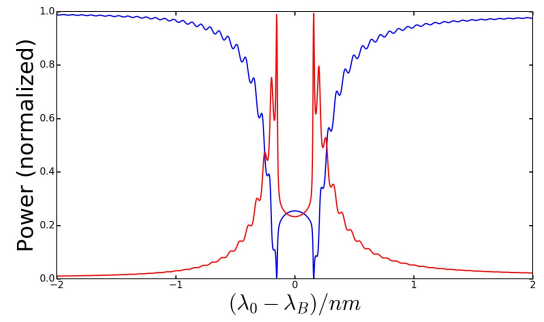


Fig. 7. Fractional output power from waveguides 1 (blue) and 2 (red) as a function of wavelength where at the input light is launched only into waveguide 1. Parameters are $\Lambda_g = 587.34 \text{ nm}$, $\theta = 17.23^\circ$, $L = 20 \text{ mm}$, $\Delta n_g = 0.001$, $\lambda_B = 1.55 \mu\text{m}$.

tion frequencies 2Ω , $\Delta K/2 \pm \Omega$ discussed in Sec. 3 (where $\Omega = \frac{1}{2}\sqrt{\Delta K^2 - 2g^2}$) that describe the coupling of light between the waveguide modes and the selected cladding mode as a function of propagation distance. Away from the bandgap, where $\Delta K > \sqrt{2}g$, we have asymptotically $2\Omega \approx \Delta K$, $\Delta K/2 + \Omega \approx \Delta K$ and $\Delta K/2 - \Omega \approx g^2/(2\Delta K)$. There are thus two dominant spatial frequencies, a fast one scaling with ΔK and a slow one proportional to $1/\Delta K$. As we can see from Fig. 6, the fast oscillation describes power transfer between the waveguides and the cladding mode, whereas the slow oscillation describes power transfer between the two waveguides. At the output of the waveguides, Fig. 7, we thus see a slow variation of power transfer with a fast variation superimposed where power is lost into the backward propagating cladding mode.

This allows us to optimize the device to achieve a particular functionality. For example, if we want to achieve maximum power transfer from waveguide 1 to waveguide 2 at a given wavelength, we need to select a device length and a grating period (and thus ΔK) such that simultaneously the slow oscillation leads to maximum power transfer at the device output while simultaneously the backscattered power in the cladding mode vanishes at $z = 0$,

$$\left(\frac{\Delta K}{2} - \Omega\right)L = \pi, \quad \Omega L = m\pi, \quad (16)$$

where m is an integer number; inserting Eqs. (16) into Eqs. (13)-(14) confirms this.

The evolution of propagating light power for devices with L and ΔK obtained by solving Eqs. (16) for $m = 1, 2, 3$ is shown in Fig. 8. In all three cases we find 100% power coupling from one waveguide to the other with 1, 2, and 3 complete oscillations of power into the cladding mode and back into the waveguides during propagation, respectively, as expected. This would allow our design to be used as a wavelength selective coupler e.g. for wavelength division multiplexing. Similar optimizations can also be performed to achieve other output power ratios, for example to form a wavelength selective 50-50 beamsplitter.

In order to assess the performance of our device as a frequency filter or wavelength division multiplexer we show in Fig. 9 the power output from the waveguides in the intermediate region between phase matching to two separate cladding modes. We choose the parameters $\Lambda_g = 587.379 \text{ nm}$, $L = 9.739 \text{ mm}$ which lead to 100% coupling at $\lambda_0 = 1.55 \mu\text{m}$ as seen in Fig. 8. Fig. 9 shows the resonances with modes 35 and 36 and a broad

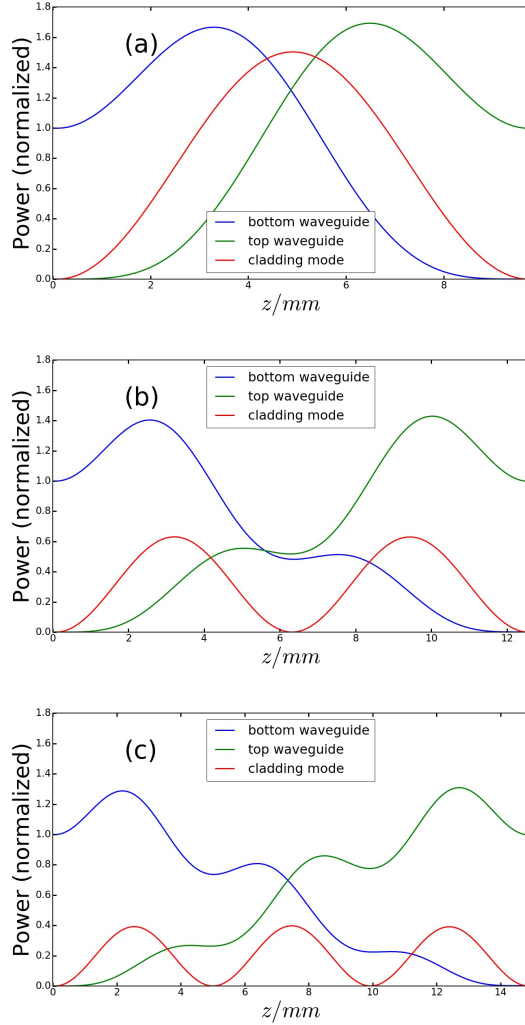


Fig. 8. Evolution of propagating power in the two waveguide modes and in the resonantly coupled cladding mode (35th mode) with parameters chosen to maximize power transfer between the waveguides with $m = 1, 2, 3$ cladding mode oscillations. Parameters are (a) $\Lambda_g = 587.379$ nm, $L = 9.739$ mm (b) $\Lambda_g = 587.391$ nm, $L = 12.573$ mm and (c) $\Lambda_g = 587.401$ nm, $L = 14.876$ mm. In all cases $\theta = 17.23^\circ$ and $\Delta n_g = 0.001$.

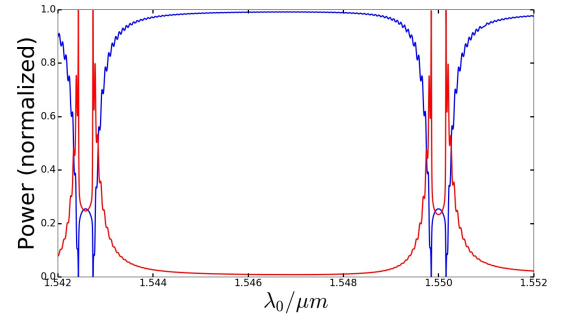


Fig. 9. Fractional output power from waveguides 1 (blue) and 2 (red) as a function of wavelength where at the input light is launched only into waveguide 1. Parameters are $\Lambda_g = 587.379$ nm, $\theta = 17.23^\circ$, $L = 9.739$ mm, $\Delta n_g = 0.001$.

wavelength region inbetween where the majority of light is transmitted in waveguide 1 and is not transferred to waveguide 2 by either of the cladding modes. At a wavelength of $1.5479 \mu\text{m}$ we find a minimum transferred power of 0.80% which corresponds to an on-off ratio of -21 dB. Our device can therefore be used as a narrow-band frequency filter, for example, for separating a narrow-band signal from a pump in Raman or parametric amplifiers. However, the existence of closely spaced narrow resonances may require the use of additional broad-band filters in other applications such as wavelength division multiplexing.

6. BANDWIDTH CONTROL

In the previous section we presented a wavelength dependent waveguide coupler. In the following, we will now investigate the bandwidth of this device and its dependence on the device parameters. Here we define the bandwidth as the full width at half maximum of one of the two peaks shown in Fig. 7.

The dependence of the bandwidth on the device parameters is shown in Fig. 10 where we again utilize the 35th cladding mode as the intermediary between the two waveguide modes.

We can understand the results shown in Fig. 10 by deriving an approximate expression for the bandwidth in terms of the phase mismatch rather than the wavelength. The edges of the bandwidth correspond to where the device length is roughly one quarter and three quarters, on the outside and inside of the peak respectively, of the spatial oscillation period defined by the spatial frequency $\Delta K/2 - \Omega$, i.e. by replacing the right hand side of Eq. (16) with $\pi/2$. Re-arranging this equation we find for the bandwidth

$$\Delta K = \frac{Lg^2}{3\pi} - \frac{\pi}{2}. \quad (17)$$

For sufficiently long gratings, we thus expect the bandwidth of the device to scale linearly with the device length L and quadratically with the coupling coefficient g . Since g is proportional to the grating index contrast Δn_g , Eqs. (5)-(7), we thus expect the bandwidth to scale quadratically with Δn_g . This is in fact confirmed by the simulation results in Fig. 10. The dependence on the tilt angle can be explained in the same way by considering its effect on the coupling strength shown in Fig. 5.

For any practical device, the maximum grating index contrast is limited by the UV writing technique to about 0.001, while short device lengths (< 10 cm) [18] are generally desired to minimize scattering propagation losses. This suggests that changing

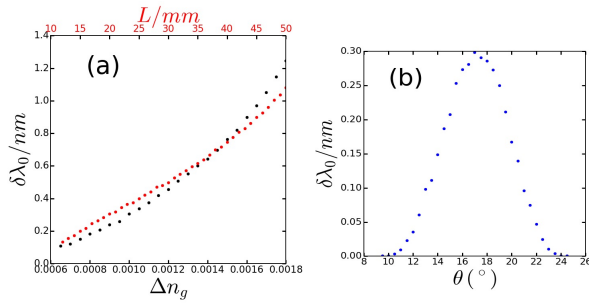


Fig. 10. Dependence of the bandwidth $\delta\lambda_0$ of the device as a wavelength-selective coupler as a function of (a) grating index contrast and device length, (b) grating tilt angle. Unless otherwise given, the parameters are $\Lambda_g = 587.34$ nm, $L = 20$ mm, $\theta = 17.23^\circ$, and $\Delta n_g = 0.001$.

the tilt angle is an interesting option to control the device bandwidth.

The bandwidth of our device is around 0.3 nm for parameters of $\Lambda_g = 587.34$ nm, $L = 20$ mm, $\theta = 17.23^\circ$, and $\Delta n_g = 0.001$. This narrow bandwidth is caused by our choice of using a counter-propagating cladding mode as intermediary between the two waveguide modes, which leads to a phase mismatch of $\Delta K = K_g - |\beta_0| - |\beta_2|$ between waveguide and cladding modes that is highly sensitive to changes of the operating wavelength. The bandwidth is much wider if a co-propagating cladding mode (and correspondingly long period gratings) are selected for the device operation [24].

7. THERMAL STABILITY

In this section we explore the effect of temperature on the modal structure of the device and thus the wavelength of operation. The temperature affects the device in two different ways: through the temperature dependence of the refractive index, and through the change of device dimensions because of thermal expansion. We model the first effect using the three term temperature-dependent Sellmeier equation [27] for silica to provide the index of the cladding. We assume for simplicity that the index contrast of the waveguide and of the grating do not depend on temperature. The thermal expansion of silica at room temperature is assumed linear with $\alpha_L = 5.5 \times 10^{-7} \text{ K}^{-1}$ [28]. We scale all dimension of our device (cladding width, waveguide width, waveguide separation, grating period and device length) linearly with temperature for a device with $H = 34 \mu\text{m}$, $x_0 = 10 \mu\text{m}$, $\sigma = 2 \mu\text{m}$, $\Lambda_g = 585.068$ nm and $L = 20$ mm that is phase matched at room temperature ($T = 300$ K).

For these parameters we find that the propagation constants of the waveguide and resonant (35th) cladding mode change by $3.38 \times 10^{-5} \text{ m}^{-1}/^\circ\text{C}$ and $4.13 \times 10^{-5} \text{ m}^{-1}/^\circ\text{C}$, respectively, while the grating wave vector K_g changes by $-5.91 \times 10^{-6} \text{ m}^{-1}/^\circ\text{C}$. We see that the largest contributions to the phase mismatch come from the changes in propagation constants of the modes and not from the shift in grating period due to thermal expansion. The changes in propagation constants are themselves largely due to the change in refractive index of the device and not thermal expansion.

Overall, this leads to a change of resonant wavelength by $11.7 \text{ pm}/^\circ\text{C}$, which is consistent with the shift reported elsewhere for Bragg gratings in the same material [29]. Figure (11) shows

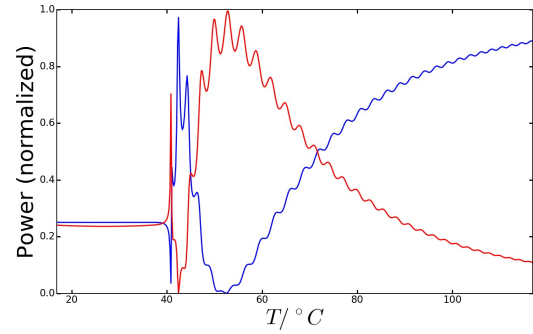


Fig. 11. Fractional output power from waveguides 1 (blue) and 2 (red) as a function of temperature where at the input light is launched only into waveguide 1. Parameters are $\Lambda_g = 587.34$ nm, $\theta = 17.23^\circ$, $L = 20$ mm, $\Delta n_g = 0.001$, $\lambda_0 = 1.55 \mu\text{m}$.

the device output as a function of temperature for a launched wavelength of 1550 nm. We note that a temperature change of approximately 30°C is required to shift the resonance curve by one bandwidth, which implies that the device is highly robust to temperature fluctuations.

8. CONCLUSIONS

We have proposed and investigated theoretically and numerically a new type of integrated waveguide coupler based on UV written tilted Bragg gratings. A ridge structure is exploited to tailor the cladding modes of the device which act as intermediaries to couple light between the waveguides. Using realistic parameters, we demonstrate that by introducing a tilt angle to the Bragg grating planes light can be efficiently coupled between the two waveguides using only a single cladding mode as an intermediary. This simplifies the system to an effective three-mode device which allows us to achieve a near lossless coupler with a very narrow bandwidth, high on-off ratio and high thermal stability. Our numerical simulations are supported by simplified analytical estimates which can be used to easily design the device functionality, for example, by controlling the operation bandwidth of the waveguide coupler.

The device has a wide range of potential applications in classical telecommunications and in quantum technology. Specifically, in this work we demonstrated applications as a waveguide coupler with arbitrary coupling efficiency up to 100%, as a narrow-band coupler and/or wavelength filter, and as a phase-sensitive switch.

FUNDING

EPSRC Quantum Technology Programme (EP/M013243/1, EP/M013294/1).

DATA AVAILABILITY

The data used in this article is openly available at [30].

REFERENCES

1. A. K. Ghatak and K. Thyagarajan, *Introduction to fiber optics* (Cambridge University Press, New Delhi, 1999).
2. D. Marcuse, "Directional Couplers Made of Nonidentical Asymmetric Slabs. Part II: Grating-Assisted Couplers," *J. Light. Technol.* **5**, 268–273 (1987).

3. J. L. Archambault, P. S. Russell, S. Barcelos, P. Hua, and L. Reekie, "Grating-frustrated coupler: a novel channel-dropping filter in single-mode optical fiber," *Opt. Lett.* **19**, 180 (1994).
4. D. Mechinn, P. Grosso, and D. Bosc, "Add – Drop Multiplexer With UV-Written Bragg Gratings and Directional Coupler in SiO₂ – Si Integrated Waveguides," *J. Light. Technol.* **19**, 1282–1286 (2001).
5. K. Ikeda, M. Nezhad, and Y. Fainman, "Wavelength selective coupler with vertical gratings on silicon chip," *Appl. Phys. Lett.* **92**, 201111 (2008).
6. D. T. H. Tan, K. Ikeda, S. Zamek, A. Mizrahi, M. P. Nezhad, A. V. Krishnamoorthy, K. Raj, J. E. Cunningham, X. Zheng, I. Shubin, Y. Luo, and Y. Fainman, "Wide bandwidth, low loss 1 by 4 wavelength division multiplexer on silicon for optical interconnects," *Opt. Express* **19**, 2401–2409 (2011).
7. W. Shi, H. Yun, C. Lin, M. Greenberg, X. Wang, Y. Wang, S. T. Fard, J. Flueckiger, N. A. F. Jaeger, and L. Chrostowski, "Ultra-compact, flat-top demultiplexer using anti-reflection contra-directional couplers for cwdm networks on silicon," *Opt. Express* **21**, 6733–6738 (2013).
8. T. Erdogan and J. Sipe, "Tilted fiber phase gratings," *J. Opt. Soc. Am. A* **13**, 296–313 (1996).
9. K. S. Lee, "Mode coupling in tilted planar waveguide gratings," *Appl. Opt.* **39**, 6144–6149 (2000).
10. C. K. Madsen, J. Wagener, T. A. Strasser, D. Muehlner, M. A. Milbrodt, E. J. Laskowski, and J. DeMarco, "Planar waveguide optical spectrum analyzer using a UV-induced grating," *IEEE J. Sel. Top. Quantum Electron.* **4**, 925–929 (1998).
11. C. Riziotis and M. N. Zervas, "Design considerations in optical add/drop multiplexers based on grating-assisted null couplers," *J. Light. Technol.* **19**, 92–104 (2001).
12. K. K. Mehta and R. J. Ram, "Precise and diffraction-limited waveguide-to-free-space focusing gratings," *Sci. Rep.* **7**, 2019 (2017).
13. C. Holmes, L. G. Carpenter, H. L. Rogers, I. J. G. Sparrow, J. C. Gates, and P. G. R. Smith, "Planar waveguide tilted Bragg grating refractometer fabricated through physical micromachining and direct UV writing," *Opt. Express* **19**, 12462–8 (2011).
14. H.-C. Liu and A. Yariv, "Grating induced transparency (GIT) and the dark mode in optical waveguides," *Opt. Express* **17**, 11710–11718 (2008).
15. B. J. Metcalf, N. Thomas-Peter, J. B. Spring, D. Kundys, M. A. Broome, H. P. C., X.-M. Jin, M. Barbieri, W. S. Kolthammer, J. C. Gates, B. J. Smith, N. K. Langford, P. G. R. Smith, and I. A. Walmsley, "Multiphoton quantum interference in a multiport integrated photonic device," *Nat. Commun.* **4** (2013). 1356.
16. J. Carolan, C. Harrold, C. Sparrow, E. Martín-López, N. J. Russell, J. W. Silverstone, P. J. Shadbolt, N. Matsuda, M. Oguma, M. Itoh, G. D. Marshall, M. G. Thompson, J. C. F. Matthews, T. Hashimoto, J. L. O'Brien, and A. Laing, "Universal linear optics," *Science* **349**, 711–716 (2015).
17. O. Alibart, J. Fulconis, G. K. L. Wong, S. G. Murdoch, W. J. Wadsworth, and J. G. Rarity, "Photon pair generation using four-wave mixing in a microstructured fibre: theory versus experiment," *New J. Phys.* **8** (2006). 67.
18. C. Sima, J. C. Gates, H. L. Rogers, P. L. Mennea, C. Holmes, M. N. Zervas, and P. G. R. Smith, "Ultra-wide detuning planar Bragg grating fabrication technique based on direct UV grating writing with electro-optic phase modulation," *Opt. Express* **21**, 15747–15754 (2013).
19. C. Sima, "Integrated Planar Bragg Grating Devices for Advanced Optical Communication Systems," Ph.D. thesis, University of Southampton (2013).
20. M. T. Posner, P. L. Mennea, N. Podoliak, P. Horak, J. C. Gates, and P. G. R. Smith, "45° tilted gratings for silica based integrated polarizers," in *The European Conference on Lasers and Electro-Optics*, (Munich, Germany, 2015).
21. M. T. Posner, P. L. Mennea, N. Podoliak, P. Horak, J. C. Gates, and P. G. R. Smith, "Integrated polarizing coupler based on tilted gratings," in *Integrated Photonics Research, Silicon and Nanophotonics*, (Vancouver, Canada, 2016).
22. Y. Bai and K. S. Chiang, "Analysis and Design of Long-Period Waveguide-Grating Couplers," *J. Light. Technol.* **23**, 4363–4373 (2005).
23. Y. Bai, Q. Liu, K. P. Lor, and K. S. Chiang, "Widely tunable long-period waveguide grating couplers," *Opt. Express* **14**, 2595–2597 (2006).
24. K. C. Chow, K. S. Chiang, Q. Liu, K. P. Lor, and H. P. Chan, "UV-written long-period waveguide grating coupler for broadband add/drop multiplexing," *Opt. Commun.* **282**, 378–381 (2009).
25. C. Holmes, K. R. Daly, I. J. G. Sparrow, J. C. Gates, G. D'Alessandro, and P. G. R. Smith, "Excitation of Surface Plasmons Using Tilted Planar-Waveguide Bragg Gratings," *IEEE Photonics J.* **3**, 777–788 (2011).
26. B. Fornberg, "Generation of Finite Difference Formulas on Arbitrarily Spaced Grids," *Math. Comput.* **51**, 699–706 (1988).
27. D. B. Leviton and B. J. Frey, "Temperature-dependent absolute refractive index measurements of synthetic fused silica," in *Optomechanical Technologies for Astronomy*, (Orlando, United States, 2006).
28. Accuratus, "Fused Silica, SiO₂ Glass Properties," (<https://www accuratus.com/fused.html> (accessed 28/03/2019)).
29. C. Holmes, D. Kundys, J. Gates, C. Gawith, and P. Smith, "150 GHz of thermo-optic tuning in direct UV written silica-on-silicon planar Bragg grating," *Electron. Lett.* **45**, 954 (2009).
30. M. J. Weisen, M. T. Posner, J. C. Gates, C. B. E. Gawith, P. G. R. Smith, and P. Horak, "Low loss wavelength-selective integrated waveguide coupler based on tilted bragg gratings (dataset)," (University of Southampton, 2019, <https://doi.org/10.5258/SOTON/D0870>).

Four-port Interference Device on an Integrated Photonics Platform Based on Tilted Bragg Gratings

EPSRC

Engineering and Physical Sciences
Research Council

Mathias J. Weisen, James C. Gates, Corin B. E. Gawith, Peter G.R. Smith, Peter Horak
Optoelectronics Research Centre, University of Southampton, Southampton, UK
m.j.weisen@soton.ac.uk

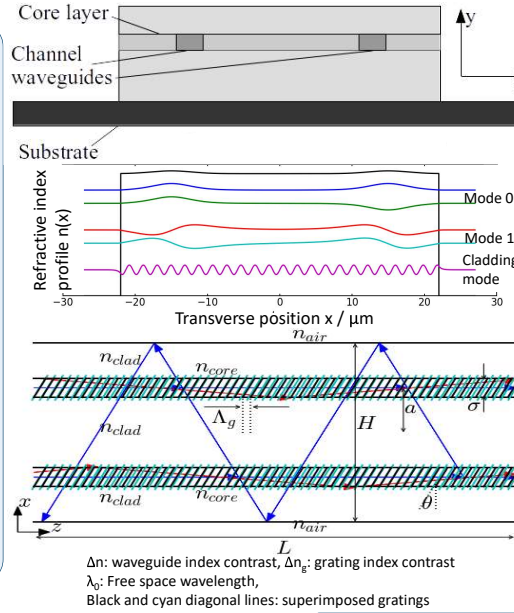
UNIVERSITY OF
Southampton

Abstract

A novel interference device is investigated numerically where all modes of two multimode integrated waveguides are coupled via superimposed tilted Bragg gratings to a common cladding mode. We show that, by varying the grating parameters, we are able to achieve any arbitrary four way power splitter in a compact device. By chaining multiple such couplers together, we can achieve any unitary transform.

Motivation

- Integrated optical waveguide-to-waveguide couplers have interesting applications in quantum information processing.
- They can be used to implement unitary matrix operations and quantum gates [1].
- They also have telecom applications, such as mode division multiplexing [2].
- We have recently developed tilted Bragg grating technology in a planar photonics platform [3].
- Can be used to couple light efficiently between waveguides and cladding/radiation modes.
- We have theoretically investigated a new type of integrated coupler based on two tilted gratings that uses a single cladding mode as a bus [4].
- We expand the capability of this device to explore new applications as a compact 4x4 multimode power splitter and for quantum information processing.**



Device Operation

- Single ridge with photosensitive core layer.
- Two parallel UV written channel waveguides, each with two modes, so four modes in total.
- Two superimposed tilted gratings in each waveguide.
- Thus all four core modes are coupled to a single backward propagating cladding mode.
- Behaviour described by **coupled mode theory**:

$$\frac{d}{dz} \vec{R}(z) = M \vec{R}(z)$$

Vector of mode amplitudes

$$M = \begin{bmatrix} \frac{i\Delta K}{2} & \cdot & \cdot & \cdot \\ \cdot & \frac{i\Delta K}{2} & \cdot & \cdot \\ \cdot & \cdot & \frac{i\Delta K}{2} & \cdot \\ \cdot & \cdot & \cdot & \frac{i\Delta K}{2} \end{bmatrix}$$

Wavevector phase mismatch $\Delta K = K_g + \beta_z - \beta_0$

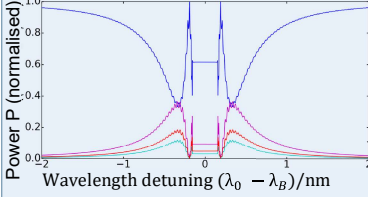
The coupling coefficients are proportional to the grating amplitudes.

Coupling coefficients: c, d, e, f

- By carefully choosing the grating parameters **we are able to couple to any desired mode superposition.**

General results

Waveguide output power vs wavelength



- System has 3 eigenvalues:
 $\gamma_0 = i\Delta K/2, \gamma_{\pm} = \sqrt{|c|^2 + |d|^2 + |e|^2 + |f|^2 - \Delta K^2}$
 - In centre, γ_{\pm} is real \rightarrow photonic bandgap similar to [4].
 - Outside bandgap, γ_{\pm} is imaginary \rightarrow oscillatory solution.
-
- Power propagation along z in launching mode (blue), other core modes (green, magenta, cyan) and cladding mode (red).
- One frequency for cladding mode oscillation but two more for core modes.

Arbitrary power splitting

- By changing the grating index contrasts (or amplitudes) and thus coupling coefficients, **we can achieve any desired superposition of modes.**
 - As we don't want light to escape via the cladding mode we need $R_{clad}(0) = 0$. This requires an integer number of oscillations in the cladding mode.
-
- The above figures show a selection of splitting ratios that we can achieve using different grating amplitudes and device lengths.

Equal power splitting

- With equal coupling coefficients we can transfer light from one mode into an equal superposition of all the modes.
-
- And by carefully choosing the grating phases we can achieve a **Walsh-Hadamard gate** (similar to [5]) which is useful for quantum information processing:

$$A = \frac{1}{2} \begin{bmatrix} 1 & 1 & 1 & 1 \\ 1 & 1 & -1 & -1 \\ 1 & -1 & 1 & -1 \\ 1 & -1 & -1 & 1 \end{bmatrix}$$

Unitary transformations and quantum gates

- By using only two gratings to couple two modes we can achieve any basis unitary transformation (see right).
 - Here φ is the phase difference between the two gratings and α describes the rotation between two modes.
 - Similar matrices are found for any pair of modes leading to all six basis unitary transforms with which we can achieve any unitary operation [1].
 - This could form the basis for **two qubit operations with a single photon.**
 - For $\alpha = \pi$ we achieve a **C-NOT gate** (bottom right) which together with 1-qubit gates can be used to make any 2-qubit gate.
- $$A = e^{\frac{i\alpha}{2}} \begin{bmatrix} e^{-\frac{i\alpha}{2}} & \cdot & \cdot & \cdot \\ \cdot & e^{-\frac{i\alpha}{2}} & \cdot & \cdot \\ \cdot & \cdot & \cos(\frac{\alpha}{2}) & -\sin(\frac{\alpha}{2})e^{i\varphi} \\ \cdot & \cdot & -\sin(\frac{\alpha}{2})e^{-i\varphi} & \cos(\frac{\alpha}{2}) \end{bmatrix}$$
- $$A = \begin{bmatrix} 1 & \cdot & \cdot & \cdot \\ \cdot & 1 & \cdot & \cdot \\ \cdot & \cdot & \cdot & 1 \\ \cdot & \cdot & 1 & \cdot \end{bmatrix}$$

Conclusions

We presented an arbitrary 4x4-mode coupler based on tilted Bragg gratings. We show how we can achieve any splitting ratio by choosing the coupling coefficients during fabrication and show how to achieve a Walsh-Hadamard transformation and any other unitary transformation.

[1] J. Carolan et. Al, *Universal Linear Optics*, Science, Vol. 349, pp. 711 - 716 (2015)

[2] Hossam M. H. Shalaby, *Bi-Directional Coupler as a Mode-Division Multiplexer/Demultiplexer*, Journal of Lightwave Technology, Vol. 34, pp. 3633 - 3640 (2016)

[3] C. Sima et al., *Ultra-wide detuning planar Bragg grating fabrication technique based on direct UV grating writing with electro-optic phase modulation*, Optics Express, Vol. 21, pp. 15747 - 15754 (2013)

[4] M. J. Weisen et al., *Low-loss wavelength-selective integrated waveguide coupler based on tilted Bragg gratings*, Journal of the Optical Society of America B, Vol. 36, pp. 1783-1791 (2019)

[5] S.-Y. Tseng, *Synthesis of a 4 x 4 Walsh-Hadamard Transformer Using Long-Period Waveguide Grating Arrays*, IEEE Photonics Technology Letters, Vol. 21, pp. 972 - 974 (2009)

Tilted Bragg Gratings as an Efficient Platform for Integrated Multimode Interference Devices

Peter Horak*, Mathias J. Weisen, James C. Gates, Corin B. E. Gawith, Peter G. R. Smith

Optoelectronics Research Centre, University of Southampton, Southampton SO17 1BJ, United Kingdom

** e-mail: peh@orc.soton.ac.uk*

ABSTRACT

We have recently developed and experimentally demonstrated the technology of tilted Bragg gratings in integrated optical waveguides to achieve polarisation selective coupling between parallel waveguides. Here I will review our ideas, designs and simulations for novel devices based on this platform. Multimode devices, tailored phase matching, and methods for significantly improved coupling efficiencies will be discussed that will be of interest for applications in quantum information processing and multimode optical telecommunication.

Keywords: Integrated photonics; Bragg gratings; phase matching; multimode waveguides; mode coupling.

Direct UV writing is a laser manufacturing technique for integrated optical waveguides and Bragg gratings in hydrogenated germanium-doped silica-on-silicon chips. This method allows us to write tightly controlled nanostructures, and in particular to write tilted Bragg gratings where the grating planes are at arbitrary angles with the waveguide. As one sample application of this technology, we recently demonstrated an integrated polariser. Here the gratings are tilted at the Brewster angle of 45° degree, which results in near perfect separation of the waveguide TE and TM modes. Experimentally we observed a polarisation extinction ratio of 28.5 dB [1]. Numerically, we have also shown that the method can be extended to multiport beam splitting and switching in arrays of planar waveguides [2].

The efficiency of such devices can be greatly improved if the waveguide modes are made to interact with a tailored cladding that only supports a few discrete modes, rather than a continuum of radiation modes as in our earlier work. Such a geometry can be realised, for example, by two direct UV written waveguides sitting on a ridge fabricated by micromachining. Ideally, Bragg gratings can then be tuned such that the two waveguide modes are coupled exclusively to a single discrete cladding mode. A grating tilt angle is again required to phase match the waveguide and cladding modes not only in the propagation direction but also in the transverse direction, similar to blazed diffraction gratings. Simulations based on coupled mode theory and full finite element analysis show that, in principle, up to 100% efficient waveguide coupling can be achieved [3]. By exploiting backward propagating cladding modes, the operation bandwidth becomes extremely narrow (sub-nanometre in wavelength) and thus the device can act as a narrow-band add-drop filter. In addition, a phase-sensitive switch can be realised when light is launched simultaneously into both waveguides: depending on the relative phase ϕ of the two fields, light is either completely reflected ($\phi=0$) or completely transmitted via a grating induced transparency effect ($\phi=\pi$).

Further degrees of freedom can be exploited if the UV written waveguides are made to support two or more spatial modes by increasing the refractive index contrast or increasing the waveguide width. In this case, a large number N of input channels (different modes in different waveguides) can be supported in a compact device. Grating-induced coupling between waveguide and cladding modes can be made highly selective, and arbitrary N -by- N coupling matrices can be achieved [4].

We envisage that devices based on such designs will find applications in classical and, in particular, in quantum information processing. Narrow band filtering, mode-division multiplexing, single-photon or multi-photon interference, optical gates, phase-selective switches and other functionalities can be realised in this compact and highly robust platform.

ACKNOWLEDGEMENTS

This work was supported by the UK National Quantum Technology Programme under EPSRC grants EP/M013243/1 and EP/M013294/1.

REFERENCES

- [1] M. T. Posner *et al.*: Integrated polarizer based on 45° tilted gratings, *Opt. Express*, vol. 27. pp. 11174-11181, Apr. 2019.
- [2] N. Podoliak *et al.*: Optical beam splitting and switching based on arrays of tilted Bragg gratings in planar waveguides, in *CLEO-Pacific Rim 2017*, Singapore, Aug. 2017, paper P3-075.
- [3] M. Weisen *et al.*: Planar waveguide coupler based on tilted Bragg gratings and a discrete cladding mode, in *SPIE Photonics Europe*, Strasbourg, France, Apr. 2018, paper 10672-135.
- [4] M. J. Weisen *et al.*: Four-port interference device on an integrated photonics platform based on tilted Bragg gratings, in *CLEO/Europe-EQEC 2019*, Munich, Germany, June 2019, paper EB-P.7.

Four-port integrated waveguide coupler exploiting bidirectional propagation of two single-mode waveguides

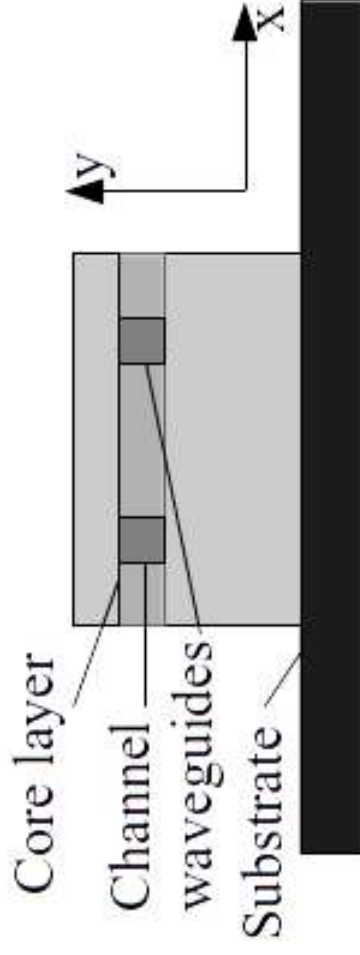
Mathias J. Weisen, James C. Gates, Corin B. E. Gawith,
Peter G. R. Smith, Peter Horak
m.j.weisen@soton.ac.uk

Optoelectronics Research Centre, University of Southampton
Southampton SO17 1BJ, UK



Outline of the talk

- Motivation
- Chip geometry
- Coupled mode model for counter-propagating fields
- “Fundamental” 2×2 couplers
- Construction of an arbitrary 4×4 coupler (symmetric unitary transfer matrix)
- Examples, incl. Walsh-Hadamard transformation
- Conclusions



Motivation

- Waveguide-to-waveguide couplers have useful applications for quantum information processing [1].
- Can implement unitary matrix operations and quantum gates [2].

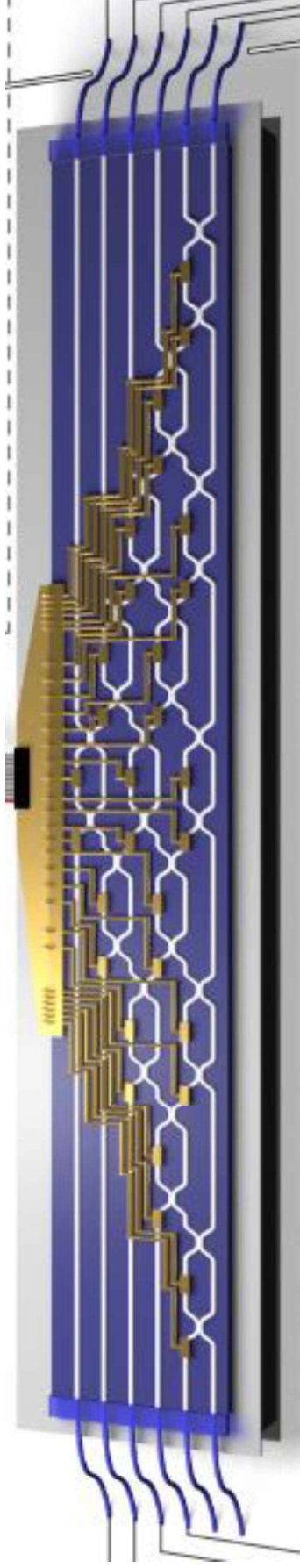
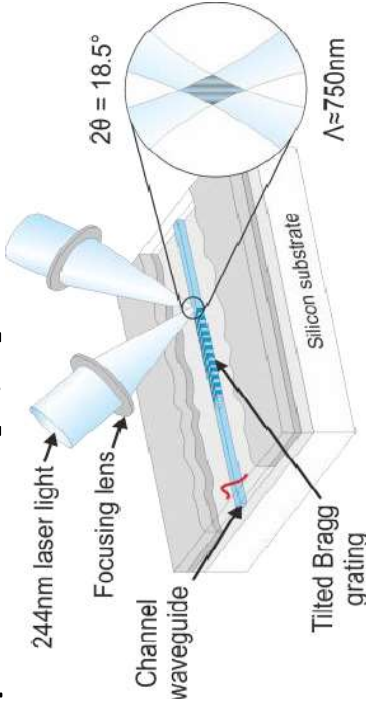


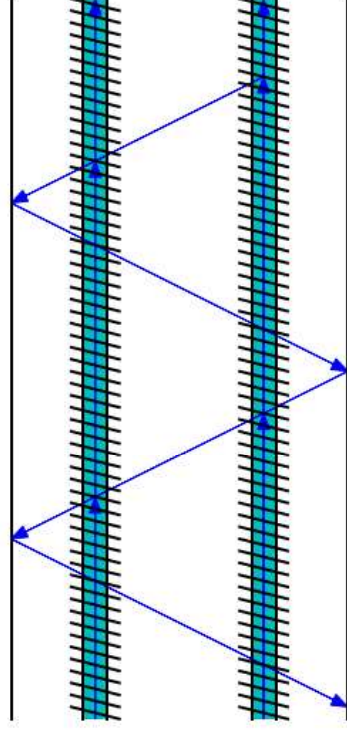
Figure from Ref. [2]

[1] J. Wang et. al, Nat. Photonics (2019), <https://doi.org/10.1038/s41566-019-0532-1>

[2] J. Carolan et. al., Science, Vol. 349, pp. 711 - 716 (2015)

Motivation

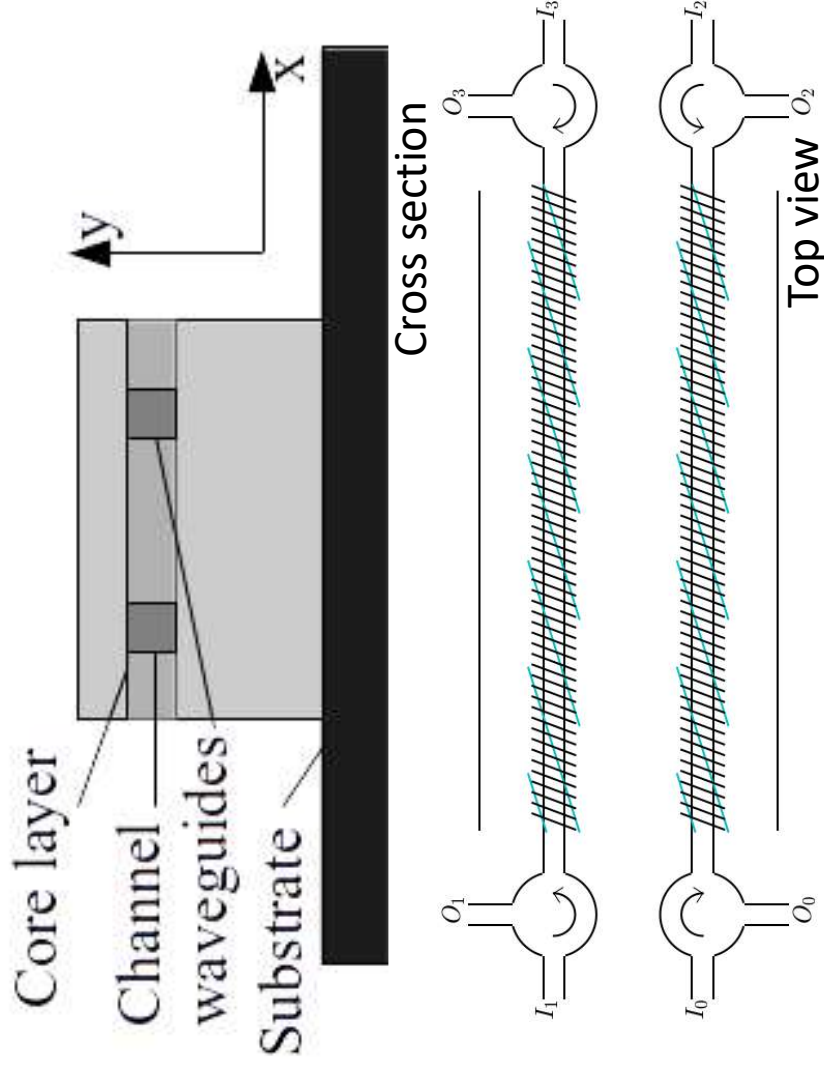
- Previously developed tilted Bragg grating technology for planar photonics [3,4].
- 
- Efficient waveguide-to-waveguide couplers can be constructed using Bragg gratings [5,6,7].
 - We exploit bidirectional propagation in order to **double the number of available modes**.
 - Since every optical component acts in both propagation directions, **what operations are possible?**



- [3] C. Sima et al., Opt. Express, Vol. 21, 15747–15754 (2013)
- [4] M. T. Posner et al., Opt. Express, Vol. 27, 11174–11181 (2015)
- [5] Y. Bai and K. S. Chiang, J. Light. Technol., Vol 23, 4363–4373 (2005)
- [6] Y. Bai et al. Opt. Express., Vol. 14, 2529–2597 (2006)
- [7] M. J. Weisen et al. J. Soc. Am. B, 1783–1791 (2019)

Device Geometry

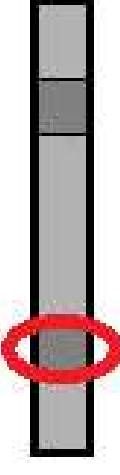
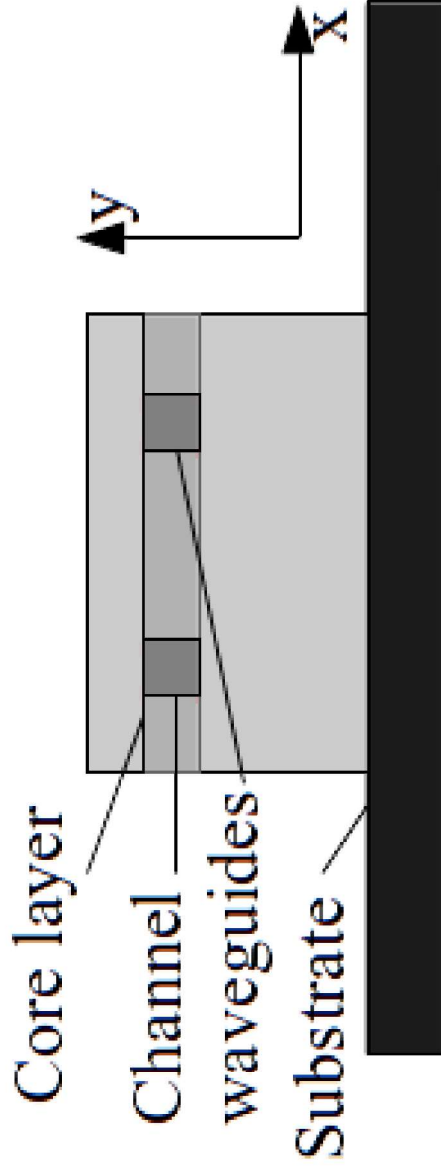
- Two parallel single-mode waveguides in a single ridge structure.



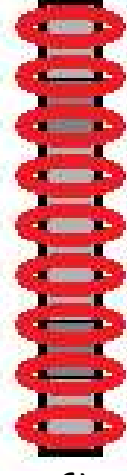
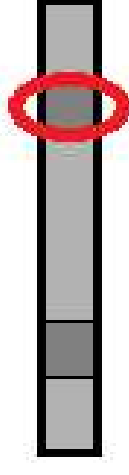
- Exploits both propagation directions
→ **double number of modes.**
- Tilted long- and short-period gratings
→ couple to co- and counter-propagating directions of cladding modes.
- Carefully selected parameters to couple to a single cladding mode.
- Connect all waveguide end facets to circulators
→ **four input and output ports.**

Possible Fabrication Method

- Silica wafer with photosensitive raised index layer for vertical confinement.
- Single micromachined silica ridge structure.



Core modes



Cladding mode

- Use direct UV-writing to fabricate tilted Bragg gratings [3].
- Device simulated using physically realisable parameters.

Device Model

- Simulate light propagation in 6 modes (4 core + 2 cladding) using coupled mode theory:

$$\frac{d}{dz}R(z) = M \cdot R(z)$$

- Where $R(z)$ are mode amplitudes and M is:

$$M = \begin{bmatrix} \cdot & \cdot & \cdot & \cdot & \cdot & \cdot \\ \cdot & \cdot & \cdot & \cdot & \cdot & \cdot \\ \cdot & \cdot & \cdot & \cdot & \cdot & \cdot \\ \cdot & \cdot & \cdot & \cdot & \cdot & \cdot \\ 1 & \frac{1}{2}g_2 & \frac{1}{2}g_3 & -\frac{1}{2}g_0 & 1 & -\frac{1}{2}g_1 \\ -\frac{1}{2}g_0^* & -\frac{1}{2}g_1^* & -\frac{1}{2}g_2^* & \frac{1}{2}g_2 & \frac{1}{2}g_3 & \frac{1}{2}g_1^* \end{bmatrix}$$

M

Coupling coefficients:

short-period gratings

long-period gratings

Phase mismatch:

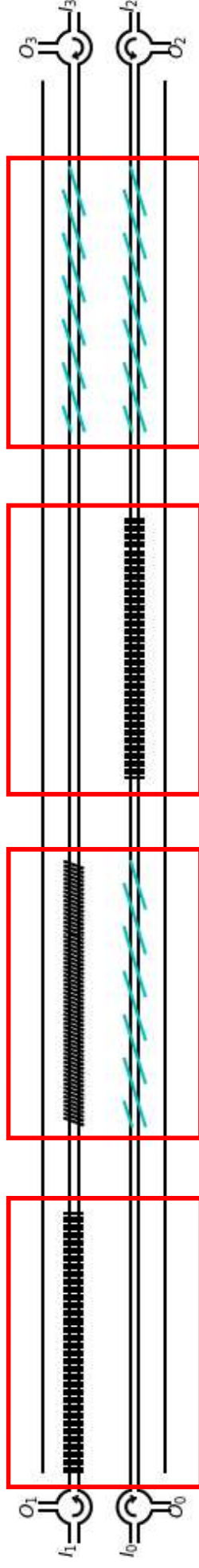
long-period gratings

Short-period gratings

- We solve this as eigenvalue/eigenvector problem.

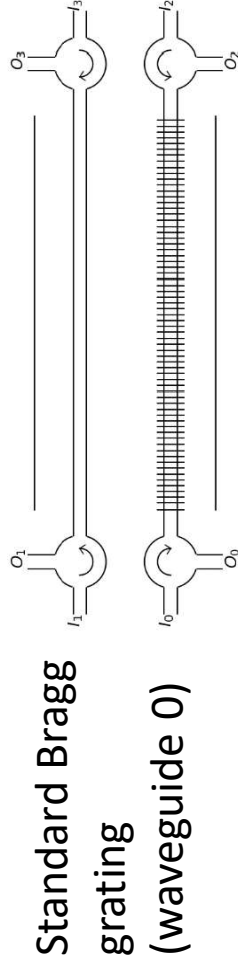
Analytical Method

- Aim to achieve widest set of operations possible on this platform.
- Concatenate individual “blocks” that represent “fundamental” transformations.
- We identify four such “blocks”.

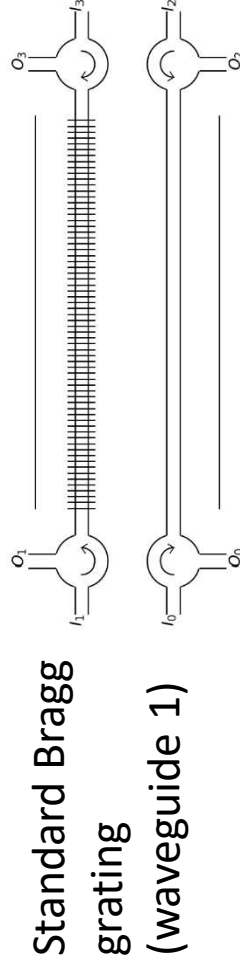


- Transfer matrices can be written in usual form (outputs in terms of inputs) or unidirectional form (right side in terms of left side).
- Express “blocks” in unidirectional form.
- Can decompose any **symmetric unitary** transformation (usual form) into individual blocks (unidirectional form).

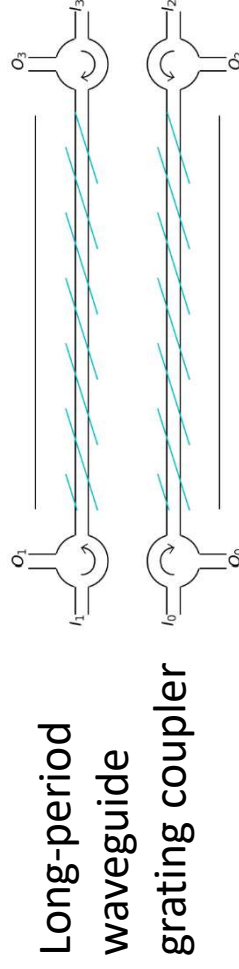
“Fundamental” transformations



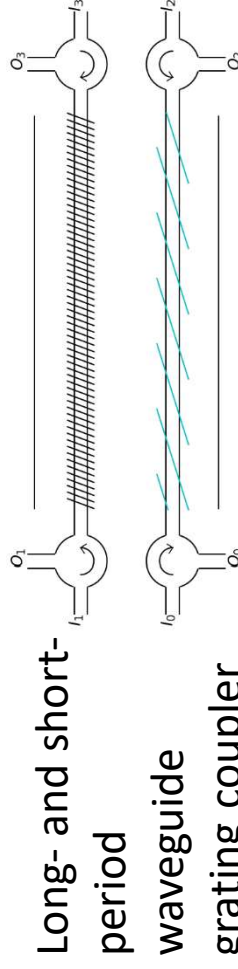
$$\Sigma_0(\phi) = \begin{bmatrix} \cosh(\phi) & \cdot & \sinh(\phi) & \cdot \\ \cdot & 1 & \cdot & \cdot \\ \sinh(\phi) & \cdot & \cosh(\phi) & \cdot \\ \cdot & \cdot & \cdot & 1 \end{bmatrix}$$



$$\Sigma_1(\phi) = \begin{bmatrix} 1 & \cdot & \cdot & \cdot \\ \cdot & \cosh(\phi) & \cdot & \sinh(\phi) \\ \cdot & \cdot & 1 & \cdot \\ \cdot & \sinh(\phi) & \cdot & \cosh(\phi) \end{bmatrix}$$

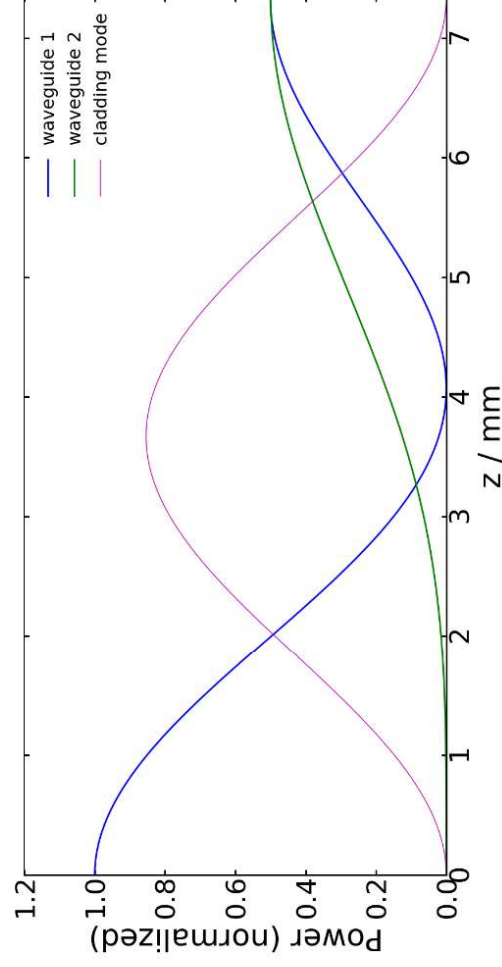
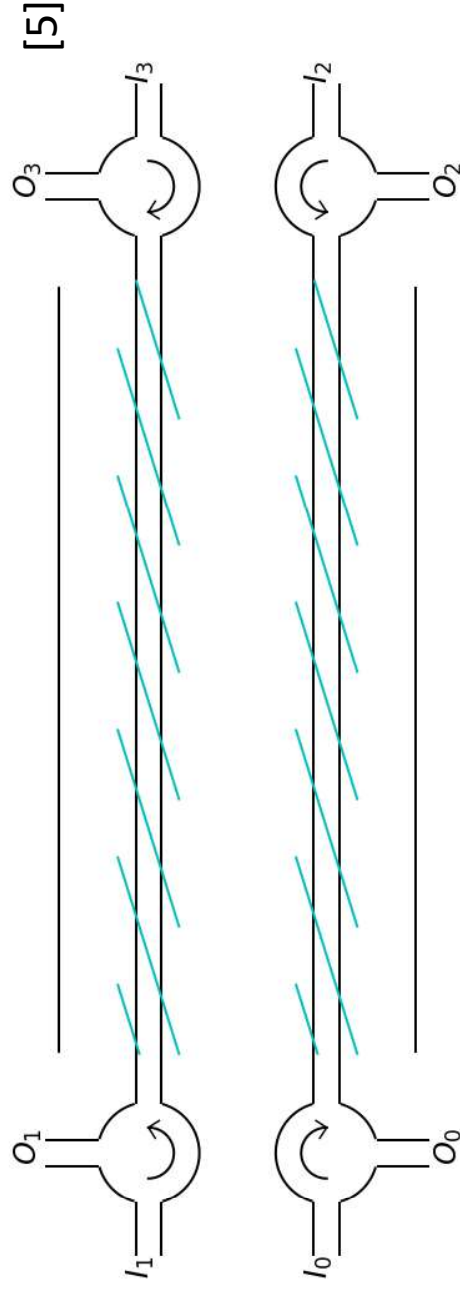


$$\Sigma_2(\phi) = \begin{bmatrix} -\cosh(\phi) & \sin(\phi) & \cdot & \cdot \\ \sin(\phi) & \cos(\phi) & \cdot & \cdot \\ \cdot & \cdot & -\cos(\phi) & \sin(\phi) \\ \cdot & \cdot & \sin(\phi) & \cos(\phi) \end{bmatrix}$$

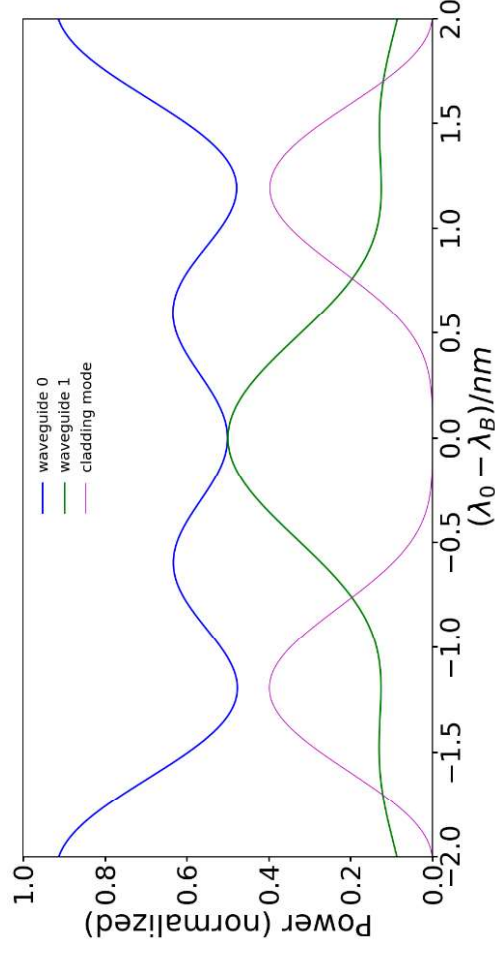


$$\Sigma_3(\phi) = \begin{bmatrix} -\cosh(\phi) & \cdot & \cdot & \sinh(\phi) \\ \cdot & \cosh(\phi) & -\sinh(\phi) & \cdot \\ \cdot & \sinh(\phi) & -\cosh(\phi) & \cdot \\ -\sinh(\phi) & \cdot & \cdot & \cosh(\phi) \end{bmatrix}$$

Long-period waveguide grating coupler

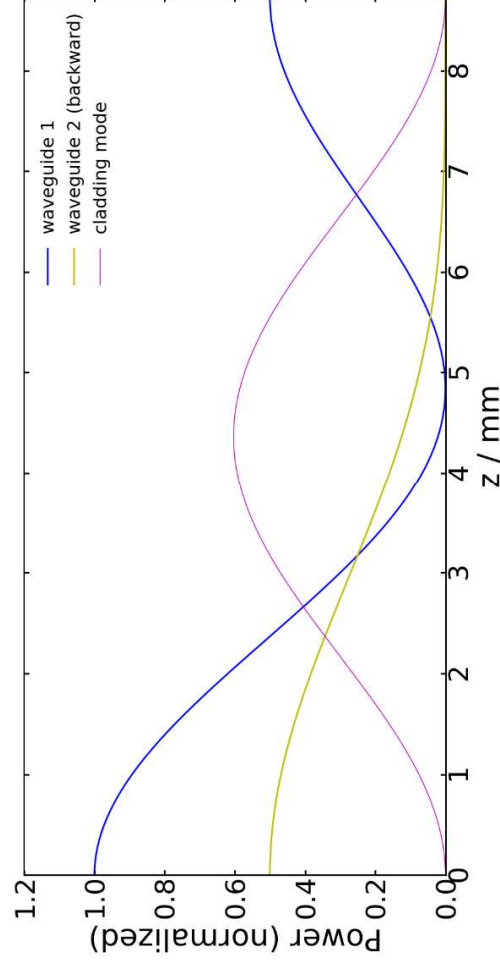
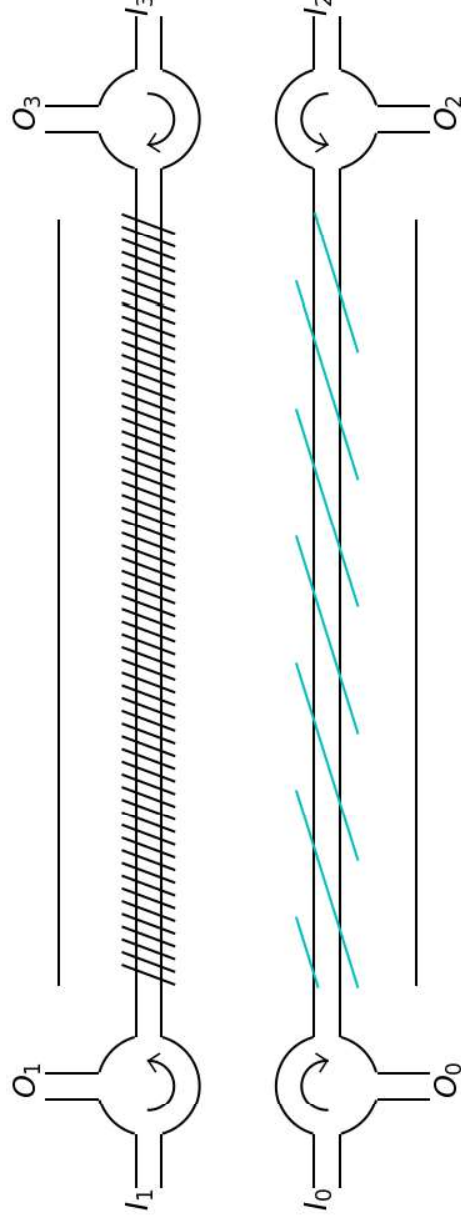


Power propagation through device (50:50 power splitting). Length chosen to avoid leakage from cladding mode at device end.

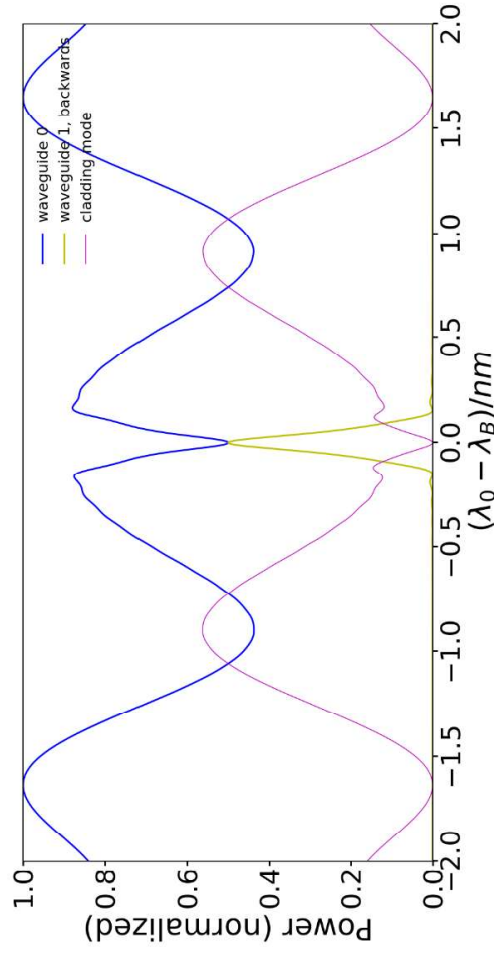


Wavelength sweep of device

Long and short-period waveguide grating coupler



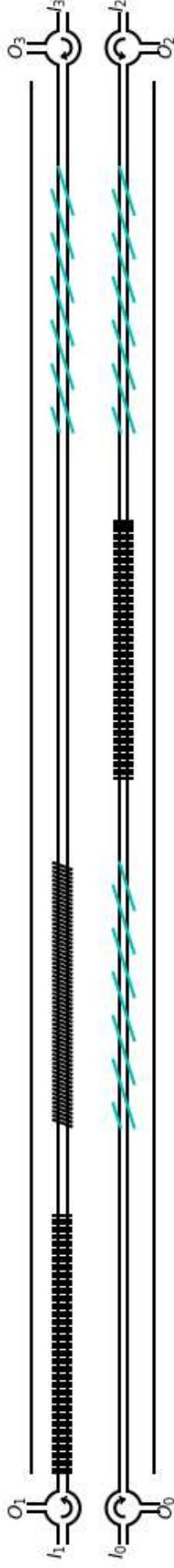
Power propagation through device (50:50 power splitting). Length chosen to avoid leakage from cladding mode at device end.



Wavelength sweep of device

Bandwidth considerably smaller due to short-period grating.

Construction of an arbitrary symmetric unitary matrix.



- Using the above blocks (plus phase shifts), can build up to any matrix of form (unidirectional form):

$$\Sigma = \begin{bmatrix} P & Q^* \\ Q & P^* \end{bmatrix} \quad (1)$$

- In usual form, any matrix that satisfies:

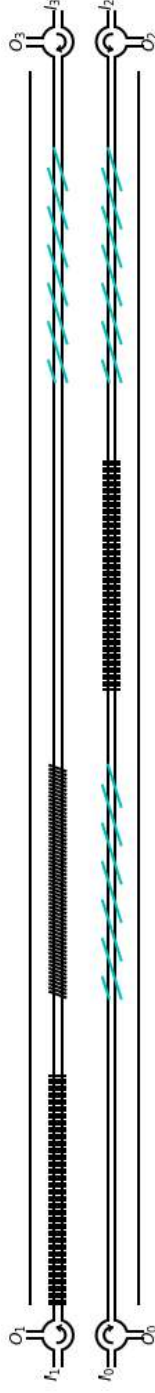
$$S^\dagger \cdot S = I \quad (2)$$

$$S = S^T$$

- Can be expressed as in Eq. (1) in unidirectional form.
- Which means we can construct any matrix that is both:
 - Unitary** ← lossless device
 - Symmetric** ← time reversal

Decomposition of an arbitrary symmetric

unitary matrix



1. Original matrix:

$$\Sigma = \begin{bmatrix} * & * & * & * \\ * & * & * & * \\ * & * & * & * \\ * & * & * & * \end{bmatrix}$$

2. Applying a long-period grating coupler:

$$\Sigma = \begin{bmatrix} * & * & * & * \\ * & * & * & * \\ * & * & * & * \\ * & * & * & * \end{bmatrix}$$

3. Applying a standard Bragg grating in waveguide 0:

$$\Sigma = \begin{bmatrix} * & * & * & * \\ * & * & * & * \\ * & * & * & * \\ * & * & * & * \end{bmatrix}$$

4. Applying a long- and short-period grating coupler:

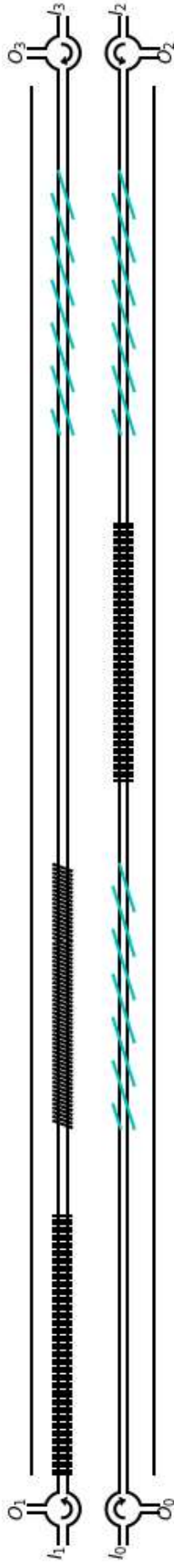
$$\Sigma = \begin{bmatrix} * & \cdot & \cdot & \cdot \\ \cdot & * & \cdot & * \\ \cdot & \cdot & * & \cdot \\ \cdot & * & \cdot & * \end{bmatrix}$$

5. Applying a standard Bragg grating in waveguide 0:

$$\Sigma = \begin{bmatrix} * & \cdot & \cdot & \cdot \\ \cdot & * & \cdot & \cdot \\ \cdot & \cdot & * & * \\ \cdot & \cdot & \cdot & * \end{bmatrix}$$

• In general includes phase-shifts.

Construction of an arbitrary symmetric unitary matrix: Examples



- Walsh-Hadamard transform:

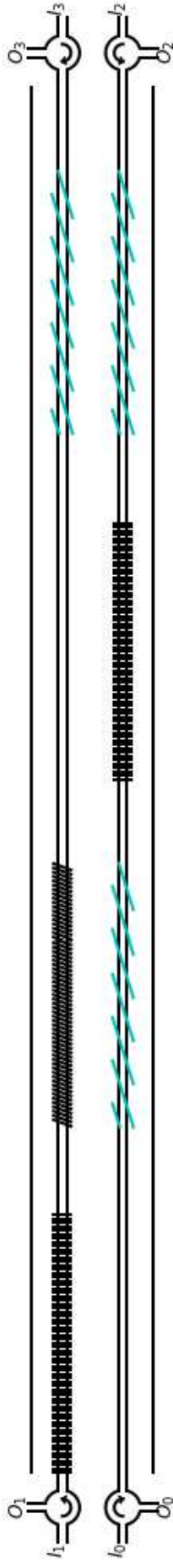
$$W = \frac{1}{2} \begin{bmatrix} 1 & 1 & 1 & 1 \\ 1 & -1 & 1 & -1 \\ 1 & 1 & -1 & -1 \\ 1 & -1 & -1 & 1 \end{bmatrix}$$

- Decomposition:

$$\Sigma_W = \Sigma_2 \left(-\frac{\pi}{4} \right) \cdot \Sigma_0 \left(\operatorname{arctanh} \left(\frac{1}{2} \right) \right) \cdot \Sigma_3 \left(-\operatorname{arctanh} \left(\frac{1}{\sqrt{3}} \right) \right) \cdot \Sigma_1 \left(-\operatorname{arctanh} \left(\frac{1}{2} \right) \right) \cdot \Theta_1(\pi)$$

- Can realise any symmetric unitary matrix by decomposing into four individual “blocks”.

Construction of an arbitrary symmetric unitary matrix: Examples



- Other matrices:

$$QFT = \frac{1}{2} \begin{bmatrix} 1 & 1 & 1 & 1 \\ 1 & i & -1 & -i \\ 1 & -1 & 1 & -1 \\ 1 & -i & -1 & i \end{bmatrix}$$

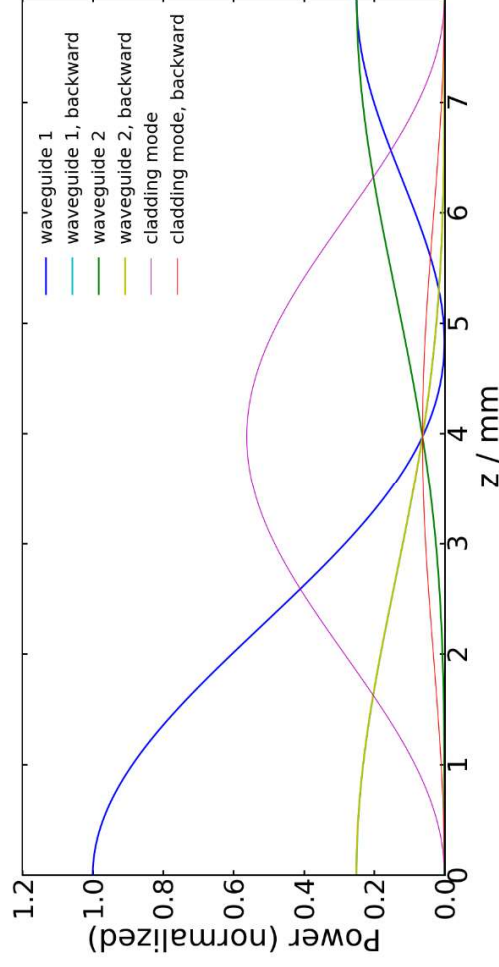
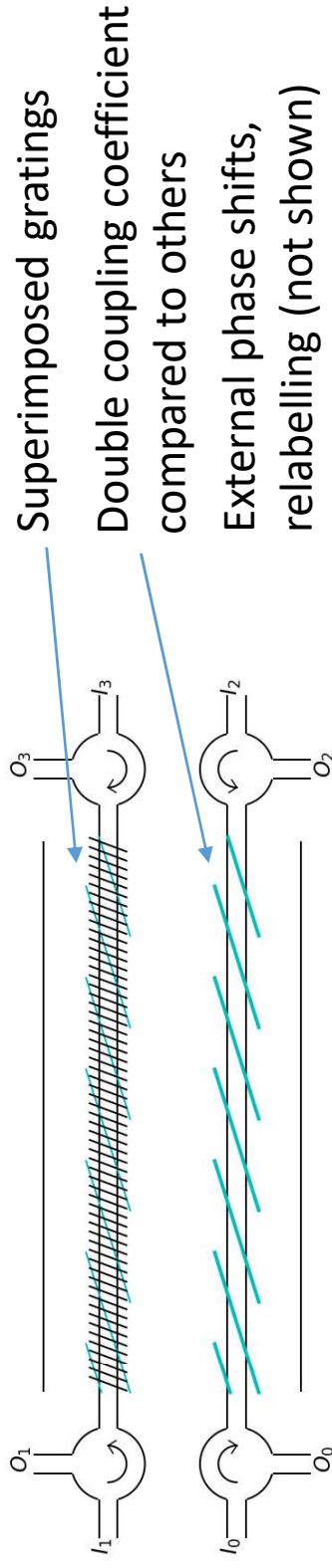
$$\Sigma_{QFT} = \Theta_0 \left(\frac{\pi}{4} \right) \cdot \Theta_1 \left(-\frac{\pi}{4} \right) \cdot \Sigma_2 \left(\frac{\pi}{4} \right) \cdot \Theta_0 \left(\frac{\pi}{4} \right) \cdot \Sigma_0 \left(\frac{\arctan \left(\frac{1}{3} \right)}{2} \right) \cdot \Sigma_0 \left(\frac{\sqrt{10}}{4} \right) \cdot \Theta_0 \left(\frac{\arctan \left(\frac{1}{3} \right)}{2} \right) \cdot \Theta_1 \left(-\frac{\pi}{4} \right) \cdot \Sigma_3 \left(\operatorname{arctanh} \left(\frac{1}{\sqrt{3}} \right) \right) \cdot \Theta_1 \left(-\frac{\pi}{4} \right) \cdot \Sigma_2 \left(\operatorname{arctanh} \left(\frac{1}{2} \right) \right) \cdot \Theta_1 \left(-\frac{\pi}{4} \right)$$

$$CNOT = \begin{bmatrix} 1 & \cdot & \cdot & \cdot \\ \cdot & 1 & \cdot & \cdot \\ \cdot & \cdot & \cdot & 1 \\ \cdot & \cdot & 1 & \cdot \end{bmatrix}$$

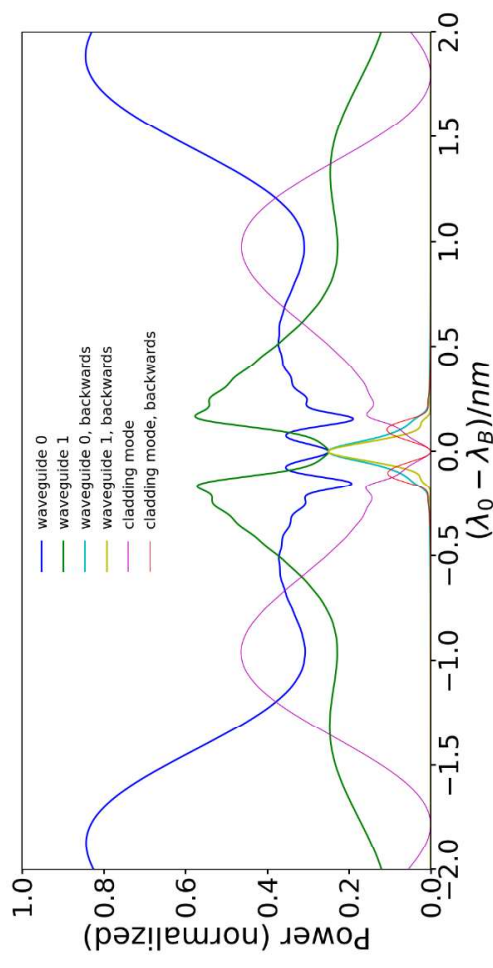
$$\Sigma_{CNOT} = \Sigma_3(\phi \rightarrow \infty) \cdot \Sigma_0(\phi \rightarrow \infty)$$

Compact Walsh-Hadamard transform

- Many transformations can be realised far more simply.
- For example, Walsh-Hadamard:
- One block with three gratings instead of four blocks with six gratings.



Power propagation through device



Wavelength sweep of device

Conclusions

- Proposed/analysed use of counter-propagating modes in an integrated photonics platform.
- Bidirectional propagation doubles the number of modes.
- With two single-mode waveguides, can implement any 4x4 coupler that is both unitary and symmetric.
- Demonstrated implementation using physically realisable parameters in integrated photonics silica platform.
- By super-imposing long- and short-period gratings, can achieve complex transformations in single short device, e. g. compact Walsh-Hadamard.

Acknowledgements

- Funding



**Engineering and
Physical Sciences
Research Council**



4-by-4 Integrated Waveguide Coupler Based on Bi-directional Propagation in Two Single-mode Waveguides

Mathias J. Weisen, James C. Gates, Corin B. E. Gawith, Peter G. R. Smith, and Peter Horak

Optoelectronics Research Centre, University of Southampton, Southampton SO17 1BJ, United Kingdom

Manuscript received July 2020. This research was sponsored by the Engineering and Physical Sciences Research Council (EPSRC) Quantum Technology Programme (EP/M013243/1, EP/M013294/1, EP/T001062/1) and an EPSRC PhD studentship.

Abstract: We propose and investigate theoretically the use of bi-directional propagation of light in silica integrated coupled waveguide structures for linear optical processing of fiber-coupled photons. We show that the class of linear operations that can be implemented in such a system is given by symmetric and unitary matrices. We present how an arbitrary 4×4 coupler of this form can be realized by a linear sequence of more fundamental 2×2 couplers and single-waveguide phase shifters and discuss in detail the implementation in a silica integrated platform utilizing direct UV-written waveguides and long- and short-period grating couplers with tilted gratings for optimized coupling efficiency.

Index Terms: Optical waveguides, Bragg gratings, quantum processing.

1. Introduction

The use of photonic technology for quantum information processing has been the topic of extensive research [1]. Of particular interest are integrated photonic platforms for the manipulation of quantum states, typically using an architecture based on directional couplers between multiple waveguides [2], [3], [4]. For example, a C-NOT gate [5], [6], [7], fast Fourier transforms [8], and quantum transport simulations [9] have been demonstrated with this technology.

More generally, this platform has been used to implement universal linear optics [4], i.e., to implement any linear, classical transformation of light modes represented mathematically by a $N \times N$ unitary matrix, where the condition for a unitary matrix represents a lossless device. This is achieved by decomposing the unitary matrix into a product of simple transformations that can be implemented by directional couplers [10], [11], [12].

These implementations have so far only been made using a single propagation direction with directional couplers based on evanescent field coupling between waveguides. However, other directional couplers exist that utilize Bragg gratings, for example to assist waveguide-to-waveguide coupling in a frequency selective way [13] or for wavelength division multiplexers [14], [15]. Directional couplers have also been constructed as long-period waveguide grating couplers [16], [17], [18] that use a forward propagating cladding mode as an intermediary “bus” mode. This has been proposed as a possible basis for constructing a Walsh-Hadamard transform [19]. Recently we also demonstrated an extension of this scheme in a silica platform exploiting UV-written tilted Bragg gratings and higher order cladding modes in the backward direction for enhanced wavelength

selectivity [20].

Here we target in particular linear operations on a small number of fiber-coupled narrow bandwidth light pulses, e.g, for applications in optically connected quantum networks [21]. Direct UV-written waveguides in a planar silica platform provide an ideal implementation of such devices since they allow for fiber coupling with small insertion loss of 0.1 dB [22] and low propagation losses of 0.2 dB/cm [23], [24]. With direct UV-writing technology it is also possible to simultaneously inscribe waveguides and Bragg gratings [25].

In order to minimize the number of waveguides required, while still maintaining single-mode operation, we here propose the use of both forward and backward propagating modes in UV-written silica waveguides, thereby doubling the number of input and output channels compared to uni-directional systems. However, since every waveguide coupler affects light propagating in both directions, not every arbitrary unitary input-output transfer matrix can be achieved in this system. Instead, we show in the case of 4 input and 4 output modes (i.e., two forward and two backward propagating modes) that every *symmetric* unitary 4×4 matrix can be realized.

Specifically, we consider two UV-written single-mode waveguides contained in a single silica ridge structure that confines light in the transverse direction in multiple cladding modes. Both propagation directions of the two waveguides are exploited, leading to a device with four input and output ports. Tilted gratings are used to couple between all input and output ports via a single high-order cladding mode. Light is coupled to and from each of the ports to optical fibers and the inputs and outputs are separated via optical circulators. We identify a set of fundamental mode couplers that can be concatenated to build up any symmetric and unitary transfer matrix, simulate their implementation, and discuss the realization of several optical processors (Walsh-Hadamard, quantum Fourier transform, CNOT gates).

2. Device Geometry and Theoretical Description

We show a schematic of the proposed device geometry in Fig. 1. It consists of a single silica ridge structure which can be fabricated e.g. by micromachining two parallel trenches in a planar substrate [26]. The ridge structure contains a photosensitive germanosilicate planar core layer with raised refractive index surrounded by top and bottom claddings. Light in this layer is confined to a single mode vertically, but is able to support a number of discrete modes in the transverse direction with well-separated effective mode index. Through direct UV writing [25] two parallel single-mode waveguides are written into the core layer. In the following we refer to the guided modes of the waveguides as “core modes” and to those guided by the core layer as “cladding modes”. Note that these cladding modes are bound in the vertical direction by the higher refractive index of the core layer compared to the surrounding silica and in the transverse direction by the glass-air interfaces of the ridge.

Light from an optical fiber can be coupled at both ends into the two waveguides using waveguide-to-fiber interconnects with high modal coupling [22]. Likewise, the device output occurs at both ends of the waveguides back into the fiber and these outputs are separated from the inputs via four optical circulators as indicated in Fig. 1. Bragg gratings are written by the same direct UV writing technique into the two waveguides and are used to couple light between the forward and backward propagating modes of the two waveguides by using a cladding mode as an intermediary. By carefully choosing the grating parameters we can achieve arbitrary waveguide-to-waveguide coupling ratios while simultaneously ensuring that none of the light escapes via the cladding modes at the input and output ends of the device, see Sec. 3.

Two types of Bragg gratings are used in the device: short-period gratings for coupling of waveguide modes to counter-propagating cladding modes and long-period gratings to couple to co-propagating cladding modes. The gratings are designed for phase matching and, via tilted grating planes, for optimized coupling efficiency to a single cladding mode in order to avoid interference from light coupled via other cladding modes which would reduce the performance of the device. Details of this coupling scheme can be found in Ref. [20]. The combination of

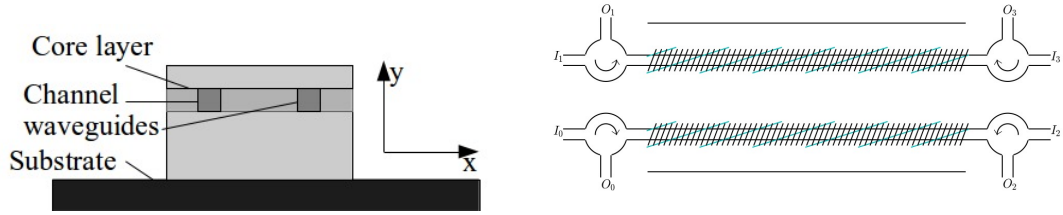


Fig. 1: Left: Cross section of the device in the transverse direction showing the higher refractive index photosensitive core layer with two single-mode waveguides and top and bottom cladding layers. Right: Top view of the core layer showing the two waveguides with incorporated tilted long- and short-period Bragg gratings. Also shown are the optical circulators to separate input and output channels.

short- and long-period gratings allows us to couple light between all four input and output ports. We aim to achieve as wide a range of 4×4 coupling matrices on a single chip as possible, either with a single device or by concatenating individual, more fundamental couplers on a single chip. In either case, the waveguides are coupled to optical fibers at the edge of the chip.

The use of a single-mode core layer allows us to simplify the problem from three to two dimensions using the effective index method [27].

We model this device using coupled mode theory. We first calculate all optical eigenmodes of the structure using a finite differences method and then the coupling coefficients of each grating using the overlap integrals between the core and the cladding modes. Light propagation along all modes is then calculated by solving the coupled mode equations as an eigenvalue/eigenvector problem.

In the following we will assume that light is coupled from the waveguide modes to a *single* forward and backward propagating cladding mode. Such selective coupling is achieved by phase matching with narrow bandwidth gratings of mm to cm length [23], [25], [28], as we will discuss in Sec. 7. With direct UV writing, the gratings are created using the interference pattern of two laser beams and so in principle can be made perfectly sinusoidal, which minimizes higher diffraction orders that could cause unwanted coupling to other cladding modes. Coupled mode theory including *all* cladding modes in this geometry has previously also confirmed that the approximation of a single coupled cladding mode is well justified for the chosen parameters [20] and comparisons of calculated coupling coefficients with full finite element simulations of tilted Bragg gratings have shown excellent agreement [28].

We denote the amplitudes of the light fields propagating in the device by R_n where $n = 0, 1$ refers to the forward propagating modes of waveguide 0 and 1, $n = 2, 3$ refer to the corresponding backward propagating modes and $n = 4, 5$ refer to the forward and backward propagating cladding mode that is used as a bus. The coupled mode equations can then be written as

$$\frac{d}{dz}\mathbf{R}(z) = M \cdot \mathbf{R}(z) \quad (1)$$

where \mathbf{R} is a column vector of the amplitudes R_n and

$$M = \begin{bmatrix} \cdot & \cdot & \cdot & \cdot & -\frac{1}{2}g_2^* & -\frac{1}{2}g_0 \\ \cdot & \cdot & \cdot & \cdot & -\frac{1}{2}g_3^* & -\frac{1}{2}g_1 \\ \cdot & \cdot & i\Delta K_t & \cdot & -\frac{1}{2}g_0^* & -\frac{1}{2}g_2 \\ \cdot & \cdot & \cdot & i\Delta K_t & -\frac{1}{2}g_1^* & -\frac{1}{2}g_3 \\ \frac{1}{2}g_2 & \frac{1}{2}g_3 & -\frac{1}{2}g_0 & -\frac{1}{2}g_1 & i\Delta K_h & \cdot \\ -\frac{1}{2}g_0^* & -\frac{1}{2}g_1^* & \frac{1}{2}g_2^* & \frac{1}{2}g_3^* & \cdot & -i\Delta K \end{bmatrix}. \quad (2)$$

Here g_0 and g_1 are the coupling coefficients of the short-period gratings in waveguides 0 and 1 respectively, g_2 and g_3 are the coupling coefficients of the long-period gratings, “*” denotes

the complex conjugate, and “.” denotes empty matrix elements. $\Delta K_t = \Delta K_h - \Delta K$ and ΔK and ΔK_h are the phase mismatch of the short- and long-period waveguide gratings defined by $\Delta K = -\beta_{core} - \beta_{clad} + K_g$ and $\Delta K_h = \beta_{core} - \beta_{clad} - K_h$ where β_{core} and β_{clad} are the propagation constants of the core modes and the cladding mode, respectively, and K_g and K_h are the grating wavenumbers of the short- and long-period gratings, respectively. While for arbitrary values of the parameters g_n , K_g , and K_h Eq. (1) can only be solved numerically, we will discuss some special analytically solvable cases in the next section. We also note that for simplicity we here assume lossless light propagation in our device. However, realistic losses of e.g. 0.2 dB/cm in silica waveguides [23], [24] will not qualitatively change the results and conclusions derived below.

Note that the waveguides are generally birefringent and we only consider vertically polarized (*y*-polarized) modes. The device can also be designed for the other polarization by appropriate choices of grating parameters.

In principle, this device could also be realized in an all-fiber implementation using a fiber with multiple cores. However, it would be difficult to write gratings of different grating period and tilt angle in different cores in a fiber geometry.

3. Analytical Solutions

In this and the following sections we will restrict our analysis to the case with exact phase matching for both the short- and long-period gratings, i.e., $\Delta K = \Delta K_h = 0$. By analytically computing the eigenvalues and eigenvectors of M , Eq. (2), we find that the general solution of Eq. (1) is:

$$\begin{bmatrix} R_0(z) \\ R_1(z) \\ R_2(z) \\ R_3(z) \\ R_4(z) \\ R_5(z) \end{bmatrix} = p_0 \begin{bmatrix} |g_3|^2 - |g_1|^2 \\ g_1 g_0^* - g_2 g_3^* \\ \cdot \\ g_3 g_0^* - g_2 g_1^* \\ \cdot \\ \cdot \end{bmatrix} + p_1 \begin{bmatrix} g_3 g_2^* - g_0 g_1^* \\ |g_0|^2 - |g_2|^2 \\ g_3 g_0^* - g_2 g_1^* \\ \cdot \\ \cdot \\ \cdot \end{bmatrix} + q_0 \begin{bmatrix} g_0 \\ g_1 \\ g_2 \\ g_3 \\ \cdot \\ 2\gamma \end{bmatrix} e^{-\gamma z} + q_1 \begin{bmatrix} g_2^* \\ g_3^* \\ g_0^* \\ g_1^* \\ 2\gamma \\ \cdot \end{bmatrix} e^{-\gamma z} \quad (3)$$

$$+ q_2 \begin{bmatrix} g_0 \\ g_1 \\ g_2 \\ g_3 \\ \cdot \\ -2\gamma \end{bmatrix} e^{\gamma z} + q_3 \begin{bmatrix} g_2^* \\ g_3^* \\ g_0^* \\ g_1^* \\ -2\gamma \\ \cdot \end{bmatrix} e^{\gamma z}$$

where $\gamma = \frac{1}{2} \sqrt{|g_0|^2 + |g_1|^2 - |g_2|^2 - |g_3|^2}$ and p_0, p_1, q_0, q_1, q_2 and q_3 are arbitrary coefficients. We can see that the device has two regimes of behavior, one for $|g_0|^2 + |g_1|^2 > |g_2|^2 + |g_3|^2$ in which the contribution from the short-period gratings dominates, a photonic bandgap opens up and the light decays exponentially along its propagation direction. The other regime is for $|g_0|^2 + |g_1|^2 < |g_2|^2 + |g_3|^2$ where the long-period gratings dominate and no photonic bandgap occurs, leading to the fields oscillating with a single spatial frequency defined by

$$\Omega = -i\gamma = \frac{1}{2} \sqrt{|g_2|^2 + |g_3|^2 - |g_0|^2 - |g_1|^2}. \quad (4)$$

At the interface between these two regimes, for $\gamma = 0$, all the eigenvalues are zero, and the matrix M becomes defective. Such a device operates at the very edge of the bandgap and becomes very sensitive to phase mismatch.

Next, we set the boundary conditions such that no light enters the cladding modes at the device ends and also no light escapes via the cladding modes at $z = 0$ and $z = L$ where L is the length of the device:

$$R_4(0) = R_4(L) = R_5(0) = R_5(L) = 0. \quad (5)$$

This is only possible in the oscillatory regime and from Eq. (3) we obtain the conditions $q_- \equiv q_0 = q_2$, $q_+ \equiv q_1 = q_3$, and $\sin(\Omega L) = 1$, i.e.,

$$\Omega L = m\pi, \quad (6)$$

where m is an integer number. The z -dependence of the waveguide mode amplitudes is then given by

$$\begin{bmatrix} R_0(z) \\ R_1(z) \\ R_2(z) \\ R_3(z) \end{bmatrix} = p_0 \begin{bmatrix} |g_3|^2 - |g_1|^2 \\ g_1 g_0^* - g_2 g_3^* \\ \cdot \\ g_3 g_0^* - g_2 g_1^* \end{bmatrix} + p_1 \begin{bmatrix} g_3 g_2^* - g_0 g_1^* \\ |g_0|^2 - |g_2|^2 \\ g_3 g_0^* - g_2 g_1^* \\ \cdot \end{bmatrix} + 2 \left(q_- \begin{bmatrix} g_0 \\ g_1 \\ g_2 \\ g_3 \end{bmatrix} + q_+ \begin{bmatrix} g_2^* \\ g_3^* \\ g_0^* \\ g_1^* \end{bmatrix} \right) \cos(\Omega z) \quad (7)$$

and that of the cladding modes by

$$\begin{bmatrix} R_4(z) \\ R_5(z) \end{bmatrix} = -2i \begin{bmatrix} q_- \\ q_+ \end{bmatrix} \Omega \sin(\Omega z). \quad (8)$$

In order to have a non-trivial solution, the fields should be different at both ends of the device and thus m should be an odd number such that $\cos(\Omega L) = -1$.

The device inputs I_m and outputs O_m as shown in Fig. 1 are then given by

$$\begin{aligned} I_0 &= R_0(0), I_1 = R_1(0), I_2 = R_2(L), I_3 = R_3(L), \\ O_0 &= R_2(0), O_1 = R_3(0), O_2 = R_0(L), O_3 = R_1(L). \end{aligned} \quad (9)$$

In later parts of the paper we will use two different ways of defining transfer matrices in our device. The first method relates the light at the output ports to the input ports by the following scattering matrix denoted as S ,

$$\begin{bmatrix} O_0 \\ O_1 \\ O_2 \\ O_3 \end{bmatrix} = S \begin{bmatrix} I_0 \\ I_1 \\ I_2 \\ I_3 \end{bmatrix}. \quad (10)$$

With reference to Figure 1, it is clear that this matrix must be symmetric as a result of the Lorentz reciprocity theorem [29] and unitary if we assume it to be lossless. The second method relates the light at the right hand side to the light at the left hand side of the device by a transfer matrix denoted as Σ such that

$$\begin{bmatrix} O_2 \\ O_3 \\ I_2 \\ I_3 \end{bmatrix} = \Sigma \begin{bmatrix} I_0 \\ I_1 \\ O_0 \\ O_1 \end{bmatrix}. \quad (11)$$

Throughout this paper we will call this second form the “unidirectional matrix”. To relate the two types of transformation matrices we write the matrix S in terms of 2×2 submatrices,

$$S = \begin{bmatrix} S_{00} & S_{01} \\ S_{10} & S_{11} \end{bmatrix}. \quad (12)$$

The corresponding unidirectional matrix Σ is then given by

$$\Sigma = \begin{bmatrix} S_{10} - S_{11} S_{01}^{-1} S_{00} & S_{11} S_{01}^{-1} \\ -S_{01}^{-1} S_{00} & S_{01}^{-1} \end{bmatrix}. \quad (13)$$

For any given input light amplitudes I_n and grating coupling strengths g_n we can solve Eq. (3) for the parameters p_0 , p_1 , q_- , q_+ and with those calculate the transfer matrices S and Σ .

4. Fundamental Transformation Matrices

In this section we introduce a set of “fundamental” transformations that each couple two input and two output ports. As we will show in Section 5, these fundamental operations can be concatenated, together with phase shifts, to achieve the most general 4×4 matrix operation that is possible in this system, in the same way as a universal *unidirectional* $N \times N$ optical transformation can be achieved as a sequence of directional waveguide couplers and phase shifters [10], [11].

The first two of these fundamental transformations can be implemented by standard Bragg gratings in single waveguides. For example, a Bragg grating in the bottom waveguide of Fig. 1 couples the inputs I_0 and I_2 leading to outputs O_0 and O_2 , while the top waveguide modes are left unchanged ($O_3 = I_1$ and $O_1 = I_3$). Analogously, a grating in the top waveguide only couples the other inputs and outputs. The unidirectional matrices corresponding to these two operations can be derived from coupled mode theory and are given by

$$\Sigma_0(\phi) = \begin{bmatrix} \cosh(\phi) & \cdot & \sinh(\phi) & \cdot \\ \cdot & 1 & \cdot & \cdot \\ \sinh(\phi) & \cdot & \cosh(\phi) & \cdot \\ \cdot & \cdot & \cdot & 1 \end{bmatrix}, \quad \Sigma_1(\phi) = \begin{bmatrix} 1 & \cdot & \cdot & \cdot \\ \cdot & \cosh(\phi) & \cdot & \sinh(\phi) \\ \cdot & \cdot & 1 & \cdot \\ \cdot & \sinh(\phi) & \cdot & \cosh(\phi) \end{bmatrix} \quad (14)$$

for Bragg gratings in waveguide 0 and 1, respectively, and $\phi = g_B L/2$ where g_B is the coupling coefficient of the grating.

The next fundamental transformation is achieved by long-period waveguide grating couplers [16], [17] in both waveguides that couple the two waveguides modes to each other via a cladding mode. Eq. (7) leads to the corresponding unidirectional transformation matrix

$$\Sigma_2(\phi) = \begin{bmatrix} -\cos(\phi) & \sin(\phi) & \cdot & \cdot \\ \sin(\phi) & \cos(\phi) & \cdot & \cdot \\ \cdot & \cdot & -\cos(\phi) & \sin(\phi) \\ \cdot & \cdot & \sin(\phi) & \cos(\phi) \end{bmatrix} \quad (15)$$

where $\cos(\phi) = \frac{1-|\alpha|^2}{1+|\alpha|^2}$ and $\sin(\phi) = \frac{2|\alpha|}{1+|\alpha|^2}$ with $\alpha = -g_3/g_2$. Note that this operation couples the two forward propagating modes, but because of the reversibility of the device simultaneously couples the backward propagating modes in the same way.

The final fundamental 2×2 transformation in our system couples the forward propagating mode in one waveguide to the backward propagating mode in the other waveguide. This novel element consists of a long-period grating in one waveguide and a short-period grating in the other. The grating periods of the two gratings are carefully chosen such that both are precisely phase-matched at the same operating wavelength to a single cladding mode. For $|g_1| < |g_2|$ and with a device of length determined by Eqs. (4) and (6), we are able to couple light with practically any coupling ratio between the two waveguide modes under consideration. From Eq. (7) the corresponding unidirectional transformation matrix is given by

$$\Sigma_3(\phi) = \begin{bmatrix} -\cosh(\phi) & \cdot & \cdot & \sinh(\phi) \\ \cdot & \cosh(\phi) & -\sinh(\phi) & \cdot \\ \cdot & \sinh(\phi) & -\cosh(\phi) & \cdot \\ -\sinh(\phi) & \cdot & \cdot & \cosh(\phi) \end{bmatrix} \quad (16)$$

where $\phi = 2 \operatorname{arctanh}(g_1/g_2)$.

Note that for $\phi = 0$, both $\Sigma_2(0)$ and $\Sigma_3(0)$ represent a single long-period grating in waveguide 0 with the device length given by Eqs. (4) and (6). This leads to coupling of the light from waveguide 0 to the cladding mode and back, such that a π phase shift is achieved relative to the light in waveguide 1.

Finally, arbitrary phase shifts of light in a single waveguide can be achieved by off-resonant coupling to the cladding mode via a long-period grating or by directly modifying the propagation

constant of the waveguide by fabricating it with a modified refractive index contrast. The unidirectional transformation matrices for phase shifts in waveguides 0 and 1 are

$$\Theta_0(\varphi) = \begin{bmatrix} \exp(i\varphi) & \cdot & \cdot & \cdot \\ \cdot & 1 & \cdot & \cdot \\ \cdot & \cdot & \exp(-i\varphi) & \cdot \\ \cdot & \cdot & \cdot & 1 \end{bmatrix}, \quad \Theta_1(\varphi) = \begin{bmatrix} 1 & \cdot & \cdot & \cdot \\ \cdot & \exp(i\varphi) & \cdot & \cdot \\ \cdot & \cdot & 1 & \cdot \\ \cdot & \cdot & \cdot & \exp(-i\varphi) \end{bmatrix}. \quad (17)$$

Note that again a phase shift will be induced in both the forward and the backward propagating mode at the same time.

We find the following properties of the matrices: $\Sigma_0(\phi) \cdot \Sigma_0(-\phi) = I$, $\Sigma_1(\phi) \cdot \Sigma_1(-\phi) = I$, $\Sigma_2(\phi)^2 = I$, $\Sigma_3(\phi)^2 = I$ where I is the 4×4 identity matrix in unidirectional space which corresponds to the light being entirely transmitted from each end of both waveguides to the other end. The first two relations predict that a standard Bragg grating with a π phase shift in the center transmits resonant light, as expected for a phase-shift grating Fabry-Perot resonator [30], [31], [32]. The final two relations follow from Eq. (7) and show that doubling the length of the device leads to an entire oscillation, $\cos(2\Omega L) = 1$, which leaves the light in its original state.

5. Construction of an Arbitrary Symmetric Unitary Matrix

By concatenating the fundamental operations discussed above, Eqs. (14)-(17), we can now build up more complex 4×4 couplers. Below we show that we can achieve any arbitrary matrix on this platform that is both *unitary and symmetric*, that is, any matrix S that satisfies the conditions

$$\begin{aligned} S^\dagger \cdot S &= I, \\ S &= S^T \end{aligned} \quad (18)$$

where T and \dagger are the transpose and the conjugate transpose, respectively. The restriction to symmetric matrices is due to the time reversal property of light propagation. Using Eqs. (12) and (13) it can be shown that these conditions are equivalent to unidirectional matrices Σ of the form

$$\Sigma = \begin{bmatrix} P & Q^* \\ Q & P^* \end{bmatrix} \quad (19)$$

where P and Q are 2×2 matrices. Conservation of energy also implies

$$\begin{aligned} 1 &= |\sigma_{00}|^2 + |\sigma_{10}|^2 - |\sigma_{20}|^2 - |\sigma_{30}|^2, \\ 1 &= |\sigma_{01}|^2 + |\sigma_{11}|^2 - |\sigma_{21}|^2 - |\sigma_{31}|^2, \\ 0 &= \sigma_{00}^* \sigma_{01} + \sigma_{10}^* \sigma_{11} - \sigma_{20}^* \sigma_{21} - \sigma_{30}^* \sigma_{31}, \\ 0 &= \sigma_{00} \sigma_{21} + \sigma_{10} \sigma_{31} - \sigma_{20} \sigma_{01} - \sigma_{30} \sigma_{11}, \end{aligned} \quad (20)$$

where σ_{mn} are the elements of Σ .

We will first discuss the case of *real-valued* matrices of the form (18), i.e. the case of symmetric orthogonal matrices S . It can be seen that our four fundamental matrices (14)-(16) are of the form (19). Moreover, real matrices of the form (19) have 8 degrees of freedom (8 real matrix elements of P and Q) but 4 of them are constrained by Eqs. (20), thus leaving 4 independent degrees of freedom and therefore the same number as of our fundamental transformations.

Any arbitrary symmetric and orthogonal (i.e. real-valued) matrix S can be composed by a sequence of our fundamental 2×2 couplers (14)-(16) as follows.

- First, we apply Eq. (13) to convert S into its unidirectional form Σ .
- We apply the matrix $\Sigma_2(\phi)$, corresponding to a long-period grating waveguide coupler, to our matrix with ϕ chosen to set the matrix element σ_{10} to zero. Because of the matrix form (19) this also sets $\sigma_{32} = 0$.

- We apply the matrix $\Sigma_0(\phi)$, corresponding to a standard Bragg grating in waveguide 0, with ϕ chosen to set $\sigma_{20} = 0$. This also sets $\sigma_{02} = 0$ while leaving the matrix elements set to zero in the previous step unchanged.
- Next we apply the matrix $\Sigma_3(\phi)$, which corresponds to our new type of coupler with a long-period grating in one waveguide and a short-period grating in the other. Here we choose ϕ to set $\sigma_{30} = \sigma_{12} = 0$ without changing any of the matrix elements set to zero above. From Eqs. (20) and (19) follows also $\sigma_{01} = \sigma_{03} = \sigma_{23} = \sigma_{21} = 0$.
- Finally, we apply the matrix $\Sigma_1(\phi)$, corresponding to a standard Bragg grating in waveguide 1, with ϕ chosen such that $\sigma_{31} = \sigma_{13} = 0$. We are then left with a diagonal matrix, which can only have entries of ± 1 on the diagonal because of (20).

With this procedure we have therefore found a decomposition of any arbitrary symmetric and orthogonal transformation matrix S into a sequence of fundamental 2×2 couplers (apart from trivial phase shifts of ± 1 which could be corrected at the output ports O_n).

For complex-valued matrices S , a similar decomposition is possible if the matrix S is symmetric and *unitary*. In this case, before any of the matrices Σ_n ($n = 0, 1, 2, 3$) is applied in the decomposition procedure described above an additional phase shift needs to be applied by using one of the phase shift operations, Eq. (17), to make the relevant matrix elements real-valued.

6. Examples of Matrix Decompositions

Using the results of the previous section, we here present a few 4×4 transformations that are of interest for optical information processing and that can be realized in our platform.

As a first example, the Walsh-Hadamard gate S_W in the form

$$S_W = \frac{1}{2} \begin{bmatrix} 1 & 1 & 1 & 1 \\ 1 & -1 & 1 & -1 \\ 1 & 1 & -1 & -1 \\ 1 & -1 & -1 & 1 \end{bmatrix} \quad (21)$$

can be written in the unidirectional form Σ_W as a sequence of binary couplers as

$$\Sigma_W = \Sigma_2 \left(-\frac{\pi}{4} \right) \cdot \Sigma_0 \left(\operatorname{arctanh} \left(\frac{1}{2} \right) \right) \cdot \Sigma_3 \left(-\operatorname{arctanh} \left(\frac{1}{\sqrt{3}} \right) \right) \cdot \Sigma_1 \left(-\operatorname{arctanh} \left(\frac{1}{2} \right) \right) \cdot \Theta_1(\pi). \quad (22)$$

Similarly, the 4×4 quantum Fourier transform S_{QFT}

$$S_{QFT} = \frac{1}{2} \begin{bmatrix} 1 & 1 & 1 & 1 \\ 1 & i & -1 & -i \\ 1 & -1 & 1 & -1 \\ 1 & -i & -1 & i \end{bmatrix} \quad (23)$$

is expressed in unidirectional form as

$$\begin{aligned} \Sigma_{QFT} = & \Theta_0 \left(\frac{\pi}{4} \right) \cdot \Theta_1 \left(-\frac{\pi}{4} \right) \cdot \Sigma_2 \left(\frac{\pi}{4} \right) \cdot \Theta_0 \left(\frac{\operatorname{arctan}(\frac{1}{3})}{2} \right) \cdot \Sigma_0 \left(-\operatorname{arctanh} \left(\frac{\sqrt{10}}{4} \right) \right) \\ & \cdot \Theta_0 \left(\frac{-\operatorname{arctan}(\frac{1}{3})}{2} \right) \cdot \Theta_1 \left(-\frac{\pi}{4} \right) \cdot \Sigma_3 \left(\operatorname{arctanh} \left(\frac{1}{\sqrt{3}} \right) \right) \cdot \Theta_1 \left(-\frac{\pi}{4} \right) \\ & \cdot \Sigma_1 \left(\operatorname{arctanh} \left(\frac{1}{2} \right) \right) \cdot \Theta_1 \left(\frac{\pi}{4} \right). \end{aligned} \quad (24)$$

Various C-NOT transforms can also be implemented. Consider the form

$$S_{\text{CNOT},1} = \begin{bmatrix} 1 & 0 & 0 & 0 \\ 0 & 0 & 0 & 1 \\ 0 & 0 & 1 & 0 \\ 0 & 1 & 0 & 0 \end{bmatrix} \quad (25)$$

that gives $O_0 = I_0$, $O_2 = I_2$ and swaps $O_1 = I_3$ and $O_3 = I_1$. A simple Bragg grating in waveguide 0 in the limit of strong grating strength, $\Sigma_0(\phi \rightarrow \infty)$, gives

$$S_0(\phi \rightarrow \infty) = \begin{bmatrix} -1 & 0 & 0 & 0 \\ 0 & 0 & 0 & 1 \\ 0 & 0 & 1 & 0 \\ 0 & 1 & 0 & 0 \end{bmatrix} \quad (26)$$

which only requires a π phase shift at the output port O_0 to achieve $S_{\text{CNOT},1}$. A C-NOT gate of the form

$$S_{\text{CNOT},2} = \begin{bmatrix} 1 & 0 & 0 & 0 \\ 0 & 1 & 0 & 0 \\ 0 & 0 & 0 & 1 \\ 0 & 0 & 1 & 0 \end{bmatrix} \quad (27)$$

can also be achieved (up to a π phase shift at the output O_0 again) as a sequence of two unidirectional operations

$$\Sigma_3(\phi \rightarrow \infty) \cdot \Sigma_0(\phi \rightarrow \infty), \quad (28)$$

i.e., a highly reflective Bragg grating in waveguide 0 followed by a strong coupler of the forward and backward modes between the two waveguides. Note that the matrix (27) cannot be converted by (13) because $S_{01} = 0$ but the conversion is possible in the limit of negligible but non-zero grating transmissions.

7. Numerical Results

In this section we discuss the implementation of the fundamental transformations introduced in Sec. 4 in our physical platform, Fig. 1. The parameters used for the simulations are the same as in our previous work [20]. We use a refractive index of the cladding of 1.4398 (in practice, this would be the effective index of the slab mode of the core layer), a device width of $34.0 \mu\text{m}$, two waveguides of Gaussian index profile with a $1/e$ half-width of $2.0 \mu\text{m}$, a waveguide index contrast of 0.01 and placed at a distance of $10 \mu\text{m}$ from the center on both sides of the device. The operation wavelength is $1.55 \mu\text{m}$. We compute the modes using 4001 grid points inside the ridge and also simulate an air layer of $5 \mu\text{m}$ outside of the ridge on either side to ensure correct boundary conditions.

This system has 46 different modes propagating in a single direction in total. Modes 0 and 1, as found using the finite differences method, are the symmetric and anti-symmetric core modes of the device and have an effective index of 1.4445. As a “bus” cladding mode we use mode 35 with an effective refractive index of 1.1946. The grating periods are chosen to phase match the modes we want to couple longitudinally and the tilt angle is set to maximize the coupling coefficient. Thus, for standard Bragg gratings coupling counter-propagating waveguide modes the required grating period is 536.53 nm with a tilt angle of 0° . For short-period gratings coupling a waveguide mode with a counter-propagating cladding mode the period is 587.338 nm and the tilt angle 17.23° . Finally, for long-period gratings the period is $6.202 \mu\text{m}$ and the tilt angle is chosen as 72.936° which creates long-period gratings of equal coupling coefficient to short-period gratings with the same index contrast.

For standard Bragg gratings with a grating index contrast of $\delta n_g = 0.001$ we find a grating coupling coefficient $g_B = 2.637 \times 10^{-3} \mu\text{m}^{-1}$. Using Eq. (14) we find that a 50:50 power splitting

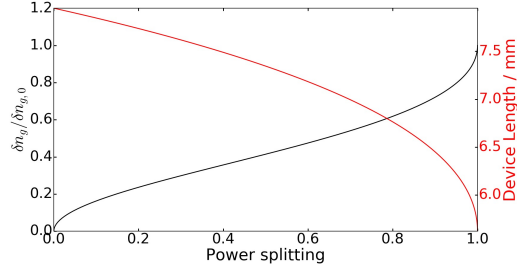


Fig. 2: Grating index contrast ratio (black) and device length required (red) for desired power at output O_3 , normalised to input I_0 , for a long-period waveguide grating coupler with $\Lambda_g = 6.202 \mu\text{m}$, $\theta = 72.936^\circ$ and $\delta n_{g,0} = 0.001$.

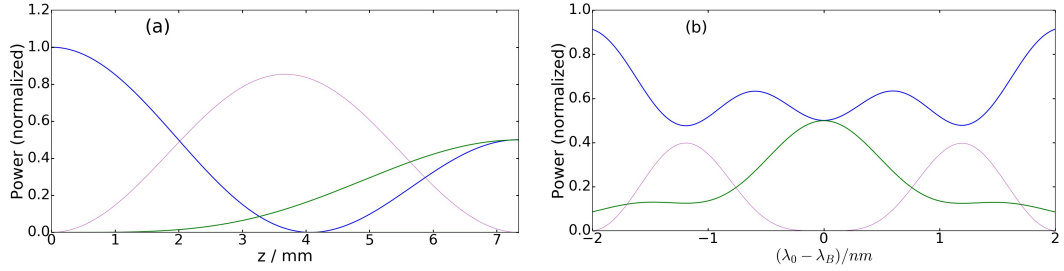


Fig. 3: (a) Power propagation along the forward propagating waveguide (blue and green) and cladding (magenta) modes for a 50:50 beam splitter from Fig. 2. (b) Power output per mode versus wavelength (same colors). Parameters as in Fig. 2 with $L = 7.346 \text{ mm}$ and grating index contrast $\delta n_g = 0.0004142$ in the second waveguide.

is achieved by a 0.668 mm grating and a backreflection of 99% with a length of 2.270 mm . The full-width half-maximum bandwidth in the two cases are found to be 1.392 nm and 0.875 nm , respectively.

With our implementation of long-period waveguide-to-waveguide grating couplers we achieve a coupling coefficient of $g_2 = 7.903 \times 10^{-4} \mu\text{m}^{-1}$ between the core mode and the forward propagating cladding mode with a grating index contrast of $\delta n_g = 0.001$. However, to achieve a given power coupling ratio between the waveguide modes while also ensuring that no light is lost through the cladding mode at the device end facets we need to change both the device length and one of the grating strengths. Using the results of Sec. 3, Fig. 2 shows the grating index contrasts and the device lengths needed to achieve any unidirectional power splitting. We see that device lengths are of the order of $6\text{-}8 \text{ mm}$ for most couplers. As an example, a 50-50 beam splitter requires a grating index contrast $\delta n_g = 0.001$ in waveguide 0 and $\delta n_g = 0.0004142$ in waveguide 1 over a device length of $L = 7.346 \text{ mm}$ which is comparable to the lengths of the devices in [17], [18]. For this device, we also show in Fig. 3(a) the power in each mode along the device, clearly demonstrating that the power in the cladding mode vanishes at both ends. The dependence of the device output as the light wavelength is shifted away from the design wavelength is depicted in Fig. 3(b). We find that the full-width half-maximum bandwidth is 0.637 nm .

Next, we discuss the implementation of the device with a long-period grating in one waveguide and a short-period grating in the other to achieve any splitting ratio between light propagating forward in one waveguide and backward in the other waveguide. The required grating contrast ratios and device lengths calculated with the model of Sec. 3 are plotted in Fig. 4(a). Compared to the device with two long period gratings, Fig. 2, this new device typically requires longer device lengths of order $8\text{-}20 \text{ mm}$. The wavelength dependence of the corresponding 50:50 coupler is also shown in Fig. 4(b). In this case, we find a full-width half-maximum bandwidth of 0.0533 nm .

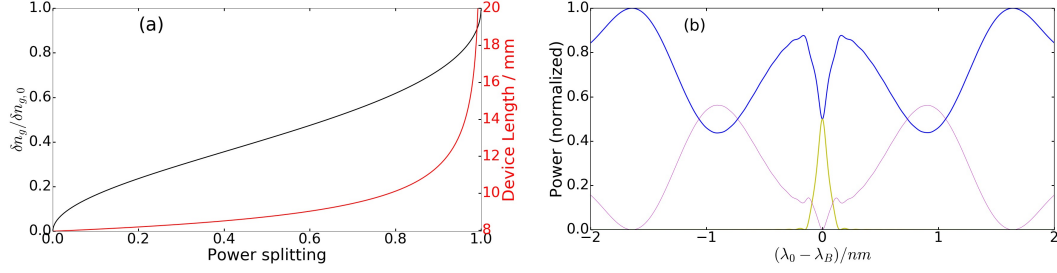


Fig. 4: (a) Grating index contrast ratio (black) and length (red) required for arbitrary power output O_2 , normalised to input I_0 , for the grating coupler with one long- and one short-period grating with $\Lambda_g = 6.202 \mu\text{m}$, $\theta = 72.936^\circ$, and $\delta n_{g,0} = 0.001$ for the grating in waveguide 0 and $\Lambda_g = 587.338 \text{ nm}$, $\theta = 17.23^\circ$, and δn_g in waveguide 1. (b) Wavelength dependence of output power in the forward propagating mode of waveguide 0 (blue), the backward propagating mode of waveguide 1 (yellow) and the forward propagating cladding mode (magenta) of the 50:50 beam splitter found in (a) with $\delta n_{g,0} = 0.0004142$ and $L = 8.734 \text{ mm}$.

We note that the bandwidth of this device is considerably smaller than that of the coupler with two long-period gratings shown previously in Fig. 3(b). This is due to the higher wavelength selectivity of the short period grating where a small change of light wavelength leads to a large change in the phase mismatch because of the counter-propagating nature of the coupled beams, whereas in a co-propagating long-period grating coupler the phase mismatch with changing wavelength is much smaller.

To show how precise our grating periods need to be in order to achieve this implementation of the long- and short-period waveguide coupler, we vary both grating periods around the optimized values for the 50:50 coupler of Fig. 4(b). The resulting power output of the backward propagating mode of waveguide 1 is shown in Fig. 5. We find that the device is much more sensitive to deviations of the grating period of the short-period grating than to that of the long-period grating because of its greater wavelength selectivity, as already discussed above. To ensure correct device operation will therefore require very precise manufacturing of the gratings.

For comparison, with our current experimental setup [23], [24], [25], [26] we estimate that the ridge structure can be micromachined to a precision of $1 \mu\text{m}$ and positioning of the waveguides with respect to the structure is accurate to about 100 nm . The central Bragg wavelength can be defined to a precision of around 0.05 nm . We thus expect that some active tuning, e.g. by temperature, may be required to achieve the accuracy required for the devices discussed in this paper.

8. Compact Walsh-Hadamard Transform

In Sec. 5 we found the most general class of transformations that our platform allows and showed how any such 4×4 coupler can be implemented as a sequence of more fundamental 2×2 couplers. However, such a concatenated device may be impractical to fabricate and sensitive to fabrication limits in each of the constituent fundamental couplers.

Here we demonstrate that it is possible to implement at least some transformations in a much more compact form. In particular, we discuss an alternative implementation of the Walsh-Hadamard transform of Sec. 5 using a single device of superimposed long- and short-period gratings in each waveguide. This solution requires that the two short-period gratings and one of the long-period gratings have the same coupling coefficient while the second long-period grating has a three times larger coupling coefficient. The two short-period gratings must be in phase with each other and

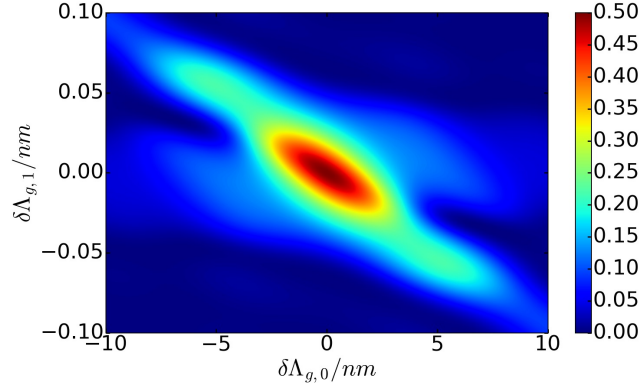


Fig. 5: Power output of the backward propagating mode of waveguide 1 of the 50:50 coupler from Fig. 4(b) as a function of variations of the long- and short-period grating periods $\delta\Lambda_{g,0}$ and $\delta\Lambda_{g,1}$, respectively. Light is launched into waveguide 0; parameters as in Fig. 4.

the two long-period gratings must be out of phase. We therefore require

$$\begin{aligned} g_0 &= g_1 = g_2 e^{i\psi}, \\ g_3 &= -3g_2 \end{aligned} \quad (29)$$

where ψ is an arbitrary phase difference between the short- and long-period gratings. We note that we also found another implementation of the Walsh-Hadamard gate where all gratings have coupling coefficients of equal amplitude and both sets of gratings are in phase. However, as seen in Eq. (4), such a solution is at the interface between the oscillatory and exponential regimes, which leads to an extremely narrow device bandwidth and sensitivity to fabrication imperfections.

In the following we consider the solution of Eq. (29) with $\psi = 0$. Using Eqs. (7) - (9), we find that the transformation matrix relating the outputs to the inputs is

$$S_M = \frac{1}{2} \begin{bmatrix} 1 & -1 & 1 & 1 \\ -1 & -1 & 1 & -1 \\ 1 & 1 & 1 & -1 \\ 1 & -1 & -1 & -1 \end{bmatrix}. \quad (30)$$

By applying a couple of trivial transformations in the form of a π phase shift at the output O_3 and the input I_1 , and by swapping the inputs I_0 and I_2 (i.e., re-labeling them) we recover a Walsh-Hadamard gate of the form

$$\Upsilon_{O,3} \cdot S_M \cdot \Upsilon_{I,1} \cdot \Lambda_{I,02} = \frac{1}{2} \begin{bmatrix} 1 & 1 & 1 & 1 \\ 1 & 1 & -1 & -1 \\ 1 & -1 & 1 & -1 \\ 1 & -1 & -1 & 1 \end{bmatrix} \quad (31)$$

where

$$\Upsilon_{O,3} = \begin{bmatrix} 1 & \cdot & \cdot & \cdot \\ \cdot & 1 & \cdot & \cdot \\ \cdot & \cdot & 1 & \cdot \\ \cdot & \cdot & \cdot & -1 \end{bmatrix}, \quad \Upsilon_{I,1} = \begin{bmatrix} 1 & \cdot & \cdot & \cdot \\ \cdot & -1 & \cdot & \cdot \\ \cdot & \cdot & 1 & \cdot \\ \cdot & \cdot & \cdot & 1 \end{bmatrix}, \quad \Lambda_{I,02} = \begin{bmatrix} \cdot & \cdot & 1 & \cdot \\ \cdot & 1 & \cdot & \cdot \\ 1 & \cdot & \cdot & \cdot \\ \cdot & \cdot & \cdot & 1 \end{bmatrix}. \quad (32)$$

Figure 6(a) shows the power flow between the device modes when power is launched into one of the waveguide modes. As expected, all four output ports then contain 25% of the launched input power while no power exits through the cladding mode at the end facets of the device. The

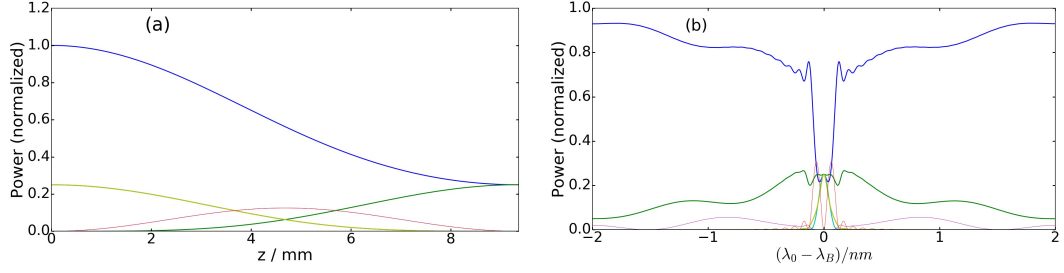


Fig. 6: Compact Walsh-Hadamard gate. (a) Power propagation along the forward propagating waveguide modes (blue and green), backward waveguide modes (cyan and yellow) and along the forward and backward propagating cladding mode (magenta and red). (b) Power outputs of the same modes versus wavelength. Here $\delta_{n,g} = 0.0003$ and $\theta = 17.23^\circ$ for the short-period gratings in both waveguides, $\theta = 72.936^\circ$ for the long-period gratings with $\delta_{n,g} = 0.0003$ in waveguide 0 and $\delta_{n,g} = 0.0009$ with a grating phase-shift of π , in waveguide 1. Light is launched in waveguide 0, device length is $L = 9.364$ mm.

corresponding wavelength dependence is shown in Fig. 6(b). Similar to the device containing one short- and one long-period grating, Fig. 4, this Walsh-Hadamard transform has a limited operating bandwidth of 0.0480 nm, full-width half-maximum and calculated using the power backreflected at output O_1 , because of the wavelength selectivity of the short-period grating. This implementation of the Walsh-Hadamard transform is more compact than the one in [19] because it requires only two as opposed to four waveguides.

Solutions like the one of Eq. (29) for the Walsh-Hadamard gate can be found for arbitrary transformation matrices either by systematic parameter sweeps of coupling coefficients, similar to the figures of Sec. 7, or by numerical optimization, e.g., using Newton's method or the basin-hopping method. However, in contrast to the systematic approach described in Sec. 5 there is in general no guarantee that such optimization algorithms will converge. In general, the solutions that we find using this method can all be built using the "fundamental" transformations we introduce in Sec. 4.

9. Conclusion

We have proposed and analyzed the use of counter-propagating modes in an integrated silica waveguide structure for linear optical processing of fiber-coupled narrowband light for applications in quantum networks. Allowing light to propagate in both directions effectively doubles the number of available modes compared to unidirectional propagation devices. For the specific case of two coupled single-mode waveguides, i.e., two forward and two backward propagating modes, we have shown the class of 4×4 couplers that can be implemented is given by matrices that are both unitary and symmetric. A simple recipe has been presented to decompose any such transformation matrix into a linear sequence of 2×2 couplers and single-waveguide phase shifters.

We have also presented a physical implementation of the scheme by an integrated photonic device with UV-written waveguides and both short- and long-period grating couplers and discussed the parameters and device performance of the different types of 2×2 couplers. Instead of concatenating fundamental couplers, more complex transformations can also be achieved by direct superpositions of short- and long-period gratings, as we demonstrated with a compact Walsh-Hadamard transform.

The data used in this article is openly available at [33].

References

- [1] F. Flamini, N. Spagnolo, and F. Sciarrino, "Photonic quantum information processing: a review," *Rep. Prog. Phys.*, vol. 82, 2019, Art. no. 016001.
- [2] M. G. Thompson, A. Politi, J. C. F. Matthews, and J. L. O'Brien, "Integrated waveguide circuits for optical quantum computing," *IET Circ. Devices Syst.*, vol. 5, no. 2, pp. 94–102, 2011.
- [3] F. Flamini, L. Magrini, A. S. Rab, N. Spagnolo, V. D'Ambrosio, P. Mataloni, F. Sciarrino, T. Zandrini, A. Crespi, R. Ramponi, and R. Osellame, "Thermally reconfigurable quantum photonic circuits at telecom wavelength by femtosecond laser micromachining," *Light. Sci. Appl.*, vol. 4, 2015, Art. no. e354.
- [4] J. Carolan, C. Harrold, C. Sparrow, E. Martín-López, N. J. Russell, J. W. Silverstone, P. J. Shadbolt, M. N., M. Oguma, M. Itoh, G. D. Marshall, M. G. Thompson, J. C. F. Matthews, T. Hashimoto, J. L. O'Brien, and A. Laing, "Universal Linear Optics," *Science*, vol. 349, no. 6249, pp. 711–716, 2015.
- [5] A. Politi, J. C. F. Matthews, M. G. Thompson, and J. L. O'Brien, "Integrated Quantum Photonics," *IEEE J. Sel. Top. Quant. Electron.*, vol. 15, no. 6, pp. 1673–1684, 2009.
- [6] A. Crespi, R. Ramponi, R. Osellame, L. Sansoni, I. Bongioanni, F. Sciarrino, G. Vallone, and P. Mataloni, "Integrated photonic quantum gates for polarization qubits," *Nat. Commun.*, vol. 2, 2011, Art. no. 556.
- [7] X. Qiang, X. Zhou, J. Wang, C. M. Wilkes, T. Loke, S. O'Gara, L. Kling, G. D. Marshall, R. Santagati, T. C. Ralph, J. B. Wang, J. L. O'Brien, M. G. Thompson, and J. C. F. Matthews, "Large-scale silicon quantum photonics implementing arbitrary two-qubit processing," *Nat. Photon.*, vol. 12, pp. 543–539, 2018.
- [8] A. Crespi, R. Osellame, R. Ramponi, M. Bentivegna, F. Flamini, N. Spagnolo, N. Viggianiello, L. Innocenti, P. Mataloni, and F. Sciarrino, "Suppression law of quantum states in a 3D photonic fast Fourier transform chip," *Nat. Commun.*, vol. 7, 2016, Art. no. 10469.
- [9] N. C. Harris, G. R. Steinbrecher, M. Prabhu, Y. Lahini, J. Mower, D. Bunandar, C. Chen, F. N. C. Wong, T. Baehr-Jones, M. Hochberg, S. Lloyd, and D. Englund, "Quantum transport simulations in a programmable nanophotonic processor," *Nat. Photonics*, vol. 11, pp. 447–452, 2017.
- [10] M. Reck, A. Zeilinger, H. J. Bernstein, and P. Bertani, "Experimental Realization of Any Discrete Unitary Operator," *Phys. Rev. Lett.*, vol. 73, no. 1, pp. 58–63, 1994.
- [11] C.-K. Li, R. Roberts, and X. Yin, "Decomposition of Unitary Matrices and Quantum Gates," *Int. J. Quantum. Inf.*, vol. 11, 2013, Art. no. 1350015.
- [12] W. R. Clements, P. C. Humphreys, B. J. Metcalf, W. S. Kolthammer, and I. A. Walmsley, "Optimal design for universal multiport interferometers," *Optica*, vol. 3, no. 12, pp. 1460–1465, 2016.
- [13] D. Marcuse, "Directional Couplers Made of Nonidentical Asymmetric Slabs. Part II: Grating-Assisted Couplers," *J. Lightw. Technol.*, vol. 5, no. 2, pp. 268–273, 1987.
- [14] D. Mechin, P. Grosso, and D. Bosc, "Add – Drop Multiplexer With UV-Written Bragg Gratings and Directional Coupler in SiO₂ – Si Integrated Waveguides," *J. Lightw. Technol.*, vol. 19, no. 9, pp. 1282–1286, 2001.
- [15] W. Shi, H. Yun, C. Lin, M. Greenberg, X. Wang, Y. Wang, S. T. Fard, J. Flueckiger, N. A. F. Jaeger, and L. Chrostowski, "Ultra-compact, flat-top demultiplexer using anti-reflection contra-directional couplers for CWDM networks on silicon," *Opt. Express*, vol. 21, no. 6, pp. 6733–6738, Mar 2013.
- [16] Y. Bai and K. S. Chiang, "Analysis and Design of Long-Period Waveguide-Grating Couplers," *J. Lightwave Technol.*, vol. 23, no. 12, pp. 4363–4373, 2005.
- [17] Y. Bai, Q. Liu, K. P. Lor, and K. S. Chiang, "Widely tunable long-period waveguide grating couplers," *Opt. Express*, vol. 14, no. 26, pp. 2595–2597, 2006.
- [18] K. C. Chow, K. S. Chiang, Q. Liu, K. P. Lor, and H. P. Chan, "UV-written long-period waveguide grating coupler for broadband add/drop multiplexing," *Opt. Commun.*, vol. 282, no. 184, pp. 378–381, 2009.
- [19] S.-Y. Tseng, "Synthesis of a 4×4 Walsh–Hadamard Transformer Using Long-Period Waveguide Grating Arrays," *IEEE Photon. Technol. Lett.*, vol. 21, no. 14, pp. 972–974, 2009.
- [20] M. J. Weisen, M. T. Posner, J. C. Gates, B. E. Gawith, P. G. R. Smith, and P. Horak, "Low-loss wavelength-selective integrated waveguide coupler based on tilted Bragg gratings," *J. Opt. Soc. Am. B*, vol. 36, no. 7, pp. 1783–1791, 2019.
- [21] H. J. Kimble, "The quantum internet," *Nature*, vol. 453, pp. 1023–1030, 2008.
- [22] D. Zauner, K. Kulstad, J. Rathje, and M. Svalgaard, "Directly uv-written silica-on-silicon planar waveguides with low insertion loss," *Electron. Lett.*, vol. 34, no. 16, pp. 1582–1584, 1998.
- [23] H. L. Rogers, A. S., C. Holmes, P. G. R. Smith, and J. C. Gates, "In situ loss measurement of direct UV-written waveguides using integrated Bragg gratings," *Opt. Lett.*, vol. 35, no. 17, pp. 2849–2851, 2010.
- [24] P. C. Gow, R. H. S. Bannerman, P. L. Mennea, C. Holmes, J. C. Gates, and P. G. R. Smith, "Direct UV written integrated planar waveguides using a 213 nm laser," *Opt. Express*, vol. 27, no. 20, pp. 29133–29137, Sep 2019. [Online]. Available: <https://www.osapublishing.org/abstract.cfm?URI=oe-27-20-29133>
- [25] C. Sima, J. C. Gates, H. L. Rogers, P. L. Mennea, C. Holmes, M. N. Zervas, and P. G. R. Smith, "Ultra-wide detuning planar Bragg grating fabrication technique based on direct UV grating writing with electro-optic phase modulation," *Opt. Express*, vol. 21, no. 13, pp. 15747–15754, 2013.
- [26] C. Holmes, L. G. Carpenter, H. L. Rogers, I. J. G. Sparrow, J. C. Gates, and P. G. R. Smith, "Planar waveguide tilted Bragg grating refractometer fabricated through physical micromachining and direct UV writing," *Opt. Express*, vol. 19, no. 13, pp. 12462–8, 2011.
- [27] K. Okamoto, *Fundamentals of optical waveguides*, 2nd ed. Elsevier, 2005.
- [28] M. T. Posner, N. Podoliak, D. H. Smith, P. L. Mennea, P. Horak, C. B. E. Gawith, P. G. R. Smith, and J. C. Gates, "Integrated polarizer based on 45° tilted gratings," *Optics Express*, vol. 27, no. 8, pp. 11174–11181, 2019.
- [29] G. K. Svendsen, M. W. Haakestad, and J. Skaar, "Reciprocity and the scattering matrix of waveguide mode," *Phys. Rev. A*, vol. 87, 2013, Art. no. 013838.

-
- [30] L. Poladin, B. Ashton, W. E. Padden, A. Michie, and C. Marra, "Characterisation of phase-shifts in gratings fabricated by over-dithering and simple displacement," *Opt. Fiber Technol.*, vol. 9, no. 4, pp. 173–188, 2003.
 - [31] J. Zhou, K. Guo, J. He, M. Hou, Z. Zhang, C. Liao, Y. Wang, G. Xu, and W. Y., "Novel fabrication technique for phase-shifted fiber Bragg gratings using a variable-velocity scanning beam and a shielded phase mask," *Opt. Express*, vol. 26, no. 10, 2018, Art. no. 13311.
 - [32] Y. Zhao, J. Ni, F. Zhang, Z. Song, L. Li, T. Chen, and S. Li, "Study on the Characters of Phase-Shifted Fiber Bragg Grating in Asymmetric Perturbation and Its Application in Fiber Laser Acoustic Sensor," *Photonic Sens.*, vol. 8, no. 4, pp. 351–357, 2018.
 - [33] M. J. Weisen, J. C. Gates, C. B. E. Gawith, P. G. R. Smith, and P. Horak, "4-by-4 integrated waveguide coupler based on bi-directional propagation in two single-mode waveguides (dataset)," University of Southampton, 2019, <https://doi.org/10.5258/SOTON/D1639>.
-